Universität Bremen

IMSAS
Institut für Mikrosensoren, -aktoren und -systeme

Development of Wireless Sensor Nodes for Integration into Fiber Reinforced Composites

Dissertation
zur Erlangung des Grades eines Doktors
der Ingenieurwissenschaften
– Dr. Ing. –

von

Lukas Bertram

– Digitalversion –

Referent: Prof. Dr.-Ing. Walter Lang
Koreferent: Prof. Dr.-Ing. Klaus-Dieter Thoben

Eingereicht am: 25.01.2024
Datum des Kolloquiums: 07.11.2024

Vorgelegt im Fachbereich 1
Physik / Elektrotechnik
der Universität Bremen

Acknowledgements

First and foremost, I would very much like to thank my supervisor Prof. Dr. Walter Lang for supporting and generally making possible the research described in this work. It has been a pleasure to be able to work in your team, in a great and open-minded atmosphere where I could independently pursue my research, while always finding valuable counsel and discussion when needed. Also, I would like to thank Prof. Dr. Klaus-Dieter Thoben for his advice and for taking the time to act as the second reviewer of this work.
I further want to give thanks to all my current and former colleagues at IMSAS for their support and all work-related and not-so-work-related discussion, especially those held over cups of coffee. Moreover, I would like to express my gratitude for the invaluable support provided by my fellow researchers at other institutes, who helped me with many of the experiments, especially Michael Brink and Marvin Richrath at BIBA, and David Droste at the Faserinstitut (FIBRE). This also applies to the people at MicroSensys GmbH, in particular Sylvo Jäger and Jesús Vergara, whom I would like to thank for their assistance with programming the RFID reader, and my former student Euphemia Agwa who helped me with the temperature experiments of the first sensor.
Last but not least I want to mention all my friends and family, and the value of their continued support. Thank you, you are great people.
For the encore, here is a shout out to all musicians and the entity of music in general, for always being able to push me. The world would be a far less interesting place without it.

Lukas Bertram

Bremen, Januar 2024

Abstract

Rising importance of energy efficient technology increasingly gives rise to usage of Fiber Reinforced Polymers (FRP) due to the huge potentials offered for lightweight, durable structures. In order to achieve the desired material properties and subsequent behavior, FRP production has to be carefully monitored and controlled. This thesis presents a collection of novel approaches for monitoring FRP fabrication processes and subsequent structural health monitoring applications, by developing flexible, wireless sensors for integration into FRP. To facilitate industrial application, sensor concept explicitly focuses on simple and cost-efficient producibility, and intentionally targets automated sensor placement in an automated FRP production context. In order to minimize impact on FRP material integrity and ease vacuum setup and part handling, the sensors need neither wires nor battery for operation, by making use of Radio Frequency Identification (RFID) technology. Two sensor types have been designed, individually targeting the two main applications with a different focus. Both sensors are able to precisely measure local material temperature. This gives insights into FRP fabrication processes, e. g. resin presence and curing temperatures, and later on FRP operation conditions. Additionally, the first sensor presented is able to measure bi-axial mechanical strain of the finished FRP material by using a temperature-compensated full bridge strain gauge. The second sensor uses a structure of substrate-integrated, interdigital electrodes to give real-time insights into polymer curing behavior by measuring the changing capacitance between the electrode fingers, similar to a common dielectric sensor. To support electrode design for usage with the sensors, a thorough investigation is conducted regarding basic properties of interdigital electrodes, that have been fabricated on flexible polyimide foil via common PCB production technology. This thesis elaborates on development, characterization and limitations of the sensors, and it is shown how they can be used to monitor FRP production and mechanical strain of sensor-integrated specimens.

Zusammenfassung

Die zunehmende Relevanz energieeffizienter Technologien führt zu verstärktem Einsatz von Bauteilen aus Faser-Kunststoff-Verbund (FKV), da diese ein großes Potenzial für leichte und robuste Strukturen aufweisen. Um gewünschte Materialeigenschaften und beabsichtigtes Verhalten zu gewährleisten, muss sowohl bei der Herstellung als auch bei der späteren Verwendung von FKV besondere Sorgfalt aufgebracht werden. In dieser Arbeit werden neuartige Ansätze für die Überwachung der FKV-Fertigung und der Zustandsüberwachung vorgestellt, indem flexible, drahtlose Sensoren für die Integration in FKV entwickelt werden. Um industrielle Anwendung zu erleichtern, konzentriert sich das Sensorkonzept speziell auf eine einfache und günstige Herstellbarkeit, und zielt explizit auf eine automatisierte Sensorplatzierung in einer automatisierten FKV-Produktion ab. Um negative Auswirkungen auf die mechanische Integrität des FKV-Materials zu minimieren und Vakuumaufbau und Handhabung der Teile zu erleichtern, arbeiten die Sensoren vollständig draht- und batterielos, was durch Nutzung von RFID-Technologie (Radio Frequency Identification) möglich wird. Es wurden zwei Sensortypen entwickelt, die die beiden Hauptanwendungen jeweils mit unterschiedlichen Schwerpunkten angehen. Beide Sensoren sind in der Lage, die lokale Materialtemperatur präzise zu messen. So können sowohl Einblicke in die FKV-Fertigungsprozesse, wie z.B. das Vorhandensein von Harz und die aktuelle Aushärtungstemperatur, als auch in die späteren Betriebsbedingungen von FKV gewonnen werden. Darüber hinaus ist der erste Sensortyp in der Lage, biaxial mechanische Dehnung des fertigen FKV-Material zu messen, indem ein piezoresistiver Dehnungsmessstreifen genutzt wird. Der zweite Sensor verwendet eine planare Struktur aus interdigitalen Elektrodenfingern, um kapazitiv Aushärtung des polymeren Matrixsystems messen zu können, ähnlich einer dielektrischen Messung. Diese Struktur ist dabei direkt im Layout des Schaltungsträgers vorgesehen, um so den Aufwand für die Sensorproduktion zu minimieren. Hierfür wurde im Voraus eine tiefegehende Charakterisierung von - mit üblichen Herstellungsverfahren produzierten - Interdigitalstrukturen auf Polyimidfolie durchgeführt, um Eigenschaften und Verhalten im Anwendungskontext zu untersuchen. In dieser Arbeit werden die Entwicklung, Charakterisierung und Limitierungen der genannten Sensoren erläutert, und es wird untersucht, wie sie zur Überwachung von FKV Herstellung und mechanischer Dehnung des FKV Materials im Betrieb genutzt werden können.

Contents

1 Introduction 1
1.1 Fabrication Monitoring . . . 2
1.1.1 Infusion . . . 2
1.1.2 Curing . . . 4
1.2 Load Monitoring / SHM . . . 4
1.3 Conducted Work . . . 6
1.4 Structure of this document . . . 7

2 Theoretical Background 9
2.1 Fiber Reinforced Polymers . . . 9
2.1.1 General Principle . . . 9
2.1.2 Fiber Types . . . 11
2.1.3 Matrix Types . . . 12
2.1.4 Fabrication . . . 13
2.2 RFID . . . 14
2.2.1 General principle . . . 15
2.2.2 Established Standards . . . 15
2.2.3 Inductive Coupling . . . 16
2.2.4 Antenna Design for NFC tags . . . 18
2.3 Strain Gauges . . . 22
2.3.1 Mechanical Strain . . . 22
2.3.2 Piezoresistive Effect . . . 23
2.3.3 Wheatstone Bridge Circuit . . . 24
2.3.4 Lateral contraction . . . 25
2.3.5 Full Bridge Configuration . . . 26
2.4 Interdigital Capacitors . . . 27
2.4.1 Capacitance . . . 27
2.4.2 Dielectric . . . 28
2.4.3 Polarization . . . 28
2.4.4 Permittivity . . . 30
2.4.5 Parallel-Plate Capacitor . . . 30
2.4.6 Interdigital Capacitor . . . 31
2.4.7 Capacitive Strain Gauges . . . 33
2.4.8 Capacitance Measurement . . . 34
2.4.8.1 Method used in this work . . . 35

3 ”Sensor Tag” Concept 37

4 State of the Art and Motivation **41**
4.1 State of the Art - Fabrication Monitoring . . . 41
4.1.1 Differential Scanning Calorimetry . . . 41
4.1.2 Dielectric Analysis . . . 41
4.1.3 Interdigital Sensors for DEA . . . 43
4.1.4 Temperature Monitoring . . . 45
4.1.5 Pressure Monitoring . . . 46
4.1.6 Optical Measurements - Fiber Bragg Gratings . . . 46
4.1.7 Other Techniques . . . 46
4.2 State of the Art - Load Monitoring . . . 47
4.2.1 Strain Gauges . . . 47
4.2.2 Capacitive Strain Gauges . . . 48
4.2.3 Fiber-Bragg-Gratings . . . 49
4.2.4 Other Techniques . . . 49
4.3 Problems with wired sensors for Load and Fabrication Monitoring . 50
4.4 Solution: Wireless Sensors for FRP Integration . . . 51
4.5 Related Work - Wireless Sensors . . . 52

5 Piezoresistive Sensor Tag **54**
5.1 Sensor Design and Fabrication . . . 55
5.1.1 Sensor Concept . . . 55
5.1.2 RFID-Transponder and Micro Controller . . . 55
5.1.3 Antenna . . . 56
5.1.3.1 Calculation . . . 56
5.1.3.2 Validation . . . 58
5.1.4 Strain Measurement . . . 59
5.1.4.1 Strain Calculation from Bridge Voltage . . . 61
5.1.5 Temperature Measurement . . . 63
5.1.6 Sensor Fabrication . . . 63
5.1.6.1 Sensor Substrate . . . 64
5.1.6.2 Assembly . . . 64
5.1.6.3 Software . . . 65
5.2 Characterization and Results . . . 67
5.2.1 Fabrication Monitoring Experiments . . . 67
5.2.1.1 Setup . . . 67
5.2.1.2 Results . . . 69
5.2.2 Strain sensor characterization . . . 70
5.2.2.1 Setup . . . 71
5.2.2.2 Results . . . 72
5.2.3 Tag Influence on FRP Strength . . . 81
5.2.3.1 Setup . . . 81
5.2.3.2 Results . . . 81
5.3 Investigation of System Limitations . . . 86
5.3.1 Power supply . . . 86
5.3.2 Reading Distance . . . 87
5.3.2.1 Setup . . . 88

5.3.2.2 Results . . . 89
5.3.3 Operating Temperature . . . 91
5.4 Conclusions – Piezoresistive Sensor Tag . . . 93

6 Investigations on Interdigital Capacitors **95**
6.1 Analytical Calculation of IDC capacitance . . . 95
6.1.1 Igreja and Dias . . . 96
6.1.2 Endres et. al. . . . 97
6.1.3 Mukhopadhyay et. al. . . . 98
6.1.4 Comparison and Results . . . 99
6.2 Experiments with IDCs . . . 104
6.2.1 IDC design and fabrication . . . 105
6.2.2 IDC Nomenclature . . . 108
6.2.3 Frequency Dependency of IDCs . . . 108
6.2.4 Qualification of Measurement Circuitry . . . 110
6.2.5 Substrate Dependency and Reproducibility . . . 113
6.2.6 Capacitance for different IDC sizes . . . 114
6.2.7 Epoxy Cure Measurements . . . 119
6.2.8 Temperature Dependency . . . 126
6.2.9 XY IDCs . . . 128
6.2.10 Strain Sensitivity . . . 129
6.2.11 Double-sided IDC Layout . . . 131
6.2.12 Summary and Conclusions . . . 132
6.2.12.1 General Findings . . . 132
6.2.12.2 Application-related Findings . . . 133
6.2.12.3 Summary . . . 135
6.2.12.4 Conclusion . . . 136

7 Capacitive Sensor Tag **137**
7.1 Motivation . . . 138
7.2 Sensor Design and Fabrication . . . 139
7.2.1 RFID-Transponder and Micro Controller . . . 141
7.2.2 Antenna . . . 141
7.2.3 Sensor Element: Interdigital capacitor . . . 142
7.2.4 Capacitance Measurement . . . 144
7.2.5 Temperature Measurement . . . 146
7.2.6 Sensor Fabrication . . . 146
7.2.7 Software . . . 146
7.3 Experiments and Results . . . 149
7.3.1 Temperature Influence on Capacitive Measurement . . . 149
7.3.2 Epoxy Cure Test with Sensor Tag . . . 152
7.3.3 Fabrication Monitoring . . . 154
7.3.3.1 Setup . . . 154
7.3.3.2 Results . . . 155
7.3.3.3 Temperature Influence . . . 157
7.3.3.4 Discussion . . . 159

7.3.4 Strain Sensor Characterization 161
7.3.4.1 Setup 161
7.3.4.2 Results 162
7.3.4.3 Discussion 164
7.3.5 Effects of Mechanical Loading on Resonant Circuit 165
7.3.6 Continuous Variation of Capacitance 169
7.4 Investigation of System Limitations 170
7.4.1 Power supply 170
7.4.2 Noise level 172
7.4.3 Reading Distance 174
7.4.4 Operating Temperature 175
7.5 Conclusions – IDC-based Sensor Tag 177

8 Thesis Conclusion **180**

Acronyms **183**

List of Figures **184**

List of Tables **188**

References **189**

A Appendix **203**
A.1 Tag-Reader Interface Specification and command list 203
A.2 Additional Figures 208
A.3 Schematics 212
A.4 PCB Layouts 214
A.5 Publications 216
A.6 Supervised Works 216

Chapter 1
Introduction

Relevance of components and structural parts made from Fiber Reinforced Polymers (FRPs) has been increasing during recent years, as they offer several advantages that make them highly interesting for construction purposes. Especially important in that regard are the unique combinations of weight, strength and stiffness ratios that can be realized with FRP [1]. With only a fraction of the weight, mechanical properties can be achieved that are similar to those of metals, sometimes even outperforming them. Apart from these material properties, FRPs exhibit several more advantages regarding construction of lightweight and application-specific components. Depending on production principle, FRP materials can be made in complex, i. e. freely formed shapes, allowing for highly optimized designs. This is aided by some FRP materials being anisotropic by design, allowing for construction of mechanical parts for specific loading scenarios, i. e. posed by the intended application, reducing overall material input and saving energy during usage. As presented in [1], in comparison to the same components made of steel, FRP components require less energy during production and especially during usage. With drastically rising cost of energy and resources, FRP materials are consequently interesting for construction of lightweight and energy efficient components.

While a multitude of fiber materials exist for polymer reinforcement, glass, carbon and aramide fibers are the most commonly used materials in technical applications [1]. Though usage of carbon fibers can result in even stronger parts in relation to weight, glass fibers are cheaper in comparison [1]. Therefore, production volume and market shares of glass fibers are considerably larger than for any other fiber type [2, 3], which is primarily due to heavy usage of Glass Fiber Reinforced Polymers (GFRPs) in high-volume sectors of wind energy, building and transport.

Despite all their unique advantages, FRP materials also have their respective downsides. Regarding material prices, FRPs are at a disadvantage as compared to metals, as the raw materials are generally more expensive [1, 4]. This is also true for component design processes – due to the complex behavior of FRP materials, design and development of FRP components is comparably expensive. This similarly applies for production. To achieve the outstanding properties previously described, fabrication processes need to be carefully controlled, as they are also very complex. Moreover, during FRP usage, fatigue behavior is a subject of concern, as composite materials react very differently to unforeseen events – this is elaborated in Section 1.2.

This thesis intends to give new approaches for improvement of two major

aspects for FRP components. To this end, two sensor systems have been designed, focusing on different aspects each, by implementing different sensing principles. The first aspect is monitoring of FRP fabrication for improvement of process control and optimization, while the second aspect is concerned with monitoring of FRP component load during usage. As several disadvantages are associated with wired sensors for FRP fabrication monitoring and material integration (see Section 4.3), the sensors are made to be completely wireless. The following section will provide an overview and background information on motivation for development of the sensors. Parts of this work have already been published in [5–8]. This includes parts of Sections 1.1-1.2, and parts of Chapter 4 and Chapter 5, which are extensions of the published texts.

1.1 Fabrication Monitoring

Fabrication techniques for FRP are numerous and the resulting product properties vary depending on the process used [9]. The overall principle is usually similar – in order to combine the advantageous properties of the two ingredients, the fibers need to be surrounded by the matrix material, and arranged into the desired shape. The latter usually implies that the matrix needs to be fluid at some point, in order to enclose the fibers and adjust to the shape. Some techniques use preimpregnated textiles (”prepregs”), i.e. textiles covered in matrix material before arrangement in the mold, but most techniques relevant for structural parts combine fibers and matrix after placement in the mold [9].

1.1.1 Infusion

Before the matrix is introduced in fluid form, dry fiber textiles are arranged in the desired shape and thickness, and fixed into position. Sometimes this can be preceded by an additional ”preforming” process that shapes the textile into a pre-product, simplifying correct placement of the fibers in the mold [9]. After insertion of the textiles, resin infusion usually is supported by application of a vacuum inside the closed mold, so the mold needs to be sealed and evacuated before infusion starts. Evacuation also prevents formation of holes and voids caused by local pockets of residual air. Additionally, the fluid resin itself is degassed in advance, also using a vacuum, to let any dissolved gas and bubbles rise to the surface and leave the resin. For single sided molds, as used in Vacuum Assisted Resin Infusion (VARI) processes, a flexible vacuum foil forms the secondary part of the mold. The resulting pressure difference between inside and atmospheric pressure forces the resin into the form, while also compressing the fibers to achieve a high fiber density and consequently a higher part strength. Double sided molds, e.g. as used in Resin

Transfer Molding (RTM) processes, employ this compression by closing the halves of the molds. The two different principles are schematically displayed in Figure 1.1.

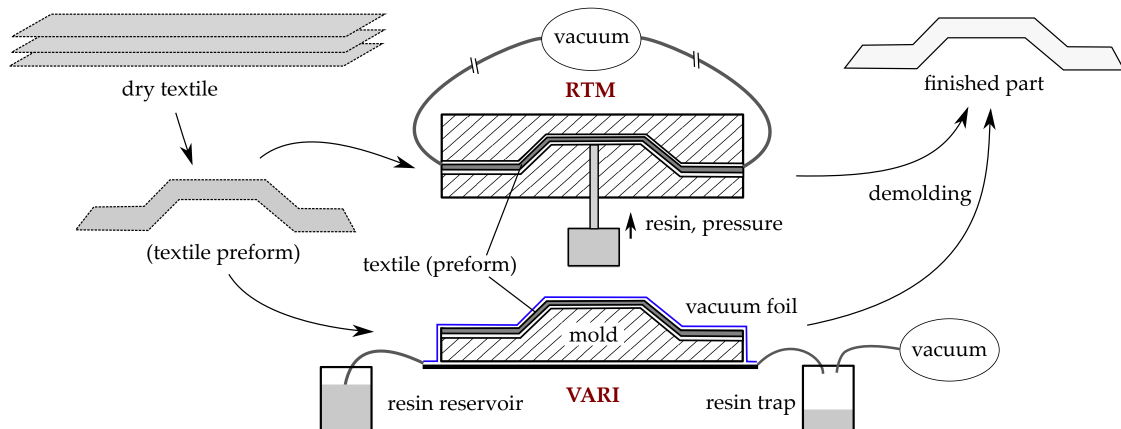

Figure 1.1: Schematic representation of RTM and VARI processes with optional preforming step, according to [9].

As material properties of the fabricated part are strongly influenced by various process parameters, the relevant parameters require detailed control. The most important parameter for FRP fabrication is temperature [10, 11], as it decides about both resin behavior (e.g. viscosity) and behavior of the hardening reaction. Before resin infusion starts, mold and resin temperature are therefore adjusted to achieve desired resin viscosity, flow rate and thereby obtain complete impregnation of the fiber material, while temperature still needs to be low enough to not start resin hardening [11]. Temperature consequently needs to be controlled carefully during infusion, as it affects the progression of the resin flow front through the fiber material. Incomplete impregnation can lead to formation of holes or voids, which degrade loading capabilities of the produced part. In some cases, impregnation can to some degree be monitored visually, e.g. if transparent vacuum foil and resin are used and the part / mold geometry is sufficiently simple, but especially for complex shapes and thick layups this is either impossible or imprecise. In this context, inhomogenous distribution of temperature can therefore adversely influence mechanical part properties.

As temperature distribution can vary throughout the mold over layup thickness due to several reasons – e.g. non-uniform heating or unintended heat dissipation – monitoring and control of processing temperature is a challenging task and holds huge potential for process optimization and quality control. Direct monitoring of the flow front and impregnation could therefore also aid in achieving higher product quality and reduce wastage and energy consumption [12]. The sensors developed in this work consequently aim to optimize monitoring of both infusion flow front and temperature distribution.

1.1.2 Curing

After infusion, in order to make the final part or structure, the fluid matrix needs to become solid again. This hardening process is generally known as curing, and also needs to be controlled carefully to achieve desired mechanical behavior of the resulting structure. Most curing reactions are exothermic, i.e. produce heat, in turn creating another influence on temperature distribution throughout the layers [11]. As curing reaction rate is also dependent on temperature, this can create a feedback loop, potentially creating local temperature maxima, which can degrade the quality of the finished part [13].

To prevent these temperature peaks, curing temperature is usually chosen to be comparably low, resulting in long curing times. As cure state usually is not monitored directly, and especially not inside the laminate, curing progress is often subject to estimation. To ensure sufficient resin cure throughout the whole laminate, curing times are conventionally chosen to be longer for safety reasons, resulting in high cost both in terms of production and energy [10]. Time needed for curing is therefore a major part of production. According to [14], curing takes up to 88% of overall processing time, presenting huge potential for time and energy savings. The systems presented in this work aim to use some of that potential by providing information about actual, local cure status inside the material. Firstly, material integrated temperature monitoring can help shorten curing times, as on the one hand, processing temperature can be controlled more efficiently and potentially harmful temperature peaks can be prevented, that could degrade material quality. On the other hand, if curing kinetics (i.e. correlation of reaction progress and time) of the specific resin material are known, monitoring of local temperature inside the laminate can allow for estimation of curing degree [10], in turn reducing processing time and cost by enabling cure-state-based termination of heating. Secondly, measurement of the local dielectric material properties can be correlated to local matrix viscosity [11, 15, 16]. As matrix cure state is directly connected to viscosity, dielectric measurements can be used to quantify actual curing progress. This correlation has been used for decades in a principle known as Dielectric Analysis (DEA), see Section 4.1. An adaption of this approach is used by the second system developed, which therefore targets actual quantification of local cure state, instead of estimating cure status indirectly via temperature measurement. Consequently, both systems provide information that can be used for process optimization, and especially for reduction of curing duration. If, as presented in [14], a variothermic temperature profile is used instead of commonly used isothermic cure, this potential is further multiplied.

1.2 Load Monitoring / SHM

The second motivation for this work is monitoring of mechanical loads that an FRP material is subjected to during its application. Over a component life cycle,

these can have an influence on its structural health and integrity, for example due to wear symptoms or material fatigue. Additionally, a component may witness extraordinary loads caused by unforeseen scenarios like extreme weather or human failure. Though this is the case for components of every structural material and therefore no new problem for design engineers, it is of a higher relevance for structural parts made from FRP. This is caused by a major disparity in the different material's reactions when subjected to mechanical loads – while a component made of metal will very likely show a dent or other visual mark following e.g. a high impact, FRP materials usually do not show any visual sign of wear, even though the experienced load might have been critical, damaging the part [17]. Additionally, failure mechanisms of FRP structures are difficult to predict, as due to their anisotropic nature, fatigue behavior is dependent on several factors (e.g. layup sequence, fiber directions, materials, etc.). Local delamination or broken fibers, which are a common result of overloads in FRP, can frequently be invisible from the outside [17–19]. Other than common construction materials like metals, a component may therefore look unharmed during visual inspection, but may already be damaged internally. Even though these damages might not directly lead to part failure, they can be a cause for unexpected failure during later usage of the structure, with potentially dangerous or fatal outcomes [17].

To reduce the associated risk, techniques helping with assessment of both the amount of the experienced loads and the actual structural health of a component are of high interest for FRP construction and application, and are referred to as Structural Health Monitoring (SHM) technologies. In a more general sense, SHM describes principles for sensing and recording data about the health and or condition of a structure in an automated way, so that it can be used with devices to detect critical scenarios and consequently damages and risks to the structure [20]. Apart from improvement of FRP reliability and safety, SHM technologies offer further potential advantages. When a structure's health is known, maintenance can be conducted on demand, as opposed to scheduled maintenance, reducing both cost for maintenance and cost for prophylactic exchange of parts. Additionally, data acquired with SHM sensors can potentially be used for control of the overall machine or structure, as it offers a much larger set of information about the structure's current condition, like current temperature or mechanical loading. For example, in a wind turbine, current temperature of the wings could be used for optimized regulation of the internal heating systems needed for prevention of ice buildup, thereby reducing power consumption. Actual wing loading could also be used for optimization of the mechanical regulation relative to current wind speeds, possibly increasing lifetime or reducing unwanted vibrations.

1.3 Conducted Work

This thesis presents a collection of novel approaches for sensor systems aiming to give solutions to the above problems, that is easy and cost effective to produce, and that can be used in increasingly automated FRP production environments. Moreover, the sensors aim to offer advantages for component handling and maintenance during FRP application. To this end, the sensors are designed for integration into FRPs, operating completely wirelessly and without need for a battery. As a result, the negative effects of wire presence on mold vacuum setup, part handling, and sensitivity of the wires themselves are eliminated. For fabrication monitoring, the systems are able to monitor local resin temperature, indicating both local arrival of the resin flow front during infusion, and progression of the curing reaction. This way, processing temperatures and their distribution throughout the laminate can be monitored and used for process optimization and quality control. Furthermore, an approach of making usable the advantages of dielectric cure measurement systems on a wireless sensor is presented, showing great potential for high resolution cure monitoring applications. During FRP usage, the sensors provide an information basis for SHM application. The first sensor can be used to monitor both local material strain and temperature, giving insights into mechanical and thermal loading conditions. While the second sensor system also provides temperature information, simultaneous usage for strain measurement has additionally been investigated, but cross-sensitivities are found to be too high for the current hardware prototype.

The general sensor concept is illustrated in Figure 1.2. The first system incorporates a temperature-compensated, full bridge strain gauge for bidirectional strain measurement, while the second uses an arrangement of interdigital electrodes, i. e. an InterDigital Capacitor (IDC), as its main sensor element. While usage of the strain gauge requires additional steps for mounting and contacting, the IDC is directly incorporated in sensor tag substrate, i. e. on its Printed Circuit Board (PCB), which very much facilitates overall assembly and decreases cost. For communication and power supply, both systems use commercial Radio Frequency Identification (RFID) transponders and micro controllers for data acquisition and storage. To ensure broad compatibility, established RFID communication standards (ISO 14443 and ISO 15693, 13.56 MHz) are used. For usability in increasingly automated production environments, sensor designs specifically target easy applicability for automated sensor positioning, e. g. via robot, by implementing a "sticker-based" sensor tag approach. In order to allow for easy and economical producibility, only off-the-shelf components were used and the sensor substrates (i.e. PCBs) were fabricated in a common industrial process.

Both systems have been characterized regarding accuracy, system limitations and applicability for material integration. Mechanical impact of a sensory inlay on the host material has also been investigated. It could be proven that material-

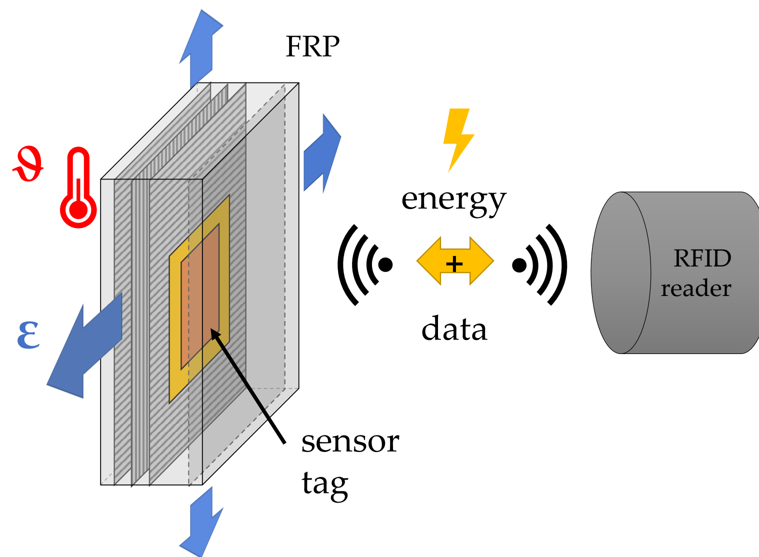

Figure 1.2: Schematic representation of sensor-integrated FRP and RFID reader

integrated sensor nodes with active measurement electronics can be powered without need for wires nor battery, providing detailed information about the FRP fabrication process and subsequently component strain and temperature. Experiments show that strain measurement with the strain gauge is able to yield good results, while the IDC-based approach needs more refinement due to strong cross-sensitivities. Additionally, the material-integrated "intelligence" can be used for further functionality, e. g. for part identification or maintenance. In conclusion, the presented sensor approaches lay a groundwork for usage of the great potential and advantages lying in process optimization and SHM of FRP, in turn saving time, energy and resources, and reducing fatigue-related component failures.

1.4 Structure of this document

The contents of this document are organized as follows. In this first chapter, the motivation for development of the sensors and corresponding background information were introduced. To give a more detailed basis for understanding the presented work, Chapter 2 then provides theoretical fundamentals of the technologies used in this work. As sensor development builds on a "sticker-like" approach, Chapter 3 introduces the underlying concept and the advantages associated. Subsequently, both an overview and an evaluation of the current State of the Art for all relevant technologies is given in Chapter 4. The chapter closes with presenting the motivation for making the sensors wireless, by describing the problems associated with wired sensors for FRP fabrication monitoring and material integration. Building on the information provided up to this point, Chapters 5 and 7 then present the design, implementation, and experiments conducted with the two sensors developed in this thesis. Experimental results are given at

the ends of the two chapters, respectively. In order to lay a groundwork for the sensory element used with the second sensor tag, a detailed study of properties and behavior of IDCs is given in between these two chapters, focusing on IDCs fabricated on flexible polyimide PCBs. To ease understanding of the individual results, a brief summary is given at the end of each chapter. Finally, overall findings are summarized and discussed in Chapter 8, relating and evaluating the results in the application context. The appendix provides supplementary information on the sensors, the communication protocol, additional figures, schematics, and PCB layout.

Chapter 2
Theoretical Background

This chapter will briefly summarize the basic theoretical background for development of the wireless sensors developed in this work. To begin with, some general background information on FRPs is laid down, including their general principle, fiber and matrix types and fabrication techniques. Secondly, theoretical background and working principle of RFID in general, and HF-RFID in particular are given, focusing on working principles, different frequencies and corresponding standards, and the principle of inductive coupling and respective antenna design. Subsequently, the theoretical background on the two main sensor elements is presented, namely piezoresistive strain gauges and IDCs. For strain gauges, this encompasses details on basic function, circuit layout, and respective formulas for calculation of bridge voltage and strain, mainly for the full bridge configuration. Regarding IDCs, this includes general theory of capacitance, factors influencing it, and the transformation from parallel plate capacitor to planar, i. e. interdigital capacitor. Several approaches on analytical calculation of IDC capacitance can be found in Section 6.1. Finally, some light is shed on different principles for capacitance measurement. The background for FRP fabrication monitoring and SHM related aspects is described in Sections 1.1, 1.2, while the current state of the Art for related sensing systems is presented in Chapter 4.

2.1 Fiber Reinforced Polymers

As all the different types of FRPs and techniques used for their production are very high in number, this section will only give a very broad overview of the topic. For detailed insights, the interested reader is pointed to corresponding literature, i. e. [1, 3, 9, 21, 22].

2.1.1 General Principle

As the name suggests, fiber reinforced polymers are polymer materials, i. e. plastics, that have been strengthened by the addition of fibrous materials. The general principle can be studied in nature, e. g. wood, muscle, bone, etc., and has been used in technology for a long time. Table 2.1 compares tensile strength and density for some exemplary FRPs and metals. Comparably flexible or brittle materials, which would on their own not be able to bear high loads, are combined with strong fibers, that on their own would not be able to stay in position or withstand

exterior influences. This way, advantages are combined in a new material with completely new properties. The fibers can take up the forces, while the matrix encloses the fibers, protecting them from outside influences and fixing them in position. Figure 2.1 schematically displays combination of fibers and surrounding polymer, i. e. matrix, into an unidirectional layer and the combination of layers to form a multidirectional composite.

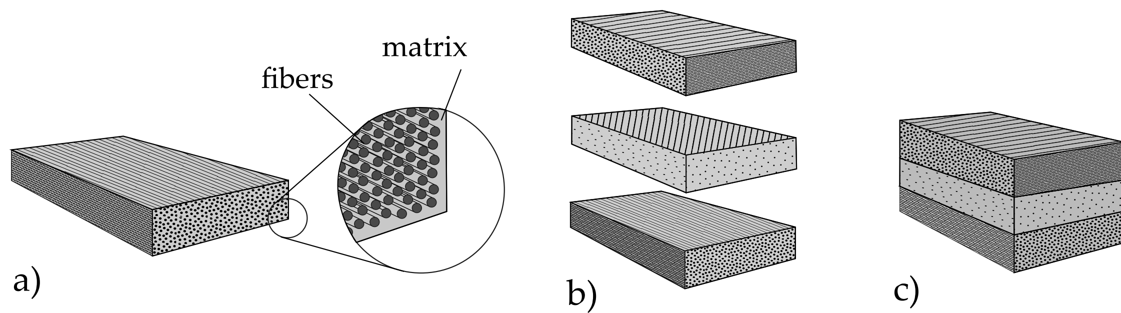

Figure 2.1: Schematic representation of fibers and matrix; a) unidirectional layer; b) joining of multiple layers with different fiber direction; c) multidirectional composite. Adapted and redrawn from [1].

Table 2.1: Tensile strength and density of exemplary FRP and metals [4]

Material	Tensile strength (N/mm^2)	Density (g/cm^3)
GFRP	3400	2.6
CFRP	5600	1.8
Aluminum	400	2.7
Steel	600	7.9
Brass	460	8.0

As materials, and direction and amount of the fibers can be adjusted, FRP properties can be tailored to the intended application. This way, FRPs can offer several advantages over common materials [1, 4]:

- high strength and stiffness in relevant directions while having very low density
- very good shapeability, i. e. design of custom forms
- due to the easy shapeability, complexly formed prototypes can be made with comparably low cost, supporting design and part development
- excellent corrosion and temperature resistance of both fibers and matrix
- electrical properties can be influenced by choosing the right materials for fibers and matrix, allowing for either conductive or isolating behavior of the FRP

- compared to metals, FRPs are able to take up much more energy e. g. in a crash situation, which can be used in failure calculations of different applications
- regarding overall energy footprint, FRPs can outperform conventional construction materials like metal especially during usage, as much less energy is needed for movement

Of course, FRPs also have disadvantages, the most prominent of which are high material and production cost. The latter being mostly due to long times needed for production and high percentage of manual labor during the production process. Also, at the end of the FRP life cycle, recycling FRP materials is a topic that has still not yet been sufficiently investigated, especially for industrial scale application [23, 24]. In context of limited resources, this aspect remains a downside of FRP materials.

2.1.2 Fiber Types

Depending on intended properties, a multitude of fibers can be used for reinforcement of the polymer. Some examples are glass, carbon, metal, plastics (e.g. polyethylene, polyamide, aramide, etc.) or natural fibers (e.g. hemp, wool, etc.). Regarding sustainability, natural fibers are gaining in relevance, but at the time being, glass, carbon and aramide fibers are mainly used for load-bearing technical applications or structural parts [1]. Glass fibers in particular make up about 90 % of the overall production [3], mainly due to comparably low cost. This is reflected in Table 2.2, which summarizes properties for different fiber materials.

Depending on fiber length, fibers can be introduced into the material either directionally, if they are long, or randomly, if they are short, resulting in different material properties of the final FRP. Composites with directional fibers are more able to bear high loads, while shorter fibers are cheaper and still able to reinforce the matrix significantly [3]. This allows for tailoring material properties according to the application.

As fibers are generally only able to take up loads in longitudinal direction, fibers are usually aligned prior insertion into a mold, to achieve high material strength. This is done by making pre-products, e. g. by sewing unidirectional fiber bundles into a fiber mat or by weaving or knitting fiber bundles to form textiles [4]. These textiles can then be easily arranged and stacked up in the mold, ensuring desired fiber orientations and layup sequence (see Figure 2.1), so that the resulting component is able to take up the loads in relevant directions. The alignment of stacked directional textiles is usually denoted in the description, e. g. biaxial, triaxial, quadraxial, etc., commonly referring to configurations of 0,90 °/±45 °; 0,±45 °; 0,±45,90 °. The more fiber directions are part of a layup, the closer the resulting material properties get to being isotropic – quadraxial layups are correspondingly often called quasi-isotropic.

Table 2.2: Tensile strength, density, and relative cost of some fiber materials, adapted from [22]

Material	Tensile strength (MPa)	Density (g/cm^3)	Relative cost
Carbon (Type HS)	4000	1.6	high
Glass (Type E)	3200	2.6	low
Glass (Type S)	4000	2.5	low
Aramide	3000	1.3	medium
Polyethylen	3500	0.9	medium

2.1.3 Matrix Types

Matrix materials used for FRP production are as manifold as materials used for fibers. The main purposes that the matrix fulfills in a composite are as follows [1]:

- fixing the fibers in position, preventing them from rubbing at each other and glueing together the fibers, thereby optimally transferring loads into and across the fibers
- taking up loads occuring different from fiber direction and preventing fibers from creasing
- glueing together the fiber layers, thereby transferring loads throughout the whole composite
- protecting fibers from exterior influences (e. g. mechanical, chemical or radiation)

Consequently, choice of matrix material strongly influences resulting properties of the final composite. Generally, matrix materials can be divided into three groups, based on their plasticity:

The first group encompasses all materials that cannot be reshaped after curing, i. e. hardening, neither by temperature or any other way. These are generally called duroplastic, and are usually made via a chemical reaction, resulting in large, interconnected macro molecules. For this, usually two components are mixed for the reaction, which are commonly called resin and curing agent. After mixing, they are introduced into the mold, and the chemical reaction is initiated, e. g. by heat, radiation or catalysts. As duroplastic matrices exhibit several distinct advantages, they are the most used kind of matrix materials [1]:

- Due to the highly interconnected molecular structure, mechanical and chemical resilience are very good.
- The low viscosity of the initial component mixtures allows for easy handling and good impregnation, making usage comparably easy.

- As they have been in use for a long time, applications can profit from extensive knowledge about material behavior.

Needless to say, duroplastic matrices also show some adverse properties. If not reinforced by fibers or fillers, they can be very brittle, making them unsuitable for construction. Moreover, as they are not meltable, they are neither weldable nor easy to recycle. Some frequently used examples for duroplastic matrices in FRP are: Epoxy resins (EP), (Unsaturated) Polyester resins (UP) and Vinyl Ester resins (VE).

The second group consists of thermoplastic materials – aggregate state of these can be influenced by temperature, i. e. they can be melted, introduced into the mold, and solidified in the desired shape by decreasing temperature [1]. In contrast to duroplastic materials, their molecular structure is not interconnected. Instead, their long molecule chains are entangled and crystalline structures can be formed, resulting in their solid form at lower temperatures. Depending on the specific material, both amorphous and crystalline structures can form, even at the same time, influencing the overall mechanical properties. With rising temperatures, Brownian molecular motion increases, enabling the molecules to move more freely, thereby allowing for plastic deformation of the overall material. Given sufficiently high temperatures, viscosity decreases further, resulting in a fluid phase that can be easily shaped in molds, e. g. by injection molding. As this process is reversible, they can be welded and recycling of thermoplastic matrices is much easier, making these materials gain in relevance for sustainable composite production. For FRP production, polypropylene (PP), saturated polyesters (PBT and PET), and polyamides (PA) are mainly used.

The latter group contains materials that are highly elastic, which is why these are called elastomers. Due to their low strength, these are generally not usable for usage in components that have to take high loads. They are mainly used for parts that are elastically stretched, e. g. belts, pressure hoses, tires, etc..

2.1.4 Fabrication

Making up about a quarter of the overall production volume, larger components are made in huge molds with fluid resins and reinforcements, using mainly VARI and manual lamination techniques in open-faced molds [3, 22]. These processes generally employ pre-produced textiles, and are mostly used for production of smaller numbers, e. g. for boats and wind turbines. Correspondingly, the associated cost is relatively high due to the high amount of manual labor necessary. In comparison with other fabrication techniques, mechanical properties of the resulting materials are not quite as good though [22]. Initial cost i. e. investment is comparably low, as not much is needed in terms of technology or machines, making these techniques optimal for prototyping.

Resin injection techniques like RTM, but also injection molding of thermoplastic

matrices reinforced with short fibers, are also used for many applications [3]. Using two-sided molds, usually made of metal, these techniques provide the advantage of being able to produce smooth i. e. flat surfaces on both sides, as opposed to open-faced molds. Mainly, smaller parts are made in mass production, using automated processes and pre-products, e. g. for the electronic and automotive industry. The high amount of automation allows for relatively low production cost and production of large quantities, though initial investment is correspondingly high.

Pre-impregnated textiles, instead of combining fibers and matrix in the mold, can also be used for FRP production [22]. These techniques use so-called "prepregs", which are a combination of fiber pre-products and partially cured matrix, that are arranged in a mold, both open-faced or double faced, and cured e. g. by hot pressing or inside an autoclave. Though production cost in general is comparably high, and production rates are rather low, this technique is able to yield highest mechanical properties [22]. For this reason, prepregs are used for applications requiring high component performance, e. g. aerospace or aviation.

Another principle, mainly used for production of beams, pipes and profiles, is called pultrusion [22]. It is able to produce continuous, i. e. endless, structures with constant cross section, by impregnating continuous fiber strands, that can optionally be woven or braided, pulling the wet fibers through a shaping cross section and subsequently curing it in an oven. Both thermoplastic and duroplastic matrices can be used. As with other highly automated techniques, cost for equipment is comparably high, but FRP production cost is proportionally low.

Regarding applicability of the sensor systems developed in this thesis, more information on FRP fabrication techniques is given in Section 1.1.

2.2 RFID

Radio Frequency Identification principles in general have been in use for more than 3 decades now [25]. Applications are numerous and their number is growing increasingly, also due to ever progressing miniaturization of electronics and decreasing power requirements thereof. While initially RFID was intended for simple identification tasks, similar to optical identification systems, e. g. bar codes, capabilities of RFID systems have increasingly grown. As of now, applications like contact-less payment or ticketing have already been integrated into everyday life, and new application fields are emerging, e. g. for wireless sensors and in context of the Internet-of-Things (IoT). This section will briefly outline the most relevant aspects of RFID and principles necessary for the scope of this work. An in-depth account on RFID, its principles, subclasses, applications, frequency bands and more is given in [25], while [26] and [27] comprehensively review RFID technologies in context of wireless sensors.

2.2.1 General principle

In general, an RFID system is always made up of at least two components [25]: One is the wireless part, which is called transponder and is generally instationary, as it is connected to the object to be identified. It is usually built from a coupling element, i. e. an antenna, and some electronics in the form of Integrated Circuits (ICs), providing transponder function, which is usually at least a basic data storage (e. g. for simple identification systems). More complex transponders also incorporate other electronics and functions, e. g. micro controllers calculating authorization-related information on a credit card or sensoric elements. Usually, the wireless communication and energy reception is handled by a dedicated IC, that optionally allows for powering other electronics on the transponder by providing a dedicated energy harvesting output. Though some transponders do comprise an energy storage, e. g. battery, most transponders are completely passive – they are solely supplied wirelessly via the reader.

The second component is called reader, and it is usually stationary, though this distinction increasingly diminishes, e. g. due to Near Field Communication (NFC)-enabled smartphones. The reader wirelessly supplies the transponder with energy via its own coupling element, i. e. antenna, and communicates data to and from the transponder, also via the antenna. This is done using electromagnetic waves / inductive coupling (see Section 2.2.3)g, utilizing different frequencies and amplitudes. In general, the reader is connected to the overall application, e. g. a computer system or a Programmable Logic Controller (PLC), which makes use of the information supplied by the transponder.

2.2.2 Established Standards

Several standards for RFID systems have been established, targeting different application fields. Depending on application, different reading distances are desirable, and depending on utilized frequency, different reading ranges can be achieved. For RFID, the frequency bands are commonly divided into LF (Low Frequency), HF (High Frequency) and UHF (Ultra High Frequency). Table 2.3 lists some of these standards and associated properties (this overview is not comprehensive though). Mainly, the standards were designed for contact-less chip cards, e. g. for payment and authentication, but for the emerging trend in wireless sensors that are not actually based on a card-like shape, the usage of established standards obviously suggests itself. Depending on frequency and standard, different amounts of power are transmitted from the reader to the transponder. For sensoric applications, transmitted power must be sufficiently high to power the sensor electronics, which is why especially the HF-Band is relevant in this case. Especially for transponders employing active electronics, technology in the HF-band is currently the only one capable of supplying enough power for continuous operation, via energy harvesting.

A good overview of different RFID standards for wireless sensors based on energy harvesting is given in [26]. Passive sensors without dedicated electronics exist, which usually employ the "sensoric antenna" approach (see also Section 4.4).

Table 2.3: Comparison of different RFID standards, achievable reading distances, data rates and obtainable power via energy harvesting [25, 26, 28].

Band	Frequency	Standards	Reading distances	Data rates	Power (EH)
LF	<135 kHz	ISO11784/5, ISO18000-2	Medium – high	low	low
HF	13.56 MHz	ISO14443, ISO15693, NFC	Low – medium	medium	up to 10 mW[26]
UHF(passive)	868-950 MHz	ISO18000-4, ISO18000-6	high	high	few µW[26]
UHF(active)	135 kHz-5.8 GHz	ISO18000-7	highest	high	n.a.

No publications could be found for energy harvesting (EH) in the LF band, that actually provided numbers regarding harvested power. Energy harvesting at LF is definitely possible though, see e. g. [29].

Systems using NFC are a subclass of HF-RFID and are therefore based on electromagnetic communication in the 13.56 MHz band [25, 26, 28]. NFC is defined in a standard of its own, but systems implementing NFC can often also be used with equipment implementing ISO 14443 or ISO 15693 [25]. Especially due to its extensive use in payment systems, usage of NFC technology has immensely increased over the last decade [26]. This also applied for NFC-based sensors – the number of sold sensors drastically increased from 2012 to 2018, showing a trend similar to an exponential growth [26]. As sensors are an integral part of the IoT [27], it is expected that NFC-based sensors will continue to gain in relevance, as NFC allows for very simple sensor powering and readout (e. g. no pairing is necessary). In contrast to common HF-RFID, NFC devices not necessarily operate passively, i. e. communication between two active NFC devices is also possible.

2.2.3 Inductive Coupling

As both of the sensor systems developed in this work utilize HF-RFID, the following section will briefly illuminate the overall working principle of such systems. Energy and data transfer for HF-RFID is based on electromagnetic coupling of two loop antennas in the near-field region, which is why their combination can be described similar to loosely coupled transformer coils [25]. Figure 2.2 schematically displays simplified equivalent circuit models for an inductively coupled reader and transponder.

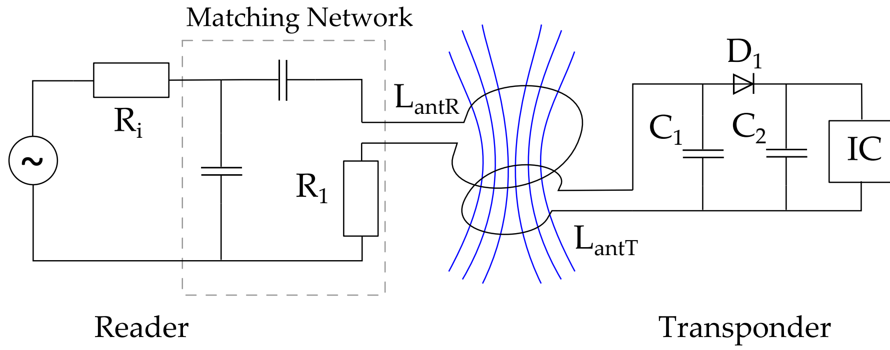

Figure 2.2: Schematic representation of inductive coupling betweeen reader and transponder using antenna coils, redrawn from [25]

The reader antenna generates a magnetic field, a small part of which passes through the transponder antenna, inducing a voltage. This voltage is then rectified to supply the transponder IC (indicated by the diode D_1). To generate a high field strength, a matching network is connected to the reader antenna L_{antR}, which is dimensioned in a way that creates a resonant circuit with the antenna inductance. Due to resonance, very high currents are achieved in the reader antenna, in turn leading to high field strengths.

The transponder also implements a resonant circuit by connecting capacitors in parallel to antenna inductance L_{antT}. To achieve best possible energy transfer, the resonant frequency of the transponder circuit should be as close as possible to that of the reader. This implies that antenna inductance, resonant capacitance (usually integrated into the transponder IC) and parasitic elements need to be carefully adjusted to match the intended frequency.

A more precise approximation of a transponders equivalent circuit is given in Figure 2.3. There, the IC is modeled as a parallel combination of R_{IC}, presenting IC current consumption, and C_{IC}, representing the internal tuning capacitance and parasitics. The antenna is modeled as combination of L_a and parasitic elements R_a, C_p, R_{pa}, which represent the resistive losses and stray capacitance of the antenna. For planar loops, i. e. coils, the latter is a function of conductor area, the dielectric substrate and the gap between the turns [26].
The resonance frequency of the tag circuit model is given [26] as

$$f_r = \frac{1}{2\pi}\sqrt{\frac{R_{IC} + R_a}{L_a(C_{IC} + C_p + C_{tune})R_{IC}}}, \tag{2.1}$$

which, for small resistive losses R_a, can be simplified to

$$f_r = \frac{1}{2\pi\sqrt{L_a(C_{IC} + C_p + C_{tune})}}. \tag{2.2}$$

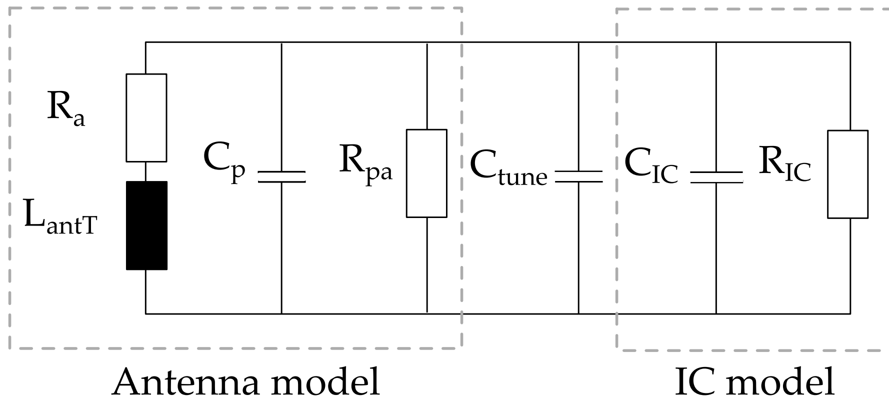

Figure 2.3: Equivalent circuit of transponder side, modeled as parallel resonance circuit, redrawn from [26].

Efficiency of the power transfer is proportional to the utilized frequency, number of turns N and overall area of the transponder coil, and relative orientation and distance of the coils [25]. This implies that with rising frequency, the number of turns necessary decreases (LF: N=100-1000, HF: N=3-10). Also, for best coupling, the overall size, i. e. radius of the transponder antenna should approximately match that of the reader antenna [26]. Regarding the actual value of best resonance frequency for the transponder circuit, conflicting recommendations are given in literature. While some publications recommend to match reader frequency as best as possible, e. g. [30], some recommend higher values, e. g. to make up for manufacturing tolerances [31], surrounding material influence [30], or to leave room for anti-collision techniques [25].

2.2.4 Antenna Design for NFC tags

As IC capacitance is usually fixed and parasitic capacitance is usually small, antenna inductance must be chosen in a way to achieve desired resonance frequency. For RFID transponders, several approximate formulas exist for inductance calculation of the most frequently used coil shapes, which are usually planar. Figure 2.4 illustrates the generic shape of a spiral, planar antenna in square shape.

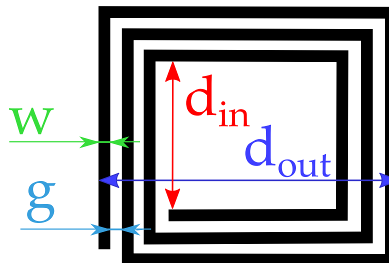

Figure 2.4: Spiral, planar antenna coil (square) and relevant dimensions.

For approximation of square-shaped, planar coil inductance, modified versions of the equations originally proposed by Wheeler [32] are frequently used (e. g. by

[30]), which have originally been published in [33]. Using these, the inductance of a planar, spiral, square-shaped coil calculates to

$$L_a = K_1 \mu_0 \frac{N^2 d_{avg}}{1 + K_2 \rho} \tag{2.3}$$

where:

$$K_1 = 2.34$$
$$K_2 = 2.75$$
$$N = \text{number of turns}$$
$$d_{avg} = \text{average diameter}$$
$$\rho = \text{fill ratio}$$
$$\mu_0 \approx 1.25663706212 \cdot 10^{-6}\ \text{H m}^{-1}\ \text{(permeability of vacuum)}.$$

K_1 and K_2 are layout dependent coefficients given in [33], while the average diameter and fill ratio can be calculated with

$$d_{avg} = \frac{d_{out} + d_{in}}{2} \tag{2.4}$$

$$\rho = \frac{d_{out} - d_{in}}{d_{out} + din}. \tag{2.5}$$

Different values for K_1 and K_2 are given for both circular and octagonal shapes [33]. Strictly speaking, equation 2.3 only applies to square-shaped, rectangular coils, as illustrated in Figure 2.4. Figure 2.5 schematically illustrates a rectangular, spiral antenna coil with a non 1:1 aspect ratio.

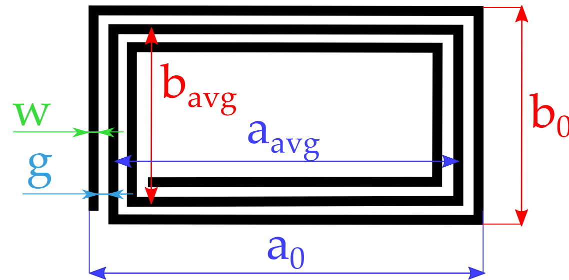

Figure 2.5: Spiral, planar antenna coil (rectangular) and relevant dimensions.

In [31], a formula is given for generic, rectangular, spiral inductances:

$$L_a = \frac{\mu_0}{\pi}[x_1 + x_2 - x_3 + x_4]N_c^p \tag{2.6}$$

where

$$\begin{aligned}
d &= \frac{1(t+w)}{\pi} \\
a_{avg} &= a_0 - N_c(g+w) \\
b_{avg} &= b_0 - N_c(g+w) \\
x_1 &= a_{avg} \cdot ln\left[\frac{2a_{avg}b_{avg}}{d(a_{avg} + \sqrt{a_{avg}^2 + b_{avg}^2})}\right] \\
x_2 &= b_{avg} \cdot ln\left[\frac{2a_{avg}b_{avg}}{d(a_{avg} + \sqrt{a_{avg}^2 + b_{avg}^2})}\right] \\
x_3 &= 2\left[a_{avg} + b_{avg} - \sqrt{a_{avg}^2 + b_{avg}^2}\right] \\
x_4 &= \frac{a_{avg} + b_{avg}}{4}
\end{aligned}$$

Here, the variables a_0 and b_0 represent the outer length and width of the spiral, while a_{avg}, b_{avg} indicate the average coil diameter (see Figure 2.5). t, w and g describe the track i.e. conductor dimensions, with t being track height (in 3D), w being track width, and g being gap between the tracks, respectively. These are combined to calculate an equivalent track diameter, which is denoted with d. Finally, N_c is the number of turns, while p is the so-called turn exponent, values for which are given in Table 2.4. For estimation of C_p, some common values are given in [31], which are also included in Table 2.4.

Table 2.4: Turn exponents for planar, rectangular, spiral inductors, [31].

Manufacturing Technology	p	C_p **(pF)**
Wired	1.8 – 1.9	5-7
Etched	1.75 – 1.85	2-4
Printed	1.7 – 1.9	2-4

Using the formulas presented, antenna dimensions can be calculated for known values of the other elements of the transponder circuit (see Figure 2.3), if approximate dimensions for overall antenna geometry are given. The latter is usually depending on the intended size of the overall transponder, as often the antenna is the largest part of a transponder. As some of the parameters in the calculation are subject of estimation and fabrication tolerances occur, common practice is to design and fabricate at least three or five antenna versions both of slightly lower and slightly higher inductance. These are then characterized regarding their

actual behavior and the best fitting geometry is chosen. Sometimes, if actual inductance differs strongly from the one expected, another design iteration can be necessary [31].

For measurement of antenna performance, several methods are applicable, which are e. g. described in [30, 31, 34–36]. For characterization of the antennas designed in this thesis, the technique employing a loop antenna and an impedance analyzer was used, which shall briefly be described here. With this technique, resonance frequency of the overall resonant circuit is measured, so the antenna inductance needs to be connected to a capacitive element to complete the circuit. This can either be done using the actual RFID transponder IC, or a dummy capacitor of the same value as the internal IC capacitance.

The impedance analyzer is either set to measure absolute impedance and phase, or real and imaginary parts of the impedance (i. e. R and X) around the desired resonance frequency, in this case 13.56 MHz. To cancel out parasitic elements of the setup and the instrument itself, compensations must be carried out, as described in the respective manual. These usually are compensations for the open, short and load case.

A single-turn loop antenna with high quality factor, i. e. low resistance, and low parasitic capacitance is used for measurement, which is connected to the instruments measurement terminals, and which is also short-compensated for. The antenna dimensions should approximately match those of the transponder antenna. Regarding output power, the highest possible oscillation amplitude should be used [31], though care must be taken to not emit sufficient power for the IC to power on, if using it on the tag, as this has been observed to influence the measurement results. Distance from loop antenna to transponder antenna should be lower than or equal to 10 mm.

Depending on settings of the impedance analyzer, resonance of the overall tag can be determined from the measurement results. For a parallel equivalent circuit, resonance occurs where resistance R is maximal and the imaginary part of the impedance X reduces to zero [37]. For absolute impedance and phase, this is equivalent to a local maximum in $|Z|$. An example measurement for determination of resonance frequency is shown in Figure 2.6. [1]

Another common technique utilizes measurement of the reflection coefficient S11, which is described in e. g. [30]. Measurement of the antenna inductance on its own is also a viable approach, e. g. as described in [36], which can then be used to calculate overall resonance using known values for the other circuit elements, e. g. using the Thomson equation. For more details on antenna design and measurement techniques, the interested reader is pointed to the literature mentioned throughout this paragraph.

[1]Regarding a series resonance circuit, the inverse is true, i. e. R gets minimal at resonance, while $|Z|$ also becomes minimal. This is mentioned only for completeness though, the transponder is commonly modeled as parallel resonant circuit.

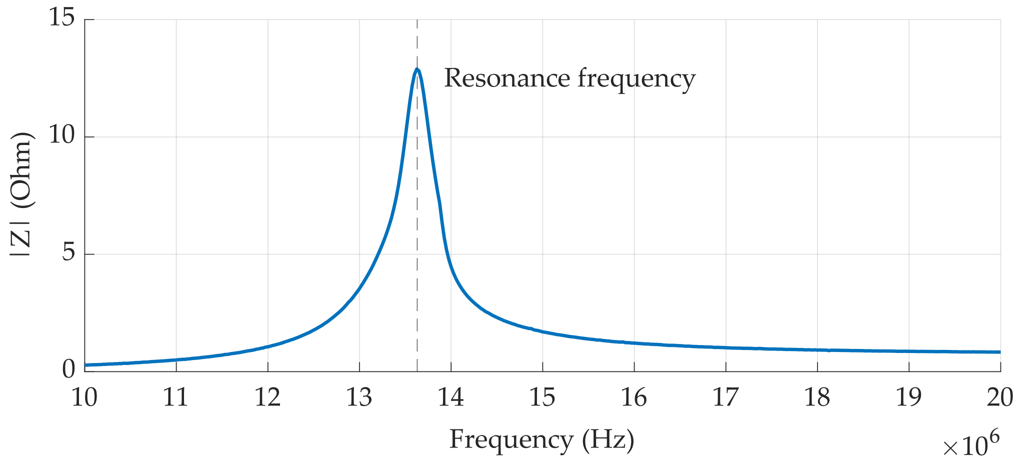

Figure 2.6: Example measurement for determination of transponder resonance frequency, using a loop antenna and impedance analyzer.

2.3 Strain Gauges

As one of the main sensor elements used for research in this work are strain gauges, this section will briefly provide an overview of the relevant background information regarding their principle and usage.

2.3.1 Mechanical Strain

Load-induced changes of a materials' geometry can be quantified using the entity of mechanical strain, which is defined by [38] as the ratio of the change in geometrical length dl relative to the original length l_0:

$$\varepsilon = \frac{dl}{l_0} \tag{2.7}$$

This way, a dimensionless number can give information about a materials' deformation, independent of actual component dimensions. For a three-point bending test setup as displayed in Figure 2.7, specimen tension and strain at the lower specimen surface, i. e. at the extreme fiber, can be calculated from the following equations [38]:

$$\sigma_f = \frac{3FL}{2bh^2} \tag{2.8}$$

$$\epsilon_f = \frac{6fh}{L^2} \tag{2.9}$$

This way specimen strain can be calculated just from deflection values and setup parameters. If strain different from the extreme fiber plane needs to be calculated, a variation of Equation 2.9 can be used [39]:

$$\epsilon(z) = \pm z\frac{12f}{L^2} \tag{2.10}$$

In this, z is the distance from the neutral plane, which, in the case of a common three-point bending test setup, is situated in the middle of the specimen. In the neutral plane, no strain or compression occurs.

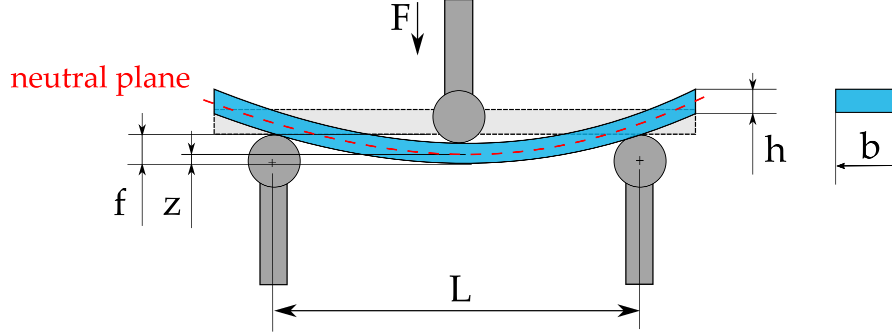

Figure 2.7: Schematic illustration of three point bending test setup

2.3.2 Piezoresistive Effect

In order to electrically measure strain, the piezoresistive effect can be used, which is a phenomenon observed for a variety of conductors and semiconductors, relating a geometrical change of the material to a change of the material resistance.
For a wire of a length l_0, a specific resistivity ϱ, with the cross section A and corresponding volume of $V = lA$, the wire resistance R can be calculated [40]:

$$R = \frac{\varrho l}{A} = \frac{\varrho l^2}{V} \tag{2.11}$$

When the wire is stretched, its resistance changes correspondingly [40]:

$$dR = \frac{\partial R}{\partial l} dl + \frac{\partial R}{\partial V} dV + \frac{\partial R}{\partial \varrho} d\varrho = 2\frac{\varrho l}{V} dl - \frac{\varrho l_0^2}{V^2} dV + \frac{l_0^2}{V} d\varrho \tag{2.12}$$

Relating this change to the initial resistance R (Equation 2.11) we get:

$$\frac{dR}{R} = 2\frac{dl}{l_0} - \frac{dV}{V_0} + \frac{d\varrho}{\varrho_0} \tag{2.13}$$

From this it is deducible that the change in resistance caused by the geometrical deformation is reflected in terms one and two, while $\frac{d\varrho}{\varrho}$ reflects a deformation induced change of the materials specific resistivity. The latter is therefore commonly called “intrinsic effect”.

Depending on material, the individual influence of the different terms changes. For metals, small deformations usually do not influence their specific resistivity [40], and changes in volume are commonly negligible, giving

$$\frac{dR}{R} \approx 2\frac{dl}{l_0}.$$

For other materials, e. g. semiconductors, this can change significantly, as deformation can influence the level of the energy bands [40], influencing the specific resistivity and increasing the corresponding changes in resistance for a given strain by several magnitudes. To generalize this material dependency, a dimensionless number is used that is called piezoresistive coefficient k. Correspondingly, it is defined as

$$\frac{dR}{R} = k\frac{dl}{l_0} \tag{2.14}$$

Using deformation as defined in equation 2.7, the change in resistance caused by a given strain ε is given by

$$dR = Rk\varepsilon. \tag{2.15}$$

Correspondingly, k can be defined as the amount of resistance change relative to occurring strain, giving

$$k = \frac{dR/R}{\epsilon}. \tag{2.16}$$

Strain gauges are a common implementation of the piezoresistive effect. Using a piezoresistive material, e. g. a metal, that is distributed as a thin, continuous structure onto an elastic substrate, a sensing element is made. This can be mounted on the surface the strain of which is to be measured (see Figure 2.8).

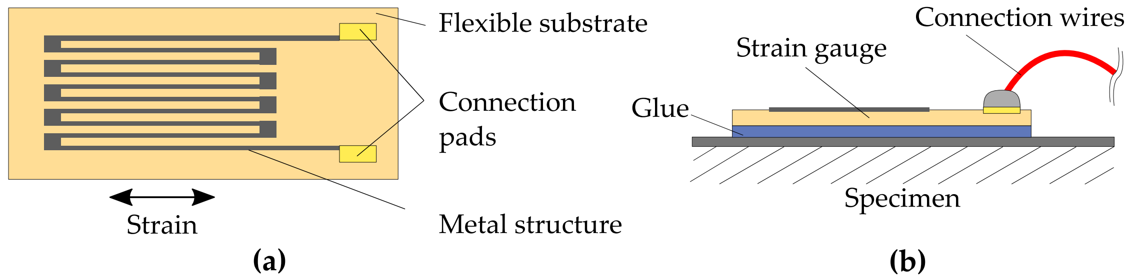

Figure 2.8: Schematic representation of (a) strain gauge principle; (b) strain gauge application to a specimen surface [7].

2.3.3 Wheatstone Bridge Circuit

As strain-induced changes in strain gauge resistance are comparably small, bridge circuits are usually used to make the change easier to measure. These circuits comprise two serial resistor pairs connected in parallel, as shown in Figure 2.9. Instead of directly measuring strain gauge current or voltage, the (usually small) voltage between the bridge arms is measured, which is therefore called bridge voltage dU. In general, bridge voltage can be calculated [41] using

$$dU = U_0\left(\frac{R_1}{R_1 + R_2} - \frac{R_4}{R_3 + R_4}\right). \tag{2.17}$$

If all resistors are equal, dU is zero, while bridge voltage changes if one or several resistors change in relation to the others. This way, variations in resistance directly result in a voltage change that can easily be measured. Depending on the configuration and number of strain gauges used, bridge voltage is influenced differently, allowing for application-specific circuit design.

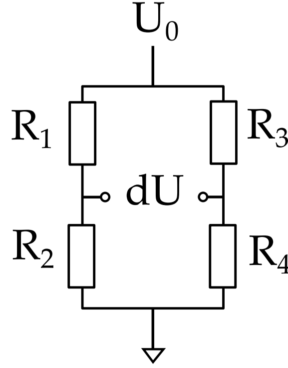

Figure 2.9: Wheatstone bridge circuit [42].

If all resistors are of same nominal value, Equation 2.17 can be simplified for small changes in resistance [41]. The relation of bridge voltage dU and supply voltage U_0 is then given as

$$\frac{dU}{U_0} = \frac{1}{4}\left(\frac{\Delta R_1}{R_1} - \frac{\Delta R_2}{R_2} + \frac{\Delta R_3}{R_3} - \frac{\Delta R_4}{R_4}\right). \tag{2.18}$$

Using equation 2.16, this reduces to

$$\frac{dU}{U_0} = \frac{k}{4}\left(\epsilon_1 - \epsilon_2 + \epsilon_3 - \epsilon_4\right), \tag{2.19}$$

with k being the piezoresistive coefficient of the strain gauge material.

2.3.4 Lateral contraction

Depending on number and orientation of the strain gauges used in the bridge circuit, lateral contraction of the material, i. e. deformation occurring perpendicular to main strain direction, can influence the measured strain value. The amount of lateral contraction actually occurring is very much depending on material properties. In [1], lateral contraction ν is defined as the amount of material compression, i. e. negative strain, happening orthogonal to normal strain direction, the relation thereof is reflected in their ratio, which is usually named Poisson's ratio:

$$\nu = -\frac{\epsilon_{\text{lateral}}}{\epsilon_{\text{normal}}} \tag{2.20}$$

As lateral strain commonly is negative, ν is made positive by addition of the minus sign. Multiple indications i. e. numbers for Poisson's ratio are possible, depending

on strain direction, if the material is anisotropic. For FRP, this is usually the case, which is why ν is usually assigned with an index, indicating the direction. According to [1], nomenclature for the index is not standardized. For German literature, the order of the indices is usually *consequence,reason*, e. g. for transversal contraction $\epsilon_{transversal}$ occuring due to a strain in normal direction $\epsilon_{longitudinal}$, the corresponding ν is given as

$$\nu_{\text{transversal, longitudinal}} = \nu_{\perp\|} = -\frac{\epsilon_{\text{transversal}}}{\epsilon_{\text{longitudinal}}}$$

While influence of lateral contraction usually is negligible for a single strain gauge, e. g. in a quarter bridge configuration, this is not necessarily the case for other configurations.

2.3.5 Full Bridge Configuration

Numerous configurations for usage of strain gauges in bridge circuits exist, e. g. quarter, half or full bridge configuration, where either one, two or all four resistors are substituted by strain gauges. Depending on physical orientation of the gauges, bridge voltage is influenced according to different directions of strain and in different magnitudes. Regarding influence of temperature, full bridge configurations are at an advantage – if all four strain gauges are subjected to the same temperature, i. e. by being mounted closely together, their temperature-induced resistance change is the same for all gauges, and bridge voltage is not influenced.

In context of this thesis, the full bridge configuration shall be briefly explained here, as it is the one used with the piezoresistive sensor tag (see Chapter 5). In-depth descriptions of other configurations are given in literature, e. g. [41, 42]. To calculate actual strain from dU, strain gauge configuration and orientation needs to be taken into account. For a Wheatstone bridge as displayed in Figure 2.10, comprised of four active, in-plane resistors, two of which are oriented perpendicular to the other two, the measured strain ϵ_a calculates to [41]:

$$\epsilon_a = 2(\epsilon_{\text{normal}} + \epsilon_{\text{lateral}}) = 2(\epsilon_x + \epsilon_y) = 2(1 + \nu_{xy})\epsilon_x \tag{2.21}$$

In this configuration, all strain gauges influence bridge voltage. R_{1X} and R_{4X} measure strain in normal, i. e. X-direction, while R_{2Y} and R_{3Y} measure lateral contraction, i. e. strain in Y-direction. Therefore, lateral contraction is superimposed on the actual measurement signal and consequently needs to be accounted for during calculation of the actual strain value from the measured voltage.

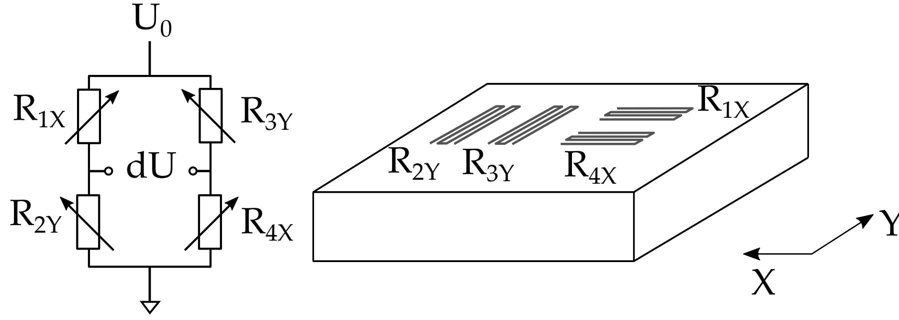

Figure 2.10: Full bridge Wheatstone bridge circuit for measurement in two directions, all resistors in plane.

Using equations 2.19 and 2.21, this can be used to calculate normal strain for a given ν_{xy}:

$$\frac{dU}{U_0} = \frac{k}{4} \cdot 2(1+\nu_{xy}) \cdot \epsilon_x$$
$$\epsilon_x = \frac{2}{k(1+\nu_{xy})} \frac{dU}{U_0} \tag{2.22}$$

For details on strain calculation for the sensor tag using digitized bridge voltage, see Section 5.1.4.

2.4 Interdigital Capacitors

As the second sensor system designed in this thesis uses an interdigital capacitor, this section shall give a brief overview of relevant fundamentals regarding IDCs and their usage as sensor elements.

2.4.1 Capacitance

Generally speaking, a capacitor is a device or basically every arrangement of two conductors, separated by an isolating, but polarizable material, i. e. a dielectric (see Section 2.4.2), that is able to store charge [43]. If no space charge is present between two electrodes A and B, the capacitance C_{AB} is defined as

$$C_{AB} = \frac{Q_{AB}}{U_{AB}}, \qquad [C] = \frac{[Q]}{[U]} = \frac{\text{As}}{\text{V}} = \text{F (Farad)} \tag{2.23}$$

with Q_{AB} being the charge stored and U_{AB} being the voltage between the electrodes. Depending on the arrangement of the electrodes, temperature, the properties of the dielectric, frequency of the voltage and other factors, the size of C_{AB} can change. The reason for capacitance being dependent on frequency is that permittivity of the dielectric changes with frequency (see also Section 2.4.4). Figure 2.11 illustrates the common arrangement of electrodes and dielectric in a parallel plate capacitor setup.

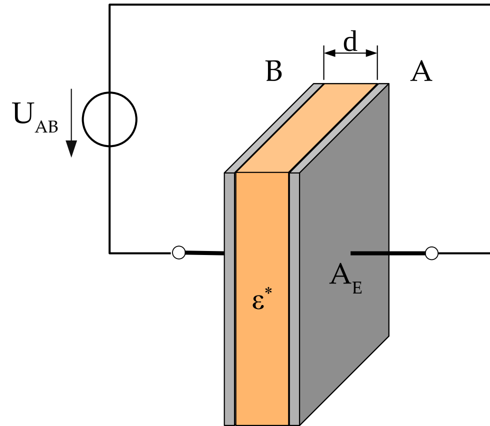

Figure 2.11: Schematic display of a parallel plate capacitor. Electrodes A and B of area A_E separated by a dielectric with permittivity $\epsilon^\star$ and thickness d.

For an ideal capacitance, i. e. incorporating no ohmic resistance, its impedance is defined as

$$Z = jX_C, \qquad X_C = \frac{1}{2\pi f C} = \frac{1}{\omega C} \tag{2.24}$$

2.4.2 Dielectric

A dielectric is a material in any aggregate phase that is characterized by two major properties [43]:

- very low specific conductivity ($\sigma < 10^{-10}$ S/cm [44]), i. e. nearly no free charges are present in the material that could be moved by an electric field
- the material is polarizable (see Section 2.4.3), resulting in charge separation, i. e. dipole moment, and a corresponding electric field, which weakens the exterior electric field.

Summarizing, a dielectric is an insulator that can be easily polarized. For that reason, dielectrics are used in numerous technical applications, one prominent of which is the capacitor.

2.4.3 Polarization

In a material, the process of local separation of charge centers due to an external electric field is called polarization [43]. This separation of charges leads to formation of an electric field with opposing sign relative to the initial field. As this process cannot be measured on its own, its magnitude is expressed by the relative permittivity ϵ_r or $\epsilon^\star$ (see Section 2.4.4).

Several mechanisms can contribute to dielectric polarization, as several effects can influence the charges in a material when subjected to an electric field. Figure 2.12 schematically summarizes the effects and their respective contribution to the real and imaginary parts of permittivity [45].

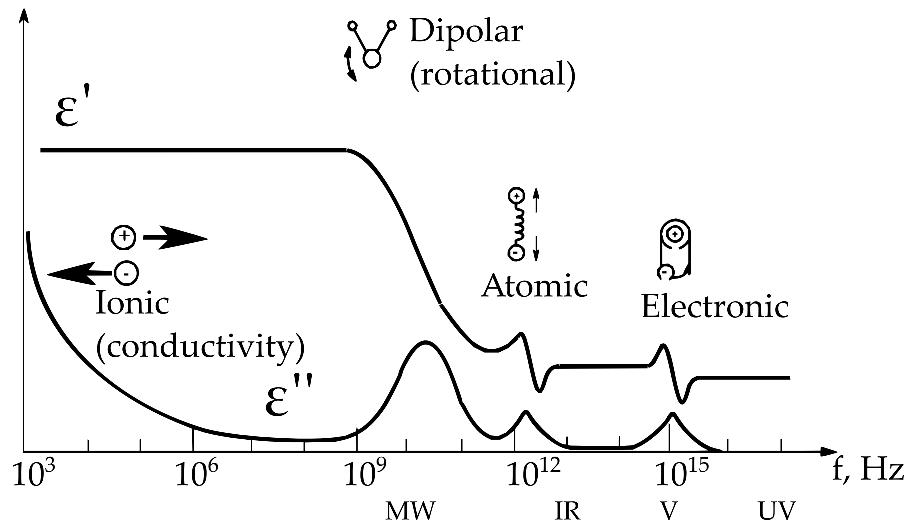

Figure 2.12: Different effects contributing to polarization across the frequency spectrum. Redrawn from [45].

The most macroscopic and therefore slowest effects are dipolar roation and ionic conduction, as they involve movement of molecules. Consequently, they happen in the lower part of the spectrum and also are quite lossy in terms of heat generated due to friction (the same effect is used in microwave ovens). Dipolar molecules, which are randomly oriented in absence of an electric field, will rotate and align themselves according to the polarity of the electric field. Ionic conductivity, i. e. migration of charge carriers due to the electric field, can also lead to a polarization effect, if their movement is impeded, e. g. at a boundary layer. The charges cannot move further and therefore accumulate at the boundary or interface, consequently causing a distortion of the overall electric field. Accordingly, this effect is called interfacial or space charge polarization and can strongly increase permittivity and therefore capacitance at low frequencies [45]. Over a certain frequency, due to their weight, dipoles and ions are too slow to follow the electric field, and contribution of these effects to the overall polarization subsequently reduces and then vanishes. Consequently, these two mechanisms are also strongly temperature dependent, as increasing number of molecule collisions inhibit their overall movement [44].

This "drop-out" behavior is visible for every polarization effect, resulting in a "cutoff frequency" that is characteristic for every mechanism and material. At these critical frequencies, the loss factor (i. e. ϵ'') shows a local maximum. The other two polarization effects are called atomic and electronic polarization. While atomic polarization happens because of a relative shift of differently charged ions of a crystal lattice, electronic polarization is caused by a displacement of an atom core and its electrons. Both effects are associated with a resonance effect (see Figure 2.12).

2.4.4 Permittivity

To describe the ability of a material, i. e. a dielectric, for storing charge in a capacitive setup, the entity of permittivity ϵ is used [43]. Depending on material properties, the electric displacement field **D** in a material resulting from an electric field **E** is influenced by its absolute permittivity ϵ [43]:

$$\mathbf{D} = \epsilon \mathbf{E} \tag{2.25}$$

Absolute permittivity ϵ is usually correlated to the permittivity of free space, i. e. the electric field constant ϵ_0:

$$\epsilon = \epsilon_r \epsilon_0 \tag{2.26}$$

with:

$$\epsilon_r = \text{Relative permittivity}$$
$$\epsilon_0 = 8.8541878128 \cdot 10^{-12}\ \text{Fm}^{-1}$$

In this, ϵ_r is the material-specific relative permittivity, which is sometimes also ambiguously referred to as dielectric constant, even though it is very much dependent on multiple conditions, e. g. temperature and frequency of the applied electric field [46]. This is due to the underlying effects that contribute to the materials ability of storing energy, which is called polarization (see Section 2.4.3).

To be more precise, permittivity can also be written as a complex entity, consisting of a real part ϵ' and an imaginary part ϵ'' [46]:

$$\epsilon^\star = \epsilon' - j\epsilon'' \tag{2.27}$$

In a dielectric, ϵ' represents the energy storage part for external energy of an electric field. ϵ'' represents the dielectric loss, i. e. the energy dissipation in the dielectric, e. g. due to heat generated during polarization. For this reason, ϵ'' is also called loss factor, and is generally smaller than ϵ', though always bigger than zero [45].

2.4.5 Parallel-Plate Capacitor

The most basic representation of a capacitor is the parallel-plate capacitor [43], which consists of two parallel, plate-shaped electrodes with the surface area A_E, which are separated by a dielectric of permittivity ϵ (see Figure 2.11). The capacitance of this arrangement then calculates to:

$$C_{AB} = \frac{Q_{AB}}{U_{AB}} = \frac{\epsilon A_E}{d}, \qquad \text{with } A \gg d \tag{2.28}$$

C_{AB} consequently rises with increasing electrode area, increasing permittivity and decreasing electrode distance. As ϵ commonly decreases with increasing frequency, C usually reduces for higher frequencies.

2.4.6 Interdigital Capacitor

If the arrangement of the plates of a parallel-plate capacitor is changed, so that the plates are no longer parallel but coplanar, i. e. in the same plane (see Figure 2.13), behavior of the arrangement changes [47]. The lines of the electric field still span from electrode A to electrode B and through the dielectric, but the field is no longer homogenous. Instead, the field lines form a fringing field passing through the dielectric above the electrodes [48], and capacitance significantly reduces.

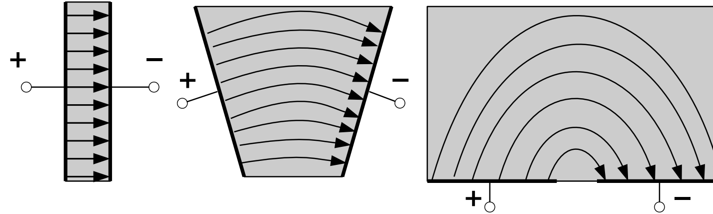

Figure 2.13: Schematic display or transition from parallel plate to planar capacitor. Arrows represent the lines of the electric field. MUT: gray. Redrawn from [48].

Despite this reduction in capacitance, for sensoric applications, this arrangement provides a significant advantage in comparison to the parallel-plate. If the dielectric is the material that is meant to be investigated by a capacitive sensor, i. e. the Material Under Test (MUT), changes in its dielectric properties can still be measured with a coplanar electrode arrangement, as the field lines still pass through it. This allows for single side access of the sensor and can be very advantageous for sensing applications. To make up for the reduced capacitance of the arrangement, it is possible to simply multiply the number of electrodes (N), so that the capacitances add up. This way, an InterDigital Capacitor (IDC) is formed (see Figure 2.14). Unfortunately, calculation of resulting capacitance is not as simple as for the parallel-plate capacitor. Section 6.1 presents some analytical approaches for estimation of IDC capacitance.

Apart from one-sided access, several other advantages arise for IDCs, that are useful for sensoric applications, which make them a widely used type of sensoric element. IDC design, i. e. size and geometry, can be done according to each application, as electrode shape and length can be fitted to the desired outline. This allows for highly specialized sensor geometry and unintrusive sensor design. Also, flexible substrates can be used, so that the sensor can be made to conform to different shapes.

In an IDC, the N parallel electrodes of length L and width w are equally separated by a distance g ("gap"), which is illustrated in Figure 2.14. The correlation between electrode width and spacing is commonly called the spatial wavelength [47–49], which is denoted via the letter λ:

$$\lambda = 2 \times (W + g). \tag{2.29}$$

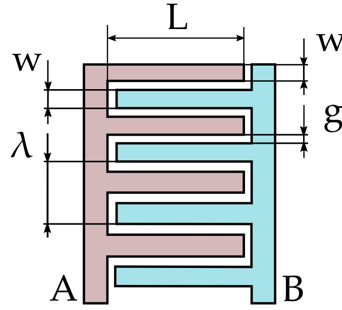

Figure 2.14: Schematic illustration of an interdigital capacitor arrangement of electrodes A and B, with finger width w, finger lenght L, finger spacing ("gap") g and spatial wavelenght λ.

The maximal spatial sensitivity of an IDC, i. e. penetration depth of the electrical field lines, is half of λ [47], which could also validated in [49, 50]. It is not influenced by the dielectric properties of the MUT [15]. As usable penetration depth of an IDC is commonly limited by conditions present in a real measurement system, e. g. noise, penetration depth can also be described as the maximal distance between an MUT and IDC, at which a measurable difference in signal occurs [48].

Another important aspect for description and evaluation of IDCs is a parameter called metallization ratio, which is commonly denoted with η [50]. It is used to describe the relation of metallized surface to unmetallized surface, and is defined by

$$\eta = \frac{w}{w+g}. \tag{2.30}$$

The higher η is, the higher overall IDC capacitance for a fixed number of fingers and fixed finger length [51]. Increasing the amount metallization therefore can be used for higher sensor signal. For applications where minimal IDC size is relevant though, this correlation can be misleading – increasing finger width w for limited overall IDC width, finger number N consequently reduces. For this reason, the sensor sensitivity per unit area β can be used to describe sensor sensitivity

$$\beta = \frac{k}{A}, \tag{2.31}$$

where k stands for IDC sensitivity to a change in dielectric properties of the MUT and A is overall sensor area. As several publications, including [15, 50, 52] have shown, a metallization ratio of $\lambda = 0.5$ results in the highest sensitivity per unit area, making this the best suited metallization ratio for smaller sensors. In this work, this correlation could also be analytically shown in Section 6.1.

Some applications of IDCs additionally employ a shielded backplane, i. e. a "third electrode" spanning the back side of the sensor substrate. For double layer PCBs, this would be equivalent to a copper pour on the other side of the IDC structure. For FRP fabrication monitoring, [52] found that usage of a backplane mainly increases overall capacitance, but also can reduce noise and sensitivity per

unit area. Regarding distribution of the field lines, usage of a shielded backplane moves IDC sensitivity to one side, i. e. away from the shield [47, 48]. This also affects penetration depth – in [48] it was found that usage of a backplane can give less penetration depth and overall sensitivity.

Due to their numerous advantages, IDCs are widely used for many applications, not limited to cure and strain measurements, which are presented in this work. They can be used for a variety of physical measurements (e. g. object presence), or chemical or biological measurements, by e. g. coating the electrodes with a chemically or biologically active material that changes properties according to certain conditions [48].

2.4.7 Capacitive Strain Gauges

As IDC capacitance also depends on electrode spacing g, IDCs can also be used for strain measurement, similar to piezoresistive strain gauges. To this end, an InterDigital Capacitor (IDC) is made on a flexible substrate, which is then attached to the strained surface. If the IDC is oriented perpendicular to the main strain direction, electrode distance is influenced by the strained surface (see Figure 2.15). The strain applied to the IDC therefore results in a variation of electrode distance, i. e. an increase in g, that in turn leads to a reduction of capacitance (see Section 2.4). The relation of strain to IDC geometry is accordingly given as

$$\epsilon_{mech} = \frac{\Delta g}{g}. \tag{2.32}$$

The influence of strain on capacitance of IDCs commonly shows a linear response, as shown in e. g. [53–55], and suggested by the formulas given in Section 6.1. For sensoric applications, this is therefore an advantageous property.

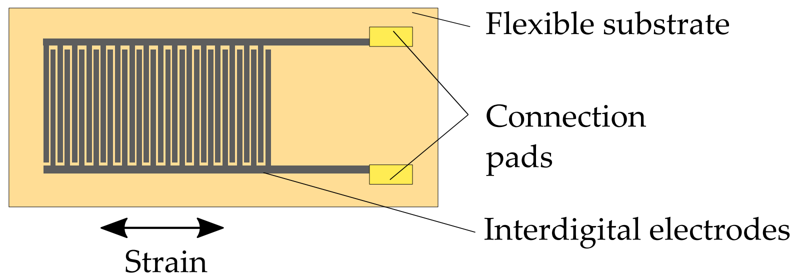

Figure 2.15: Schematic representation of capacitive strain gauge concept, direction of strain sensitivity indicated.

As with piezoresistive strain gauges, a gauge factor can be determined for capacitive strain gauges, that quantifies the change of capacitance relative to the applied strain. To avoid confusion with the modulus of the elliptic integral k and k' used for analytical capacitance calculation (see Section 6.1), the gauge factor for

capacitive strain gauges is given by [54] as:

$$G_F = \frac{\Delta C}{C_0 \epsilon_{mech}}. \tag{2.33}$$

Comparing gauge factors found for different IDCs, results differ. The experiments presented in [53] showed a capacitance response of about 0.04 % per 0.1 % strain for an IDC on polyimide substrate with $\eta = 0.5$, without any covering (e. g. one side of the IDC is exposed to air). Using equation 2.33, this corresponds to a gauge factor of about -0.4. Results in [54] measured a gauge factor of -1.38 for an IDC with $\eta = 0.25$, encapsulated in between polyimide films, the geometry of which had numerically been optimized for high strain sensitivity. As capacitance depends on permittivity of the material in contact with the electrodes, these differences might also be caused by the different dielectrics used in the experiments. Using a knitted fabric, [56] presented results on a printed IDC with a positive gauge factor of $G_F \approx 0.83$, that was due to the transversal orientation of the IDC on the fabric, increasing capacitance due to lateral contraction. Opposed to piezoresistive metal thin film strain gauges, where the gauge factor is commonly around 2, the individual gauge factor for capacitive strain gauges can therefore not be given in a general sense, as it depends on several factors.

In comparison with resistive strain gauges, capacitive strain gauges present no low impedance circuit element, which can be an advantage for low power sensing systems. One of the disadvantages of capacitive strain gauges are cross sensitivities of IDC capacitance with temperature and humidity, influencing strain measurement precision. Using compensation techniques, e. g. differential measurement, it is possible to reduce these [54]. Nonetheless, capacitive strain gauges can be used for sensoric applications, as numerous publications show (see e. g. Section 4.2.2 for some examples).

2.4.8 Capacitance Measurement

To measure capacitance, several methods exist, that differ in complexity. One of the easiest ways is to periodically switch the unknown capacitor on an off, resulting in an average current that is influenced by switching frequency, voltage and value of the capacitance [42]. This way, if frequency and voltage are known, capacitance can easily be calculated. Another way is usage of bridge circuits, analogous to the Wheatstone bridge mentioned above, but using complex elements, i. e. capacitors and inductances [42, 57]. Multiple bridge configurations can be used, with which, depending on configuration, both capacitance and inductance can be calculated from frequency and values of the known elements. Furthermore, resonant circuits are also a possible way for measurement of complex elements. To this end, a resonant circuit is built from the unknown element, an opposite element of precisely known value, e. g. an inductance for measurement of an unknown capacitance, and a voltage source. Figure 2.16 displays a schematic representation of a parallel

resonant circuit for capacitance measurement, though serial resonant circuits can also be used [57]. By measuring the voltage U_m across the complex elements, as indicated by the volt meter, capacitance (or inductance) can be calculated if source voltage U_0, resulting resonance frequency, and values of the other circuit elements are known. In this context, the parasitic resistors present in the circuit only influence the damping of the resonance, but not the resonance frequency itself.

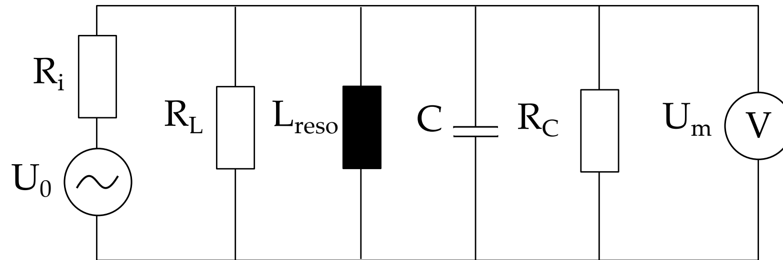

Figure 2.16: Parallel resonant circuit for measurement of an unknown capacitance C with known inductance L_{reso} and parasitic resistances R_L and R_C. Redrawn from [57].

2.4.8.1 Method used in this work

In contrast to the major part of prior publications on FRP cure measurement using IDCs, the sensor presented in this work measures IDC capacitance instead of permittivity or loss factor. The reason for this is that for IDC readout, usage of a very low power IC with minimal form factor is essential for application on a passive sensor tag. During the research presented in this work, the IC best fulfilling these requirements was the *FDC2x1x* series by Texas Instruments, Inc. [58]. As the sensor presented shall only demonstrate conceptual feasibility of the wireless IDC-based sensor node, this is not a disadvantage, as experimental results show (see Section 7.3).

The working principle of the FDC is not published in high detail, but it also uses shifts in resonance frequency for calculation of capacitance. Similar to the method presented in the prior paragraph, a resonant circuit is built from a known inductance, a known capacitance, and the capacitive sensor, as illustrated in Figure 2.17. The circuit resonates at a specific resonance frequency that depends on the values of the circuit elements. Measuring the resulting resonance frequency with high resolution (up to 28 Bit for the FDC), it can be used to precisely calculate the amount of all capacitive elements in the circuit.

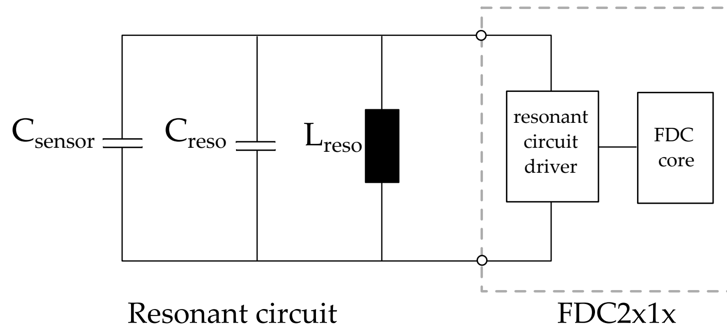

Figure 2.17: Schematic layout of resonant circuit for FDC2212 operation, redrawn from [58].

With all element values known except for the unknown capacitance, Thomson's equation can be used to calculate the value of the unknown capacitance:

$$f_R = \frac{1}{2\pi\sqrt{LC}} = \frac{1}{2\pi\sqrt{L_{reso}(C_{reso} + C_{sensor})}} \tag{2.34}$$

Solving this for C, we get:

$$C_{sensor} = \frac{1}{L_{reso}(2\pi f_{reso})^2} - C_{reso} \tag{2.35}$$

Chapter 3
"Sensor Tag" Concept

As the conceptual approach for the sensor systems developed in this work fundamentally influences the way the systems are designed and the way they operate, this chapter will briefly introduce the general idea of a "sensor tag". This idea was created in collaboration with another institute (Bremer Institut für Produktion und Logistik GmbH (BIBA)) during a joint project. The approach is motivated by the idea of supporting cost-effective production of FRP, both financially and resource-wise. The latter is mainly targeted with usage of the sensor itself for monitoring matrix cure and infusion, thereby allowing for process optimization. Regarding the former, i. e. reduction of FRP production cost, an increased need for process automation is result of rising costs for human resources, especially in high-wage countries like western Europe. This is generally due to FRP production currently being a mainly manual process, especially for structural or generally larger parts. In context of still increasing globalization, competitiveness of local, high quality FRP production against low-wage countries also plays a role. One of the building blocks for automation in FRP production is automated cutting, preforming and draping of the fiber textiles, as envisioned and described in e. g. [59] and [60]. A schematic representation of a possible robot-based setup is shown in Figure 3.1.

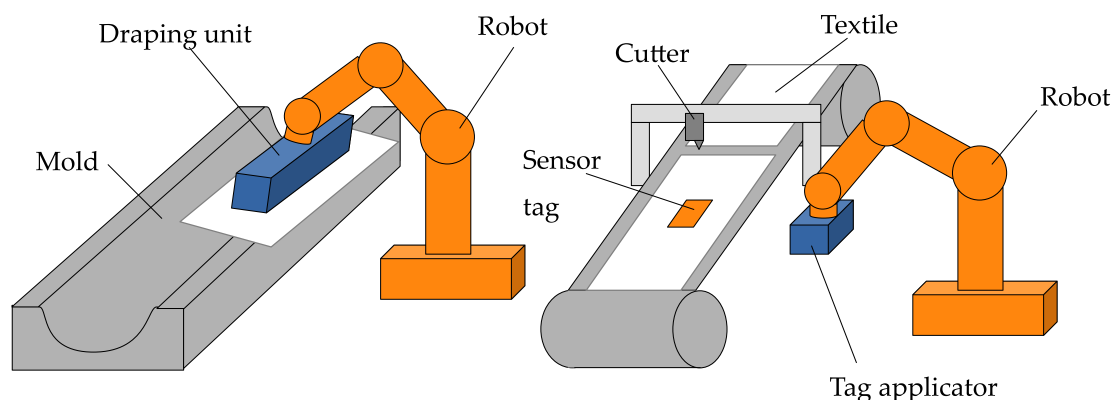

Figure 3.1: Automated application of sensor tags and handling of textiles as envisioned by [59]

In this context, a sensor system for FRP integration also needs to allow for simple incorporation into the increasingly automated FRP production process. To make this possible, the sensors presented in this work are based on a "sticker-like" approach, that can easily be integrated into a robot-based production flow. The

approach makes use of the circumstance that application of labels and tags onto products is already a technique that is heavily used in automated production of goods, and is therefore an established and well-known technology.

A conceptual implementation of this approach could already be shown in the report of the project mentioned above [61]. There, the sensor tags were stored on a storage roll of pre-applied adhesive on a carrier foil. During application, the tags are pushed to the textile surface via a spring loaded barrel with a soft surface (see Figure 3.2). The apparatus is designed to be mounted to a conventional buckling arm robot, which can also be used for textile cutting and placement of the textile pieces in the mold. Additionally, it incorporates both a distance sensor for measurement of sensor tag position on the carrier foil prior to application, and an RFID-reader, which can be used to communicate with the applied tag. This way, sensor function can be tested and production relevant data or sensor specific information can directly be stored on the sensor tag during the application process.

A ”sensor tag” consequently aims to be a sensor, the geometry of which is similar to a common sticker, so that it can be applied to the fiber textile in a similar fashion as a ”common” sticker, i. e. using a similar, well established technique. A sensor tag therefore needs to be both thin, flexible, and sufficiently small. These properties are also principal requirements for material-integrated sensors, as they heavily influence sensor impact on the host material, in terms of the resulting wound effect [62]. Additionally, common stickers suggest a rectangular shape, as this simplifies automated application – rectangular shapes can mechanically be guided easier, especially if resulting sticker orientation is relevant, which is usually the case. This also applies to the sensor tags presented, as orientation of the tag relative to the host component is also of concern, due to the directional nature of strain measurement.

For common label sticker applications, the question of glue for sticker adhesion is usually not of great concern, as long as the sticker adheres sufficiently to the material and does not cause any negative effects to the surface. In context of FRP material integration, adhesion of the sensor tag to the textile poses a different challenge – as the matrix will completely surround the tag, the glue should not negatively affect adhesion of the matrix to either the textile or the tag itself. This is especially important, as delaminations of matrix and fiber i. e. textile are one of the major causes for FRP component failure. For the experiments conducted in this thesis, a specialized glue was therefore chosen, which is designed to dissolve in epoxy-based matrix material (see Chapter 5 for details). This way, the glue is only present as long as it needs to be to hold the tag in position on the textile during handling and arrangement in the mold.

Regarding the wound effect mentioned above, another aspect relevant for material integration of any sort of inlay is the relation of Young’s modulus of the inlay to that of the host material. As [62] and [63] have shown, the wound effect created by the inlay is especially pronounced when Young’s modulus of the

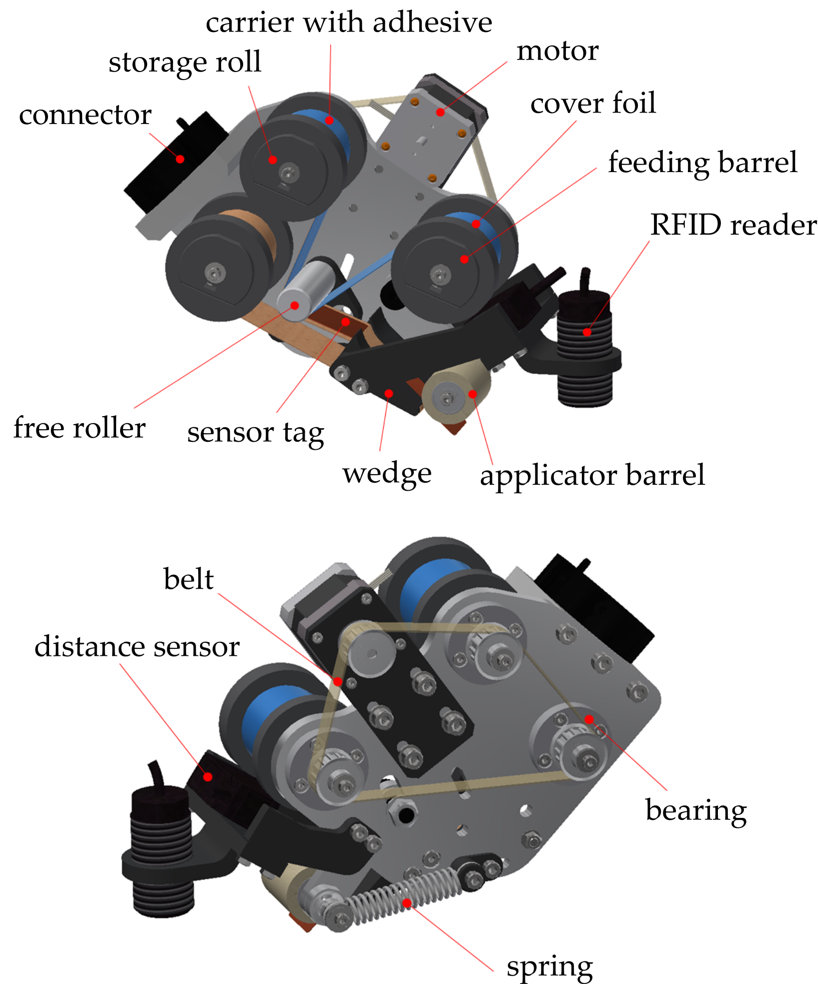

Figure 3.2: CAD rendering of sensor tag applicator for robot operation. Reproduced with permission from [61]

inlay is higher than that of the surrounding matrix, especially when the inlay is placed close to positions of high local strain. Consequently, the inlay should be at least as stretchable than the matrix. In other words, Young's modulus of the inlay should be equal to or smaller than that of the matrix. In this work, inlay substrate was chosen to be polyimide, which, according to [64] has a Young's modulus of 3.1 GPa. Table 3.1 gives example values for some duroplastic matrix materials that are frequently used for FRP production [1]. Regarding the majority of duroplastic materials, polyimide therefore seeems to be a usable material in terms of modulus comparison. As it additionally is the material most widely used for Flexible Printed Circuit Boards (FPCBs), it is an evident choice for cost-effective production of the sensor tags designed in this work. It has also been used for several material integrated sensors, e. g. in [12, 65–67]. Using very thin (5 µm) interdigital sensors with patterned perforation, [67] could show that CFRP samples with integrated

polyimide substrates could attain values for inter-laminar shear strength similar to pure CFRP.

Table 3.1: Young’s modulus for some exemplary duroplastic matrix materials, [1]

Matrix	Young’s modulus (GPa)
Epoxy (EP), cold cure	3.4
Vinyl Ester (VE), medium reactive	4.0
Polyester resins (UP), highly reactive	4.8
Epoxy (Hexion RTM135/RIMH137), [68]	5.4

In order to further reduce the wound effect, all tags developed in this work include resin holes for the fluid matrix to flow through during infusion, similar to the idea described in [12]. This is to allow the formation of resin bridges through the tag itself, to reduce the risk of local delamination and generally reduce the surface area of the foreign body present in the surrounding material. Additionally, the holes are meant to improve mechanical coupling of tag and matrix by not uniquely relying on matrix-tag adhesion but adding the resulting matrix ”fingers” reaching through the tag itself. As the tags are meant to measure strain of the surrounding matrix, best possible coupling is beneficial for minimal sensor error.

In summary, a sensor tag for FRP integration generally needs to meet the following requirements:

- ”sticker-like” behavior
- minimal thickness
- small outline, i. e. footprint
- Young’s modulus of the sensor should be equal to or smaller than surrounding host material
- usage of suitable glue for initial application, depending on material
- incorporation of openings for resin to flow through and around the tag

A detailed description of the actual implementations for the sensors presented is given in chapters 5 and 7.

Chapter 4
State of the Art and Motivation

This chapter is intended to give an overview of the techniques currently used for monitoring of FRP fabrication and later-on SHM, to provide context for the sensors presented in this thesis. These two topics are therefore introduced in the first and second section. Based on this, the third section summarizes the corresponding problems and challenges that arise when using these techniques with wired sensors, as is commonly done, to present the motivational basis for the work of this thesis. Subsequently, wireless sensors are introduced to give a potential solution to the problems connected to material integration, by eliminating wires from the material altogether. Finally, an overview is given on prior and related work on wireless sensors for material integration. The chapter is a detailed extension of the overview on the topics that has been previously given in [7].

4.1 State of the Art - Fabrication Monitoring

Due to the huge potential for process optimization and quality control, monitoring of FRP fabrication has been subject of manifold research. Several general principles have emerged, which will briefly be summarized in the following paragraphs.

4.1.1 Differential Scanning Calorimetry

A very precise technique uses measurement of the heat generated by the curing reaction for calculation of degree of cure. It is called Differential Scanning Calorimetry, and is the state of the art for detailed cure characterization. Though very precise, it is not applicable for in-line process monitoring due to its general principle, as it requires a special reaction chamber and usually only uses small amounts of resin [10, 65].

4.1.2 Dielectric Analysis

The most prominent technique is called Dielectric Analysis (DEA). It is able to yield good insights into curing status by measuring changes in electrical permittivity of the polymer, that are caused by reduced mobility of charge carriers inside the matrix material [10, 65, 69]. As both the chemical constitution of the polymer and mobility of the charge carriers change with progression of the curing reaction, the dielectric permittivity also changes, which can be measured and correlated

to cure progress. This is usually achieved by applying an alternating voltage to electrodes that are in contact with the resin and measuring the electrical impedance of the resulting setup (see Figure 4.1). As the arrangement of two electrodes around a dielectric is generally called capacitor (see Section 2.4.1), DEA can also be described as a technique using capacitive sensors. This can be done using a parallel-plate configuration, but interdigital electrodes offer some distinct advantages as described in Section 4.1.3. For analysis, dieletric loss and mobility of the charge carriers, which is commonly also called ionic viscosity, can then be used to calculate mechanical viscosity, actual progression of cure, i. e. glass transition temperature (T_G) and reactivity of the matrix [70, 71]. In this context, both parts of the complex matrix permittivity (ϵ' and ϵ'') can be used to gain information about the curing reaction, though the latter is very much dependent on the specific matrix material [50]. For this reason, measurement of dielectric response, i. e. the real part of the permittivity (ϵ'), is generally preferred [50]. Similar techniques using direct current also exist, (e.g. [72–74]).

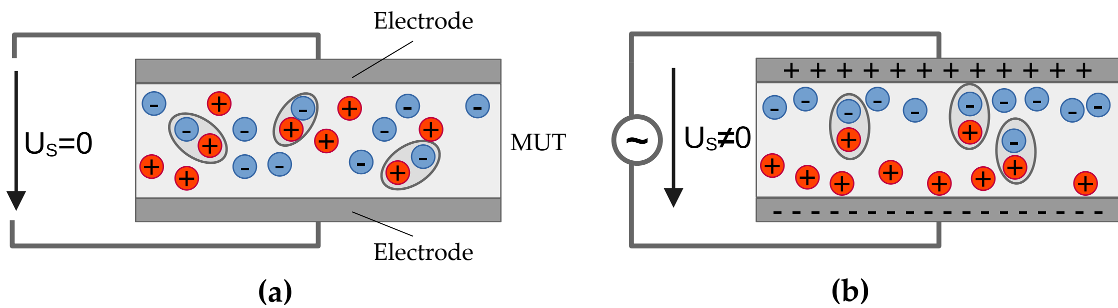

Figure 4.1: Schematic representation of DEA working principle. a) No voltage applied to electrodes. b) Alignment of MUT charge carriers / dipoles according to resulting electrical field. Adapted and redrawn from [71].

As of now, DEA techniques require complex and cost-intensive measurement equipment. For actual usage in FRP fabrication, cure measurement using DEA is restricted to surface-based sensors, as the dielectric sensors need direct contact to resin i. e. component surface [10, 71]. While material integrated sensors for DEA exist, these are intended for usage in prototyping, to gain information about matrix and curing behavior prior to actual component production. These sensors usually are connected to outside measurement equipment via wires [71]. This fundamentally complicates setup of the mold vacuum and also makes actual usage of the resulting part unfeasible, due to protruding wires, that are both sensitive to breakage and make part handling difficult. These and several other aspects (see Section 4.3) are part of the motivation for development of the wireless sensors presented in this work (see Section 4.3 for a summary).

4.1.3 Interdigital Sensors for DEA

One of the sensor types used for DEA employs interdigital electrodes (see Figure 2.14), as these offer the advantage of working with only single-sided access to the MUT, i. e. the polymer matrix, as opposed to parallel-plate electrodes [15, 47]. The main conceptual difference is schematically displayed in Figure 4.2. By fixing the electrodes and thereby their distance on a single substrate, variations in electrode spacing can be prevented that would influence a measurement with parallel plates. This allows for sensor placement both on MUT surface, i. e. in the mold surface, and inside the material itself. Also, interdigital electrodes can be used with big or complex part geometries, for which usage of parallel-plates would be geometrically impossible. As both electrodes used for DEA in general and interdigital structures form a capacitor, sensors with interdigital electrode configurations will here be referred to as InterDigital Capacitors (IDCs).

During FRP fabrication monitoring, IDCs can be used for multiple purposes. Before actual measurement of matrix cure, IDCs can be used during matrix infusion. As permittivity of dry textile and fluid resin are very different, resin arrival and therefore progression of the flow front through the mold is distinctly detectable [50, 65]. Using intelligent placement of sensors, this can be used to monitor infusion progress and thereby for prevention of dry spots, which would lead to voids in the finished part and consequently scrap production.

After infusion, IDC sensors can be used for detailed dielectric monitoring of matrix cure, as described in Section 4.1.2. Contrary to other electrode configurations like parallel plates, IDC sensors measure matrix properties very close to their position, i. e. only that in direct contact with IDC surface. This allows for very localized measurements. Measurement depth is directly connected with IDC geometry, as penetration depth of the electric field depends on its spatial wavelength, i. e. finger width and spacing (see Section 2.4).

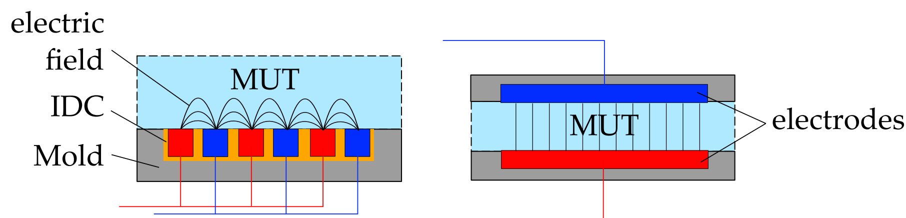

Figure 4.2: Schematic comparison of DEA sensors for FPR production monitoring. Left: Interdigital electrode sensor (IDC); Right: Parallel plate electrodes.

Scientifically, a lot of publications have investigated usage of IDCs for FRP production monitoring. Focusing on resin infusion, detailed resin flow front monitoring with IDCs could be demonstrated in [75] for a VARI process, unsaturated polyester resin and glass fiber textiles. The sensors were arranged in a 5×5 grid situated on the mold surface beneath the textiles, so that the resin flowed over the

sensor area. During infusion, dry spots and progression of the flow front could be successfully detected by measuring grid impedance at 800 Hz. Experiments on sensor response during curing were not reported there.

For cure monitoring, [12] integrated micro-scale interdigital structures into a GFRP sample. They used a perforated polyimide sensor substrate to allow the resin to flow through and build "resin bridges", reducing the resulting wound effect. In a VARI process, they were able to monitor cure of epoxy resin. For measurement, the sensors were connected to a commercial DEA system using wires, giving a reading of the ion viscosity. Similarly targeting minimal sensor size for minimized wound effect, [65] fabricated micro-scale IDCs on thin films of polyimide and provided an in-depth characterization thereof. The sensors were made in a clean room with photolithography, and were connected to impedance measurement spectroscopy equipment via thin wires. Excitation frequencies in the range of 1 Hz-1 kHz were used, thereby mainly measuring effects of ion migration and electrode polarization. These effects are limited to lower frequencies, as they involve actual mass transport and are strongly dependent on the material composition. Using the sensors, detailed insights into matrix and adhesive curing could be gained. Though not specifically reported in detail, infusion monitoring in terms of local resin presence is also possible with the miniaturized sensors.

In [50], larger IDCs were fabricated in a FPCB process, to allow for low-cost sensor production by using off-the-shelf technology. The IDCs were intended for monitoring of infusion and cure in a VARI process. For measurement, they were connected to a dedicated LCR-meter positioned next to the VARI setup, using 4-wire interconnects. From their results, they could show that a metallization ratio of $\eta = 0.5$ yields< the best sensitivity per unit area for the changing resin permittivity. Also, they found that the influence of electrode polarization on the real part of permittivity, which is due to ion transport, first reduces and then vanishes with higher excitation frequencies, i. e. frequencies above 10 kHz. In summary, they could prove that IDCs made on flexible PCBs can be used for dielectric monitoring of resin infusion and cure, giving insights on flow front progression, i. e. resin presence, and cure progress. In another paper [52], similar in-situ monitoring of FRP production was reported, that employed shielded IDCs, i. e. IDCs using a metallized back plane. The sensors were attached to the surface of a VARI mold made of PMMA and connected to an LCR meter using wires. In comparison to the unshielded IDCs, an increase in nominal capacitance and a slightly higher sensitivity per unit area could be found. Also, due to the shield, sensor capacitance was found to be largely independent of the application surface, i. e. substrate, which is beneficial for mounting the sensors on the mold surface. As with the other sensors based on singular IDCs, flow front monitoring is only possible with multiple sensors placed at different positions, as a single IDC can only be used to report resin presence. To overcome this, the work reported in a later paper [76] shows that, using flexible interconnections, a matrix of IDCs can be used to

monitor larger areas and two-dimensional flow front progression, similar to the IDC network presented in [75]. Opposed to the experiments using single IDCs, this method allows for a higher level of detail.

As matrix cure can result in intramaterial tension and therefore deformation, [53] investigated the relation of strain-induced capacitance change versus cure induced capacitance change for embedding in RTM6, which is a matrix frequently used in aerospace industry. They found that indeed an influence of strain on capacitance of a miniaturized IDC could be measured, showing a linear response of ca. 0.04 % per 0.1 % strain. However, compared to the capacitance measurements for resin cure, the influence is albeit negligible, as change in capacitance is more than 100 % during the first phase of curing. Consequently, measurements of matrix cure should not be significantly influenced by cure-induced material strain. Nevertheless, also due to the linear response, the IDC could theoretically be used for strain measurement in context of a capacitive strain gauge (see section 4.2.2 for details). For more information on IDC theory and IDCs in general, see Section 2.4.

4.1.4 Temperature Monitoring

Continuous measurement of temperature is also a possible approach for FRP fabrication monitoring [10, 11], and due to its simplicity, it is probably the most straightforward approach. Therefore, it is usually employed in at least a very basic form (e.g. placement of wired temperature sensors on the mold surface or in the resin reservoir). Countless principles for measurement of temperature exist, like the thermoelectric effect, the thermoresistive effect, or the photoelectric effect and many can be used for FRP fabrication monitoring [11, 40]. Both thermoelectric and thermoresistive thermometers can be used for mould temperature measurement, and infrared thermometers can deduce surface temperature even from a distance. For open faced moulds, infrared thermography can even be used to detect dry spots by detecting surface temperature gradients [11]. But, as mentioned above, surface-based temperature measurements can often not yield sufficiently precise information for accurate process monitoring, due to inhomogeneous temperature distribution throughout the laminate. Especially as temperature can vary over laminate thickness for parts with many textile layers, local temperature inside the laminate can very much differ from surface temperature. This was proven by [66]. They integrated wired temperature sensors both into an FRP layup and onto the mold surface for a VARI process, and showed that surface based measurement was not able to provide the same amount of information as the integrated sensors. Experiments in [77] show that flow front monitoring is possible using wired laminate-integrated thermocouples for non-metallic moulds, while [78] showed that resin flow monitoring is possible with wired thermocouples distributed over carbon fiber preforms for usage in a VARI process.

4.1.5 Pressure Monitoring

As pressure plays an important role for infusion and resin flow through fibers, pressure sensors can also be used for monitoring of flow front and impregnation, as the local pressure changes with resin arrival, especially in a vacuum [11]. This can be detected using the piezoresistive effect. A change in pressure results in a change of the electrical resistance of e.g. a strain gauge on a membrane, covering a chamber containing a reference pressure [40]. Alternatively, the piezoelectric effect can also be used, utilizing a voltage generated by deflection of a piezoelectric material like some crystals. Wired piezoresistive pressure sensors were used by [79] to measure the pressure gradient during a VARI production process of wind turbine blades. Similarly, [12] and [67] used wired pressure sensors during FRP fabrication, measuring the local matrix pressure during infusion, to allow for curing initiation only after full impregnation.

4.1.6 Optical Measurements - Fiber Bragg Gratings

For implementation in fiber composites, usage of optical fibers for fabrication monitoring is also a rather obvious possibility, as intensive research and the numerous publications about FRP fabrication monitoring show. Primarily, these utilize sensors based on Fiber Bragg Gratings (FBGs) (e.g. [80–82]). The measurement principle employs partial reflections of light introduced into the optical fiber, that are caused by reflective micro-surfaces along the fiber length [11]. The spectrum of the reflected light changes with environmental conditions (e.g. temperature or strain) and can therefore be used to quantify environmental changes. With these systems, monitoring of both flow front and cure status is possible, and, depending on the system, later usage of the FBGs for SHM of the host component is possible (see also Section 1.2). A major downside of systems using FBGs is the sensitive nature of the fibers themselves, making them fragile, complicating handling and resulting in a laborious and therefore cost-intensive installation process [11]. Also, measurement equipment necessary for interpretation of the light signals is complex and comparably expensive.

4.1.7 Other Techniques

Regarding FRP infusion and cure monitoring, a multitude of other principles and techniques exists, using e.g. reflection properties of electromagnetic waves (Electric Time Domain Reflectometry), optical cameras, or ultrasonic transducers. The latter use dampening of the ultrasonic waves that is caused by resin presence i. e. arrival (see e. g. [83, 84]). A monitoring of cure can also be realized via ultrasonic transducers, as resin cure changes the local speed of sound, e. g. used in [84–86]. Due to the measurement principle, this yields a more or less geometry-averaged measurement – differences in local cure and especially over high material thickness

can therefore not be discerned. In-depth reviews of the techniques mentioned and other non-destructive testing methods can be found in [11] and [87].

4.2 State of the Art - Load Monitoring

One of the basic ways to monitor a structure's load is quantification of mechanical strain [38]. In order to quantify strain in context of SHM, a multitude of principles has been investigated, as comprehensively reviewed in [87] and [17].

4.2.1 Strain Gauges

A very basic principle for strain quantification is usage of the piezoresistive effect, i.e. measurement of deformation induced changes in electrical resistance (see Section 2.3). One of the advantages of strain gauges is their simple and well known measurement principle, resulting in a very straightforward circuitry for readout with low power consumption, depending on gauge resistance. This makes strain gauge application very easy. Measurement errors caused by differences in thermal expansion of strain gauge and host material can be eliminated by fitting the thermal expansion coefficient to the intended material. Combined with different possible circuit configurations, very high measurement precision and also insensitivity to environmental changes can be achieved with strain gauges [40]. Usually, strain gauges are applied to the component surface with specialized glues to achieve good coupling and therefore transfer of strain into the gauge. Glue properties and glue lifetime are therefore highly relevant factors for accurate strain measurements, and the elasticity of glue can have a negative impact on tension transfer from surface to gauge [63]. This surface application in turn exposes the gauge to environmental influences, like water or mechanical impacts, that would damage the system over time, making necessary a protective encapsulation around the gauge and the connecting wires.

For application with FRP, these downsides could be eliminated by [63] and [88]. They embedded strain gauges into FRP with good results, thereby showing that material integration of strain gauges into FRP is possible, obviating the need for a glued connection and encapsulation, while also protecting the gauge from environmental influences. Additionally, it could be shown that strain gauge integration can yield a higher sensitivity compared to glued strain gauges due to better mechanical coupling, while also giving insights into strain distribution throughout the component [63]. In general, strain gauges have been used for numerous SHM applications, a few of which shall be mentioned here: [89] used strain gauges for vibration measurement in a new SHM method that was able to localize different damage categories to an aluminum plate. [90] applied several high sensitivity strain gauges to the surface of a steel bridge surface, allowing for health monitoring of the entire structure during usage.

For SHM of buildings, strain gauges can also be used, as shown by [91]. They made a wireless SHM system by reading out strain gauges distributed in a building that were equipped with a battery powered measurement unit. Regarding applications with FRP, [92] used strain gauges for monitoring of an FRP bridge, proving that strain gauges can be used for long and short term SHM. [93] used strain gauges for vibration-based SHM of an aircraft wing, while [94] integrated several strain gauges into FRP forming a net, enabling strain measurement during production and application of a wind turbine blade.

4.2.2 Capacitive Strain Gauges

Another principle that can be used for strain quantification uses changes of capacitance that are induced by a change of electrode spacing, similar to plate distance in a parallel plate capacitor. As parallel plates are principally unfitting for many strain measurement tasks, IDCs are used instead, resulting in a capacitive strain gauge (see Section 2.4.7). Though capacitive strain gauges are not a new technology in general, not much work has been published on applications for SHM that use them, especially in the field of FRPs. This might be due to the more complex circuitry necessary for capacitance readout or the presence of cross sensitivities between capacitance value and environmental influences like temperature and humidity. In [53], the capacitance response to strain applied to an FRP sample with integrated IDC was investigated. Results show a linear dependency between applied strain and IDC capacitance. Though capacitance change in response to strain is very small as compared to capacitance change caused by curing of a surrounding matrix material, usage in FRPs should theoretically be possible given a sufficiently precise measurement circuit. Regarding development basics on capacitive strain gauges, the aforementioned cross-sensitivities and techniques for their compensation, a very detailed account is given in [54].

Nonetheless, some works employ IDCs in a general SHM context, which shall briefly be mentioned: The results published in [95] present usage of an ink-jet printed IDC for dielectric monitoring of epoxy resin cure and subsequent SHM of an adhesively bonded composite joint. SHM functionality was yet not implemented by using the IDC as a strain gauge, but by correlating sensor impedance directly to damages in the MUT, i. e. its mechanical degradation. Printed IDCs were also used in publications on capacitive strain gauges for SHM of soft structural textiles in the space industry [55, 96], e. g. kevlar straps used in parachutes. In [97], laser-cut brass IDCs are employed for wireless strain measurement in an SHM context for buildings. Contrary to the classical capacitive strain gauge principle explained above, the capacitance in the system presented is not mainly based on fringing field effects but parallel plate capacitances occurring in between the comb electrodes cut from the relatively thick (127 µm) metal sheet. Regarding system architecture of the readout circuitry, the results presented in the publications for wireless strain measurement, e. g. [54, 97], use commercial Capacitance to Digital Converters

(CDCs) for capacitance measurement, similar to the IC used for the capacitive sensor tag presented in this thesis. More precisely, the resonant circuit principle is used (see Section 2.4.8). For more information on IDC theory, see Section 2.4.

4.2.3 Fiber-Bragg-Gratings

As with fabrication monitoring, techniques employing FBGs for usage in FRPs have been subject of intensive research [17, 98]. On the one hand, these systems combine several advantages: As optical fibers can be embedded in the textile, near non-intrusive integration into FRP materials is possible, reducing the impact of sensor presence on the host components' structural integrity. As integration is done prior or during FRP fabrication, FBG systems can enable in-situ monitoring of relevant processing parameters (see Section 4.1), thereby improving process and quality control. During component usage, they allow in-depth measurement of multiple parameters, e.g. both strain and temperature, as opposed to conventional piezoresistive strain sensors. Last but not least, SHM systems using FBGs enable monitoring of large area structures due to possible lengths of the optical fibers, which makes the technology especially appealing for long structures (e.g. wind turbine blades [99]). On the other hand, FBG based systems also have several severe disadvantages. As already stated in 4.1, specialized analysis equipment is required in order to make use of the optical fibers. This makes the overall system comparably expensive [17]. Also, optical fibers are very sensitive, requiring very careful handling during FRP production and usage [19, 98, 100]. This in turn increases cost and makes SHM systems based on FBG feasible only for some scenarios, e.g. involving high-risk structures. In context of possibilities for automated system application during FRP fabrication - by e.g. a robot - this fragility of the optical fibers is a disadvantage.

4.2.4 Other Techniques

Additionally, a multitude of other techniques for SHM of FRP exist, that shall be mentioned for completeness' sake, without giving to much detail here, as most of these techniques are either very specialized or are not useful for on-site application due to their principle. [87] summarizes techniques for SHM and differentiates between external and internal methods. For external methods, testing with different forms of x-rays can detect both voids, cracks and delamination, while both conventional and infrared cameras can be used for optical testing with mixed results and detectable defects. Ultra sonic waves are also applied in several techniques, both with external and guided waves, giving location and severity information about damages. For internal methods, apart from FBGs, [87] mentions several methods that use a form of electrical testing involving different sorts of conductive filling material (e.g. carbon nanofillers or metallic reinforcements). Both strain quantification and detection / localization of damages could be achieved. Further

references and details on these techniques can be found in the corresponding literature (e.g. [17, 87]).

4.3 Problems with wired sensors for Load and Fabrication Monitoring

As shown in the preceding paragraphs, numerous techniques and principles have been developed and are employed for monitoring both FRP fabrication and structural health of FRP components. Compared to surface based measurements, material-integrated sensors are gaining in relevance due to higher overall sensitivity and superior protection of the sensor system against exterior influences [87]. A mutual property of nearly all systems mentioned is the usage of wires for interconnection of the sensors and measurement devices for transmission of energy and measurement data. This paragraph summarizes the problematic aspects arising with material integration of wired sensors for FRPs:

- During FRP production, integration of the aforementioned sensors and wires is a complicated and therefore time-consuming process, especially for sensitive sensor elements, and usually has to be done manually, resulting in high cost [11].
- Apart from the sensors themselves, wire presence thoroughly complicates setup of the vacuum seals, as the wires need to be lead through the vacuum seal while still ensuring air tightness. Though this is possible, it is expensive and also prone to errors, potentially compromising vacuum buildup and thereby quality of the infusion process. Additionally, wires can negatively affect the flow front during infusion by creating flow channels along their length.
- To eliminate sensors from the production process without relinquishing the advantageous knowledge about resin flow and cure for a specific part geometry or specific loading scenarios, sensor-integrated prototypes can be used to gather information that is used later on as an estimation basis for sensor-less components. Besides the question of precision, this practice is not economically or ecologically feasible, especially in context of rising resource prices, as these prototypes cannot actually be used for real application.
- Apart from fabrication-related aspects, wires of integrated sensors also need to be taken special care of during FRP lifetime, as they are very sensitive, especially in comparison with the FRP material itself. This is mainly due to the general arrangement of protruding wire and surrounding matrix where the wire exits the FRP, that is very likely to create shear stress to the wire, possibly leading to breakage. This is compounded by the difference in the two materials Young’s modulus and different thermal expansion coefficients.

Once a wire is broken, the sensor system is often rendered useless, as exchange of the integrated sensor is mostly either impossible or economically unreasonable.

- Regarding fatiguing behavior of wired, sensor-integrated FRP samples, [101] observed that failure often occurred at the positions where the wires exited the matrix, supporting the conclusion that wire presence can degrade fatigue behavior of FRP.

4.4 Solution: Wireless Sensors for FRP Integration

To circumvent the problems associated with wired sensors, recent research has investigated development of wireless sensors for integration into FRP. This section will briefly summarize the current state of the art in that regard.

In order to supply a wireless sensor system with energy, the most straightforward idea is usage of a battery. For material integration, this approach is not feasible for two major reasons. Firstly, batteries have a comparably large size, which is disadvantageous in terms of the wound effect generated in the host material. In other words, batteries are generally too big to not negatively influence the mechanical integrity of the surrounding material. Secondly, apart from size constraints, all available battery systems eventually run out of power. This fundamentally limits lifetime of a material-integrated sensor system, as battery replacement is impossible for obvious reasons. These two constraints make wirelessly supplying the sensor system necessary, e. g. via RFID. Though the term RFID encompasses numerous distinct subtechnologies and corresponding standards, the general principle of electromagnetically coupled *reader* and to-be-read *tag* is universal and can also be used for sensoric tags.

Sensor systems comprising their own power source are usually called *active*, while systems powered remotely are usually called *passive*, as they rely on wireless power transmission to function [25]. Passive systems are therefore employing a principle commonly known as *energy harvesting*, i.e. collection of energy from their immediate environment. Though several principles for energy harvesting exist (e.g. heat, vibration, light, etc.), most sensoric RFID systems use electromagnetic fields for energy supply, which are supplied by the reading device [25]. The electromagnetic field induces a voltage in an antenna structure connected to the sensoric system, which in turn supplies the sensor (see Section 2.2.3 for theoretical background).

Two basic principles for implementation of passive sensor tags have emerged: The first and most widely used concept makes direct use of the antenna itself, i. e. employs the antenna as sensing element [25, 102]. This is possible, as the antenna is subjected to the immediate environment of the sensor and therefore influenced by it (e. g. changes in resonance frequency due to temperature). This allows for very simple sensor design and therefore low production cost, which is

the greatest advantage of sensoric antenna systems. Also, as antenna structures can be designed to fit a specific application and usually do not require many additional components, these systems can be designed in an less intrusive way for a specific application. The greatest drawback of sensoric antenna systems is the high susceptibility of the measured entity to exterior influences. As sensitivity of the antenna to external influences is actually part of the system concept, cross-sensitivities of the antenna to different influences can degrade system performance, as differentiation of the actual measurement and interference can be difficult [102]. For simple measurement task though, sensoric antennas can be applicable. Regarding usage of sensoric antennas for SHM, [102] comprehensively reviews different concepts and applications.

The second principle also uses an antenna, but only for energy supply and communication, while sensoric data is gathered via a dedicated sensing element. In order for this to work, further circuitry is necessary in the sensor, which does the actual measurement acquisition, power control and communication. If designed with sufficiently low power consumption, basically all conventional measurement electronics could theoretically be used on a sensor tag, allowing for much more complex sensing functions.

Correspondingly, this work employs a passive sensor tag with active electronics for answering the need for cost-effective FRP fabrication monitoring technology, while at the same time avoiding the downsides associated with integration of wired sensors.

4.5 Related Work - Wireless Sensors

For integration into FRP, a limited amount of prior work focusing on passive RFID-based sensors has been published to date. As a basic precondition, [103] proved that wireless power transfer into FRP is possible via inductive coupling of a reader coil and an antenna coil, and that the amount of transferable power can be sufficient for basic low power electronics. Implementing the sensoric antenna approach with a custom reading unit, [104] developed a rigid PCB for wireless, substrate-integrated measurement of epoxy resin cure and local temperature. Similarly, [105] built an LC-resonator circuit using a sensoric antenna and a planar capacitance for FRP integration, to measure curing progress via changes in the resonant frequency.

Using dedicated electronics, as opposed to sensoric antennas, [106] proved that embedding passive wireless sensors into FRP is generally possible and usable for process monitoring of FRP production. In their experiments, they were able to measure local pressure during resin infusion in a VARI process, allowing for monitoring of the flow front progress. In another experiment [107], they measured both temperature and resin pressure during FRP infusion and curing, again monitoring the flow front, but the sensors dropped out as temperature increased during curing.

The sensors were therefore only usable during infusion and not for cure monitoring or measurements in an SHM context.

A different approach was taken by [108] and [109], who, in two experiments, integrated several commercially available RFID transponders into GFRP and measured received signal strength of the transponders to correlate that with infusion and curing progress. In the employed VARI process they were able to identify arrival of the flow front, but signal changes during cure were too small to allow for correlation with curing status.

Chapter 5
Piezoresistive Sensor Tag

To answer the problems mentioned in the preceding chapters, a wireless sensor was designed. This chapter will chronologically describe the steps taken to gain a working prototype before presenting the experiments and corresponding results that were conducted to test and characterize its function. It mainly builds on results previously published in [7], extending the account given there, while providing supplementary details and information on additional experiments and results. In the first main section, it will be shown how the sensor was designed and subsequently made, and what concepts and techniques were used to that end. In the second major section of this chapter, the resulting sensor is investigated, both regarding its potential usage in fabrication monitoring and later on SHM. For this, integration experiments and sensor characterization both for the lose and material-integrated sensor tag are presented. Furthermore, effects of sensor integration on the host material are examined with both non-destructive and destructive testing. Finally, overall limitations of the sensor are examined (e. g. reading distance, operational temperature range, etc.) and a summary of this chapter is given.

5.1 Sensor Design and Fabrication

This section describes sensor conceptualization and its fabrication. First, the general idea and design guidelines for the electronics are laid down, giving details on circuit layout and component selection. Next, tag circuitry is explained, elaborating on sensor circuitry for strain and temperature measurement. Subsequently, all steps taken for physical buildup of the final prototype are described, starting with sensor layout and details on calculation of fitting antenna parameters. Finally, assembly of the final prototype and programming of the micro controller are described in the last two subsections. A full schematic of sensor tag circuitry is additionally given in Figure A.9.

5.1.1 Sensor Concept

As in a lot of production environments automatically placing stickers to products is a well established process, sensor design is based on a sticker-based *sensor tag* approach to facilitate automated sensor placement in an industrial context (see Chapter 3 for details on "sensor tag"-approach). To make this possible, the sensor tag needs to be both flexible, thin, and sufficiently small, which are properties that simultaneously are necessary for material integration. To withstand the conditions present during fabrication, the sensor tag needs to be sufficiently resilient to elevated temperatures. For that reason, all components were selected to have rated maximum operating temperatures higher than or equal to 125 °C. As the tag is meant to operate without neither wires nor battery, all power needs to be harvested wirelessly via the reader-supplied electromagnetic field. Consequently, a very low-power design of the electronic circuitry is necessary. Also, to ensure broad compatibility and easy usage, a widely used RFID-standard is employed (ISO 14443). Simultaneously, this makes possible using off-the-shelf components for wireless communication, in turn simplifying design and reducing cost. As economic producibility of the sensor tag is targeted, standardized components are also used for the electronics, including several commercially available ICs to reduce size and power consumption, and to simplify circuit layout. The resulting concept for the sensor circuitry is displayed in Figure 5.1 and will be described in the following paragraphs.

5.1.2 RFID-Transponder and Micro Controller

Tag circuitry is built around an IC (NXP NHS3152,[110]) combining both a micro controller and an RFID transponder in a single package, which handles wireless communication and power supply of the sensor circuitry by harvesting power

[1]Prior version first published in 'Advances in System-Integrated Intelligence', p. 182-193, 2022 by Springer Nature

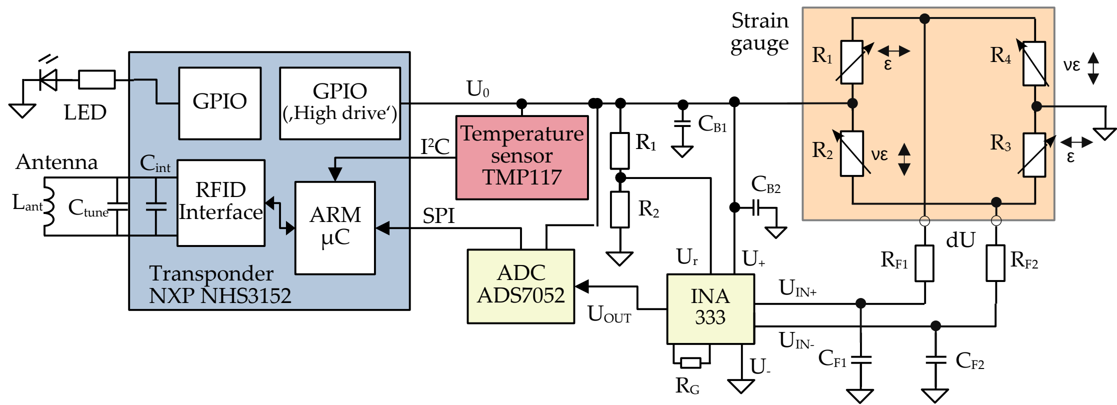

Figure 5.1: Schematic representation of the sensor tag circuit, adapted from [5].[1]

from the RFID-field via the antenna resonant circuit. The latter consists of the antenna coil L_{ant} and an internal capacitor C_{int} in the transponder. To induce maximum voltage in the antenna coil, the resulting resonance frequency needs to be very close to the frequency of the electromagnetic field output by the reader, in this case 13.56 MHz (see Section 2.2.3 for details). To compensate for possible detuning (e. g. due to fabrication tolerances etc.), a designated capacitor C_{tune} in parallel with the antenna can be chosen. The harvested power is output by a special General Purpose Input Output (GPIO) pin of the transponder, which, according to the transponder data sheet, can drive up to 20 mA depending on available power. This voltage U_0 is stabilized via several ceramic capacitors C_B for subsequent circuitry. Nominal output voltage of the GPIO pins is 1.8 V, though this is influenced by tag-reader distance. To give feedback to the user, an LED is included to indicate tag power status. The integrated micro controller (ARM Cortex M0) collects measurement data from the temperature sensor and the strain gauge, and handles wireless communication via the integrated RFID interface. As it is a full-fledged micro controller with several peripherals and interfaces, future incorporation of additional functionalities, i.e. different sensors, is possible.

5.1.3 Antenna

Using the technique described in Section 2.2.4, the antenna coil for transfer of energy and data is designed as spiral copper trace, framing the PCB on the outside.

5.1.3.1 Calculation

According to ISO 14443, the resonance frequency of the transponder antenna network needs to be 13.56 MHz (see Section 2.2.2 for more details). To calculate the antenna inductance needed, capacitance of the transponder IC needs to be known, which in this case is 50 pF, as given by the data sheet [110]. Also, parasitic capacitance (C_p) of the traces and connection pads, and the antenna itself influence resonance frequency. Exemplary data for resulting C_p of different fabrication

techniques is given in literature, e. g. in [31]. In this case, the overall parasitic capacitance of the antenna and connections is assumed to be

$$C_p = C_{conn} + C_{antenna} = 1\,\text{pF} + 3\,\text{pF} = 4\,\text{pF}.$$

Using Equation 2.2, antenna inductance can then be calculated[2]:

$$f_r = \frac{1}{2\pi\sqrt{L_a(C_{IC} + C_p)}} \Rightarrow L_0 = \frac{1}{(2\pi f_r)(C_{IC} + C_p)} \tag{5.1}$$

To achieve correct tuning of the actually fabricated resonant circuit, multiple, slightly different antenna geometries were produced with the same fabrication process, as actually resulting inductance is also dependent on material properties, and fabrication tolerances regarding antenna and substrate geometry. As any metal present in antenna vicinity affects resonance frequency, the designs already include a prototypical version of the traces and connection pads in the center of the antenna coil that are used later on for the tag circuitry. This way, tuning deviation of the final sensor tag is expected to be lower. According to literature, e. g. [30, 31], fabrication of antennas with $\pm 10\,\%$ of L_0 is usually a good starting point. For $C_{IC} = 50\,\text{pF}, C_p = 4\,\text{pF}$, the corresponding inductance values are tabulated in Table 5.1.

Using Equation 2.6, dimensions of planar rectangular coils can be estimated that fit the calculated inductance values. As a starting point for calculations, an aspect ratio of 4:3 was defined for rectangle geometry. Also, due to fabrication requirements, minimum track spacing (g_{min}) and minimum track width (w_{min}) are set to 0.1 mm. For the fabrication process, copper thickness and therefore track thickness t is about 18 µm, as given by the PCB manufacturer. Regarding the turn exponent p, a value of 1.8 is chosen according to Table 2.4, as standard PCB processes use etching. After approximating space requirements of the tag circuitry and the corresponding footprints, a fitting overall width of the tag and therefore the antenna was estimated to be about 40 mm, taking into account an additional distance of ca. 4 mm in between electronics and the respective traces, and the antenna, as recommended in [111]. The resulting geometry parameters are given in Table 5.1.

Table 5.1: Antenna geometry parameters for piezoresistive sensor tag

Geometry	***L*** **(µH)**	***N***	a_0 **(mm)**	b_0 **(mm)**	***w*** **(µm)**	***g*** **(µm)**
L_0 −10 %	2.283	5	40.3	30.23	225	280
L_0	2.536	6	38.0	28.50	348	297
L_0 +10 %	2.790	6	39.4	29.55	300	297

[2] As usage of a tuning capacitance is not intended, C_{tune} is excluded here. It can be used for correction, if necessary resonance frequency does not sufficiently match the target frequency.

5.1.3.2 Validation

For validation of the calculated geometries, these were fabricated via the same process as used later on for production of the sensor tags themselves, to assure transferability of the results to the actual sensor fabrication.

For measurement, the antenna resonant circuit has to be completed, by adding either the intended RFID transponder, containing the integrated resonant capacitance C_{IC}, or by adding the equivalent capacitance via a capacitor. The latter option is chosen in this case. Resulting resonance frequencies of the different versions were then measured with an impedance analyzer, using a loop antenna as described in Section 2.2.4, giving the best fitting antenna geometry. The corresponding data for the different antenna geometries is displayed in Figure 5.2. It can be seen that all resonance frequencies are slightly higher than initially expected, i. e. calculated. The geometry calculated for L_0 was found resonating at 14.33 MHz, while the geometry targeting a lower inductance of $L_0-10\,\%$ results in a resonance frequency of ca. 14.60 MHz. Finally, the $L_0+10\,\%$ geometry nearly marks the target frequency of 13.56 MHz with a measured resonance frequency of 13.63 MHz. Regarding the application, this deviation is negligible, so the $L_0+10\,\%$ geometry is chosen for usage with the sensor tag.

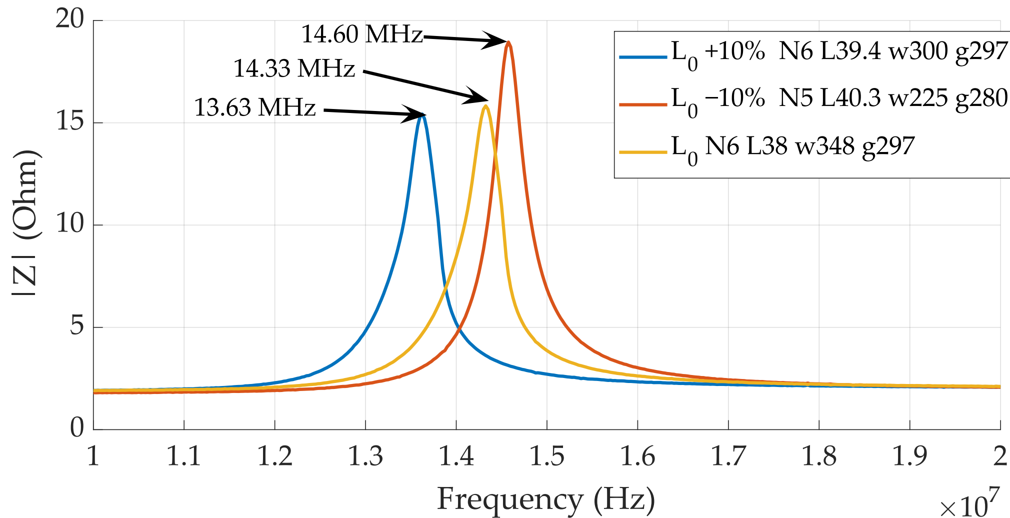

Figure 5.2: Resulting resonance frequencies for the different antenna geometries.

To validate reproducibility for the final tags, resonance frequency of six fully assembled specimens was measured. The corresponding data is displayed in Figure 5.3. It can be seen that resonance frequencies differ only slightly between the different specimens, giving an average of 13.646 MHz with a standard deviation of 0.019 MHz. For usage with the sensor tag, this deviation is also negligible.

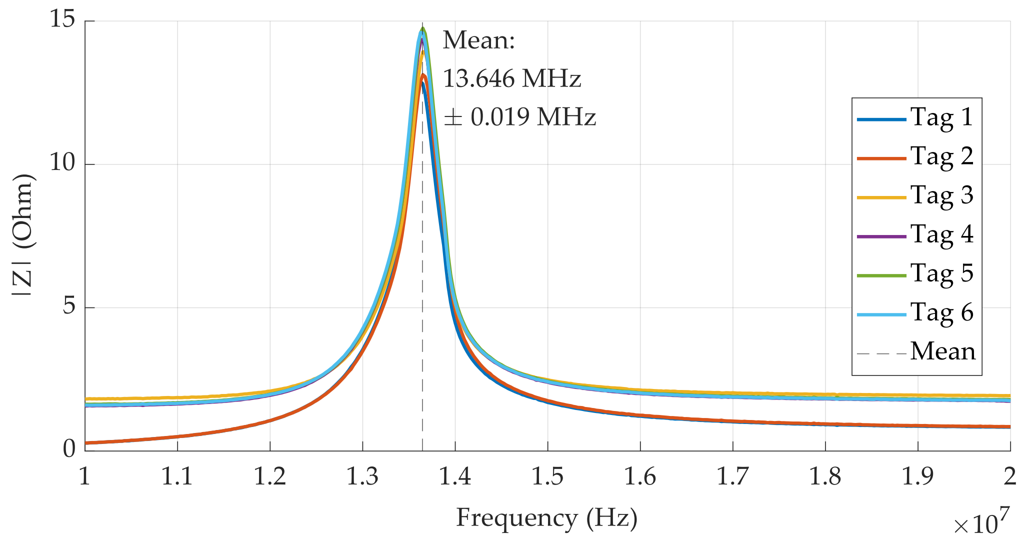

Figure 5.3: Absolute of tag impedance for identification of antenna resonance frequencies for six specimens of the final prototype of the piezoresistive Tag, mean resonance frequency indicated.

The fixture used for the measurements is depicted Figure 5.4. The integrated loop antenna is made from thick copper wire (d=1.65 mm) mounted in a 3D-printed fixture, which stabilizes the loop. Also, it is possible to use the fixture for setting a defined distance between antenna loop and transponder antenna, by providing a movable surface where the tag can be placed during measurement. A scale engraved in the side wall can be used for setting the desired distance (see Figure 5.4).

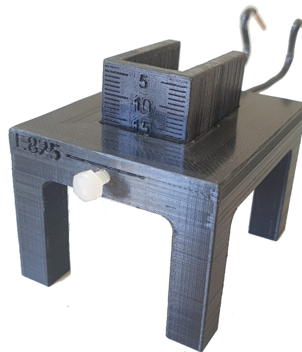

Figure 5.4: Loop antenna fixture used for measurements of tag resonance.

5.1.4 Strain Measurement

For strain measurement, a full bridge strain gauge[3] with four active gauges is selected, to ensure intrinsic temperature compensation and to provide for high sensitivity. It is based on Karma-alloy strain gauges fabricated on a polyimide

[3] S5020 by MicroMeasurements, [112]

thin film, encapsulated via an epoxy cover layer [112], and has an overall size of 4 mm×4 mm. It is specified up to an operating temperature of 205 °C and provides a gauge factor of 2.1. To enable bidirectional strain measurement, two gauges each are placed perpendicular to each other, as illustrated in Figure 5.5a, resulting in an increasing bridge voltage dU for strain in Y-direction, and a decreasing bridge voltage for strain in X direction. This gauge configuration principally results in lateral contraction ($\nu\epsilon$, occurring perpendicular to component strain with ν being Poisson's ratio of the material) being superimposed on the bridge signal, which needs to be taken into account during calculation of the actual mechanical strain from the measured bridge voltage. As the amount of lateral contraction is material-dependent, this effect needs to be taken into account during data processing. In this case, lateral contraction increases bridge output, as contraction perpendicular to main strain direction influences bridge output the same way as the actual strain itself, thereby making the overall sensor more sensitive.

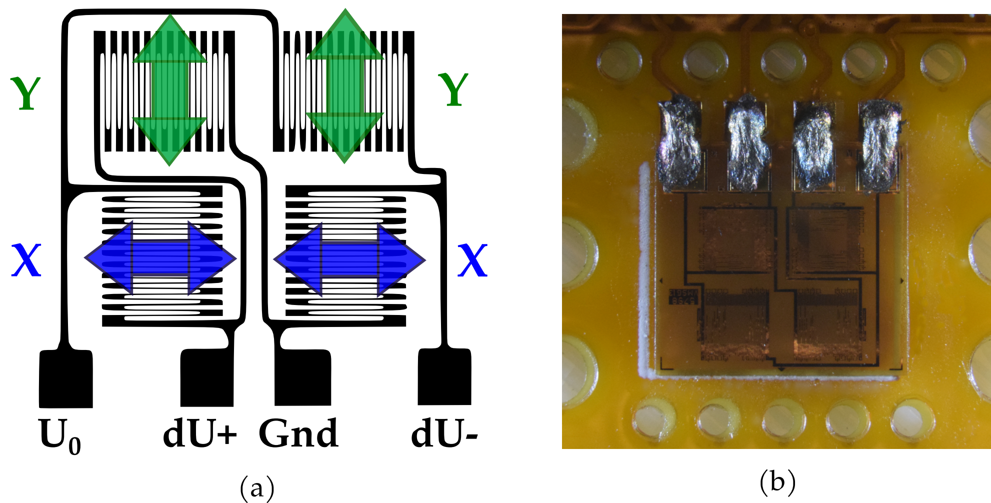

(a) (b)

Figure 5.5: a) Full bridge strain gauge configuration for biaxial strain measurement [112]. b) Strain gauge glued to sensor substrate, electrically connected with conductive glue.

In order to achieve low power consumption of the circuit, a comparably high bridge resistance of 5 kΩ is chosen. An Instrumentation Amplifier (INA)[4] is then used for amplification of the resulting bridge voltage. This is to ensure minimal influence on the measured signal by the high impedance input of the amplifier. Amplification gain is set by an external resistor R_G. Bridge voltage is filtered pre-amplification by a 100 Hz (−3 dB) R-C low pass filter to reduce noise. This is necessary, as the INA can only drive a maximum capacitive load of 500 pF according to data sheet [113], preventing placement of the low pass capacitor in the INA output path. To offset the amplified voltage for digitization, a reference voltage obtained via a voltage divider ($R_{1/2}$) is added via the reference input of

[4]INA333 by Texas Instruments, [113]

the INA, as the subsequent Analog to Digital Converter (ADC) uses a single-ended configuration.

As the input range of the ADC is *GND* to U_0, this setup minimizes measurement error caused by fluctuations of the supply voltage U_0 due to bridge voltage, reference voltage and the comparison voltage used by the ADC all being influenced the same way, similar to a common-mode noise reduction concept. As fluctuations in supply are likely, due to wireless power transmission and possibly varying distance to reader, this concept is necessary. Both bridge and reference voltages are therefore automatically centered between ground and supply voltage, ensuring that fluctuation of supply least influences measurement precision. Digitization is conducted via a 14 Bit, small footprint, low power ADC[5], which communicates with the micro controller via Serial Peripheral Interface (SPI). As ADC sampling rate is comparably high (up to 1 MHz), several conversions can be done in fast succession, allowing for higher accuracy via on-tag averaging.

5.1.4.1 Strain Calculation from Bridge Voltage

In order for the sensor tag to give a strain reading, the latter must be calculated from the digitized bridge voltage amplified by the INA. As the strain gauge used on the sensor tag employs a full bridge configuration with two of the four gauges perpendicular to the other two, Equation 2.22 can be used to calculate the magnitude of a strain in X direction from bridge voltage dU, supply voltage U_0, gauge factor k and Poisson's number v_{xy} of the material:

$$\epsilon_x = \frac{2}{k(1+\nu_{xy})}\frac{dU}{U_0}$$

Regarding the circuit supply voltage on the sensor tag, U_0 is influenced by the quality and amount of the voltage harvested from the electromagnetic field, and is therefore subject to change. Also, a numerical value for the current supply voltage available at a given point in time cannot be known, as it is not measured on the tag. For strain calculation, the ratio of bridge voltage to supply voltage is therefore used instead, without actually quantifying each voltage on its own. This is possible, as the ADC employed for digitization of bridge voltage and the bridge itself are supplied by the same voltage. Assuming that the amplified bridge voltage relates to supply the same way the digitized value relates to the full bit range of the single ended ADC, knowledge of distinct numbers for dU and U_0 is not necessary:

$$g\frac{dU}{U_0} = \frac{b}{B} \tag{5.2}$$

[5] ADS7052 by Texas Instruments [114]

with

$$g = \text{INA gain}$$
$$b = \text{digitized bit value of amplified bridge voltage}$$
$$B = 2^n = \text{full bit range of an ADC with } n \text{ Bits}$$

Using Equation 2.22, we get

$$\epsilon_x = \frac{2}{k(1+\nu_{xy})}\frac{dU}{U_0} = \frac{2b}{k(1+\nu_{xy})gB}. \tag{5.3}$$

To determine theoretical circuit resolution, the width of the quantization step U_Q is calculated:

$$U_Q = \frac{U_{ADCMax} - U_{ADCMin}}{2^n} = \frac{U_{ADCMax} - U_{ADCMin}}{B} \tag{5.4}$$

For a single-ended ADC measuring in between U_0 and GND, this reduces to

$$U_Q = \frac{U_0}{B}.$$

As U_Q is the amplified bridge voltage, the corresponding INA input voltage is

$$U_{QIn} = \frac{U_0}{Bg} = \frac{U_Q}{g}, \tag{5.5}$$

which is simultaneously the smallest variation in bridge voltage that is distinguishable by the ADC. Using Equation 2.22, the corresponding strain value, i. e. the strain quantization step ϵ_Q, is calculated:

$$\epsilon_Q = \frac{2}{k(1+\nu_{xy})}\frac{U_{QIn}}{U_0}. \tag{5.6}$$

To determine the theoretical range for strain measurement $\Delta\epsilon_{max}$, ϵ_Q is multiplied by the number of possible combinations:

$$\Delta\epsilon_{max} = \epsilon_Q \cdot 2^n = \epsilon_Q \cdot B \tag{5.7}$$

Plugging in ϵ_Q from Equation 5.6, we get

$$\Delta\epsilon_{max} = \frac{2}{k(1+\nu_{xy})}\frac{U_{QIn}}{U_0} \cdot B,$$

which, using Equation 5.5, reduces to

$$\Delta\epsilon_{max} = \frac{2}{gk(1+\nu_{xy})}. \tag{5.8}$$

For a single-ended configuration, minimum and maximum measurable strains consequently calculate to

$$\epsilon_{max/min} = \pm\epsilon_Q \frac{B}{2}. \tag{5.9}$$

5.1.5 Temperature Measurement

For measurement of matrix temperature, a digital, low power temperature sensor[6] is utilized, which is connected to the micro controller via Inter-Integrated Circuit (I²C) Bus. Maximum sensor error is guaranteed to be ±0.2 °C for −40 °C to 100 °C and ±0.3 °C for −55 °C to 150 °C. It was chosen for its small footprint and high accuracy, as it was designed to replace standard Pt-100 thermistors. Also, it is factory calibrated, ensuring accurate temperature readings over its full operating range (−55 to 150 °C, [115]).

5.1.6 Sensor Fabrication

After sensor conceptualization and initial circuit tests on a breadboard, the sensor substrate, i. e. FPCB is designed, manufactured and assembled with all necessary components.

Sensor tag circuitry is placed in the center of the tag, so that the antenna encircles the electronics (see also Figure 5.6). To optimize resin flow through and around the sensor, holes were designed in the sensor substrate, especially in between the antenna and the electronics. This allows the resin to flow through during infusion, thereby creating resin bridges in the cured structure, increasing stability and possibly reducing potential of delamination around the sensor.

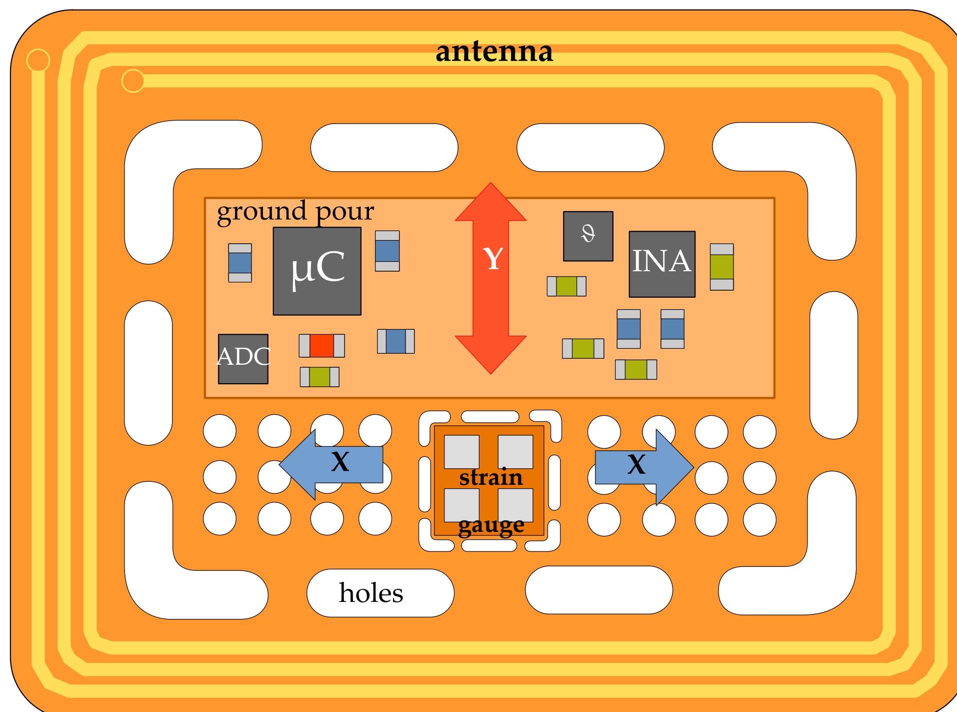

Figure 5.6: Conceptual drawing of piezoresistive sensor tag

[6] TMP117 by Texas Instruments [115]

To minimize the wound effect created by the tag, small package sizes were chosen for the electrical components (e. g. 0402 for passive components). Package size was limited though by the necessity of manual soldering and assembly. For future versions, further size reduction is possible by decreasing the sizes of the electronic components. Full tag PCB layout is additionally given in Figure A.11.

5.1.6.1 Sensor Substrate

For the sensor tag substrate, polyimide is chosen, as it is currently one of the industry standard materials for production of FPCBs, allowing for easy and cost-effective fabrication of the sensor system. The FPCB was fabricated by a commercial PCB-manufacturer in a common production process, resulting in a 180 µm, double layer copper-polyimide board (see Fig. 5.7). Figure 5.6 schematically displays tag concept and approximate layout. Following the sensor tag approach (3), sensor substrate is designed to be rectangular, with a 4:3 aspect ratio. This is to ensure a sticker-like behavior and applicability to common sticker placement techniques. It also allows for easy distinguishability of sensor orientation, which is relevant as it corresponds to the intended strain measurement direction.

To reduce mechanical tension around the substrate edges, its corners were designed to be rounded off, according to the findings in [63]. As also shown in [63], the mechanical wound effect, i. e. negative effect of a material-integrated inlay on the surrounding component's structural integrity, is minimized when Young's Modulus of the inlay is smaller or equal to that of the surrounding material. As polyimide has a Young's modulus of around 3.1 GPa [64] and Young's Modulus of cured matrix materials (e.g. epoxy resin) is usually higher (e.g. 5.3 GPa for *Hexion RIMR135/RIMH137*, [68]) this design condition is satisfied for the material chosen.

5.1.6.2 Assembly

For assembling the sensor, the electronic components and ICs were soldered to the PCB with manually dispensed soldering paste. The PCB was then briefly heated on a hotplate to reflow the solder and make the electrical connections. A fully assembled tag is displayed in Figure 5.7. At its thickest point, which is where the micro controller is mounted, it has a maximum total thickness of 1.2 mm, while the tag itself has a thickness of ca. 195 µm for both copper layers present.

The strain gauge was mounted to the tag surface with dedicated, epoxy-based strain gauge glue supplied by the strain gauge manufacturer, to ensure best mechanical coupling and minimal adhesion degradation over time. To connect the strain gauge to the electronics, the connection pads of the gauge and the PCB, which are directly adjacent, were bridged with conductive glue. This is to allow for some connection flexibility, to not influence strain measurement, and to achieve mechanical insensitivity and low profile (e. g. as compared to protruding wire bonds that would possibly break during tag handling). A close-up of the glued

connection is shown in Figure 5.5b. The strain gauge is symmetrically positioned on the Y-axis of the PCB, with maximum distance to the antenna or other components, to minimize mechanical influence on the gauge itself by adjacent structures. Also, to that end, no components placed on the PCB along the measurement axes and holes were placed directly around the gauge to improve mechanical coupling to the surrounding matrix material.

Apart from the original sensor tag prototype, a smaller version comprising a miniaturzied antenna was built, to see if reduction of overall footprint is possible, which is displayed in Figure 5.8b. The miniature version did function as expected but reading range reduced to about 21 mm.

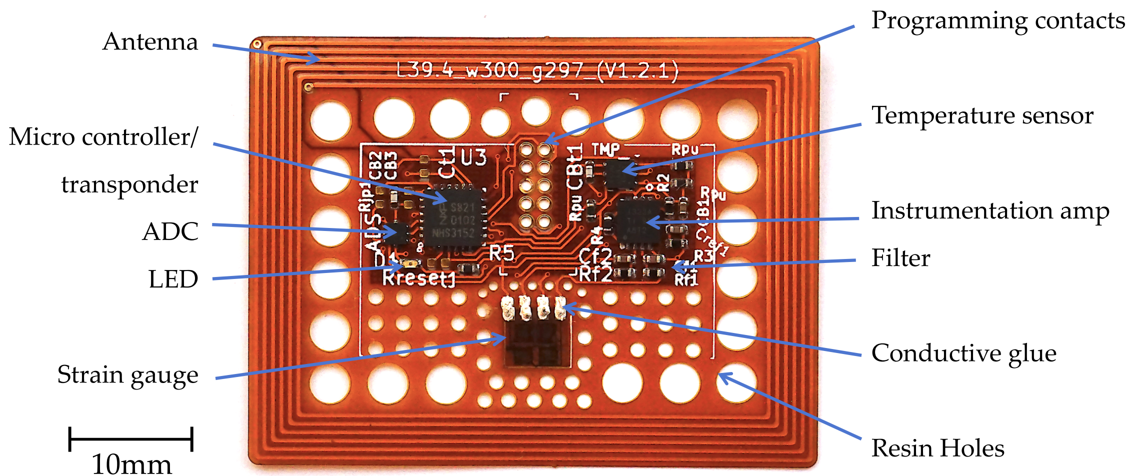

Figure 5.7: Fully assembled sensor tag with component descriptions.

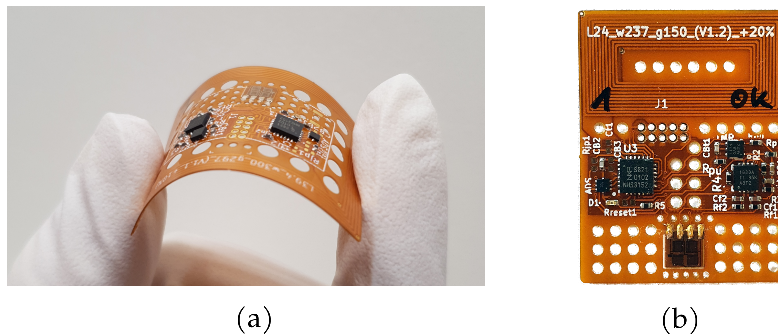

(a) (b)

Figure 5.8: a) Fully fabricated, flexible sensor tag. b) Smaller version prototype of sensor tag (not to scale with left image).

5.1.6.3 Software

All measurement acquisition on the tag is handled by the integrated micro controller. It is controlled by a custom-built firmware, that was designed to minimize sensor power consumption, while keeping time needed for wireless sensor readout

as short as possible. This is to ensure broad compatibility with different readers that differ in duration of the time the reader field is activated during readout. The software also handles power supply of the sensor electronics and controls the configurable LED for user feedback. For measurement, the micro controller reads the digitized values from both the ADC and the temperature sensor and averages strain measurements by a user definable number to increase accuracy. Temperature averaging is handled by the temperature sensor itself to reduce noise. After collecting measurement data, the micro controller writes the data to the memory of the RFID transponder, where they can be read by the reader. Additionally, the micro controller reads a specific transponder register that can in turn be written to by the reader. This allows for configuration of several sensor parameters even after integration (e. g. number of measurements for strain averaging, measurement offset, usage of the LED, etc.). Also, it can be used to configure 4 bytes of user-definable memory in the micro controller EEPROM, e. g. to allow for easy part identification during handling or maintenance, offering potential for usage in context of a 'smart' component or structure, that could be expanded for future usage in different applications. The textual interface, i. e. communication protocol, and a list of all commands implemented and corresponding functions for wireless tag control are given in Section A.1. To read data from the transponder, basically every RFID reader implementing the ISO 14443 standard can be used, as long as the electromagnetic field is strong enough and stays on for a sufficiently long time to power the tag circuitry for thee duration of a measurement cycle. As a proof of concept, the tags were also tested with some off the shelf smartphones, which worked without a problem. For the experiments conducted in this work, a *MicroSensys M30 RFID head* [116] was used for reading the tags, which allows for custom programming of the read out routine. This enables e. g. configuration of the field on-time and if anti-collision algorithms are to be used. As the latter result in short field pauses, this needs to be kept in mind to ensure sufficient field on time. Depending on the routine used for readout, different minimum cycle times could be achieved. If the reader is programmed to keep the field on continuously, sensor readout times as low as 50 ms could be achieved, equaling a readout frequency of approximately 20 Hz. For "normal" RFID operation, i. e. the field is switched off directly after data read out, minimum cycle times increase to approximately 296 ms, as the components (especially the ICs) need more time for initialization after supply voltage is switched on.

5.2 Characterization and Results

This section reports in detail the experiments conducted with the piezoresistive sensor tag. First, experiments regarding fabrication monitoring are described, and it is shown how the sensor can be used to monitor resin flow front and curing temperatures. Subsequently, mechanical tests for characterization of the strain sensor and influence of tag presence on FRP strength are presented. In the last section of this chapter, system limitations are examined, giving insights into maximum operation temperature and maximum reading range.

5.2.1 Fabrication Monitoring Experiments

In order to investigate sensor functionality for FRP fabrication monitoring, sensor tag integration was tested in two experiments, that have been published in [6]. These were conducted to ascertain correct sensor function and communication, despite the conditions present inside the laminate during infusion and curing. Two separate FRP boards were fabricated during the experiments, using a VARI process. The experiments give an insight in the possibilities to track resin flow front and monitor resin cure via the sensor tags presented. Also, significance of material-integrated temperature measurement in relation to surface-based measurements was investigated by comparison with a temperature sensor on top of the lay-up for reference.

5.2.1.1 Setup

The experiment setup and sensor position inside the laminate is schematically displayed in Figure 5.10. For each experiment, three sensors tags each were placed inside the eight-layer glass fiber lay-up. Reference temperature sensors were placed for comparison, one in the resin reservoir and one in the center of the top vacuum foil (see Figure 5.11). The sensor tags were positioned beneath the second layer from the top, with specific spacing relative to each other and the textile edges.[7] Figure 5.9 illustrates fiber orientations in the layup used in this experiment.

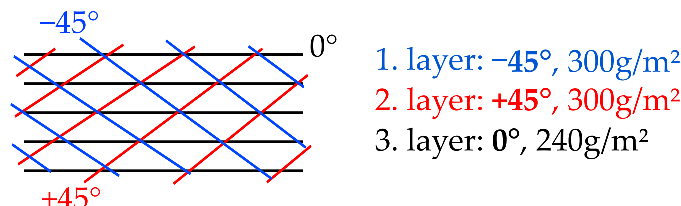

Figure 5.9: Fiber orientations used for fabrication monitoring experiments.

[7] Materials used: Triaxial glass fiber textile (0, ± 45°, 854 g/m^2) , *EPIKOTE RIMR 135* (resin) + *RIMH137* (curing agent).

Prior to the experiments, the resin and curing agent were thoroughly mixed and degassed in a vacuum chamber, to prevent formation of bubbles which would create voids in the resulting composite. To ensure no degradation of adhesion, sensor tag surfaces were cleaned and degreased with isopropanol. To fix the sensor tags in position on the textile, they were attached with an epoxy resin based glue [117], that is specifically designed for usage in FRP laminate, as it dissolves in the matrix material during infusion and curing.

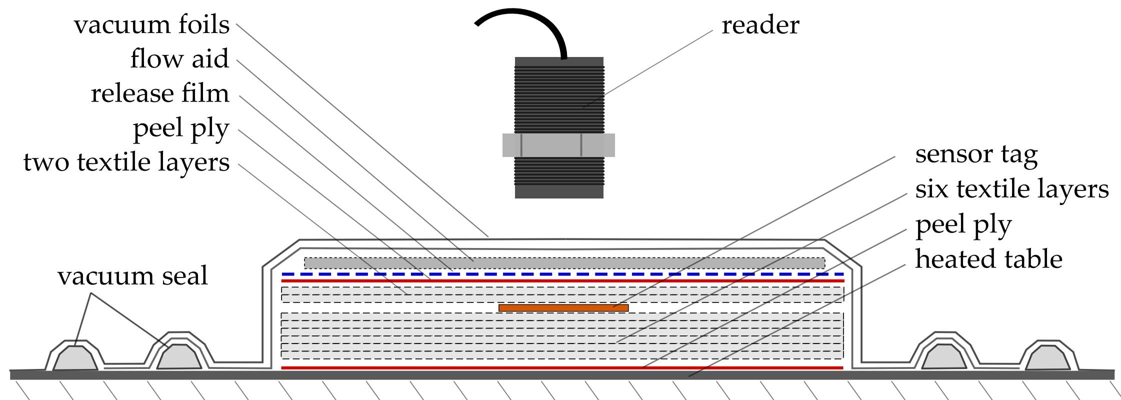

Figure 5.10: Laminate layup and experiment concept in fabrication monitoring experiment.

Before infusion start, table temperature T_R was set to 40 °C while the resin was heated to ca. 30 °C in a water bath. Opening of the infusion valves marks the start of the experiments (i. e. t=0 s). Relevant events during infusion could visually be recorded for later correlation to measurement data, as all materials used were transparent. Respective events are indicated in the temperature graphs (see Figure 5.12). The fluid resin reached the distributing omega profile after 1:05 min, marking the actual start of infusion. Visual arrival times of the flow front were recorded for each sensor tag, they are presented in the following section. After approximately 17:00 min, the whole mold was visibly filled. To ensure complete fill-up of the mold, the resin inlet valve was closed three minutes later. At 22:00 min, the whole setup was covered with an insulating fleece. This was done to reduce heat dissipation via the surface to create a more homogeneous distribution of temperature throughout the setup and thereby accomplish consistent cure over time.

For curing, table temperature T_R was subsequently increased. First, to initiate the curing reaction, T_R was set to 55 °C. After 2:12 h, T_R was increased to 65 °C to speed up reaction of the remaining components. After another half hour, at 2:32 h, T_R was again increased to 75 °C in order to ensure full and consistent cure throughout the specimen. During the whole production process, all sensors were wirelessly read out via an RFID reader [116] each, which were mounted above the

tags (see Figure 5.11). Reader-tag distance was 2 cm, while spacing between the tags was 10 cm.

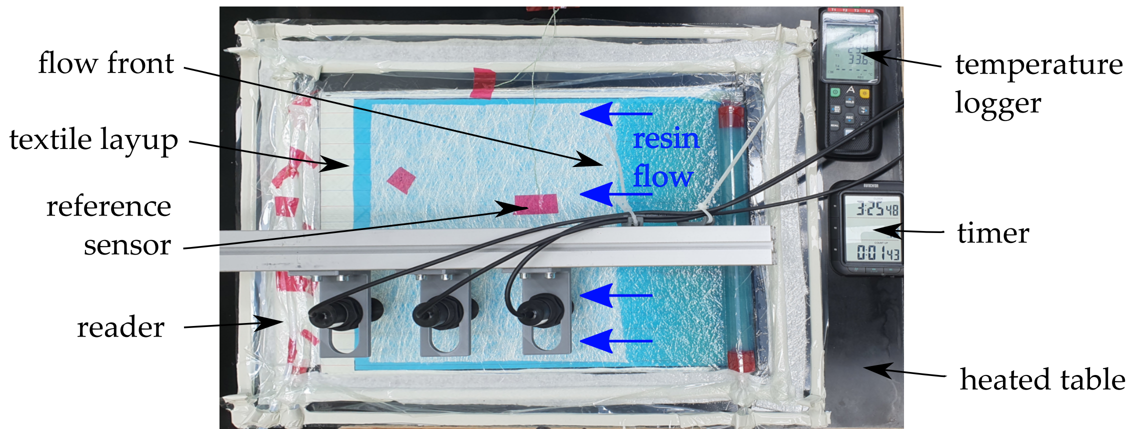

Figure 5.11: FRP fabrication setup for sensor tag integration.

5.2.1.2 Results

For both experiments, all sensor tags remained functional and were communicating measurement data throughout the whole process and after. Temperature measurements are illustrated below. Figure 5.12 shows a detailed overview of the temperatures recorded during infusion, while Figure 5.13 displays the entire process until cool down. Apart from some few random reading errors for tags two and three that could be observed from 2:12 h to 4:02 h, all communication worked as expected. These reading errors could not be reproduced later on at similar and higher temperatures, which leads to the conclusion that the errors were not due to the elevated curing temperatures.

Regarding measurement differences in between tag values, a maximum deviation of approximately 1.9 °C for board one and 2.1 °C for board two could be read, respectively. This deviation was in both cases calculated for the two tags positioned at the greatest relative distance, e. g. the first and the last. Consequently, it is assumed that the deviations were mostly caused by inhomogenous heat distribution over the heated table surface. This conclusion could later be validated by thermal imaging. To remove outliers due to reading errors mentioned above, all data was Hampel-filtered with a window size of 5.

Advancement of the flow front through the setup was both visible from the outside and apparent in the measured data. As illustrated in Figure 5.12, a close correlation of sensor data and visually recorded resin arrival times is observable. When the resin reaches the sensors, measured temperature drops distinctly, as resin temperature is lower than that of the dry, heated textile. This drop is followed by a distinct temperature increase shortly after resin arrival, which can be attributed to an increase in transported heat energy from the heated table surface to the sensors, due to higher thermal conductivity of the resin as compared to the dry textile.

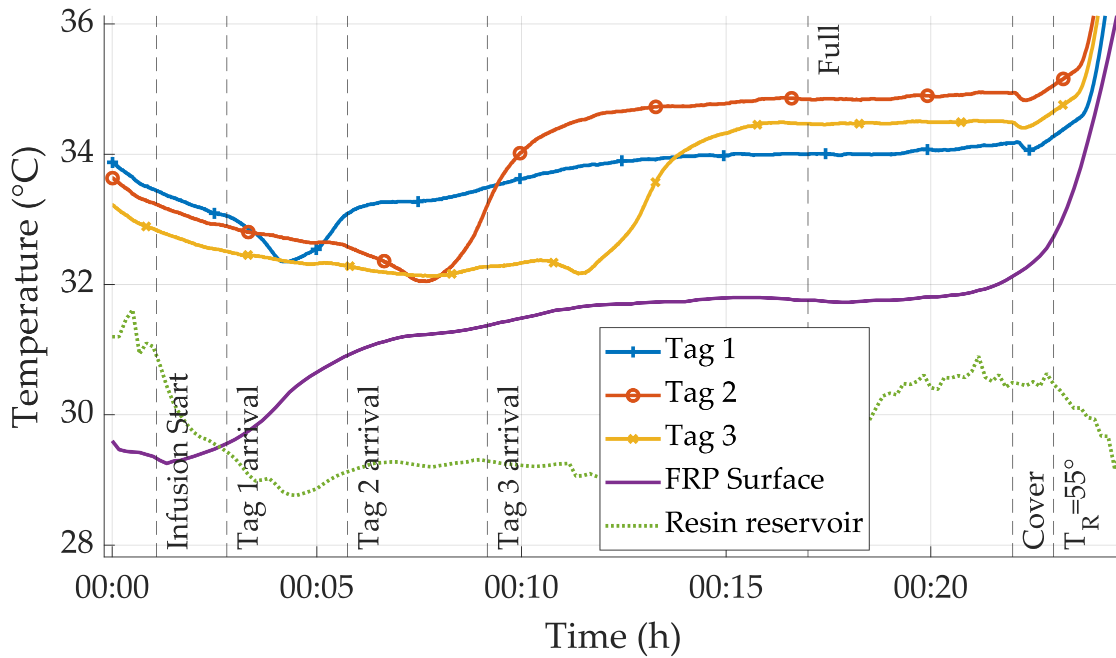

Figure 5.12: Sensor tag and reference temperature measurements during infusion. Visible arrival times of resin flow front marked by dashed lines.

Resin cure is then initiated in the first heating phase. Measurement values clearly reflect the exothermic nature of the curing reaction. Temperature measurements inside the laminate show a distinct local maximum around 1:10 h that can be attributed to the heat generated by the reaction. Despite the cover fleece, this remarkable feature is not reflected in the surface-based measurements – surface temperature stays nearly constant, showing a maximum drift of ca. 2 °C throughout the first phase of heating. Overall, surface temperature data follows sensor tag data, though the values of the reference sensor are generally smaller, i. e. temperature inside the laminate being several degrees higher. This is to be expected, as heat is dissipated into the surrounding air, despite of the insulation fleece. This difference reduces during the two subsequent heating phases, indicating a lesser amount of heat being created inside. This could be attributed to reduced activity of the curing reaction and therefore further progression of cure.

5.2.2 Strain sensor characterization

To examine correct function and accuracy of the strain sensor, bending tests were conducted with sensor-integrated FRP samples. The specimens were cut from the FRP boards made in the prior fabrication monitoring experiment (see Section 5.2.1). One of the FRP specimens used is shown in Figure 5.14b. Specimen geometry was chosen so that symmetrical loading in both X (longitudinal) and Y (transversal) direction could be achieved (see Figure 5.14b for coordinate system definition). For that reason, the strain gauge was positioned in the very center of the quadratic

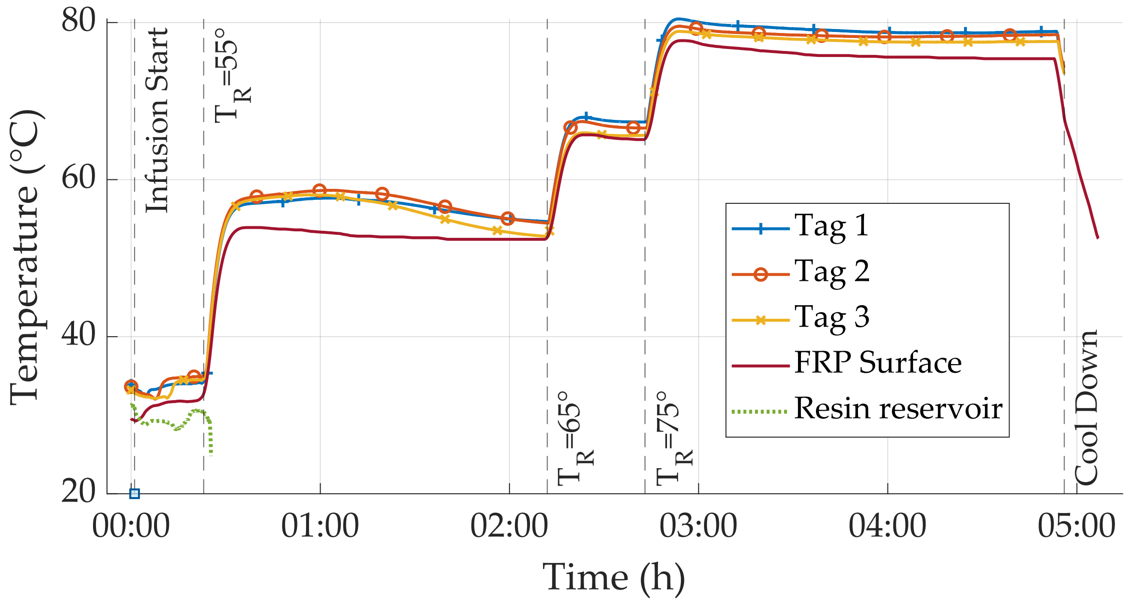

Figure 5.13: Sensor tag and reference temperature measurements for the whole production process. Changes in heating set points indicated by dashed lines.

specimen. Additionally, bending is maximized at the position of the strain gauge, and strain calculation is simplified. Calculation of the strain results was conducted according to the equations given in Section 2.3, assuming an average Poisson's ratios of $\nu_{xy} = 0.05$, $\nu_{yx} = 0.65$ for all samples. For later application with different materials, these values will need to be adjusted depending on properties of the material used.

5.2.2.1 Setup

Strain sensor characterization was conducted via a testing machine, using a three-point-bending test configuration. Measurement data for both sensor tag and reference measurement was recorded via a PLC, that was connected both to the testing machine and the RFID reader. This way, time synchronized recording is possible for both actual (i. e. reference strain) measured by the testing machine, and sensor data wirelessly read by the RFID reader, eliminating the need for later data correlation. Six sensor-integrated specimens were examined in this experiment. For bending, they were positioned so that the bending axis was parallel to the measurement direction to be examined, with the force being directly applied in the center of the tag. To achieve strain at the layer of tag and to not negatively influence the electronics, the specimens were placed with the tag facing down, i. e. away from the cylinder applying the force, and towards the reader (see Figure 5.14a). They were deflected with a constant speed of 0.01 mm/min, until a maximum force of 1 kN was measured by the testing machine. At this position, the machine stopped further movement and held the position for 5 s, after which deflection was reversed

with the same constant retraction speed. This procedure was repeated six times for each specimen and for both X and Y direction.

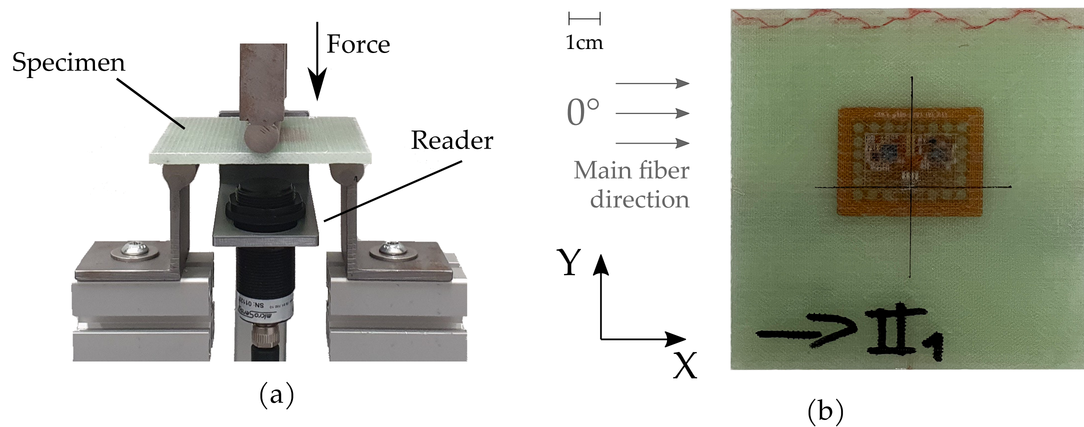

Figure 5.14: a) 3-Point-bending test setup for mechanical experiments. b) Sensor-integrated FRP specimen for bending tests, 0 ° fiber direction indicated by arrows.

5.2.2.2 Results

This section summarizes results of the bending tests conducted, after briefly mentioning some general findings. In idle state, strain readings of the integrated tags differed even before the first loading. This is probably caused by strain gauge deflection due to integration, e. g. bending of the gauges due to compression between the fibers of the textile. Also, even though low tolerance resistors were used for INA reference voltage, variations can possibly occur between tags due to resistor tolerance, influencing zero strain voltage. For an actual application, this influence could be reduced by in-place calibration after integration.

For all specimens, first loading resulted in a different force and strain response compared to subsequent loadings. Force values increased slower during bending, i. e. at larger deflection values. In other words, the specimens were deflected further before reaching the force set point of 1 kN, as displayed in Figures 5.15a and 5.15b. After this initial 'setting' of the material, force and deflection responses were repeatable and showed no signs of fatigue behavior. For this reason, all characterization measurements are based on loading iterations 2 to 6. This effect is observable for specimens both with and without sensor tag, as could be confirmed by later comparison, indicating a material-related effect (see also Section 5.2.3). As deflection was always measured from the point where the testing machine measured a force of more than 0.1 N, the deflection measurement for the first loading could have been influenced by minor deformations of specimen surface, which did not occur for later measurements.

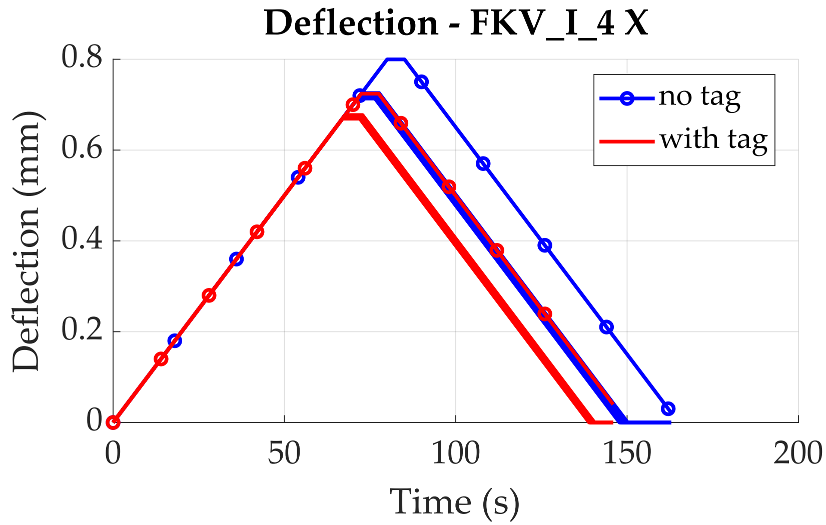

(a)

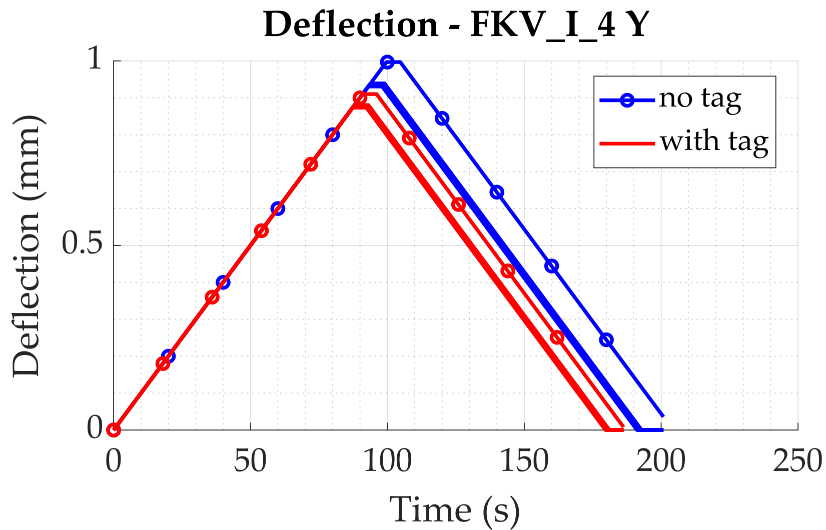

(b)

Figure 5.15: Deflection graphs for FRP specimen I_4 as measured by testing machine, comparing deflections with and without tag. First deflection yields different behavior for each direction (circle markers). a) Deflections for bending *perpendicular* to main fiber direction. b) Deflections for bending *parallel* to main fiber direction.

Deflection and Strain Measurements As shown in Figures 5.16a and 5.16b, all FRP specimens showed generally similar behavior when loaded. Mean deflections differ for bending in transversal and longitudinal direction, which is to be expected due to anisotropic material properties. Specimens are stiffer for bending in X, i. e. perpendicular to main fiber direction (see Figure 5.14b), resulting in approximately 0.2 mm/mm less deflection compared to bending parallel to main fiber direction. No significant differences are found when comparing deflections of the two different FRP boards (e. g. board I and board II), though mean deflections differ between specimens overall. Maximum deflection difference was found to be ca. 0.1 mm/m for both directions.

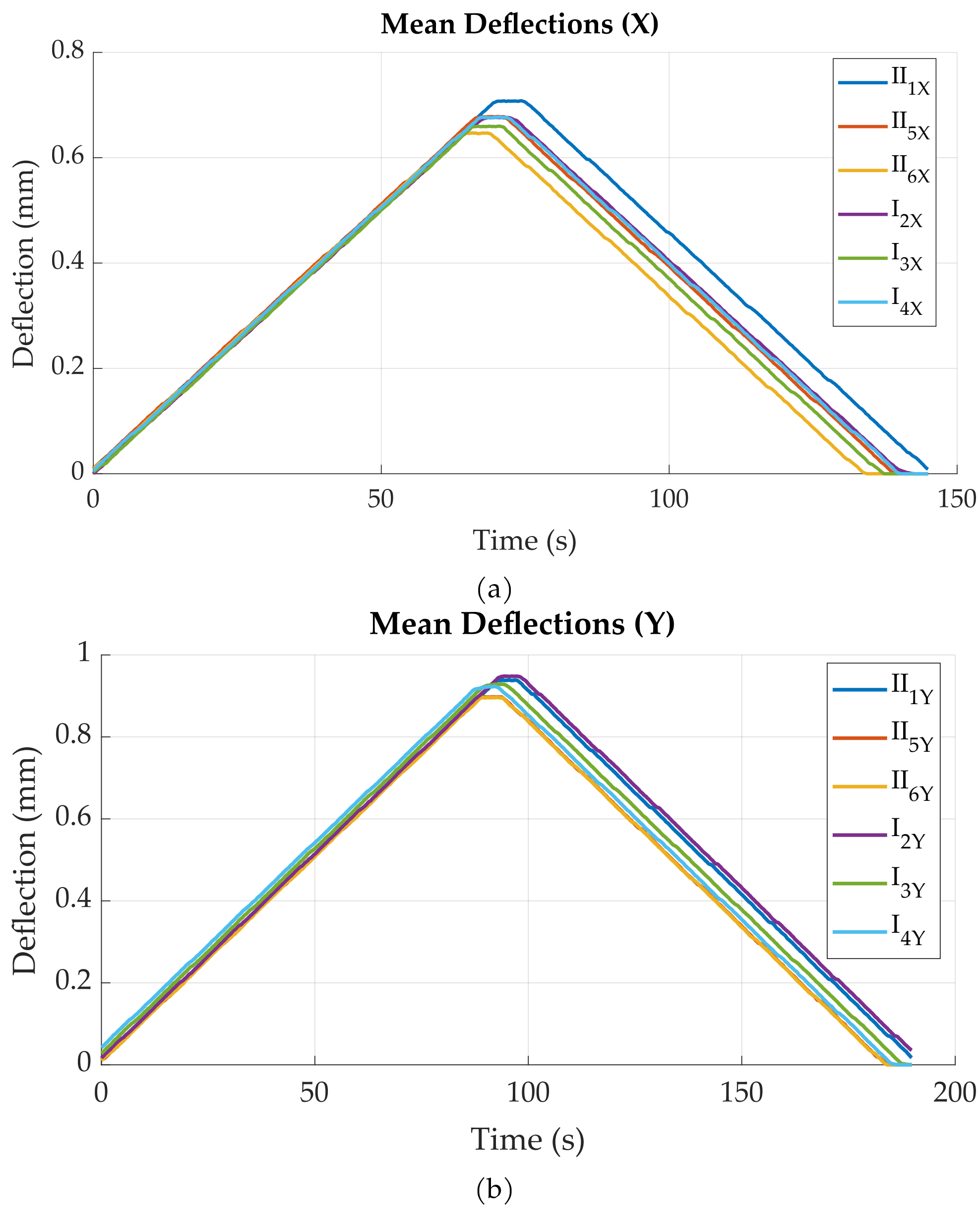

Figure 5.16: Averaged deflections (n=5) for bending a) perpendicular to main fiber direction. b) parallel to main fiber direction.

Figures 5.17 and 5.18 exemplary show bending measurement data for a single specimen, for both parallel and perpendicular bending. The dark lines show the mean value, while the lighter, shaded areas illustrate the standard deviation for both curves (standard deviation is very small for reference data). It can be found that tag measurements closely follow reference data, though with higher noise and higher standard deviation. Measurements for bending parallel to main fiber direction (Figure 5.18) result in a longer duration, as the material is less stiff and can therefore be deflected further before reaching the force set point of 1 kN. This is also cause for bending parallel to main fiber direction resulting in larger strain values for the same force. While maximum strain in X (perpendicular to main fiber direction) is ca. 1.7 mm/m, bending in Y (parallel to main fiber direction) results in approximately 2.3 mm/m for the same force.

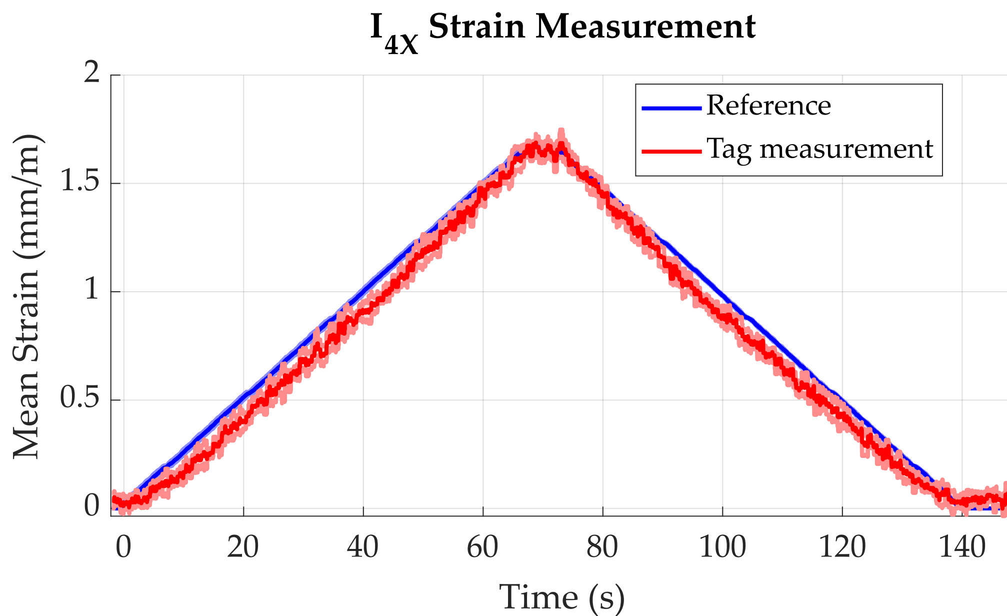

Figure 5.17: Mean strain data for FRP specimen I_4 compared to reference, n=5. Standard deviations indicated by shaded areas. Deflections for bending *perpendicular* to main fiber direction.

In general, for both loading directions, a slightly curved, i. e. non-linear behavior in sensor strain data can be observed for both increasing and decreasing deflection (see Figures 5.19a and 5.20a). This is reflected to some degree in the sensor error, i. e. difference to reference, as displayed in Figures 5.19b and 5.20b, which show local maxima during loading and unloading processes. After full unloading of the specimen, sensor tag strain values show a slight residual offset (see Figure (5.18)). This is likely caused by temporary plastic deformation of the specimen due to prior bending. For the other bending direction, this effect is probably opposed by fiber presence.

For loading perpendicular to main fiber direction (Figure 5.19a), a maximum strain of 2.0 mm/m could be measured for a force of 1 kN, for specimen II_1.

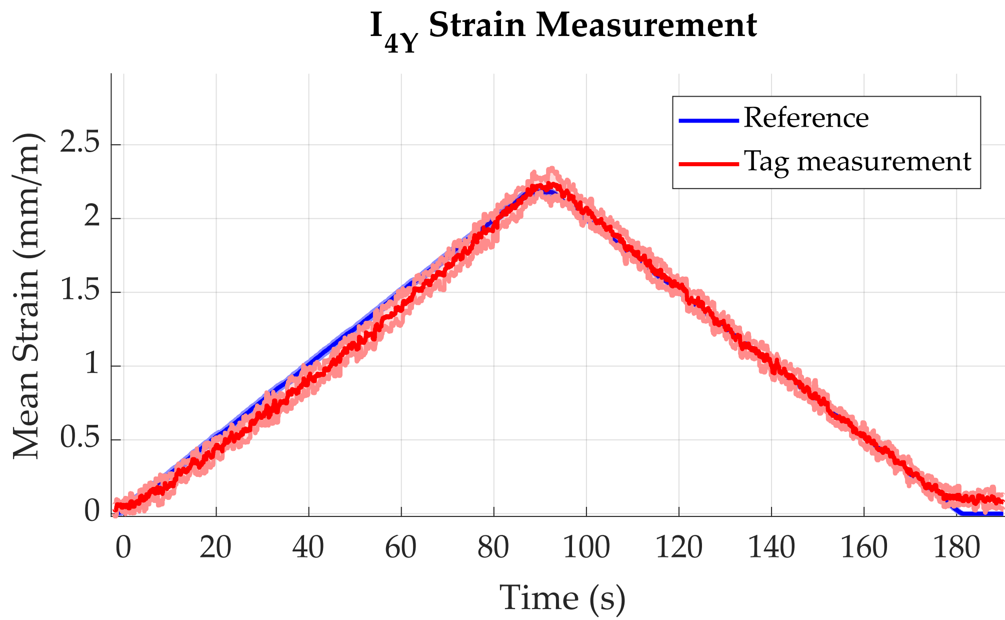

Figure 5.18: Mean strain data for FRP specimen I_4 compared to reference, n=5. Standard deviations indicated by shaded areas. Deflections for bending *parallel* to main fiber direction.

Loading parallel to main fiber direction (Figure 5.20a) causes a corresponding maximum strain of 2.6 mm/m, this time for specimen I_2. Comparing different specimens, mean strain values measured by the sensor tags differ up to approximately 0.6 mm/m for both directions.

Sensor Error As already mentioned in the previous paragraph, it could be found that sensor error, i. e. difference between actual strain (reference), as measured by the testing machine, showed variance between specimens and also between different loading states. Sensor errors for all experiments are given in Figures 5.19b and 5.20b, while mean and maximum sensor errors are given in Figure 5.2. In general, variation in sensor error is highest for maximum loading, while it is lowest for the unloaded states.

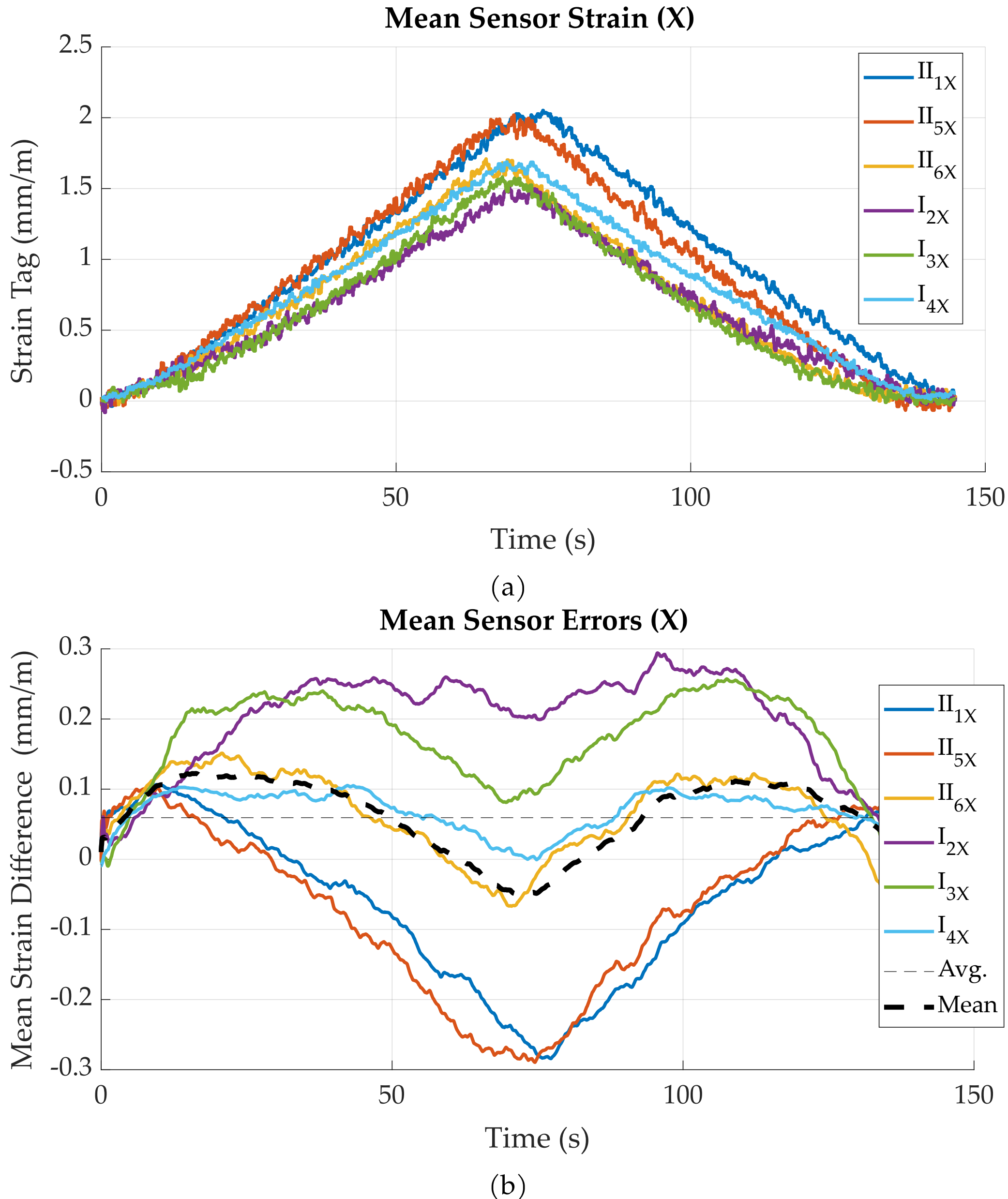

Figure 5.19: Bending perpendicular to main fiber direction: a) Averaged strain sensor readings, n=5. b) Averaged sensor errors (difference to reference), n=5.

Averaging all values for sensor error of bending perpendicular to main fiber direction, it can be found that during loading and unloading phases, the sensor tags generally measured about 0.1 mm/m more strain than given by the reference. During the holding phase, mean sensor error decreases. These effects are depicted by the black, dashed curve in Figures 5.19b and 5.20b.

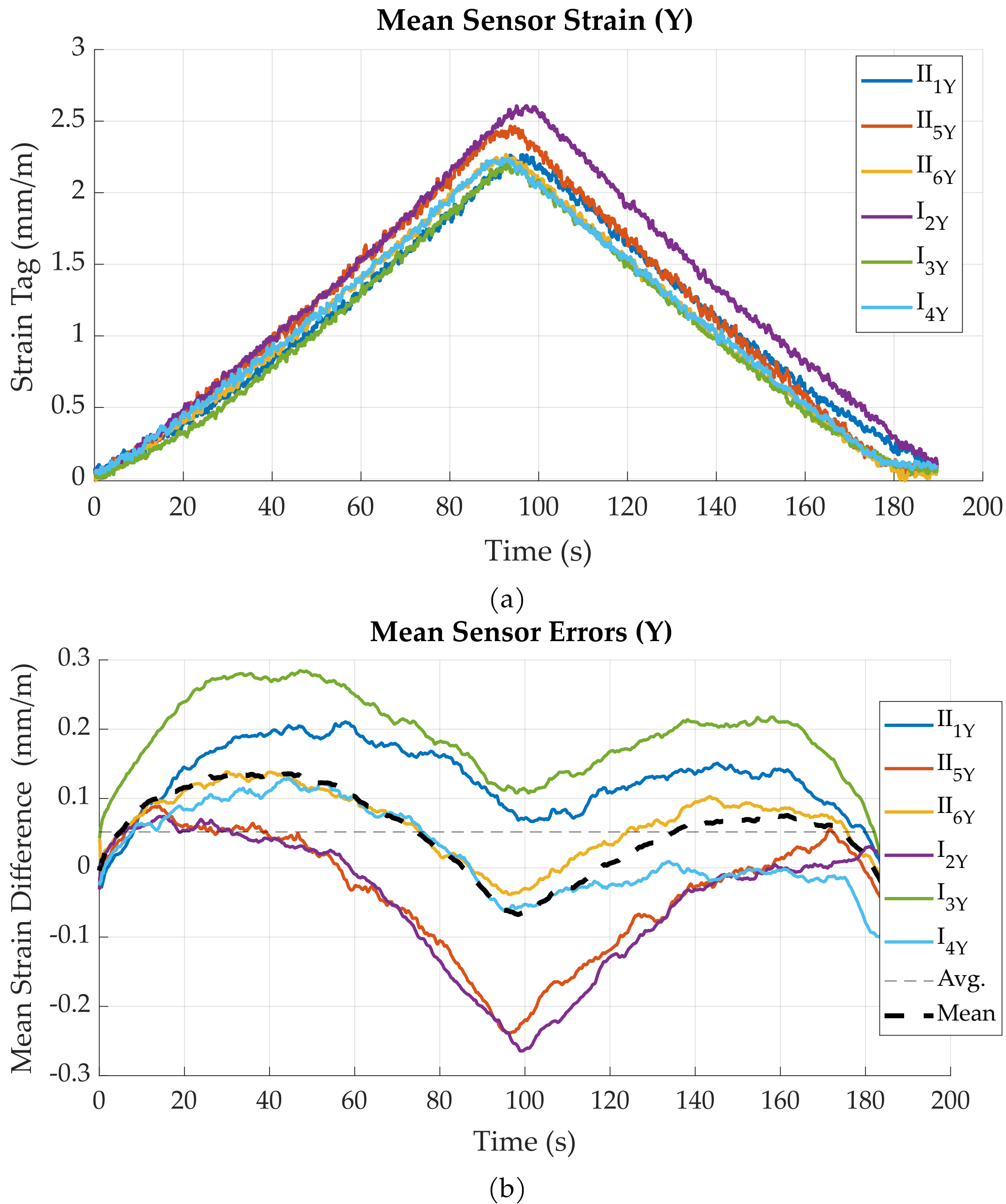

Figure 5.20: Bending perpendicular to main fiber direction: a) Averaged strain sensor readings, n=5. b) Averaged sensor errors (difference to reference), n=5.

Averaging sensor error of all specimens over time, it can be found that for bending perpendicular to main fiber direction, sensor tags measured about 0.09 mm/m less strain than actually occurred. In other words, mean strain difference of reference and sensor tag strain is about 0.09 mm (see Table 5.2). For bending parallel to main fiber direction, a mean sensor error of approximately 0.05 mm/m is found. As sensor error varies with loading, these values have only a limited significance.

Table 5.2: Maximum sensor errors for bending tests, as compared to reference. [8]

Error	X (mm/m)	Y (mm/m)
Average error (overall)	+0.059	+0.049
Max. positive	+0.290	+0.284
Max. negative	−0.290	−0.264

Overall difference in measured strain seems to at least partly depend on the individual tag or specimen, e. g. is caused by differences in coupling strength of matrix and strain gauge, as sensor error is highest for the sensor tag measuring the overall smallest strain (I_2) in X and largest strain in Y. Possible reasons also include tolerances of the electronic components, resulting in differing amplification of the bridge signal. This correlation can, to some degree, be inversely observed for the tags measuring the overall largest strain in X and smallest strain in Y (II_2 and I_3). Comparing actual deflections of the specimens, as measured by the testing machine, it can be found that not all specimens experienced the same deflection for the same amount of applied force, which contrarily indicates differences in specimen stiffness, consequently resulting in differences of occuring and measured strain.

Concerning the two boards fabricated, it can be found that for bending perpendicular to main fiber direction, board I generally showed errors higher than average, while board II showed errors lower than mean (see Figure 5.19b). A possible explanation for this is occurrence of different material behavior with regard to lateral contraction: Bending perpendicular to main fiber direction implies that no fibers are laterally stiffening the material, as a fiber layup of 0 / + 45 / −45 ° was used. Material stiffness in lateral direction is therefore mainly influenced by the matrix, which is proportionally much less stiff, possibly resulting in higher variation and therefore more influence on the lateral contraction, which is superimposed on strain sensor signal due to bridge layout (see Section 5.1.1 for details). For bending parallel to main fiber direction (Figure 5.20b), this effect cannot be observed, as main fiber directions largely prevent lateral contraction in this direction.

Regarding strain sensor accuracy, mean standard deviations for all six specimens are given in Figures 5.21a and 5.21b. For bending perpendicular to main fiber direction, standard deviation is generally below 0.1 mm/m, with specimen I_2 showing a maximum standard deviation of 0.16 mm/m. Bending parallel to

fiber direction yielded similar results (see Figure 5.21b), though a slight increase in standard deviation is observable for all specimens during maximum loading (around t= 90 s).

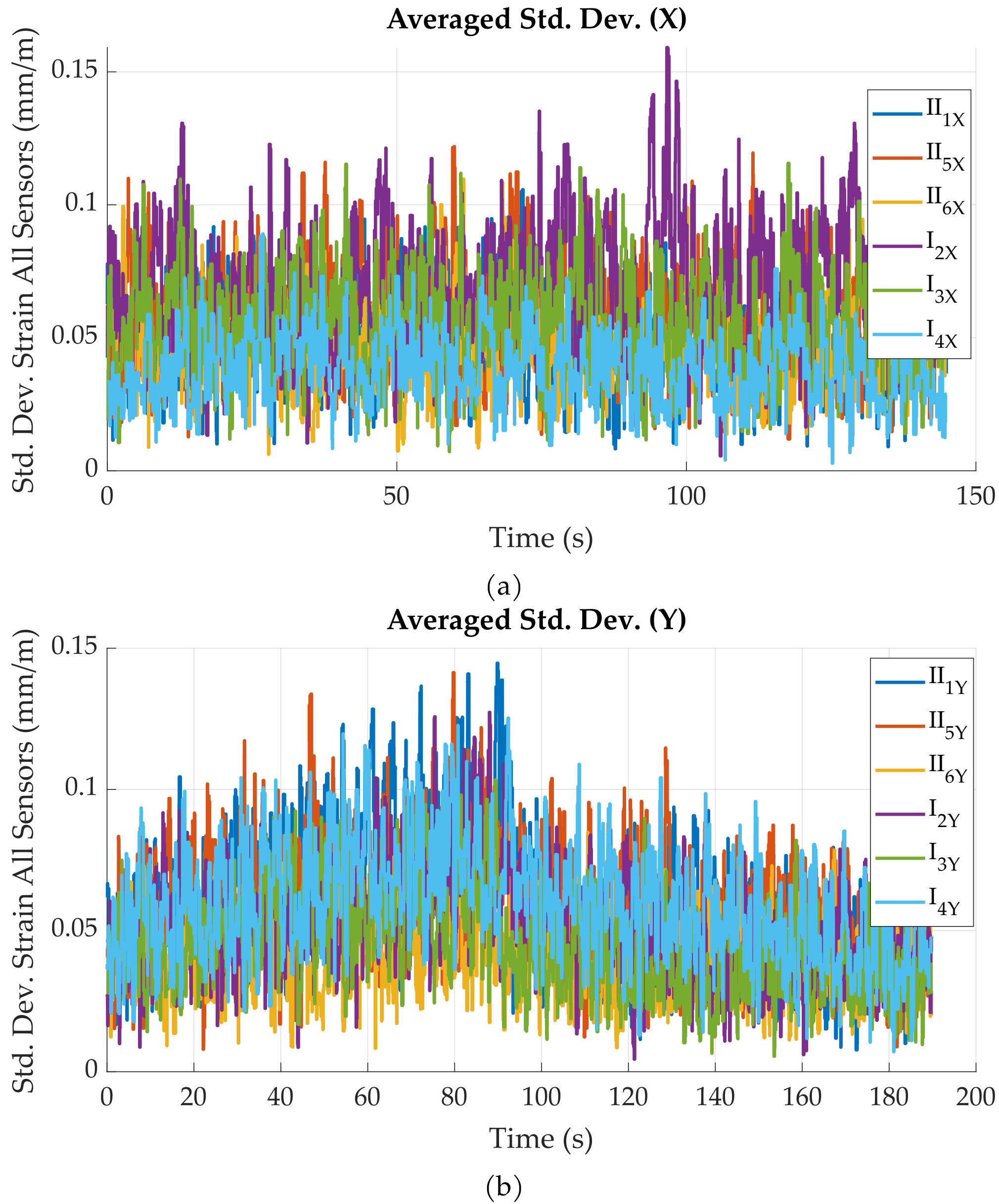

Figure 5.21: a) Mean standard deviations for bending *perpendicular* to main fiber direction, n=5. b) Mean standard deviations for bending *parallel* to main fiber direction, n=5.

5.2.3 Tag Influence on FRP Strength

To investigate the effect of tag presence on FRP strength, comparative tests were conducted with FRP samples with and without sensor tag. To ensure comparability, only specimens from the same fabrication run, i. e. FRP board were compared.

5.2.3.1 Setup

The same basic setup was used as for prior bending tests, initially comparing specimen behavior for a force of 1 kN, so as to not damage the specimens. These measurements were done for bending in both directions (X and Y). Afterwards, bending force was increased for destructive testing, to see if tag presence influenced failure behavior. For this, instead of a force value, a target deflection was used as set point, resulting in destruction of the specimens. Due to the destructive nature of the experiment, bending was done only perpendicular to main fiber direction. These experiments were done with three samples each, with and without sensor tag for comparison.

5.2.3.2 Results

Prior to destructive testing, non-destructive bending tests were conducted to quantify the impact of tag integration on material stiffness. Figures 5.22a and 5.22b illustrate mean deflection values obtained via the testing machine, i. e. the reference measurement equipment, for all specimens, in both bending directions. Each curve represents the average deflection values of bending iterations 2 to 5, as also used in Section 5.2.2.

As already observed during strain sensor characterization, deflection magnitude for the same force of 1 kN differs between specimens, both for specimens with and without tag. Nonetheless, a clear trend is observable when comparing deflection values for specimens with and without tag. All specimens with integrated sensor tag show less deflection compared to the corresponding specimens without tag, in both specmien orientations. This shows that tag integration actually seems to strengthen the material locally, i. e. stiffening the laminate. This might be explained by the sensor tag acting as an additional layer in the material, instead of actually disturbing the laminate. Still, significance of this finding is limited, as experiments do not account for other influences like fatigue that would come into play for cyclic loading during application.

Comparing deflection of different specimen orientation, results confirm findings of the experiments conducted for strain sensor characterization. Bending perpendicular to main fiber direction generally leads to less deflection as compared to bending parallel to main fiber direction. This can once again be explained by the anisotropic material properties caused by the orientations of the textile layers (0 °, ± 45 °), as fibers strengthen the material mainly in X direction (see Figure 5.14b).

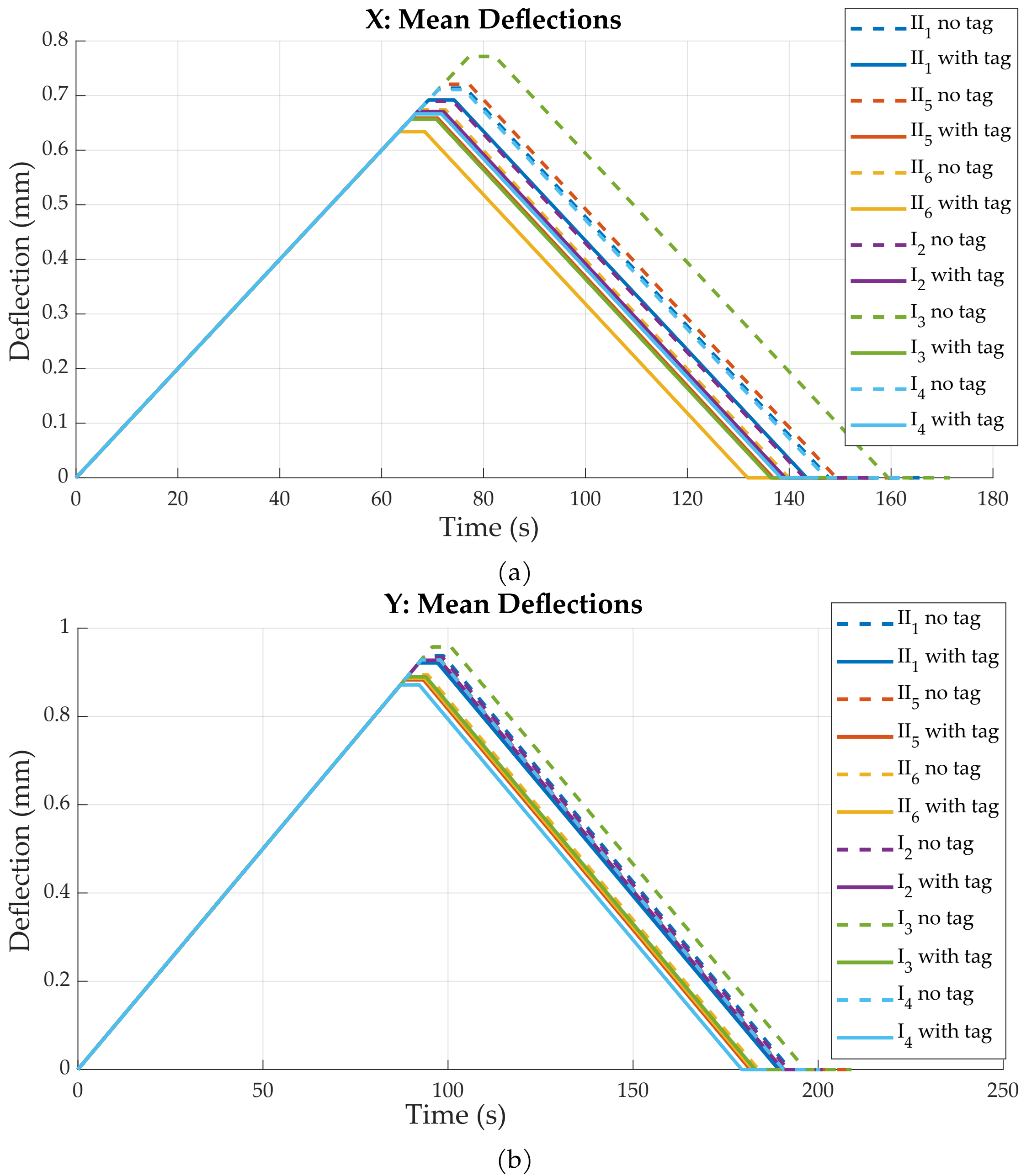

Figure 5.22: a) Mean deflections for all specimens, comparing specimens with tag (solid lines) and without tag (dashed lines). Bending count for each curve: n=5. Data for bending a) *perpendicular* b) *parallel* to main fiber direction.

Following the non-destructive tests described in the prior paragraphs, three specimens each were loaded until breakage, to see if tag integration affects FRP breaking strength. Figures 5.23 and 5.24 show results of the destructive tests. At t=0 s, an initial offset in sensor tag readings can be observed. This is due to the fact that tag strain values were not zeroed before testing, thereby measuring strain caused by integration process or voltage divider tolerance of reference voltage i. e. INA output bias. With rising deflection, strain measured by the sensor tags rises

continuously. At a strain value of ca. 9 mm/m, the output of the INA used for strain sensor amplification saturates, resulting in a constant strain sensor value for large parts of the experiment. This is due to the fact, that maximum output voltage of the INA is limited by design, it is given by the datasheet [113] as $U_0 - 0.1$ V. At some point, for each sensor integrated speciment, local minima in sensor tag measurement can be observed, even after the strain measurement saturated (see Figure 5.23). This effect can be explained by respective tags slipping inside the breaking material. After about 25 min, all FRP specimens break at a deflection value of ca. 37.5 mm/m.

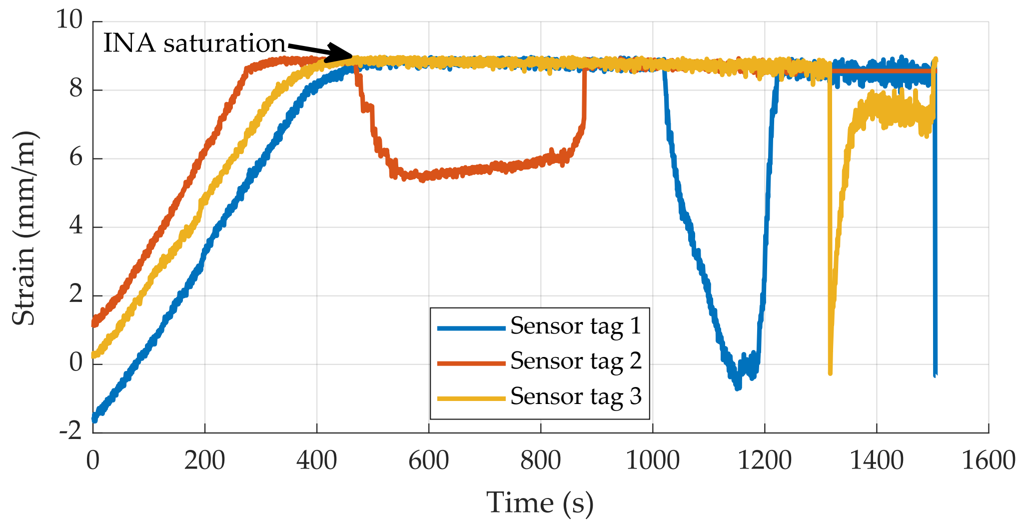

Figure 5.23: Sensor readings during destruction, INA-saturation value indicated.

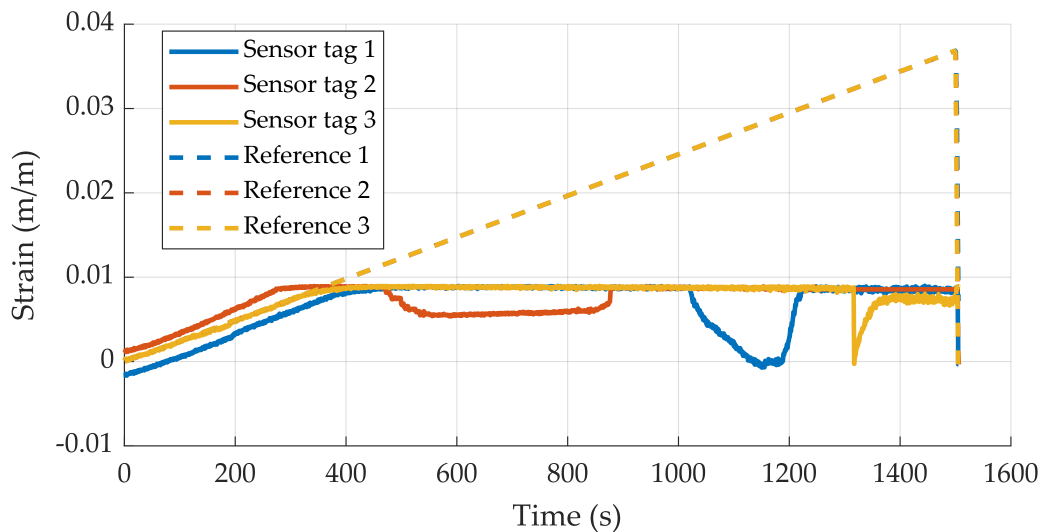

Figure 5.24: Sensor readings and corresponding reference strain values for comparison, during destruction.

Maximum forces for all specimens tested are given in Table 5.3, while the corresponding force values are given in Figure 5.26. Overall, destruction force data

shows quite a similar trend for both sensor-integrated and sensor-less specimens. Mean destruction force was calculated as 10.4 kN for samples without sensor tag, while sensor-integrated samples broke at an average of 10.0 kN. This difference is mainly due to specimen I_2 showing a reduced breaking force compared to the other specimens. This is probably due to the fact that prior to the destructive testing experiments, this specimen was used for experiments regarding maximum operation temperatures (see Section 5.3.3), possibly degrading material properties due to extreme temperatures and inherent material aging. After the first sign of breaking, visible as a drop in force data, it can be seen that the material is still able to bear load, as the measured forces do not sharply drop after the initial breaking event. Regarding actual application scenarios, this effect is desirable, as the material does not fail immediately after first overload.

After destruction, apart from fiber breakage, one major failure mechanism observed is delamination of textile layers throughout the specimens. This occurred at layers of tag presence, but was also observable for specimens without integrated sensor tag (see Figure 5.25). A correlation with sensor tag presence can therefore not be found for the experiments conducted.

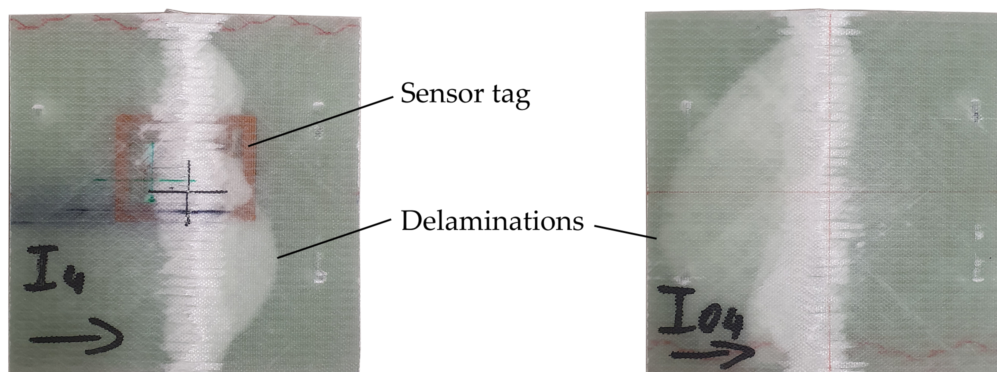

Figure 5.25: Failure comparison for FRP specimen with and without sensor tag. Both specimen show delamination close to the top layer.

Table 5.3: Maximum forces before breakage of FRP specimens.

Specimen	Max. Force (kN)	Specimen Nr.
No Sensor (1)	10.3 kN	I_{02}
No Sensor (2)	10.4 kN	I_{03}
No Sensor (3)	10.5 kN	I_{04}
With Sensor (4)	9.2 kN	I_2
With Sensor (5)	10.4 kN	I_3
With Sensor (6)	10.3 kN	I_4

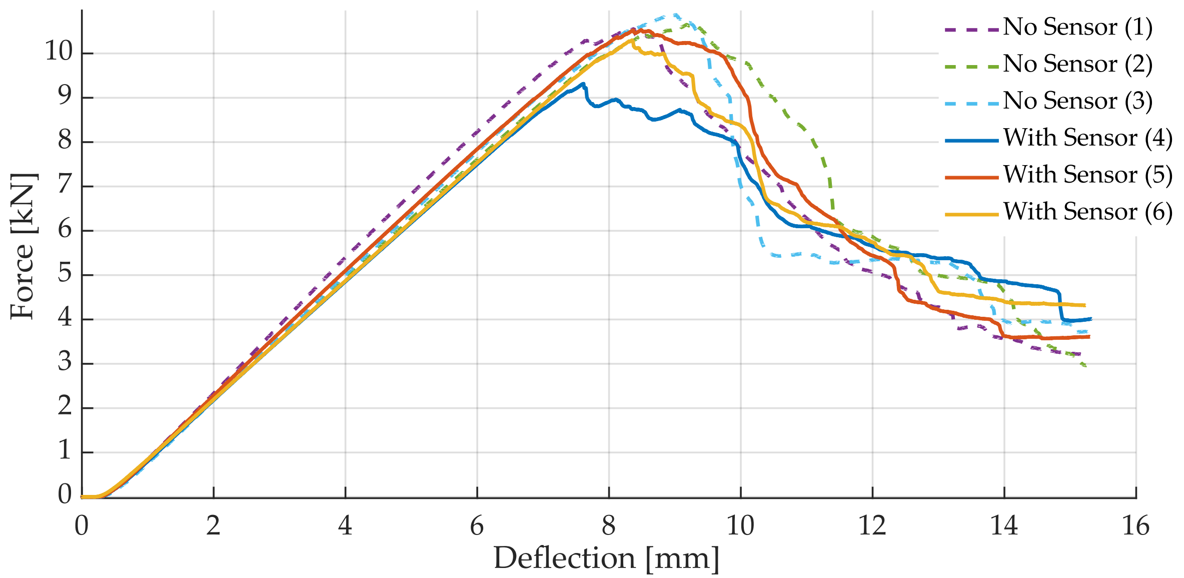

Figure 5.26: Exerted force during destructive tests for specimens with (dashed lines) and without (solid lines) sensor tags.

5.3 Investigation of System Limitations

To examine limits of the system, several experiments were conducted, which are described in the following section. Regarding limitations of the strain sensor, the limit of measurable strain was found during the destructive bending tests described in Section 5.2.3.2, as a result of INA output range. In practice, strain measurement for cyclic loading applications is limited by the strain gauge itself, as too high strain can irreversibly damage the metal structure of the gauge. For this reason, it is advisable to not strain the gauge more than 1.8 mm/m for cyclic loading, according to the gauge data sheet [112].

5.3.1 Power supply

To investigate the power available on the tag during passive operation, average voltage output of the transponder high-drive-pin pin was measured at different load resistances. For this, a tag PCB was assembled with only the micro controller, i. e. RFID transponder and placed 10 mm from the antenna of a reader development board supplied by STMicroelectronics. The reader field was activated and resistors of different size were consecutively connected to the output pin of the transponder, while measuring the resulting voltage drop with an oscilloscope, averaging the measurement results ($n = 20$). The measured voltages and the corresponding power, which was calculated from the resistance and voltage values, are displayed in Figure 5.27.

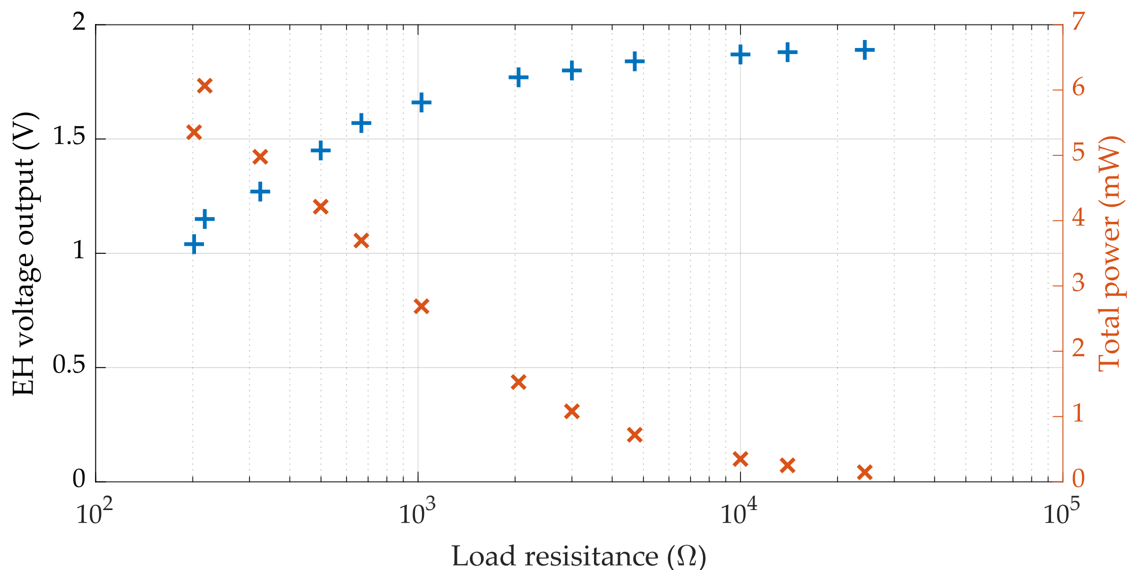

Figure 5.27: Total available power and voltage supplied by the high-drive output pin of the NHS3152, measured at 10mm distance.

According to measurement results, with the antenna used, a maximum power of ca. 6.1 mW is obtainable from the high drive output pin. At this point, pin output

voltage is 1.15 V though, which is too low for sensor tag function, and possibly for most other applications. For the sensor tag, minimum operating voltage is ca. 1.7 V, which in Figure 5.27 is equivalent to a load resistance of ca. 1.5 kΩ and a total of approximately 2 mW available power.

Regarding voltage quality, the spectrum of the output pin was recorded with an oscilloscope, calculating a Fast Fourier Transformation, and averaged with a number 10 samples. The resulting spectrum is displayed in Figure 5.28. Apart from a noticeable peak at the operating frequency of the reader field (13.56 MHz), output voltage is mainly composed of DC. Another distinctly smaller peak can be observed at ca. 4.2 MHz, for the 499 Ω load case. A similar peak could be observed during measurements with the capacitive sensor tag (see Section 7.4.1), which could lead to the assumption of a systematic error in the measurement setup or (sub)harmonic content in the reader field. Another result can be found when comparing the two different load cases. Overall noise reduces for the loaded scenario. A possible reason for this effect might be a load dependent behavior of the internal regulator of the NHS3152 (the transponder).

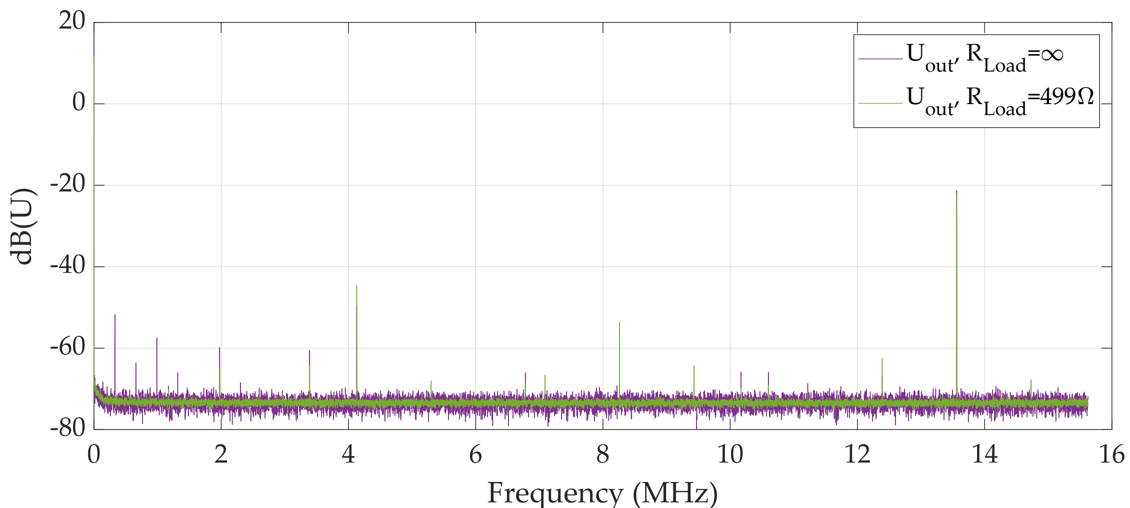

Figure 5.28: Spectrum of NHS3152 high drive GPIO output pin, averaged with n=10. Recorded with PicoScope© 2206B MSO.

5.3.2 Reading Distance

To investigate maximum reading distance of the sensor system, reading experiments with varying tag-reader distance were carried out for both loose and material-integrated sensor tags. To see if FRP presence influences reading distance and transmission of energy and data, the thickness of FRP material between RFID reader and sensor was varied as well.

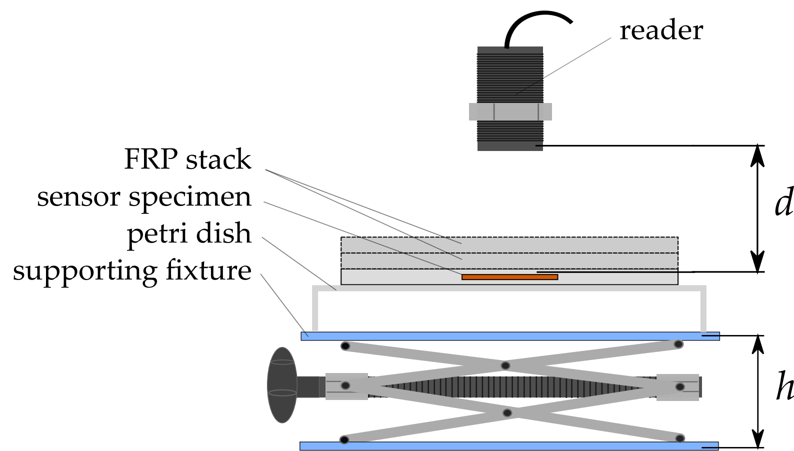

Figure 5.29: Schematic illustration of distance measurement setup. Setting of d possible by changing h via screw.

5.3.2.1 Setup

Three tags each were placed on a glass surface beneath an RFID reader that was fixed in position by a laboratory stand. In order to least influence the electromagnetic field, distance of the glass surface to the supporting fixture was set to ca. 25 mm by choosing a large Petri dish with a high brim and positioning it upside down on the supporting fixture. Figure 5.30a schematically displays the setup. Surface distance (d) to the reader could be adjusted by setting fixture height (h) via a screw attached to the supporting fixture. Tag-reader-distance was controlled manually using a caliper. For investigation of the effect of FRP presence, material thickness in between reader and tag was increased by sequentially stacking FRP plates on top of the specimen under test (see Figure 5.30b).

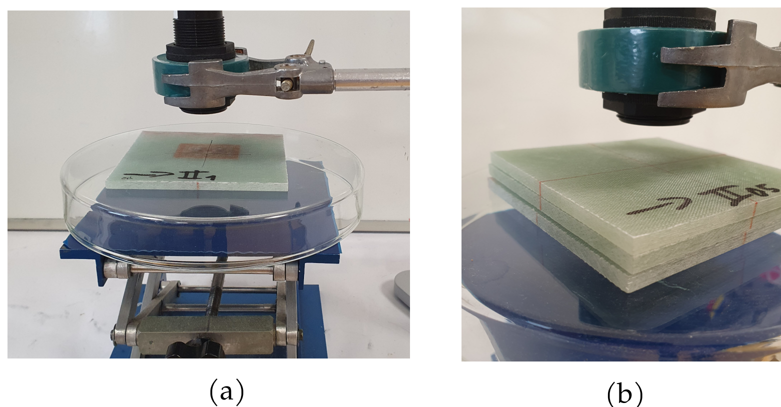

(a) (b)

Figure 5.30: (a) Measurement of FRP influence on reading distance via addition of FRP thickness by stacking (b).

5.3.2.2 Results

During the experiments, two distinct events were noticeable for increasing tag-reader distance. Before the tags actually dropped out, as indicated by no data being read by the reader, it was noticeable that measurement values did not change anymore, even though the reader was still able to read the tag memory. As voltage induced in the antenna coil decreases with increasing distance, this effect may be explained by decreasing supply voltage on the tag. At a certain distance, supply voltage output by the RFID transponder is insufficient to power the tags measurement electronics, while voltage induced in the antenna is still high enough for the RFID transponder to power its memory and communication functions. In this state, the last sensor value stays in the memory, as no new data is obtained via the measurement electronics. To distinguish this effect, results are divided into two categories. Figure 5.31 illustrates distances at which sensor values did not change anymore, while Figure 5.32 shows results for distances at which no data could be read from the transponder memory anymore. Additional to the actual distance values, a linear curve has been fitted to the data, to allow for visual identification of the general trend.

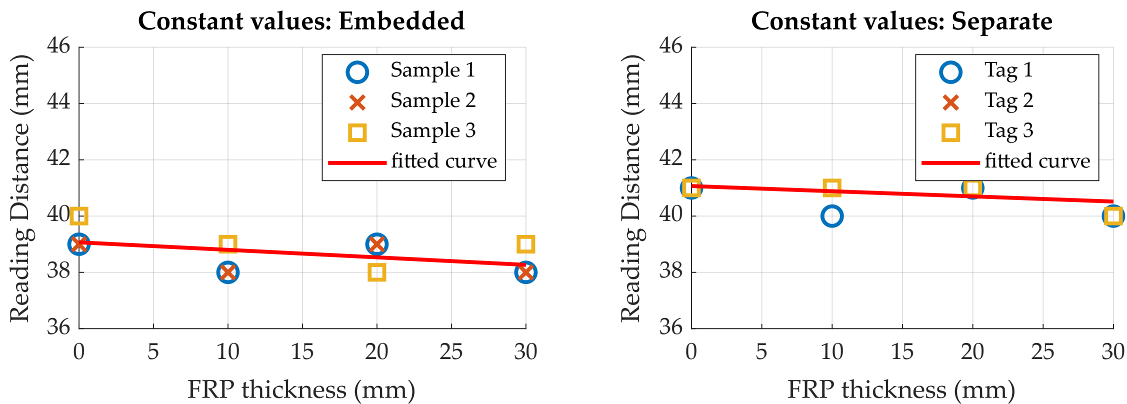

Figure 5.31: Distance at which sensor values did not change anymore vs. FRP thickness for integrated and unintegrated sensor tags.

Results show that the distance at which measurement values stay constant is not significantly influenced by FRP thickness between sensor tag and reader. Regarding maximum reading distance, this is also true for the measurements conducted. Even though a slightly decreasing trend is visible in the fitted curve, the number of samples is not high enough to allow for a qualified assessment, especially as maximum reading distance for the separate sensor tags appears to increase with increasing FRP thickness, opposing the other graphs. It can therefore be concluded that reading distance is not significantly influenced by FRP thickness.

Comparing results for embedded and separate sensor tags, both maximum reading distance and constant values distance is approximately 2 mm higher for separate sensor tags. Integration therefore seems to slightly decrease reading dis-

tance. An explanation for this finding is a possible deformation of the antenna due to the compression in between the fibers, leading to degradation of the inductive coupling.

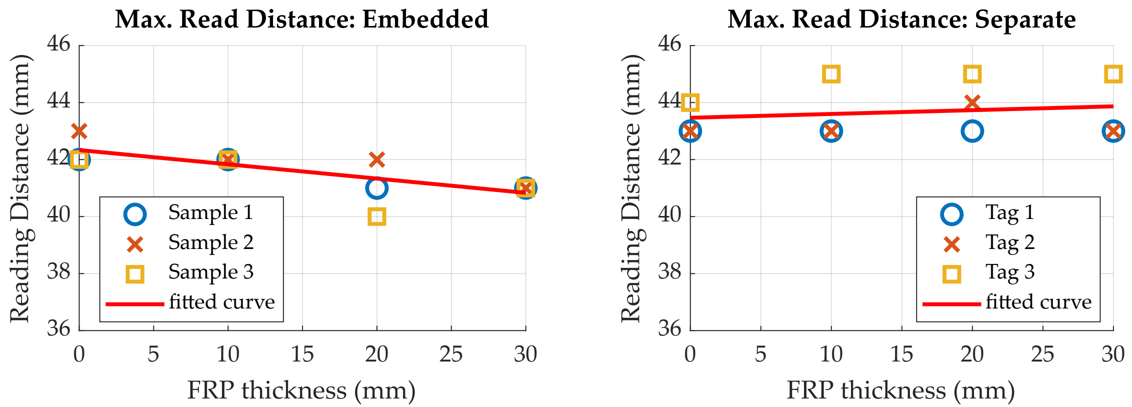

Figure 5.32: Maximum reading distance vs. FRP thickness for integrated and unintegrated sensor tags.

5.3.3 Operating Temperature

To investigate maximum and minimum limits for operation temperature of the sensor system, experiments were carried out with both material-integrated and unintegrated tags. Temperature was controlled via a climate chamber, in which the samples were put. To have an accurate value for temperature close to the specimens, a reference sensor was used. A Pt-100 in 4-wire-configuration was employed for this, which was mounted to the specimens with heat resistant adhesive tape. Temperature was increased from −40 °C to 130 °C, while the sensor tags were continuously read out wirelessly.

Results for both tags are displayed in Figures 5.33a and 5.33b. It can be seen that for both tags, a minimum working temperature could not be determined, as temperatures below −40 °C could not be established with available equipment. Regarding maximum temperature, the unintegrated tag dropped out at 126.9 °C, while the tag integrated in GFRP dropped out at a temperature of 137.2 °C as measured by the reference sensor. Apart from that it can be seen that the temperature measured by the tag closely follows the data measured by the reference.

The difference visible between sensor tag and reference data for the integrated tag might be explained by the fact that the reference, due to the integrated nature of the sensor tag, could only be applied to the surface of the FRP specimen, therefore measuring surface temperature, as opposed to the tag inside. Even though it was placed as close to the sensor tag temperature sensor as possible, minor variations in respective local temperature are likely. Regarding results of the experiments, it can be found that the tag is very well able to function in the extended industrial temperature range of −40 - 125 °C.

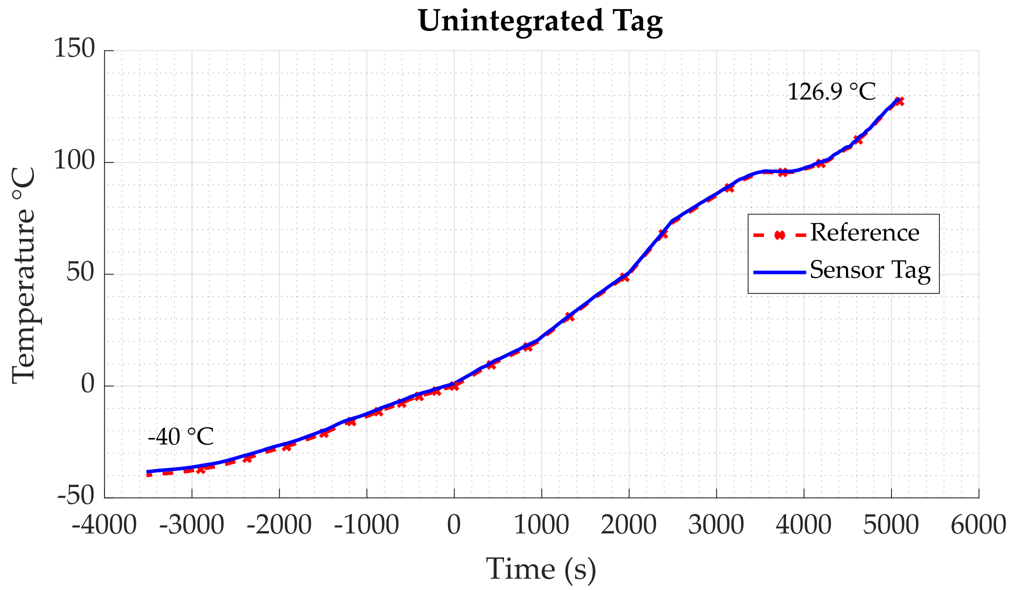

(a)

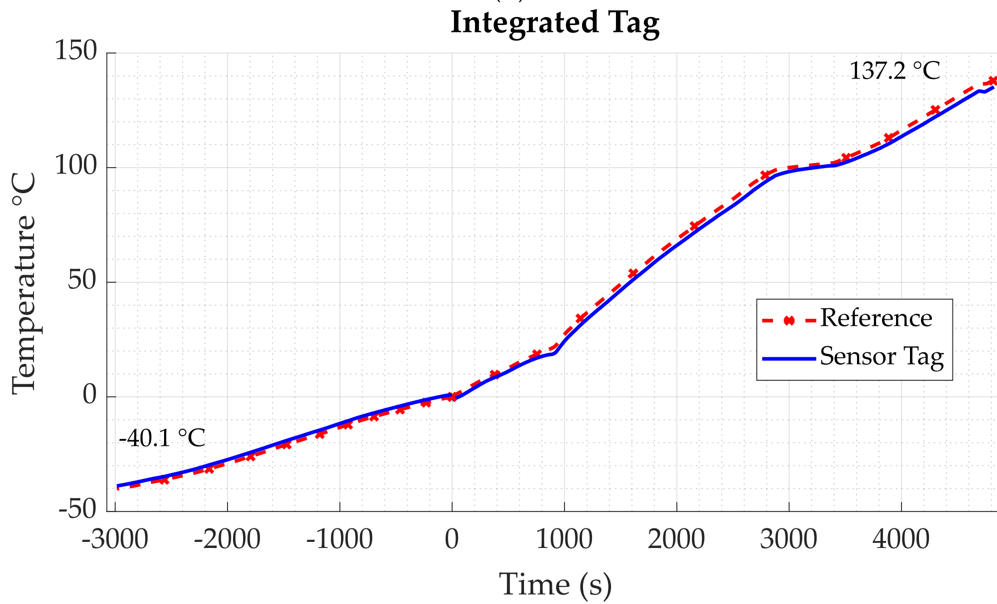

(b)

Figure 5.33: a) Minimum and maximum operational temperature for single, unintegrated sensor tag b) Minimum and maximum operational temperature for sensor tag integrated into FRP.

5.4 Conclusions – Piezoresistive Sensor Tag

This chapter presented the first design of a completely wireless and battery-less sensor for integration into FRP, based on the sensor-tag approach described in chapter 3. This way, it is especially designed for application in an automated industrial environment, allowing for easy placement by e. g. a robot. The sensor is specifically made only with commercially available "off-the-shelf" components, and sensor substrate is made via common industrial processes for FPCB fabrication, thereby being generally very cost-effective and enabling simple producibility.

After describing concept, design, and subsequent tag fabrication, experiments on material integration, sensor characterization and system limitations were presented, showing that the system can be used for several functions during FRP part life cycle. Despite of the requirements on component selection and operational environment, the resulting system was found to fulfill the intended purposes and requirements in the experiments conducted. This shows that the presented approach is generally feasible in a proof-of-concept context.

During FRP production, the temperature sensor of the tag can be used to track local resin temperature inside the laminate, thereby allowing for monitoring of the resin flow front and progression of resin cure. With this additional information, optimization of production processes is possible, allowing for saving of time, energy, and resources by helping to ensure correct resin flow and monitor cure. Nevertheless, due to the sensing principle, flow front monitoring is yet only possible if a measurable difference exists between temperatures of the fluid resin and temperature of the textile and mold. Depending on the materials and processes used, this can be a limitation.

During FRP component application, the integrated sensor tag can be used for both structural health monitoring applications and "smart component" functionality, via the integrated strain sensor and micro controller. The tag is able to measure strain of the host FRP specimens in both lateral and transversal direction with usable results, though sensor error behavior is strongly nonlinear without further calibration. Difference of sensor and reference value varies strongly with applied force and in between specimens, even though average sensor error is below 0.06 mm/m for both directions. This might be explained several ways: Possibly, differences exist between specimens in adhesion of tag and surrounding matrix. Also, as lateral contraction is superimposed on sensor signal, actual material properties and especially non-uniformities can negatively influence sensor accuracy. To circumvent this, a different strain gauge or bridge configuration could be used, e. g. a rosette pattern or two independent bridges for the two directions. Nonetheless, the work presented proves that piezoresistive strain gauges can both be powered and measured on a passive wireless sensor tag, despite the constraints on power availability.

Regarding system limitations, an averaged maximum reading distance of at

least 38 mm could be measured, while the operational temperature range was found to be at least −40 to 126.9 °C. Maximum obtainable power for supply of the measurement circuitry was found to be about 2 mW for a system voltage of 1.7 V. Mechanical impact on FRP structural integrity was examined in two experiments, giving no measurable indication of a negative effect. These results have only limited significance though, as they were small in number and only bending strength was investigated. Still, optimization of tag geometry seems reasonable to further reduce tag footprint and therefore mechanical influence on the host material. In this regard, especially a reduction of thickness would be possible by using different packages for ICs, e. g. wafer of chip scale level packages, and smaller passive components. This way, fiber ondulations caused by the ICs could be reduced.

Chapter 6
Investigations on Interdigital Capacitors

In this chapter, properties and behavior of interdigital capacitors are examined regarding their usage as sensing element, to gain a fundamental understanding of the relevant aspects for sensor design. The knowledge gained is used for development of the second wireless sensor designed in this work, though, due to its general nature, it presents valuable information for development of other IDC-based sensors. Consequently, the chapter focuses on the IDCs themselves, as opposed to the full sensor tag, which is subsequently described in Chapter 7. Even though IDCs in general have been subject of many publications, this section especially examines IDCs made via common FPCB fabrication techniques and the resulting limitations in minimum feature size, i. e. comparably large geometries.

First, in order to get an estimation of to-be-measured capacitance, the following section will compare different approaches for analytical approximation of IDC capacitance. This way, dimensioning of a usable IDC layout is simplified. With this information, several prototypical IDCs are designed and fabricated, which is described subsequently. Then, the major part of this chapter describes experimental insights gained with the IDCs, both investigating basic properties, i. e. actual size and environmental influences on IDC capacitance, and more application-related behavior like capacitance changes during epoxy cure. Different IDC geometries and designs are also investigated, varying both in finger length and number, and general layout, i. e. presence of a back plane (shield) and double sided IDC layout. Finally, this chapter concludes with an in-depth summary of the findings, differentiating between general and more application-related information.

6.1 Analytical Calculation of IDC capacitance

Numerous publications on estimating the capacitance of interdigital electrode configurations exist that date back into the 1970s, e. g. [118–120]. The most prominent approaches employ a technique using conformal mapping, based on results published in [121, 122]. In the following sections, three analytical techniques shall be described and compared as to their results in context of this thesis. All of the approaches described assume a general IDC geometry as displayed in Figure 2.14. Contrary to the nomenclature used in the other chapters of this work, the calculations presented in this chapter use the overall, i. e. absolute number of fingers

(N_{abs}), instead of the number of fingers per electrode (N, i. e. $N_{electrode}$). As there are two electrodes per IDC, the relation between the two numbers is

$$N_{abs} = 2 \cdot N_{electrode}. \tag{6.1}$$

Some of the techniques discussed allow for consideration of different dielectric layers of different height above the interdigital electrode structure (e. g. [51]), while some assume a uniform and infinite material around the electrodes. To make comparison easier, the case study presented below will assume a general epoxy material of infinite extension for material surrounding the electrodes. As relative permittivities of epoxy (ca. 3.5, [123]) and polyimide (ca. 3.4, [124]), which is used for the thin encapsulation of the electrodes on the FPCB, are very similar, it is expected that this simplification will not introduce any significant error.

6.1.1 Igreja and Dias

One of the most cited papers was published by Igreja and Dias, in 2004 [51]. It is defined for IDCs with $N_{abs} > 3$ and calculates partial capacitance for interior and exterior electrodes independently, summing them at the end. The partial capacitances C_I and C_E are calculated to include both the parallel capacitances between the fingers and the fringing capacitances above, that are partially calculated individually. Figure 6.1 illustrates the equivalent circuit and positions of the equivalent interior and exterior partial capacitances for an exemplary six electrode IDC. Calculation of the corresponding overall capacitance is also illustrated (see Equation 6.8 for the generalized formula).

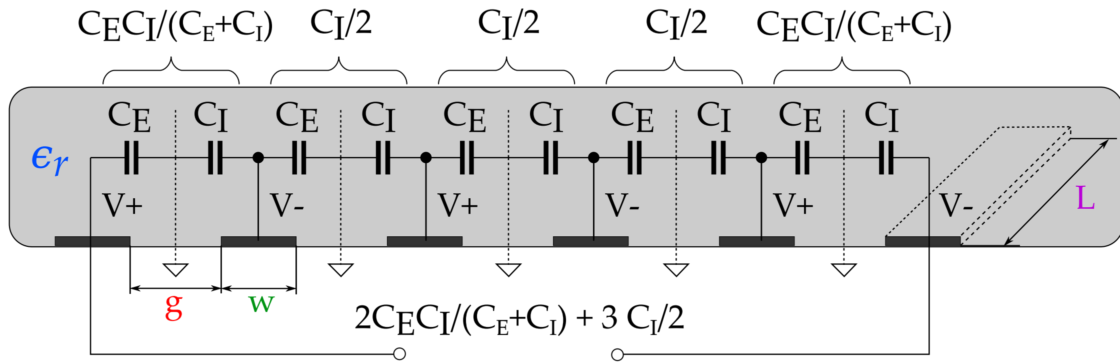

Figure 6.1: Equivalent circuit model for a six-electrode IDC with a semi-infinite layer of dielectric above the electrodes, redrawn and adapted from [51].

According to [51], the individual partial capacitances for a semi-infinite layer above the IDC are then obtained via

$$C_I = \epsilon_0 \epsilon_r L \frac{K(k_{I\infty})}{K(k'_{I\infty})} \tag{6.2}$$

$$C_E = \epsilon_0 \epsilon_r L \frac{K(k_{E\infty})}{K(k'_{E\infty})}, \tag{6.3}$$

where $K(k)$ and $K(k')$ are the the complete elliptic integrals of the first kind of the modulus k and complementary modulus k', ϵ_r is the relative permittivity of the surrounding material, and L is electrode length. For material integration of IDCs, the equations for a (semi-)infinite layer height of the dielectric above the electrodes are chosen, as penetration depth of the electric field lines is much smaller than the layer height. The geometric relation of finger width and gap size is incorporated in the calculation via the metallization ratio η (see Section 2.4 and Figure 2.14). For the infinite layer solution, the moduli are derived via

$$k_{I\infty} = sin\left(\frac{\pi}{2}\eta\right) \qquad \text{and} \tag{6.4}$$

$$k_{E\infty} = \frac{2\sqrt{\eta}}{1+\eta}, \tag{6.5}$$

respectively. To get the capacitance of a material-integrated IDC, the partial capacitances of the layer above and below the IDC are added up, resulting in partial capacitances

$$C_{I,IDC} = C_{I,upside} + C_{I,downside} = 2C_I \tag{6.6}$$

$$C_{E,IDC} = C_{E,upside} + C_{E,downside} = 2C_E. \tag{6.7}$$

In this case, capacitance of the overall capacitance is made up from the partial interior capacitances C_I and exterior capacitances C_E using

$$C_{IDC} = (N_{abs} - 3)\frac{C_{I,IDC}}{2} + 2\frac{C_{I,IDC}C_{E,IDC}}{C_{I,IDC} + C_{E,IDC}}. \tag{6.8}$$

For layer heights that are not infinite or layers of different material and height, a more complex solution is given, that allows for taking into account different layer heights and permittivities, e. g. for a typical IDC sensor. As these calculations are quite long and not directly necessary for the conducted comparison, the interested reader is pointed to [51] for further details, and details on the cases incorporating limited layer height and different layer permittivity.

6.1.2 Endres et. al.

Another approach altogether is taken in [125], where capacitance is first calculated for a "unit cell" of the IDC, i. e. an area as displayed in Figure 6.2.

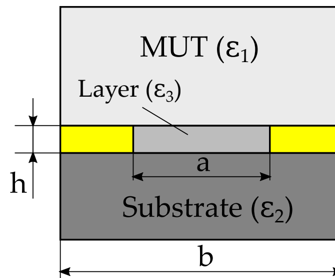

Figure 6.2: Unit cell definition for IDC C calculation, redrawn from [125].

The parameters a and b correspond to the common IDC geometry nomenclature as follows:

$$a = g \tag{6.9}$$

$$b = g + w \tag{6.10}$$

This approach allows for a different dielectric to be present on each side of the IDC, e. g. to differentiate between the IDC substrate and MUT. The corresponding capacitances are calculated as follows [125]:

$$C_1 + C_2 = \epsilon_0 \frac{\epsilon_1 + \epsilon_2}{2} \frac{K\left[\left(1 - \left(\frac{a}{b}\right)^2\right)^{\frac{1}{2}}\right]}{K\left[\frac{a}{b}\right]} \tag{6.11}$$

Here, ϵ_1 and ϵ_2 are the relative permittivities of the MUT and IDC substrate, respectively, while the two $K[x]$ terms refer to the complete elliptic integral of the first kind, similar to the equations mentioned in Section 6.1.1. This approach also takes into account the parallel plate capacitance between the parallel surfaces of the electrode fingers, i. e. the surface areas defined by $h \cdot L$, seperated by the gap distance a, filled with a dielectric of permittivity ϵ_3, which is correspondingly determined as

$$C_3 = \epsilon_0 \epsilon_3 \frac{h}{a}. \tag{6.12}$$

For the whole unit cell, the (two dimensional) capacitances add up to make

$$C_{UC} = C_1 + C_2 + C_3. \tag{6.13}$$

As so far the model is only two-dimensional, the individual unit cells are summed and multiplied by finger length L to get the capacitance C_{IDC} of the whole IDC:

$$C_{IDC} = LC_{UC}(N_{abs} - 1). \tag{6.14}$$

6.1.3 Mukhopadhyay et. al.

Another approach for IDC capacitance estimation is given in [126], based on conformal mapping an the inverse cosine transfer function. For finger electrode configurations, i. e. a geometry with $L \gg w$ and $\frac{w}{g} \gg 1$, the capacitance C_I of two coplanar finger electrodes is given by [126]:

$$C_i = \frac{2\epsilon_r \epsilon_0}{\pi} ln \left[\left(1 + \frac{w}{g}\right) + \sqrt{\left(1 + \frac{w}{g}\right)^2 - 1} \right]. \tag{6.15}$$

Similar to the other approaches, these capacitances are added up for the number of electrodes and multiplied by electrode length L, giving the total IDC capacitance as

$$C_{IDC} = LC_i(N_{abs} - 1). \tag{6.16}$$

6.1.4 Comparison and Results

In this section, the calculations presented in the prior section are used and compared as to their results. To this end, the equations have been implemented in MATLAB. All calculations assume IDC placement in an infinite space of cured epoxy resin with a relative permittivity of $\epsilon_{Epoxy} = 3.5$. For the models allowing for different dielectrics, all permittivities are set to ϵ_{Epoxy}. As common lower limit for production of FPCB are distances and copper widths of 100 µm, dimensions smaller than this are not considered for calculations. If not otherwise mentioned, an exemplary IDC geometry of $L = 10\,\text{mm}, w = g = 0.1\,\text{mm}$ is therefore used as a calculation basis. For the calculations using the formulas by Endres et. al., which specifically include electrode height, a copper thickness of $h_{electrodes} = 28\,\mu\text{m}$ is chosen. This was deemed applicable as 28 µm is a common value for copper thickness for some FPCB manufacturers.

First, variations of finger count N_{abs} and finger length L are investigated. Figures 6.3a and 6.3b show calculation results for finger number and finger length for the three different approaches. As is to be expected from the formulas, a positive, linear correlation between both finger length and finger count, and capacitance is visible, though both offset and slope of the curves differ between models. For a finger number of $N_{abs} = 80$, Endres et. al predict a capacitance of about 40 pF for a length of $L = 10\,\text{mm}$. Comparing this to the results of both Igreja et. al. and Mukhopadhyay et. al., who estimate capacitance to be around 26 pF, this value is much higher. This is possibly due to the inclusion of the partial parallel plate capacitance, that is not specifically included into the other two models.

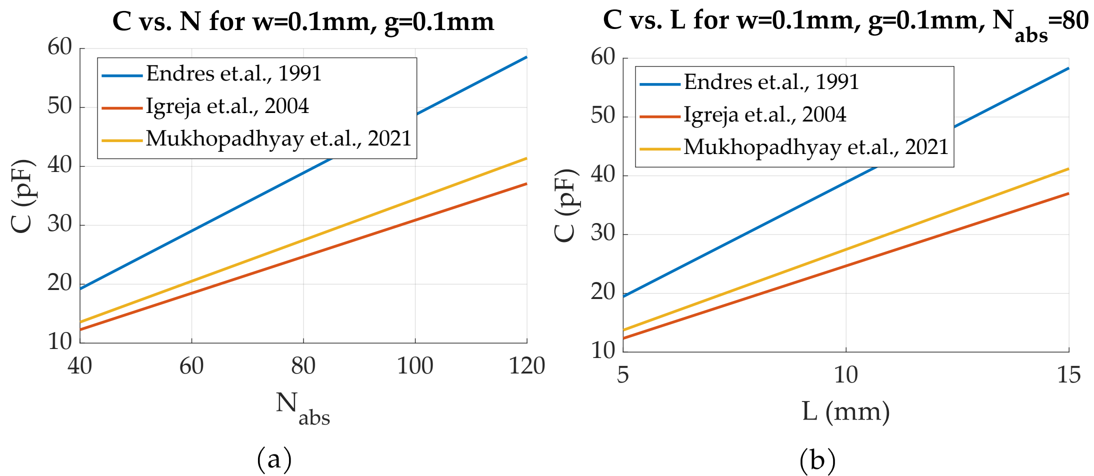

Figure 6.3: Comparison of calculation results for different analytical approaches for finger width w=g=0.1 mm. a) Capacitance for different number of fingers, finger length L=10 mm. b) Capacitance for different finger lengths, N_{abs}=80.

Regarding variations of finger width w and finger spacing g, all models show a generally similar trend, though overall magnitude of the obtained data differs

similarly to the prior calculations. Respective results are displayed in Figures 6.4a and 6.4b. Increasing finger width w for an IDC with otherwise fixed geometry of $g = 0.1$ mm and $N_{abs} = 80$, results show an increase in capacitance, the slope of which decreases with rising w. For an increasing spacing g, calculated capacitance reduces strongly, as shown in Figure 6.4b. This trend seems to be similar to that of a parallel plate capacitor with increasing plate distance, where capacitance decreases with $\frac{1}{d}$ (see Equation 2.28).

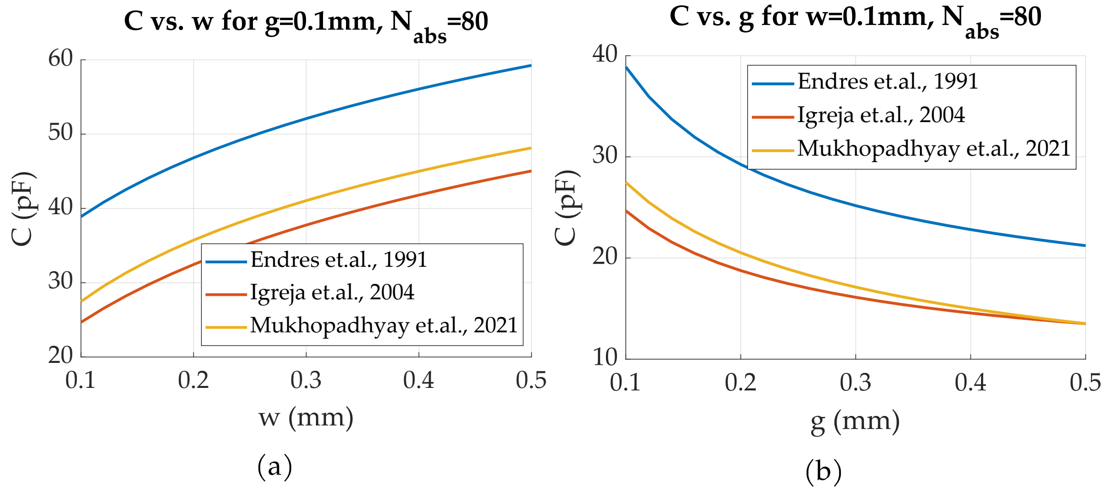

Figure 6.4: Comparison of calculation results for different analytical approaches for L=10 mm and finger number N_{abs}=80. a) Capacitance for different finger widths w, g=0.1 mm. b) Capacitance for changing gap distance w=0.1 mm.

These results suggest increasing finger width for higher IDC capacitance and therefore higher sensitivity for sensoric applications. This is misleading though, as visualized in Figures 6.5 and 6.6, which correlate finger number, width and spacing in a more realistic sensoric context, where space is limited. For a given overall IDC width, the resulting number of fingers is maximal for the smallest values of w and g, which is standing to reason. Regarding resulting capacitance values for the corresponding finger numbers, it can be seen that the increase in capacitance due to higher finger numbers is much greater than the increase induced by rising finger width. It is therefore concluded that for sensoric applications, a 1:1 ratio of w and g, i. e. a metallization ratio of $\lambda = 0.5$, is preferred to achieve highest overall capacitance and sensitivity per unit area (β, see Section 2.4.6). This is in agreement with findings presented in literature, e. g. [15, 50, 52], who found that β is maximal for $\lambda = 0.5$.

To correlate capacitance with sensor strain, e. g. for usage of the IDC as a capacitive strain gauge, strain is assumed to result in an increasing gap distance g, as the substrate material is much more flexible than the electrode metal. As strain is a relative number, calculated by dividing the change in length to the initial length

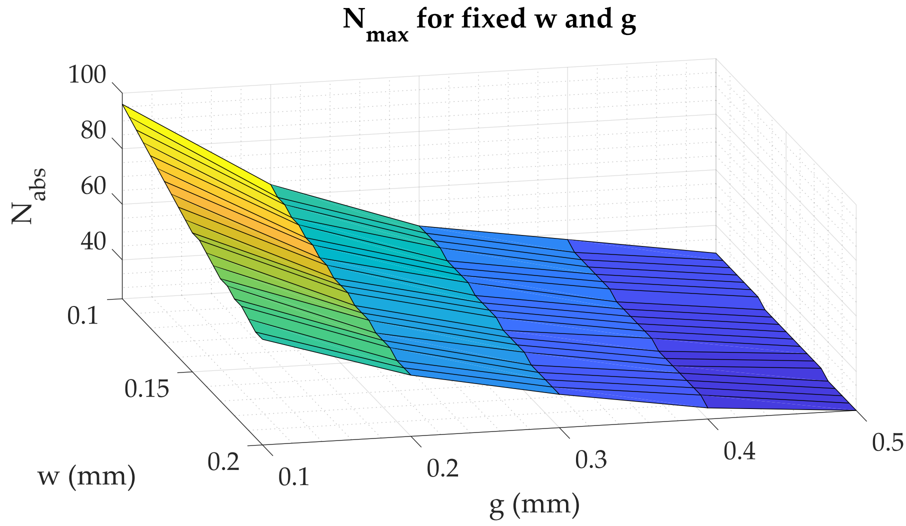

Figure 6.5: Maximum IDC finger number N_{abs} for combinations of w and g in a fixed width of 20 mm, L=10 mm

(see Equation 2.7), IDC strain is implemented into the calculations via

$$\epsilon = \frac{\Delta g}{g_0} = \frac{g - g_0}{g_0}. \tag{6.17}$$

Figure 6.7a displays the corresponding capacitance values for increasing IDC strain. Due to the relative nature, the observed trend is slightly less curved compared to the results for an absolute change in g (Figure 6.4b). In order to better visualize capacitance change over strain, capacitance of the strained IDC is subtracted from the initial capacitance, i. e. that of the unstrained IDC:

$$\Delta C = C_0 - C \tag{6.18}$$

Plotting this versus strain, Figure 6.7b suggests much greater sensitivity for the values calculated via the formulas by Endres et. al. This is though only due to the overall higher capacitance values calculated by the model – comparing normalized results for capacitance change over strain $\Delta C/C_0$, as displayed in Figure 6.7c, it can be seen that the relative change in capacitance does not significantly differ between the different calculation approaches, even though overall capacitances are dissimilar.

Using equation 2.33 and the data given in Figure 6.7c, the theoretical gauge factor of the exemplary design ($L = 10\,\text{mm}, w = g = 0.1\,\text{mm}, N_{abs} = 80$) can be calculated for small strains. Neglecting the small difference between the normalized data, a gauge factor of approximately

$$G_{F20} = \frac{\Delta C}{C_0 \epsilon_{mech}} \approx -0.4$$

can be calculated for a strain of 20 %, which is similar to the gauge factor of -0.4 that could be calculated from the experimental results presented in [53].

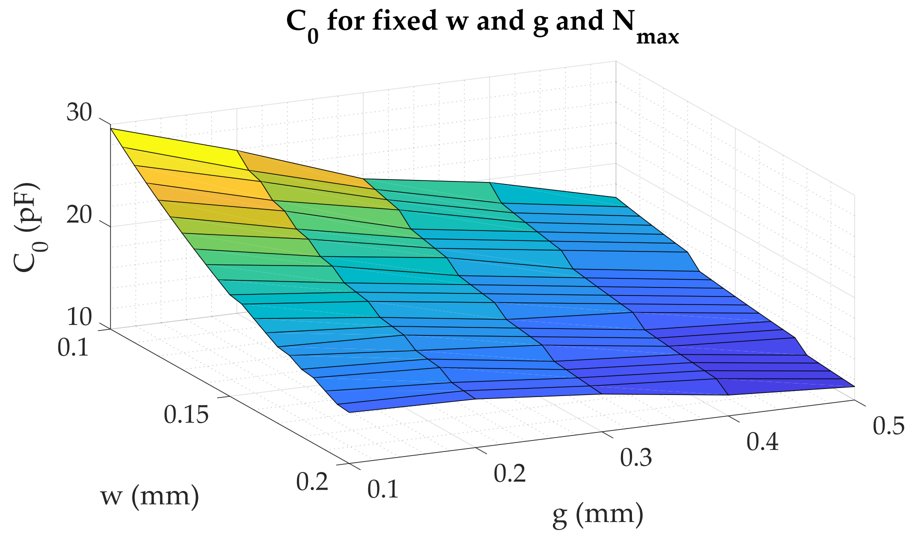

Figure 6.6: Calculated IDC capacitance for combinations of w and g in a fixed width of 20 mm, L=10 mm

Summarizing the findings of the calculations, it can be found that for maximal capacitance and therefore maximal sensitivity, N and L should in turn be made maximal. This implies that w and g should be as small as possible, to allow for a high number of fingers in a fixed space. Another reason to make gap distance as small as possible is that the change in capacitance with increasing g is higher for small initial gap sizes, improving strain sensitivity. For a sensoric context it can be found that, as calculated changes in capacitance for IDC strain are comparably small, (e. g. 2-3 pF for $\epsilon = 20\,\%$ of an IDC with $L = 10\,\text{mm}$, $w = g = 0.1\,\text{mm}$, $N_{abs} = 80$), usage of a sufficiently precise measurement equipment is necessary to actually measure strain.

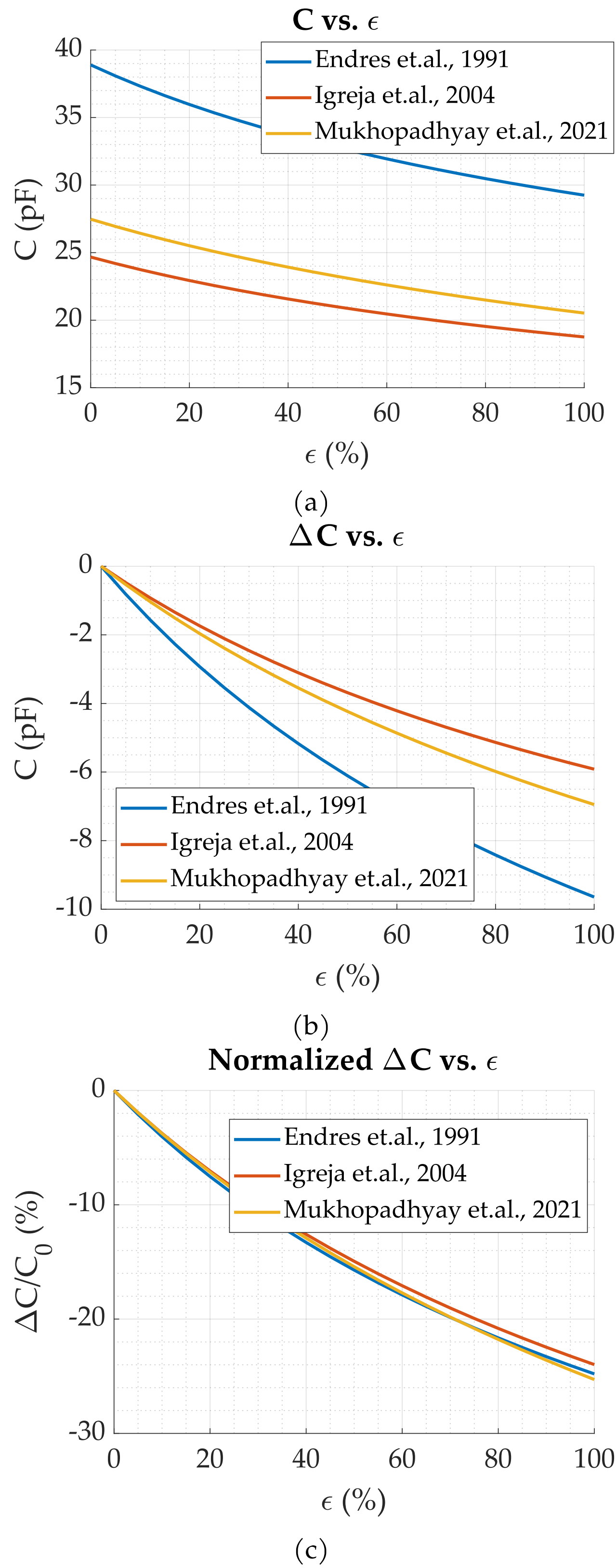

Figure 6.7: Comparison of calculation results for different analytical approaches, w=g_0=0.1 mm, L=10 mm, N_{abs}=80. a) Capacitance for changing IDC strain. b) Absolute capacitance change per strain. c) Normalized capacitance change per strain. ($\Delta C/C_0$)

6.2 Experiments with IDCs

In the following section, experiments are presented to investigate behavior of FPCB-based IDCs of different designs. First, the experiments and their results are described, before giving a concluding summary at the end about IDC selection for subsequent sensor tag design. Apart from the experiments on IDC frequency dependence or otherwise indicated, all experiments use a sensor tag circuit prototype built on a breadboard, as these were done prior to tag design and fabrication (see Figure 6.8). For capacitance measurement of the IDC, the circuit uses an excitation voltage of ca. 1.2 V at a base frequency of approximately 1.4 MHz. Accuracy of the circuit is shown in Section 6.2.4.

To compensate for parasitic capacitances (e. g. in connections, cables, etc.), a calibration routine was implemented in micro controller firmware, that can be triggered via a command over the serial interface. It measures the current capacitance and stores it temporarily in micro controller Random Access Memory (RAM), to substract this from all following measurements. If not otherwise mentioned, this function was used to reduce influence of the parasitic elements in the experimental setups.

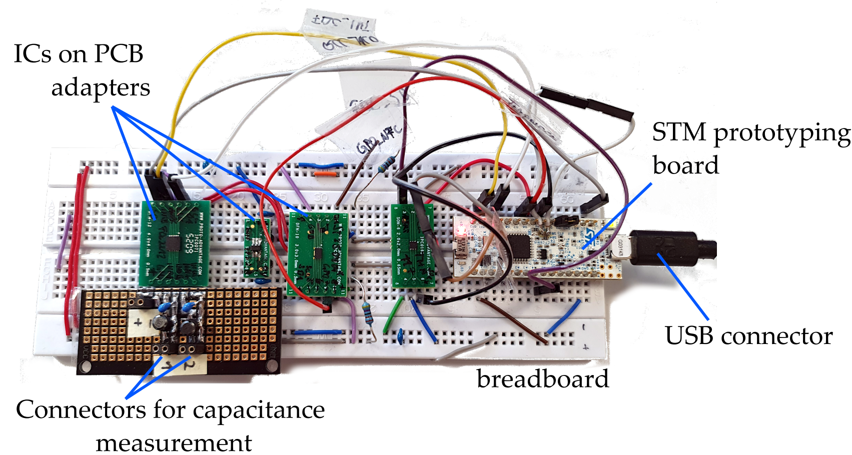

Figure 6.8: Circuit prototype for capacitive sensor tag used for development and preliminary experiments

To make connection of specimens more reproducible, a dedicated breakout fixture was attached to the circuit prototype as displayed in Figure 6.9. It includes the whole resonant circuit for capacitance measurement, i. e. the capacitances $C_{res1/2}$ and inductances $L_{res1/2}$, and pin sockets for plugging in the IDC connectors. All connections were soldered meticulously, to prevent a change of parasitic circuit elements as much as possible. Additionally to the resonant circuit connections, both supply voltage U_0 and ground potential are provided at a connector each.

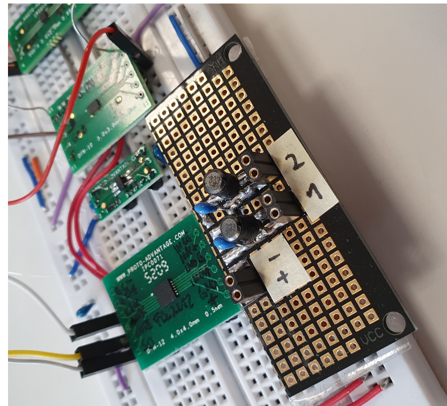

Figure 6.9: Breakout for easy and reliable connection of capacitors for testing and preliminary experiments

6.2.1 IDC design and fabrication

As suggested by results presented in [50, 52, 65] and many other publications (see Section 4.1.3), polyimide is chosen as IDC substrate material. Apart from being well suited for this application as described in the aforementioned works, this presents a major opportunity for reducing sensor production cost. By implementing the IDCs, i. e. sensor elements, directly into the FPCB structure, fabrication is very much simplified. Additional cost for IDC production and e. g. mounting and contacting steps can therefore be prevented. Similar to the work presented in Chapter 5, the resulting IDC-based sensor tag will therefore be a polyimide based FPCB, with the IDC designed in-place as a metallized structure. Corresponding sensor tag design is presented in Chapter 7.

Several IDC geometries were designed and fabricated for the experiments described further down. As space on the sensor tag is limited, two comparably small finger lengths of 5 mm and 10 mm were chosen for comparison, with different finger counts of $N = 20, 40, 60$. IDC metallization ratio is chosen to be 0.5, as suggested by literature (e. g. [15, 50, 52],) and confirmed by analytical calculations in Section 6.1, as this results in best sensitivity per unit area. In context of designing a sensor for material integration, where overall size should be minimal to reduce impact on the host component, this is very much necessary. For electrode width and spacing (w and g), 100 µm is consequently chosen, as this size is a common design limitation for many PCB manufacturers. At the end of the electrode fingers, a larger gap is intentionally inserted to reduce lateral strain sensitivity caused by electrode displacement in finger direction, i. e. perpendicular to the intended measurement direction. To reduce probability of crack formation at the corners of the interdigital structure, electrode corners have been rounded off, as illustrated in Figure 6.10. In context of IDC application for strain measurements, this precaution seemed appropriate during layout.

As suggested by [52], usage of a metallized back plane, i. e. a shielded IDC

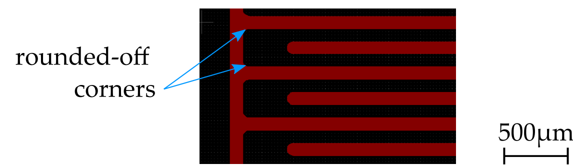

Figure 6.10: Schematic illustration of rounded-off IDC corners

backside, can yield several advantageous properties as compared to unshielded IDCs, at least for surface-based FRP production monitoring. The authors claim to achieve higher nominal capacity, less noise, and increased sensitivity per unit-area. IDCs utilizing a back plane are common for many applications aside from FRP fabrication monitoring, as comprehensively reviewed in [47]. To investigate said advantages, shielded IDCs are also designed and tested in this thesis.

For both the shielded and unshielded versions, an additional layout was created that resembles that of a full bridge strain gauge, as displayed in Figure 6.11. The idea behind this configuration is to enable a birectional strain measurement, analogous to the full bridge resistive strain gauge configuration used for the piezoresistive sensor tag (see Chapter 5). Consequently, to achieve the above mentioned advantages, two IDCs each are combined for measurement of the two axes, as this ist the most space-saving alignment, resulting in four IDCs total. Also, as could be found in literature, e. g. in [54], capacitive strain gauges with polyimide substrate show a cross-sensitivity to humidity, that, for strain measurement can be eliminated by usage of a “half bridge” configuration. Essentially, this means using another IDC that is not influenced by the strain to be measured, but experiences the same humidity conditions, to differentiate between strain-induced and humidity-induced capacitance change. Using the 2×2 configuration mentioned above, this can be achieved by measuring capacitance of the two axes independently.

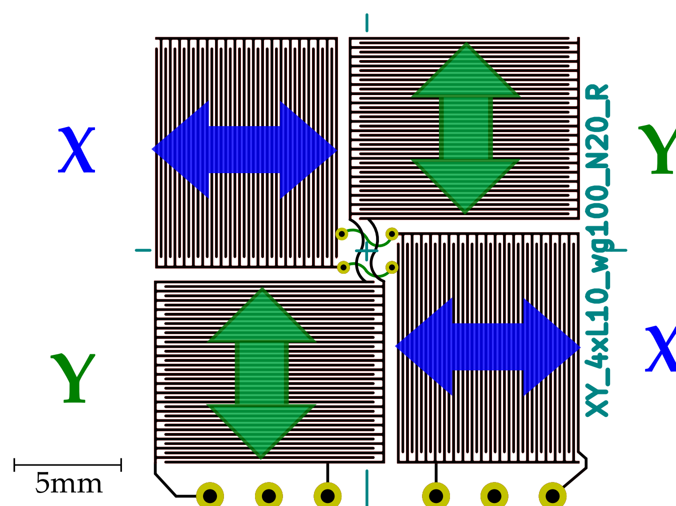

Figure 6.11: Footprint of an XY IDC configuration for birectional strain measurement

Schematic stack up of the FPCB is displayed in Figure 6.12. The IDCs are implemented as a metal structure in the top copper layer. For the unshielded designs, the back copper layer is left empty, while the shielded versions have a hatched copper pour on the back layer. To prevent short circuits and corrosion, the IDCs are isolated by a thin polyimide top layer of 13 µm thickness, which is held in place by an adhesive layer of 13 µm, made of epoxy. For cure monitoring, this has also been done in literature, e. g. in [12]. For fabrication, the IDC structures were designed with CAD software, resulting in a 3D model, the outline of which was then transferred to a vector graphics format, to be imported into the software used for PCB design (kiCad, [127]). There, the outlines were then converted into corresponding footprints, to use these in PCB layout.

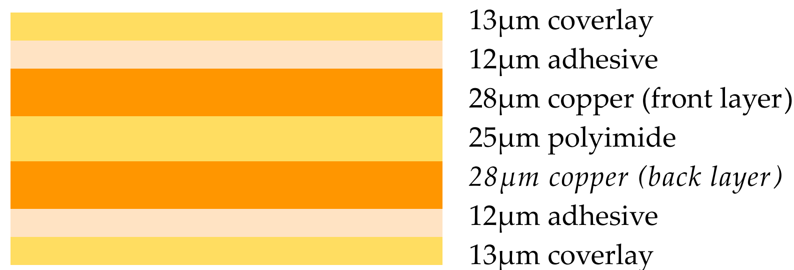

Figure 6.12: Schematic illustration of FPCB layer stack up used for IDC and sensor tag fabrication

For reliably and reproducibly connecting the prototypical IDCs, pin headers were mounted on the connection pads, as displayed in Figure 6.13. For connection of the pins, a silver based, conductive glue was used (Elecolit 414). Additionally, the pin headers are held in place by epoxy glue, to ensure good mechanical coupling, so that connections are not stressed and parasitic elements stay as constant as possible.

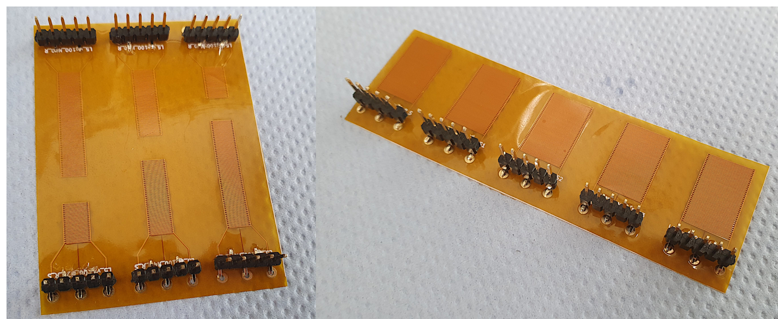

Figure 6.13: IDC prototypes with pin headers mounted for preliminary experiments

6.2.2 IDC Nomenclature

To make differentiation of IDC designs and configurations easier, the following nomenclature is used to simplify IDC classification:

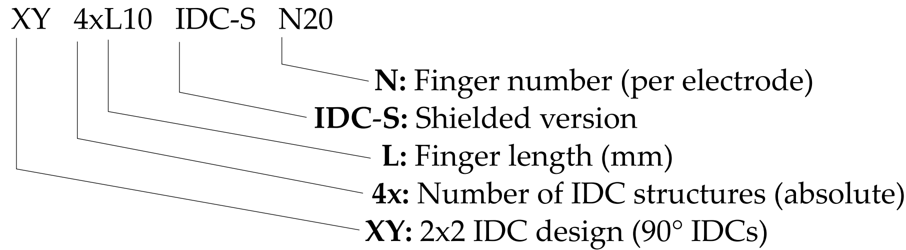

In this context, and for the rest of this document, the number of electrode fingers N is always referring to the number of fingers *per electrode*, as opposed to the absolute number of fingers N_{abs} used for the calculations in Section 6.1. The above mentioned IDC therefore would be a layout with two shielded IDCs for each of the two measurement directions X and Y, with 20 fingers per electrode for each IDC, giving an overall number of 4 IDC structures.

6.2.3 Frequency Dependency of IDCs

The first experiment conducted investigates dependency of excitation frequency on IDC capacitance. This is of interest, as the principle utilized for capacitance measurement relies on changes in resonance frequency (see Section 2.4.8 for details). To this end, both a shielded and an unshielded IDC were measured with an Impedance Analyzer (IA) over a wide frequency spectrum. The IA was set to measure equivalent series capacitance C_S at an oscillation amplitude of $V_{osc} = 0.5\,\text{V}$, and compensation was done according to device manual.

Results Figures 6.14a, 6.14b, 6.15a and 6.15b show measurement results both for a wideband sweep from 0-5 MHz and a narrower frequency band around the planned excitation frequency of approx. 1.4 MHz.[1] Subsequent experiments in this section, and following experiments with the final tag prototype are conducted at a fixed frequency, as the IC used for capacitance measurement uses a single-frequency principle. For resin cure measurements, measurement frequency is relevant.

In order to compare data of the lose IDC, i. e. the IDC in air, and the integrated state, i. e. the IDC surrounded with FRP matrix material, measurement data for an IDC integrated into epoxy glue is also included in the diagrams. For the unshielded IDCs, measured capacitance decreases slightly with rising frequency, while the shielded versions show a shallow local capacitance minimum, centered around ca. 2.5 MHz. Even though the curves suggest a significant dependency of capacitance

[1]The exact resonant frequency is measured in Section 6.2.4.

and frequency, this impression is invalidated by observing diagram scaling. In conclusion, IDC capacitance dependency on frequency is deemed insignificant for the following experiments, as excitation frequency is not expected to change in the order of MHz. This is especially true for measurements on IDC strain, where changes in capacitance, and therefore shifts of resonance frequency, are minimal.

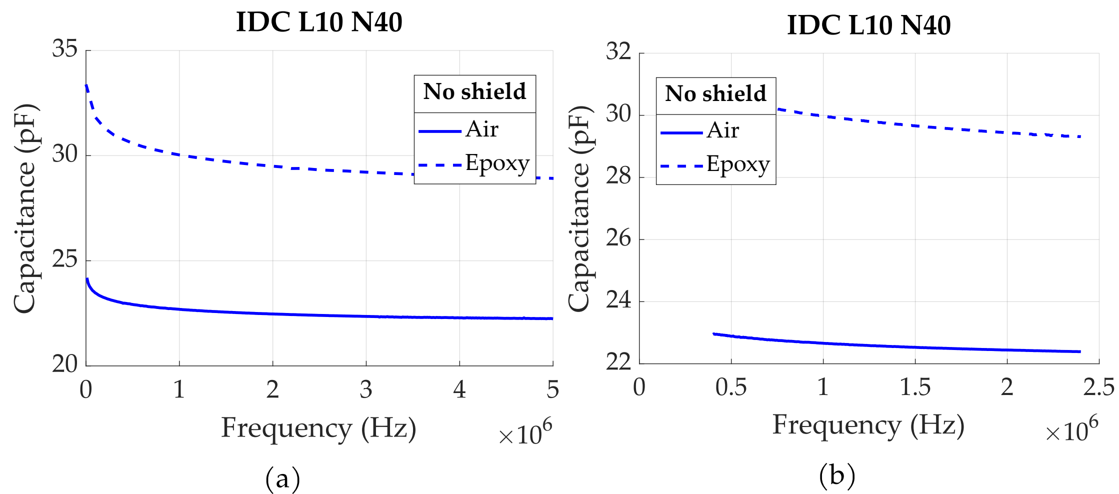

Figure 6.14: Frequency dependency of IDC capacitance for L10 N40 specimen without shield. a) Overview; b) Zoom.

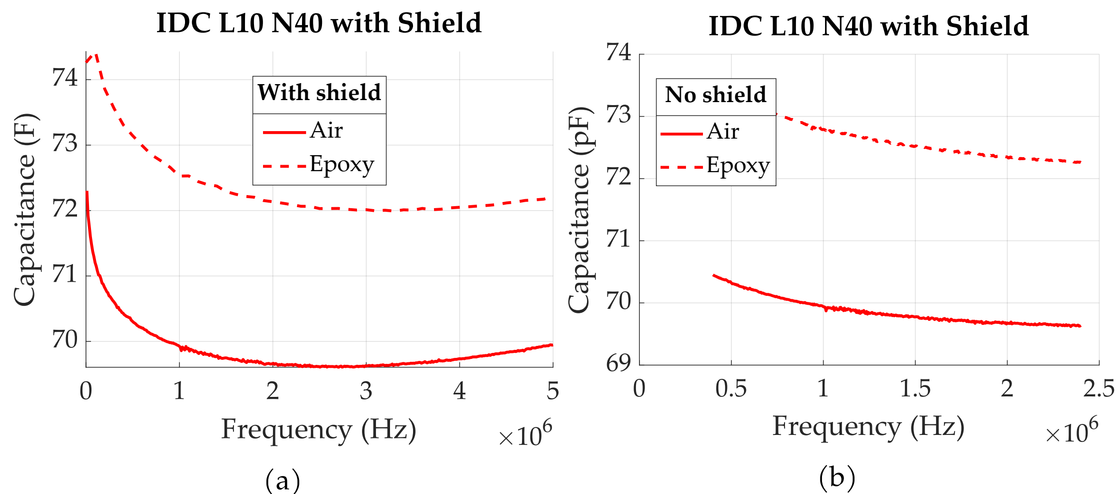

Figure 6.15: Frequency dependency of IDC capacitance for L10 N40 specimen with shield. a) Overview; b) Zoom.

6.2.4 Qualification of Measurement Circuitry

In order to investigate accuracy of the circuit designed for capacitance measurement, two experiments were done with the circuit prototype, examining excitation frequency and capacitance measurement precision. Initially, to verify baseline excitation frequency of the circuit design, output spectrum of the capacitance measurement pins was recorded, the resulting peaks indicating resonance frequency of the LC tank (see Section 2.4.8 for details on measurement principle). The resulting spectrum is displayed in Figure 6.16. Resonance of the prototypical circuit is found at 1.44 MHz, deviating approximately 85 kHz from the calculated value of 1.525 MHz for nominal L_{res} and C_{res}. This deviation is possibly due to fabrication tolerances of the components used, and oscilloscope and probe input capacitance. Generally speaking, these results confirm prior LC tank calculation, and allow for a more precise comparison of the protoype and reference at a defined excitation frequency. Depending on fabrication tolerances of the components and parasitic elements (i. e. connections, wires, etc.), actual sensor tag resonance frequency is expected to slightly differ from the data measured in this experiment, thereby influencing the absolute baseline capacitance. As this results in a systematic capacitance offset, this deviation can simply be compensated for by in place calibration, i. e. measurement of the base capacitance and subsequent subtraction.

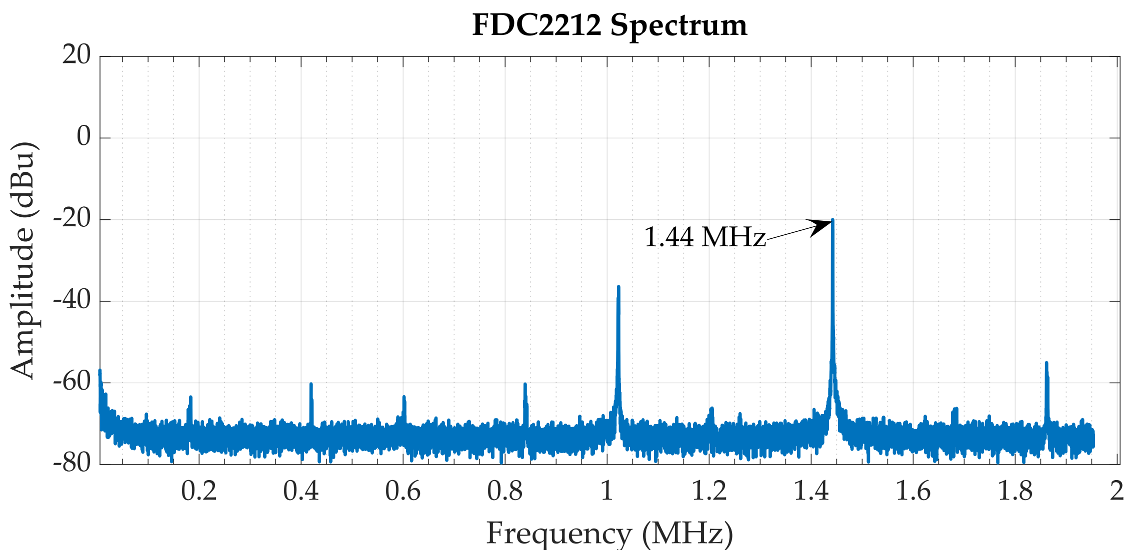

Figure 6.16: Spectrum of resulting resonant circuit with FDC2212 and resulting resonance frequency for verification of tag measurement circuit and concept. Measurement done with PicoScope© 2206B MSO.

Subsequently, comparative measurements were conducted with the circuit prototype and the IA. To this end, several capacitors of fixed size were measured with both setups, the IA serving as a reference. With the exact resonance frequency of the prototype known, measured capacitance values can then be compared with the reference data, i. e. the data measured with the IA. Nominal capacitance values

of 5 pF to 10.3 nF were used, to investigate measurement range of the FDC. For capacitances larger than this, FDC measurement returns an error, marking this as the upper limit of the LC configuration investigated. To provide an adequate data basis, a total of at least 250 samples were recorded for the prototype, allowing for statistical evaluation, e. g. calculation of standard deviation. Prior to the measurements, open and short compensation of the IA was done according to manual, and parasistic capacitance of the prototype was offset corrected.

Results are given in Figure 6.17. Generally speaking, measurement data of the FDC correlates well with the reference, considering the respective measurement range, with absolute deviation increasing with capacitance. To make results more comparable for the large differences between the different capacitor sizes, relative difference between FDC and IA values have been given in Figure 6.17. Maximum relative difference between the two systems is found to be −2.6 % for the capacitor with a nominal value of 220 pF. In the lower capacitance range, which is more relevant for the measurements done in this work, both absolute and relative difference are much smaller, resulting in a maximum deviation of 0.1 pF. Regarding the FDC measurements on their own, a maximum standard deviation of ±9.3 pF can be found for the largest capacitor measured, while standard deviation for the lower values is about ±0.2 pF.

With the experiments presented here, it can therefore be found that the system is sufficiently accurate for the intended purpose, and that its measurement range is more than wide enough. As base capacitance will likely vary to some degree anyway, depending on tag position and material present in immediate IDC proximity, differential interpretation or in-place calibration of sensor tag data is likely necessary. For more precise measurements, choice of the resonant circuit elements could be adjusted, though this probably requires higher reference clocks (see [58] for details on FDC configuration).

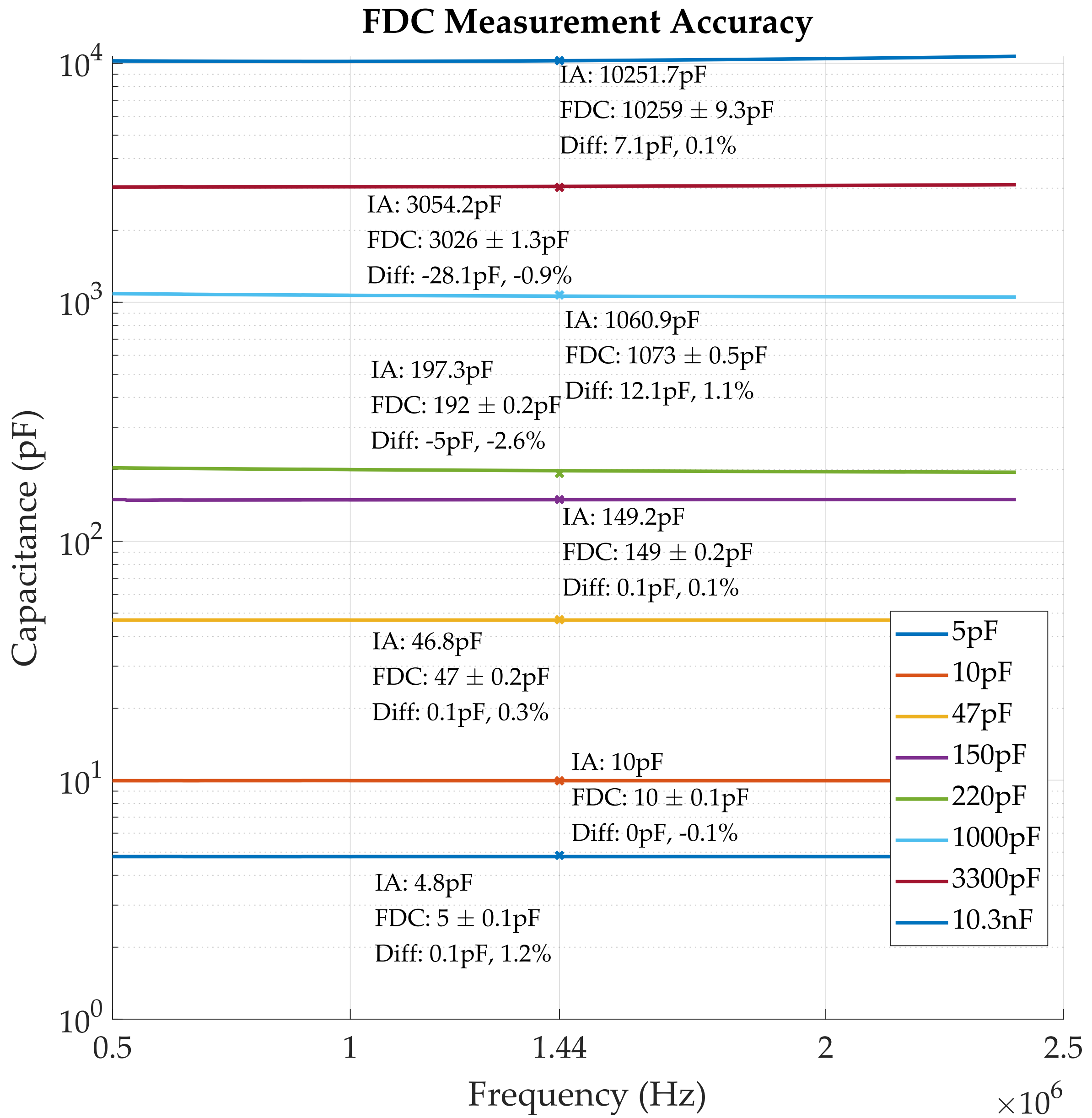

Figure 6.17: Capacitance measurements conducted with FDC2212 and impedance analyzer for qualification of tag circuitry and measurement range. Measurement difference and standard deviation indicated for different capacitors measured.

6.2.5 Substrate Dependency and Reproducibility

After verifying correct and precise function of the prototypical measurement setup as described in Section 6.2.4, dependency of IDC capacitance on background, i. e. substrate material is briefly examined, to see how much placement of the IDCs on different substrates affects measured capacitance, to provide basis for subsequent experimental setups. To this end, five IDCs both with and without shield were first measured without substrate, i. e. in air, and subsequently on a GFRP board (see Figure 6.18). Simultaneously, this setup of five sensors each can be used to estimate reproducibility of IDC capacitance if fabricated with conventional PCB processes. To mount the IDCs on the GFRP, a thin layer of epoxy glue was used and the specimens were clamped firmly until the glue was fully cured. Capacitance of each IDC was measured 40 times to acquire a sufficient number of samples for averaging and calculation of standard deviation.

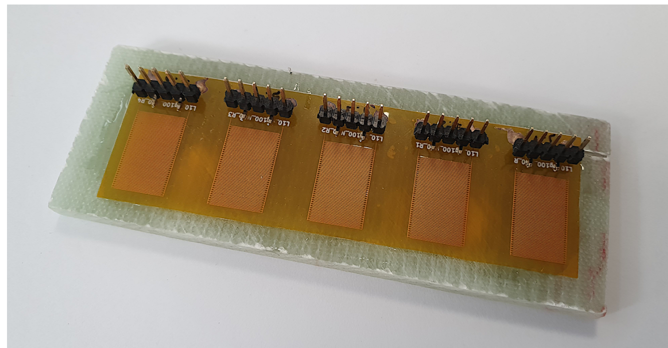

Figure 6.18: IDC prototypes mounted on GFRP via epoxy glue, for substrate dependency measurements and reproducibility assessment.

Results Figures 6.19a and 6.19b show the capacitance values for the five specimens each. Average IDC capacitance fluctuates in between specimens, reading an average of approximately 20 pF for the unshielded IDCs in air, and 22.8 pF for the unshielded IDCs on FRP. The shielded versions exhibit an average capacitance of approximately 66.5 pF, both in air and on FRP. Comparing results, it can be found that, as expected, the unshielded IDCs show a distinct dependency on substrate material, while the shielded versions do not. This confirms the effect on sensitivity relocation mentioned in literature (see Section 2.4.6), predicting a displacement of the electrical field lines due to and away from the shield. Depending on application, this can be used to make the sensor insensitive from the material it is mounted on.

Regarding reproducibility, it can be found that IDC capacitance in between unshielded specimens varies slightly, the maximum difference being ca. 0.6 pF. For the shielded version, absolute deviation in between specimens is higher, where a maximum difference of ca. 3.5 pF can be found. Relative to the overall higher capacitance, significance of this difference of course reduces. Also, as the specimens

were connected via wired pin headers, differences in overall capacitance can also be influenced by varying parasitic elements in the contacts and connections. Overall significance of these findings on reproducibility is therefore limited. Nonetheless, results show a sufficient reproducibility in context of the application on the sensor tag.

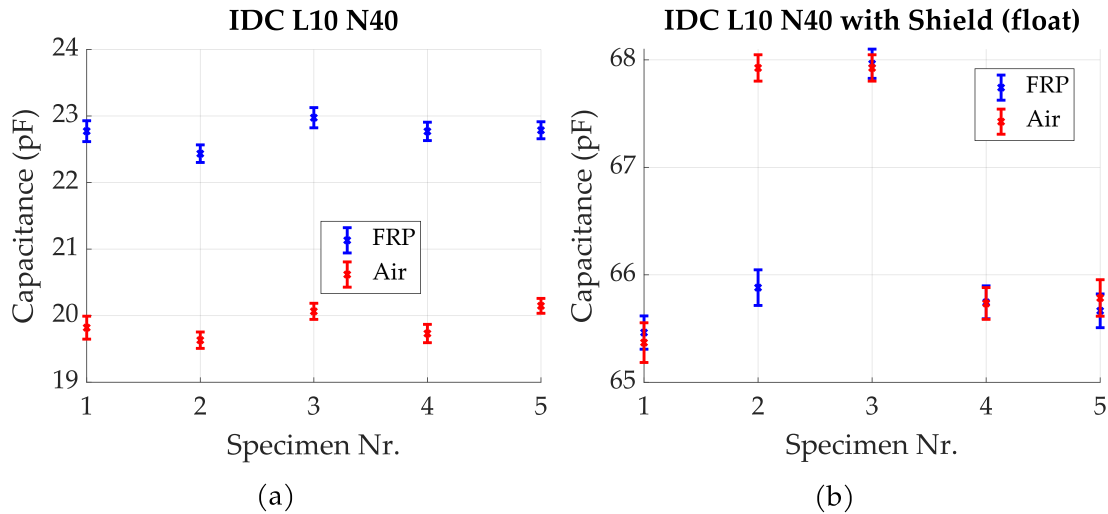

Figure 6.19: IDC substrate dependency comparison with/without shield, standard deviation indicated by error bars. a) without shield; b) with shield, floating.

6.2.6 Capacitance for different IDC sizes

To investigate the actual capacitances occuring for the IDC structures fabricated on FPCBs, IDCs of different finger length L and finger number N were fabricated. The resulting sensors are displayed in Figure 6.20. Due to the size constraints posed by the application, maximum sensor size is limited, especially for the XY-configuration as described in Section 6.2.1. For that reason, L was varied from 5 to 10 mm, while N was increased in steps of 20, for an interval of 20 to 60 fingers (per electrode).

Capacitance was measured 40 times for each specimen, giving a sufficient number of samples for averaging. Prior to the experiments, the sensors were cleaned with isopropanol, to avoid influence of any material possibly present on sensor surface. For the shielded IDCs, shield potential was varied to examine the resulting effect. First, the shield potential was left floating by leaving open the respective pin. Secondly, both GND and U_0 were connected to the shield via the pins mounted on the breakout fixture for that purpose (see Figure 6.9).

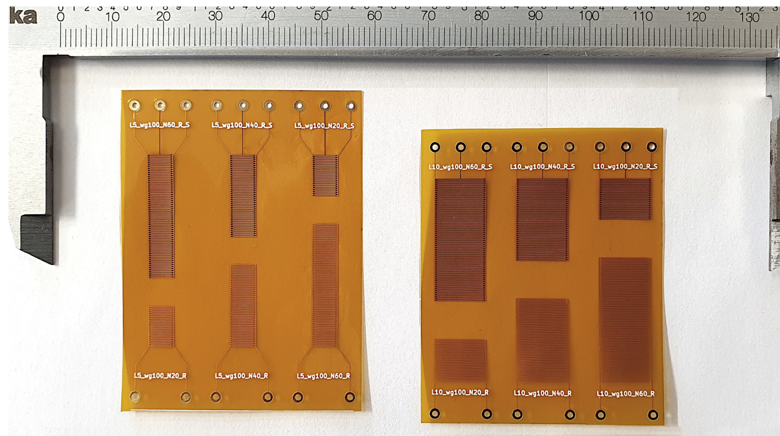

Figure 6.20: Different IDC geometries fabricated for preliminary experiments on C size, caliper displayed for reference.

Results Measurement results are displayed in Figures 6.21a-6.21d. The diagrams show a linear dependency of capacitance and finger number N for given finger length L, as observed in publications like e. g. [50], and predicted by the analytical models employed in Section 6.1. This correlation is also true for capacitance and finger length for a given N. Also, shield presence very much increases overall capacitance, resulting in about 3.5 times higher capacitance for a floating shield in comparison to the unshielded versions. In [52], a comparable increase of ca. 380 % was observed for a shielded IDC with the shield connected to one of the electrodes. Capacitance again increases for either ground or supply voltage potential present on the shield, roughly doubling capacitance in comparison to the floating shield state. Significant differences in capacitance in between the two potentials cannot be found. Also, shield presence or shield potential does also not significantly influence standard deviation of the measured data, though a trend towards higher standard deviations could be assumed for the shielded versions with applied potential. Maximum standard deviation for these is 0.19 pF, while it is 0.15 pF for the unshielded variant.

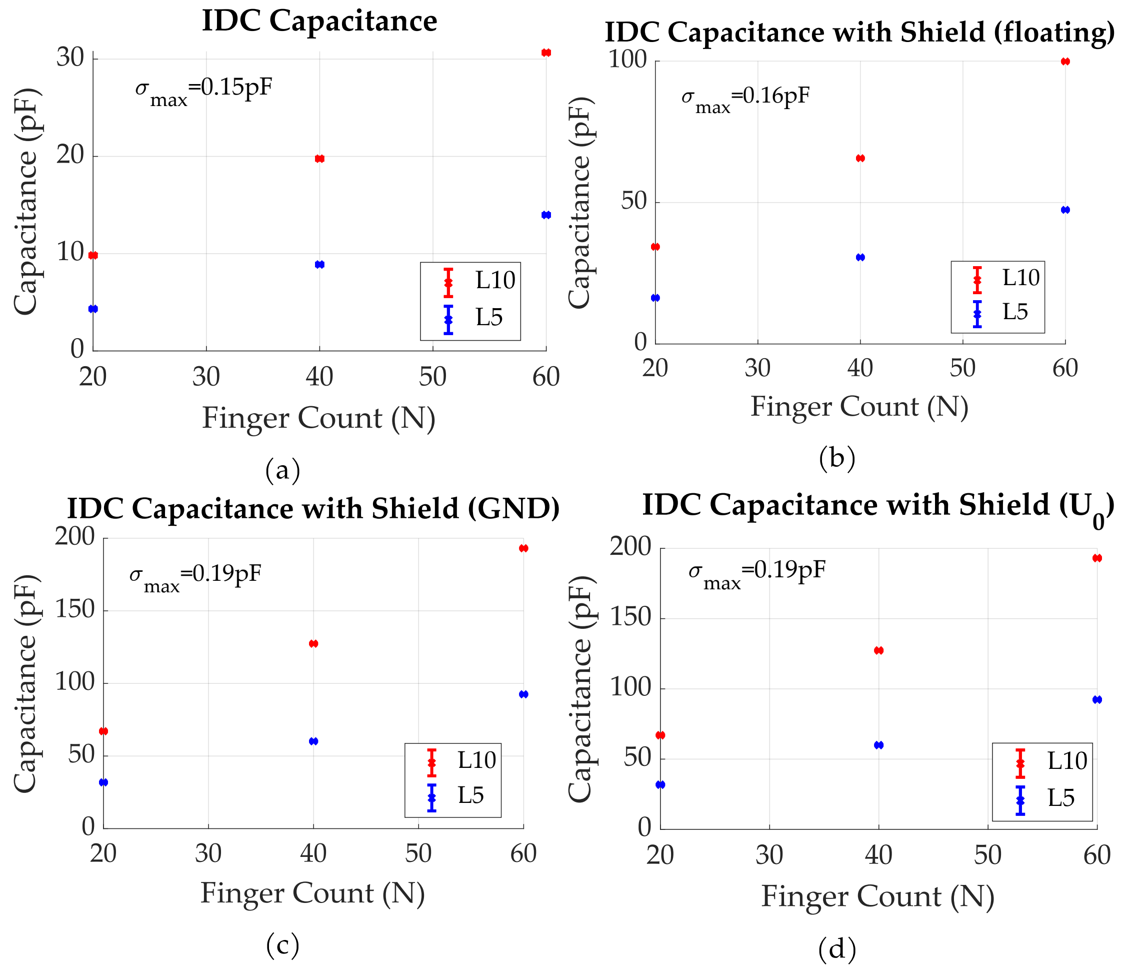

Figure 6.21: Capacitances for different IDC geometries and shield potentials, IDCs suspended in air, maximum standard deviation σ_{max} of each measurement set given for reference. a) no shield present; b) shield present, not connected; c) shield connected to ground; d) shield connected to U_0.

To summarize the measurements on IDC capacitance size and investigate contribution of a shielded back plane, results are numerically summarized in Table 6.1. For easier comparison, capacitance values normalized to finger count and length are calculated for the different cases, and normalized mean contribution to capacitance is given (bold font weight).

Table 6.1: Measured results of IDC capacitance sizes for different designs and shield potentials. Measured with IDC floating in air, $f_{osc} \approx 1.44$ MHz

L	5 mm			10 mm		
N	20	40	60	20	40	60
	C (pF)					
No shield	4.32	8.89	13.98	9.83	19.76	30.67
Shield	16.31	30.64	47.42	34.36	65.67	99.90
Shield GND	31.87	60.17	92.52	67.09	127.40	193.09
Shield U0	31.79	59.97	92.34	67.00	127.35	193.11
	C/Finger (pF)					
No shield	0.216	0.222	0.233	0.492	0.494	0.511
Shield	0.816	0.766	0.790	1.718	1.642	1.665
Shield GND	1.594	1.504	1.542	3.355	3.185	3.218
Shield U0	1.590	1.499	1.539	3.350	3.184	3.219
	Mean C/Finger (pF)					
No shield	0.224			0.499		
Shield	0.791			1.675		
Shield GND	1.547			3.253		
Shield U0	1.543			3.251		
	C/(Finger · Length) (pF)					
No shield	0.043	0.044	0.047	0.049	0.049	0.051
Shield	0.163	0.153	0.158	0.172	0.164	0.167
Shield GND	0.319	0.301	0.308	0.335	0.319	0.322
Shield U0	0.318	0.300	0.308	0.335	0.318	0.322
	Mean C/(Finger · Length), (pF)					
No shield	**0.047**					
Shield	**0.163**					
Shield GND	**0.317**					
Shield U0	**0.317**					

Comparison with Calculated Capacitances These preliminary measurements were done with the IDCs suspended in air, for reasons of simplicity. For comparison with calculated results, different permittivity values need to be taken into account. As relative permittivity of the surrounding material contributes as a simple factor to IDC capacitance, multiplication of the measured values with $\epsilon_{Epoxy} = 3.5$ initially seems to be a good approximation. In fact, this is not directly

applicable, though – for the measurements conducted with the prototypical IDCs, the metal structure of the electrodes is not only surrounded by air, as would be the case for a calculation with a relative permittivity of $\epsilon_{air} \approx 1$, but encapsulated in a polyimide film of ca. 13 µm thickness, that is in turn glued to the metal structures with ca. 12 µm of epoxy based glue (see Figure 6.12). On the lower side of the metal structure, an additional polyimide layer is present, i. e. the FPCB substrate, measuring a thickness of ca. 25 µm. The measurement results are therefore not directly comparable to the calculated data. In comparison to air, relative permittivity of polyimide and epoxy is significantly higher (ca. 3.4 and 3.5). As polyimide and glue thickness (averaged ca. 37.5 µm per side) relative to penetration depth of the electric field (ca. $\lambda/2 = 200\,\mu\text{m}$) is significant, this will increase capacitance of the real IDC in comparison to a theoretical IDC suspended in air. For reasons of simplicity, differences in permittivity of glue and polyimide are assumed to be negligible. Assuming a linear relation as an approximate extrapolation, which relates average polyimide and glue thickness per side, and penetration depth to the respective relative permittivities, e. g.

$$C_{epoxy} \approx C_{real}\, 2 \left(\frac{h_{polyimide}}{\lambda/2} \frac{\epsilon_{polyimide}}{\epsilon_{air}} \right) = C_{real}\, 2 \frac{37.5\,\mu\text{m}}{200\,\mu\text{m}} \frac{3.4}{1} = 1.275\, C_{real}, \quad (6.19)$$

it can be found that extrapolated measurement results (i. e. $C_{real} \cdot 1.275$) correlate well with the calculated data. Table 6.2 compares measured data with the data calculated via the different approaches presented in Section 6.1. The extrapolated data matches best with the values predicted by the equations published by Igreja et. al. [51]. For easier interpretation, the results have also been visualized in Figure 6.22.

For actual measurement results of IDC prototypes surrounded by epoxy, see Section 6.2.7. Comparing the capacitance value measured for the L10 N40 version, which corresponds to the second row, it can be found that measured capacitance (29.41 pF) is slightly higher for the actual experiment than the extrapolated data, but still in the general range predicted by the analytical estimations. A graphical comparison of calculated and measured capacitances is given in Figure 6.27

Table 6.2: Comparison of measured C_{real}, extrapolated C_{epoxy} and calculated capacitances, for L=10 mm, in pF. Extrapolated data according to Equation 6.19.

N_{abs}	C_{real}	C_{epoxy}	Igreja et.al.	Mukhopadhyay et.al.	Endres et.al.
40	9.8	12.5	12.3	13.6	19.2
80	19.8	25.2	24.7	27.5	38.9
120	30.7	39.1	37.1	41.4	58.6

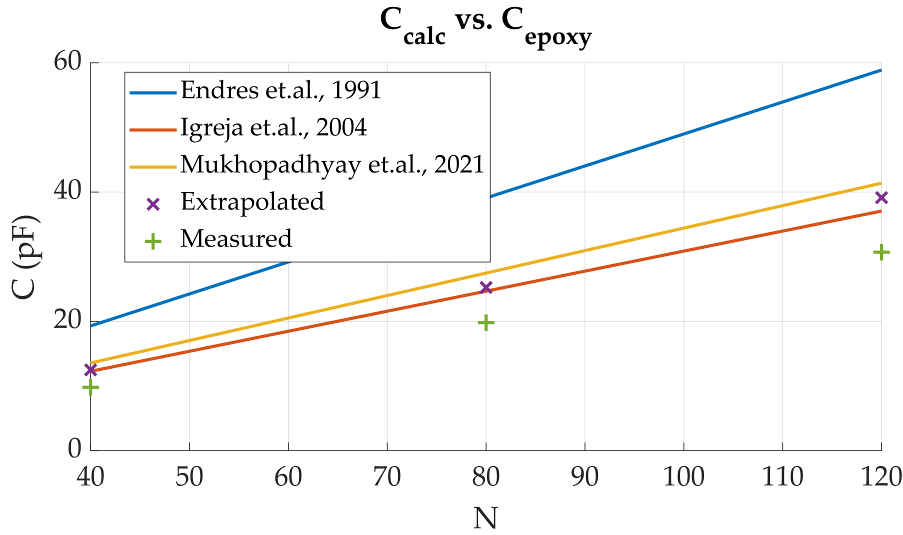

Figure 6.22: Comparison of measured C_{real}, extrapolated C_{epoxy} and calculated capacitances, for L=10 mm. Extrapolated data according to Equation 6.19. Calculations according to Endres et. al. [125], Igreja et. al. [51] and Mukhopadhyay et. al. [126]

6.2.7 Epoxy Cure Measurements

To investigate IDC capacitance behavior for monitoring of polymer cure, several experiments were conducted with IDC prototypes and two-component epoxy glue[2]. Two IDCs were measured in parallel, as shown in Figure 6.23 to investigate behavior of the same sensor type with and without shielded back plane. IDCs of both finger lengths (5 and 10 mm) were examined to see how capacitance changes during resin arrival and cure. The IDCs were connected to the circuit prototype via wires and held in position with two grippers. For resin coverage, the sensors were submerged in a small plastic cup each, that had been previously filled with fluid resin. To completely envelope the sensors, more resin was added on top of the sensors. The two resin components were thoroughly mixed just before, according to the manual provided by the manufacturer [128]. Data was continuously recorded for 24 hours after IDC coverage.

Results Measurement results for the curing experiments are displayed in Figures 6.24-6.26. Capacitance changes both with IDC coverage and cure progress, which are marked by several distinct events visible in sensor capacitance over time. Initially, submerging the IDC in resin yields a sharp increase in capacitance, which can be attributed to the changing permittivity of the dielectric surrounding the electrodes, with resin having a much higher permittivity than air.

After covering the IDC, capacitance increases slightly for approximately 4-5 minutes. This could be observed for all specimens and can probably be attributed

[2] UHU Plus Schnellfest, [128]

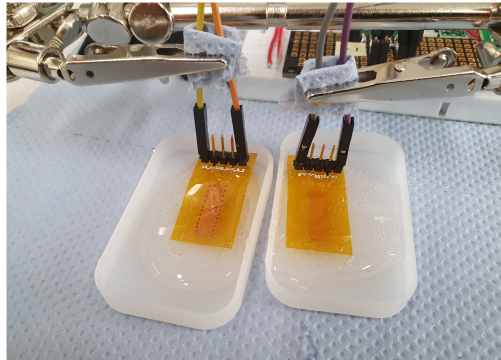

Figure 6.23: Setup for preliminary cure measurement experiments. IDCs submerged in UHU epoxy glue.

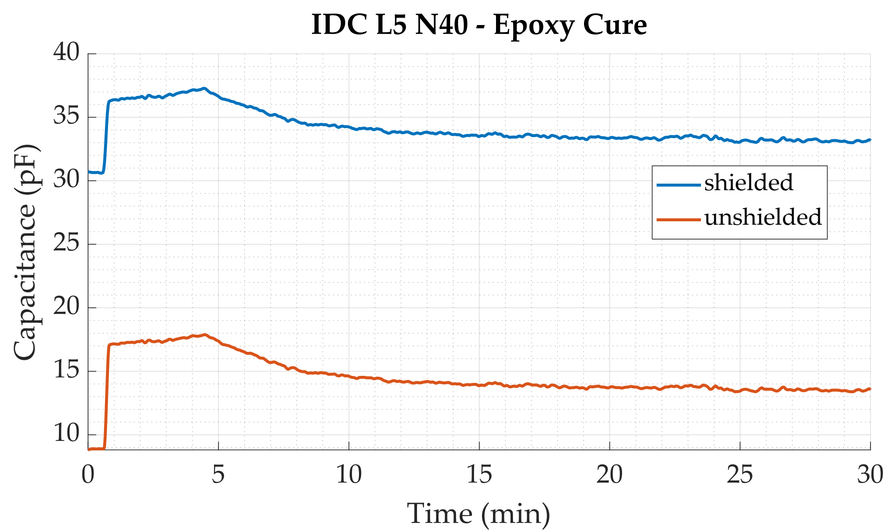

Figure 6.24: Capacitance for coverage and first period of cure for shielded and unshielded L5 N40 IDCs. Filtered with moving average filter, window size=50.

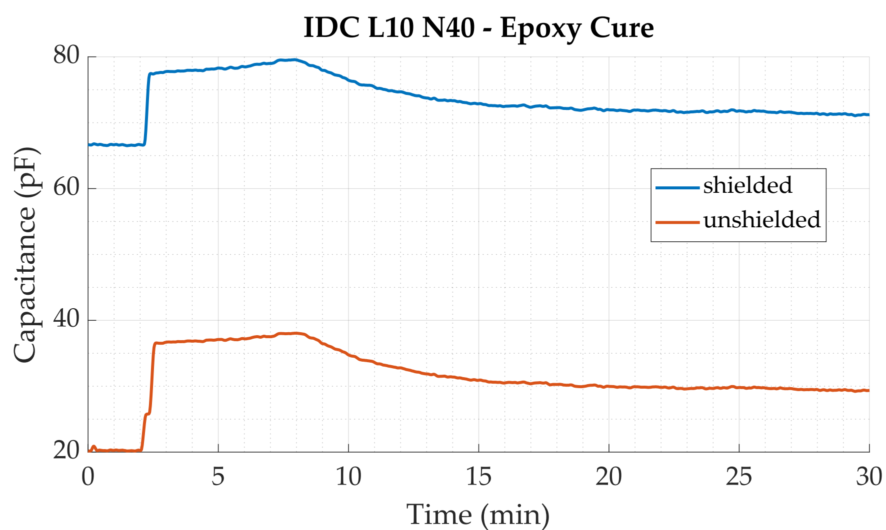

Figure 6.25: Capacitance for coverage and first period of cure for shielded and unshielded L10 N40 IDCs. Filtered with moving average filter, window size=50.

to a slight increase in resin temperature, as epoxy cure reactions are exothermic.[3] As the dielectric constant of polyimide slightly rises with temperature [129], this might contribute to the rising capacitance. Considering the data sheet of the glue, this observation can also be correlated to the pot life time, i. e. the time span after mixing, during which the glue is still sufficiently fluid to be applied to the intended place. The end of this time span is marked by a distinct local capacitance maximum after which capacitance distinctly starts decreasing, resulting in a difference of ca. 8 pF for both versions of the L10 N40 IDC, and ca. 4 pF for both versions of the L5 N40 IDC. From this point on, no significant capacitance change can be observed after about 20 min of cure. This correlates to the information given by the manufacturer, which claims that at this point, the glue is sufficiently cured for touching, i. e. tangible. As claimed by the manufacturer, the glue is completely cured after 12 hours.

Comparing IDC capacitance after 12 hours with that after 20 min, this can be confirmed, as capacitance in this period decreases slightly, but not in the same magnitude as during the first 20 minutes, yielding a maximum absolute difference of −1.8 pF for the shielded L10 N40 layout. Further discussion of measurement data is done later on in this section.

Additionally to the four experiments with unshielded and floating-shield IDCs, another experiment was conducted to investigate the effect of the shield being connected to a fixed potential. During the measurements presented in Section 6.2.6, it could be found that the effect is the same for both high (U_0) or low potential (GND). Consequently, this experiment was only conducted for the grounded case. The corresponding measurement data is shown in Figure 6.26.

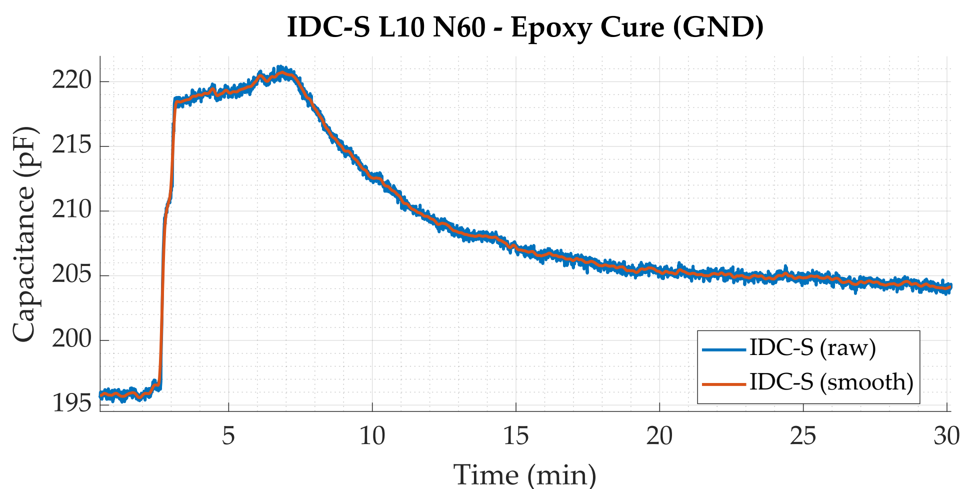

Figure 6.26: Capacitance for coverage and first period of epoxy curing for L10 N60 IDC with shield connected to GND. Smoothed curve filtered with moving average filter, window size 50.

[3]This could later be confirmed during experiments with the capacitive sensor tag, see Section 7.3.2.

Similar to the results of Section 6.2.6, baseline capacitance is much higher for the shield connected to ground, as compared to that of the IDCs with shield floating. Also, due to the higher number of electrodes, capacitance of the N60 version is of course generally higher than that of the N40 version. Apart from this, the general shape of the curve matches those of the other IDCs tested in this section. Resin coverage yields a sharp increase of capacitance, followed by a slightly rising capacitance until approximately minute seven, after which capacitance starts decreasing rapidly, similar to an exponential decrease. Correspondingly, capacitance approaches a constant value, roughly after 23 minutes following curing start, which is indicated by the local capacitance maximum.

Summary Epoxy Cure To summarize the results and conclude if either finger length, shield presence, or shield potential have a significant impact on sensor sensitivity, which is the most important aspect for the intended application, normalized capacitance values (ΔC_{snorm}) have been calculated for the relevant events, relating capacitance change (ΔC) in between events to finger length L and finger number N. This relation is given by

$$\Delta C_{norm} = \frac{\Delta C}{LN}. \tag{6.20}$$

The resulting values and measurement data of the relevant events are given in Table 6.3, which in turn summarizes the relevant findings of the curing experiments. Covering the IDC yields the strongest change in normalized capacitance, resulting in values from 0.027 pF/mm up to 0.041 pF/mm per finger. The highest sensitivity for this aspect is observed for the unshielded IDCs, which show about 50 % higher capacitance change than the IDCs with floating shield. In between these, the IDC with grounded shield shows about 0.037 pF/mm capacitance change per finger. This major difference in sensitivity may be explained by the shield covering about half the sensitive area, i. e. the back side, of the electrode structure, preventing the resin from locally affecting permittivity of the dielectric present. Sensitivity of the shielded versions is not halved though, so it could possibly be concluded that shield presence indeed shapes the electric field in a way that e. g. penetration depth of the field is increased in the other direction. Summarizing the findings for the first phase, i. e. the infusion process, the unshielded IDCs show a distinct advantage in sensitivity.

For the next phase, until reaching the local capacitance maximum, sensitivity of the different sensors does not differ significantly, resulting in about 0.004 pF/mm normalized capacitance change. With curing start, capacitance decreases significantly. An average of -0.021 pF/mm normalized capacitance change can be found for the N40 sensors, regardless of shield presence, with sensitivity of the grounded N60 IDC-S being slightly higher (-0.028 pF/mm). Generally speaking, it can thus be concluded that sensitivity for capacitance change during cure does not differ significantly in between the specimens examined. In this regard, (floating) shield

presence in general therefore does not seem to have a major effect on sensitivity for cure monitoring, with a grounded shield potentially providing a slightly higher sensitivity.

For the last phase, i. e. the time following the 20 min mark, capacitance changes are of much smaller magnitude, significance is therefore limited due to the small number of specimens. It can though still be found that a general trend towards decreasing capacitance is still measurable, indicating that material properties still change a little bit during the last phase of curing. Using the duration given by the data sheet and the experimental data, evaluation of curing status in an application context could be possible. For example, a simple approach could be to continuously calculate local, i. e. current slope of the (smoothed) capacitance curve, comparing it with a pre-defined threshold slope value previously associated with a certain cure status or viscosity. As soon as the current slope is below the threshold for a specified time, the pre-defined cure status would be reached, e. g. indicating heating shut-down.

Comparison with Calculations In order to compare the measured capacitances with the values initially calculated with the different approaches, as described in Section 6.1, the corresponding results are illustrated in Figure 6.27. It can be seen that the measured values are in very good agreement with the calculated ones, with the predictions of Mukhopadhyay et.al. and Igreja et.al. matching better than those of Endres et.al.

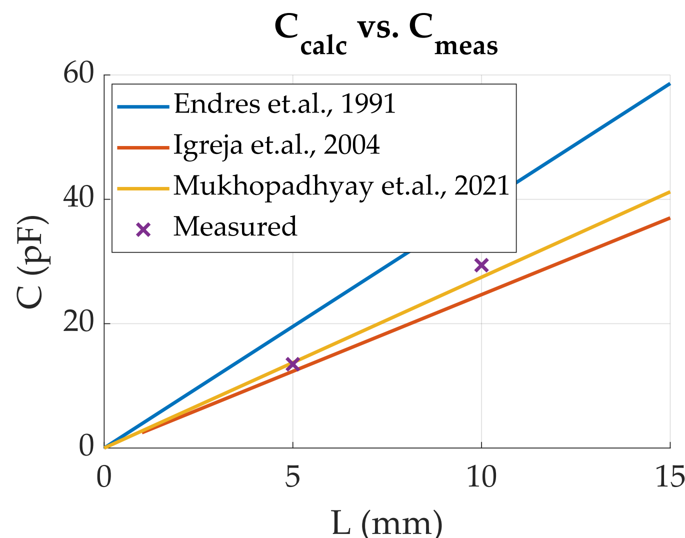

Figure 6.27: Comparison of calculated capacitances (see Section 6.1) and averaged values for measured IDCs surrounded by cured epoxy ($N_{abs} = 80, w = g = 0.1\,\text{mm}$). Calculations according to Endres et. al. [125], Igreja et. al. [51] and Mukhopadhyay et. al. [126].

Table 6.3: Capacitances and capacitance changes relative to prior event for different IDCs and relevant events during curing tests. Changes normalized to finger length and number according to Equation 6.20 given for better comparison.

	Start	**Covered**	**Peak**	**20 min**	**12 h**
No shield, L5 N40					
C (pF)	8.90	17.1	17.9	13.5	13.2
ΔC (pF)	-	8.2	0.8	-4.4	-0.3
ΔC (%)	-	92 %	5 %	-25 %	-2 %
$\Delta\ C_{norm}$ (pF/mm)	-	**0.041**	0.004	**-0.022**	-0.001
Shield, L5 N40					
C (pF)	30.6	36.3	37.3	33.2	32.6
ΔC (pF)	-	5.7	1.0	-4.1	-0.6
ΔC (%)	-	19 %	3 %	-11 %	-2 %
ΔC_{norm} (pF/mm)	-	**0.028**	0.005	**-0.020**	-0.003
No shield, L10 N40					
C (pF)	20.2	36.5	38.0	29.4	28.7
ΔC (pF)	-	16.3	1.5	-8.6	-0.7
ΔC (%)	-	81 %	4 %	-23 %	-2 %
ΔC_{norm} (pF/mm)	-	**0.041**	0.004	**-0.021**	-0.002
Shield, L10 N40					
C (pF)	66.6	77.4	79.6	71.4	69.6
ΔC (pF)	-	10.8	2.2	-8.2	-1.8
ΔC (%)	-	16 %	3 %	-10 %	-3 %
ΔC_{norm} (pF/mm)	-	**0.027**	0.005	**-0.020**	-0.005
Shield GND, L10 N60					
C (pF)	196.2	218.4	221.0	204.5	198.2
ΔC (pF)	-	22.2	2.6	-16.5	-6.3
ΔC (%)	-	11 %	1 %	-7 %	-3 %
ΔC_{norm} (pF/mm)	-	**0.037**	0.004	**-0.028**	-0.011

Noise Level As sensitivity is not the only important property of a usable sensor, another aspect is briefly considered here, which is system noise. To examine if a different noise level exists for the different IDC types, the local difference of the raw signal to the smoothed data (i. e. the one filtered with a moving average) was calculated. This way, the local difference C_{diff} between raw capacitance values (C) and the (smoothed) values calculated using local linear regression (C_{mean}) is made comparable by eliminating the different base capacitances caused by shield presence and differing finger length. To remove influence of the experiments not exactly starting at the very same point in time, minutes 30 to 60 were used.

Looking at the results plotted in Figure 6.28, it can be found that noise level does not show any significant difference for the measurements of the two different finger lengths. Shield presence does also not very much influence noise level if the shield is left floating, though a slight increase of 0.1-0.2 pF is observed for the data recorded with the floating shield. Contrary to initial expectation, for the shield connected to ground though (data fo L10 N60 in Figure 6.28), noise level actually seems to increase, as indicated by the broader distribution of values for C_{diff} around zero and a distinct increase in standard deviation. This more than doubles, resulting in 0.33 pF. This increase might be explained by the comparably large area of metal acting as an antenna for radiated electromagnetic interference.

These calculations of course only reflect the absolute noise level. Considering that both absolute and normalized capacitance change are different for the different IDC geometries, the relative influence of noise on measurement signal is consequently different. Based on the acquired data for the specimens examined, the unshielded IDC variant with 10 mm finger length therefore seems to be the one most usable, as it showed the overall best sensitivity values per area. Generalizing this for usage on the sensor tag, the experiments suggest usage of an unshielded IDC with high finger length for infusion and cure monitoring, as this exhibits the best combination of sensitivity values and noise level.

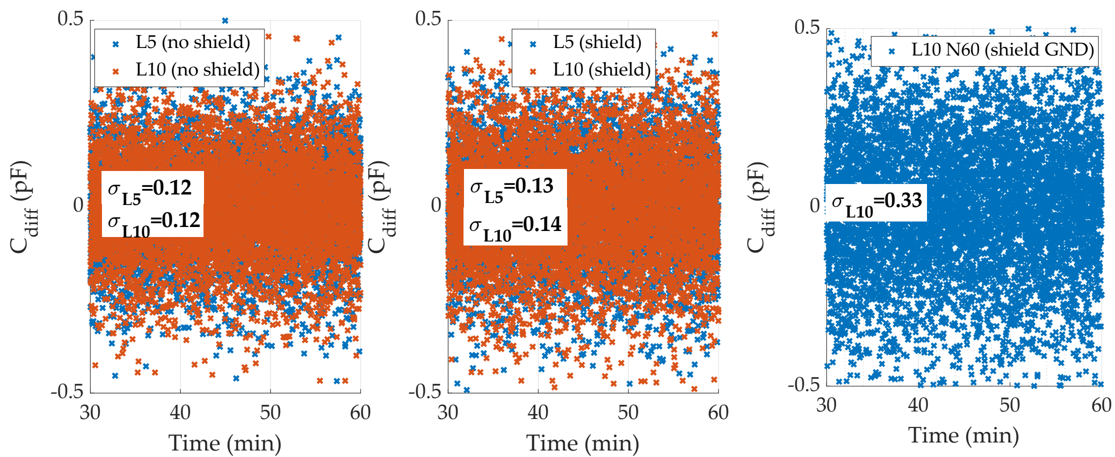

Figure 6.28: Difference of capacitance values to locally averaged capacitance for the four IDC prototypes used, standard deviation indicated.

6.2.8 Temperature Dependency

In order to investigate cross sensitivities of sensor capacitance to temperature, this relation was tested with two IDCs that had previously been integrated into an epoxy matrix (see Section 6.2.7). This dependency is especially relevant for usage of IDCs for measurement of mechanical strain, as strain induced capacitance changes are relatively small. Two sensors with a finger length of $L = 10$ mm and a finger number of $N = 40$ fingers per electrode were used, one without shield and one with a shielded backside, connected to ground. For temperature control, the sensor integrated samples were put into a climate chamber and slowly heated from 20 °C to 75 °C. For comparison, a Pt-100 reference sensor was mounted to the specimen with heat-resistant adhesive tape, to measure the actual specimen temperature. Before experiment start, the chamber was set to 20 °C until temperature of the samples had stabilized. Temperature was then slowly increased with a slope of ca. 0.46 °C / min to allow for uniform heating of the samples and an accurate reference reading in regard to the inner sample temperature. Capacitance and temperature were measured throughout the experiment.

Results Experiment results are displayed in Figures 6.29 and 6.30. With increasing temperature, IDC capacitance rises, and a linear correlation can be estimated for the temperature interval examined. From 20 °C to 75 °C, capacitance of the unshielded IDC rises about 7 pF, capacitance of the shielded IDC increases about 9 pF. An approximately linear nature of the relation in this interval is confirmed by fitting a linear curve to the data. For the unshielded IDC, the fit shows a slope of $m = 0.143$ pF/K, for the shielded IDC a slightly higher slope of 0.172 pF/K was found (see Figure 6.30). Relating this to the initial capacitances, the corresponding temperature coefficients calculate to approximately 5107 ppm/K and 1303 ppm/K. This stark difference in temperature coefficients is of course due to the large differences in base capacitance of the two sensors.

These experimental results confirm findings in [54], who investigated the temperature dependency of a similar, polyimide based IDC prototype for strain measurement. For measurements of a polyimide based IDC in nitrogen, they found a linear correlation between IDC capacitance and temperature, with a temperature coefficient of 2170 ppm/K, for a base capacitance of ca. 47 pF at 20 °C. As temperature dependency of the relative permittivity of epoxy is linearly dependent on temperature [130], the correlation found is likely at least partly due to a changing permittivity of the dielectric in vicinity of the IDC electrodes, in this case epoxy-based glue (UHU Schnellfest, [128]).

Based on this experiment, a small difference of 0.029 pF/K between temperature coefficients of shielded and unshielded IDCs can be found. Due to the singular nature of this experiment and apparent noise, the significance of this result is limited, and further experiments would be necessary to validate this. Regarding

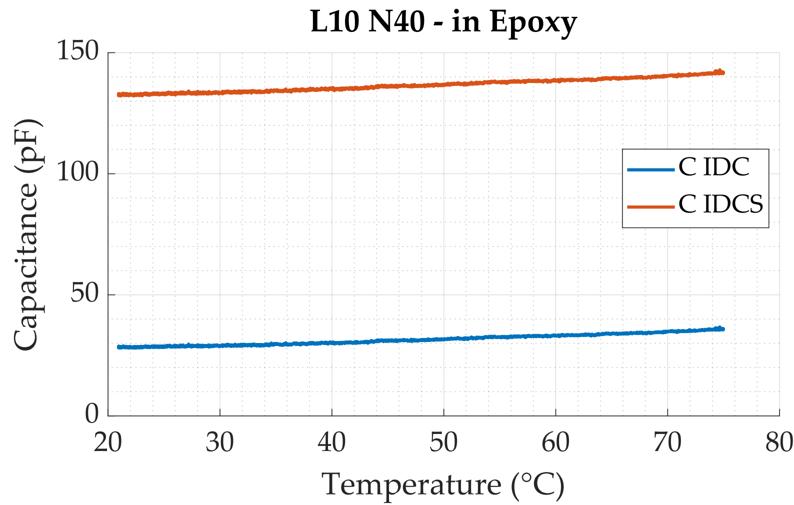

Figure 6.29: Capacitance vs temperature for two IDCs in cured epoxy glue.

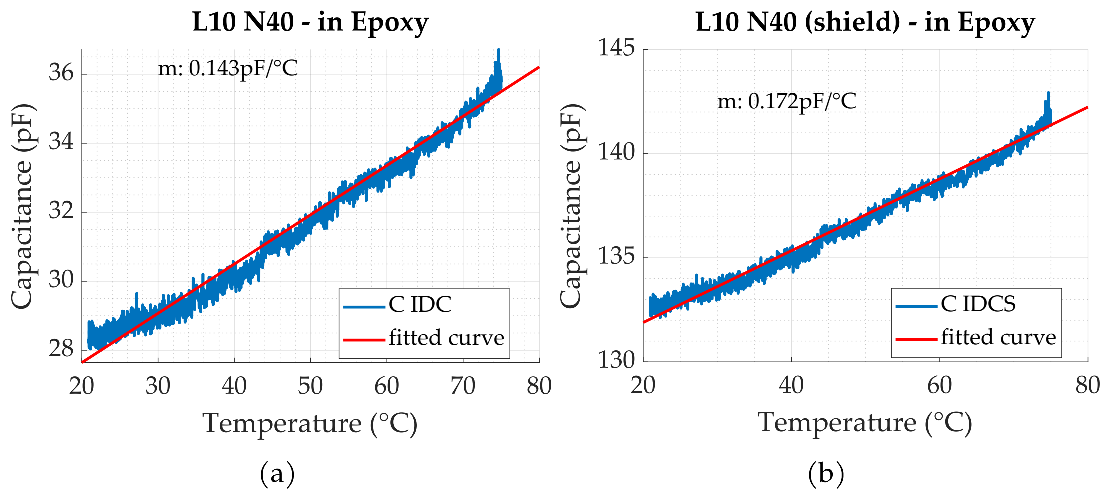

Figure 6.30: IDC capacitance temperature dependency with/without shield in cured epoxy glue and fitted linear curve, slope m of linear fit given for reference. a) IDC without shield; b) IDC with shield, GND.

IDC usage for cure monitoring, temperature cross-sensitivity of IDC capacitance can therefore probably be compensated for to a certain degree.

Considering IDC usage for strain measurement, the results show that temperature does need to be taken into account, as a temperature difference of e. g. 10 °C results in a capacitance difference of more than 1 pF, which is in the range of expected strain induced capacitance change (see Section 6.1 for respective calculations). As the correlation apparently is more or less linear though, temperature induced capacitance change of the IDC could be compensated for, especially for usage on the sensor tag, where local temperature is measured continuously.

6.2.9 XY IDCs

To investigate the possibility of bi-axial strain measurement using the IDCs as capacitive strain gauges, a configuration with perpendicular IDCs was designed, as described in Section 6.2.1, and fabricated for the two finger lengths (5 and 10 mm), both with and without shield. In order to see if this configuration behaves differently from the unidirectional IDCs, the fabricated prototypes were examined in a short experiment. To this end, the sensors were suspended in air, and capacitance of each direction was measured independently via the two channels of the FDC2212. The resulting data was averaged over a sample number of n=40 to provide a more precise result. Measurement data is displayed in Figure 6.31a.

Maximum capacitance difference between the two axes is found to be approximately 0.4 pF for the unshielded and 0.9 pF for the shielded IDCs. This could be due to slightly different sizes of the parasitic elements for the two measurement channels of the measurement circuit, or indeed fabrication-related deviations. In the application context, this is albeit negligible, as it only represents a slightly different baseline that can be compensated for. Comparing capacitance of the combined IDCs for each axis with the values measured for single IDCs of the equivalent number of fingers (N40, see Section 6.2.6), it can be found that no significant difference is measurable within the accuracy of the systems. As the XY configuration is basically only a parallel circuit of two IDCs with half the relative size, this was to be expected. Summarizing the outcome of this experiment, it can be found that overall capacitance baseline of the XY configuration behaves as expected, and that it therefore seems to be usable for the intended purpose, if sufficient strain sensitivity can be found.

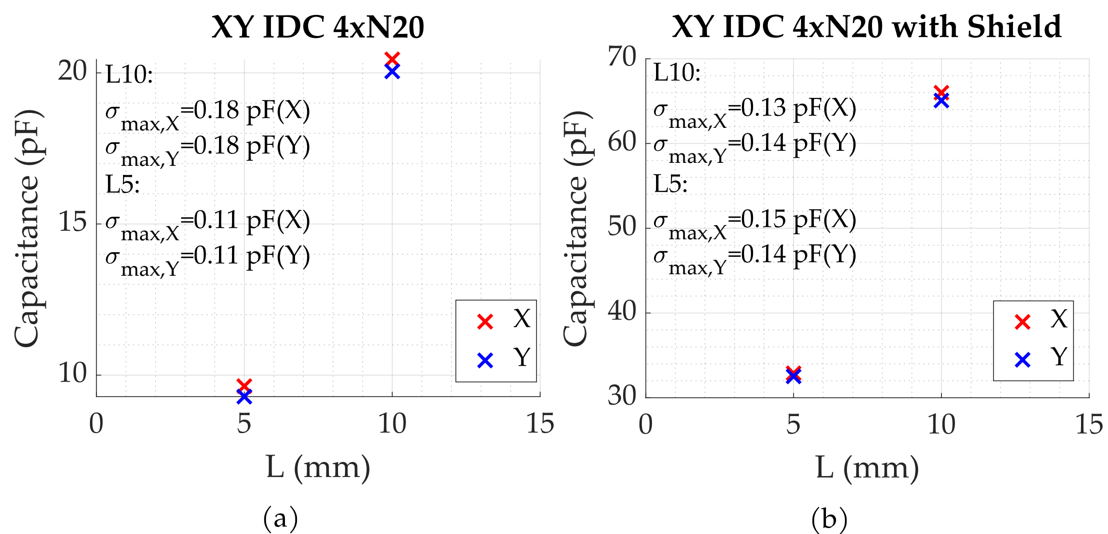

Figure 6.31: Comparison of mean XY IDC capacitances relative to finger length L, n=40. a) without shield b) with shield, floating.

6.2.10 Strain Sensitivity

To investigate usability of the IDC prototypes for strain measurement, i. e. as capacitive strain gauges, several of the fabricated IDC prototypes have been examined in a three point bending test setup.Four IDCs were measured in total, both an unshielded and a shielded version of finger lengths 5 mm and 10 mm. The IDCs were attached in the center of a 5 mm thick polysterene specimen, using strain gauge glue (HBM Z70). To strain the sensors, the specimens were loaded to a maximum of 600 N at a constant deflection speed of 0.05 mm/s, resulting in ca. 2 mm of maximum deflection. For measurement, the IDCs were connected to the protoype measurement circuit via jumper wires of about 50 cm length, the parasitic capacitance of which was offset corrected for in advance. Corresponding strain was calculated from reference data using the formulas presented in Section 2.3.1.

Resulting measurements for the IDCs with $L = 10$ mm are displayed in Figures 6.32 and 6.33. To ease deduction of a general trend, both the raw and smoothed datasets have been plotted. The latter were generated using a moving average filter with a window size of 50. Compared to measurement signal, noise level is found to be high. Relative to the smoothed curve, maximum noise amplitude is around 0.5 pF, similar to the observations during cure measurement. For strain in X direction, a decreasing capacitance of the corresponding IDCs is expected, as finger distance increases. Looking at the data, this cannot be found with any significance, neither for the unshielded nor the shielded version.

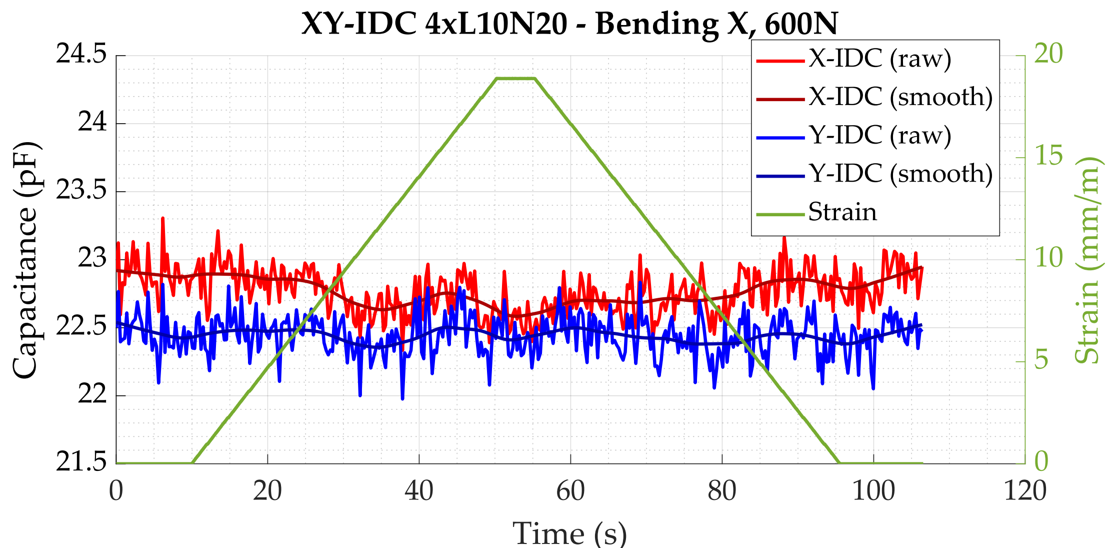

Figure 6.32: Strain sensitivity of (unshielded) XY IDC 4xL10 N20. Capacitance of IDC pair for measurement in X direction and applied strain (green), Y data similar.

Comparing the values for strain-induced capacitance change calculated in Section 6.1, a strain of 20 % should result in approximately 2 pF of capacitance reduction for an unshielded IDC surrounded by cured epoxy. Very roughly scaling measurement data via the difference in permittivities ($\epsilon_{air} = 1, \epsilon_{epoxy} \approx 3.5$), this

would result in an expected capacitance reduction of approximately 0.6 pF for an IDC completely surrounded by air. This is of course also not entirely applicable for the considered experiment, but might lead to the conclusion that, given the noise observed in the measurements, the actual capacitance change in this setup is too small to be reliably measured. For application on the sensor tag, as permittivity is a factor in capacitance calculation, i. e. the equations presented in Section 6.1, IDC strain sensitivity is assumed to be higher for the material-integrated case. Also, overall noise and parasitic elements of the connections and leads are expected to be much smaller for the final PCB version of the measurement circuit and IDC. Corresponding experiments are described in Section 7.3.4.

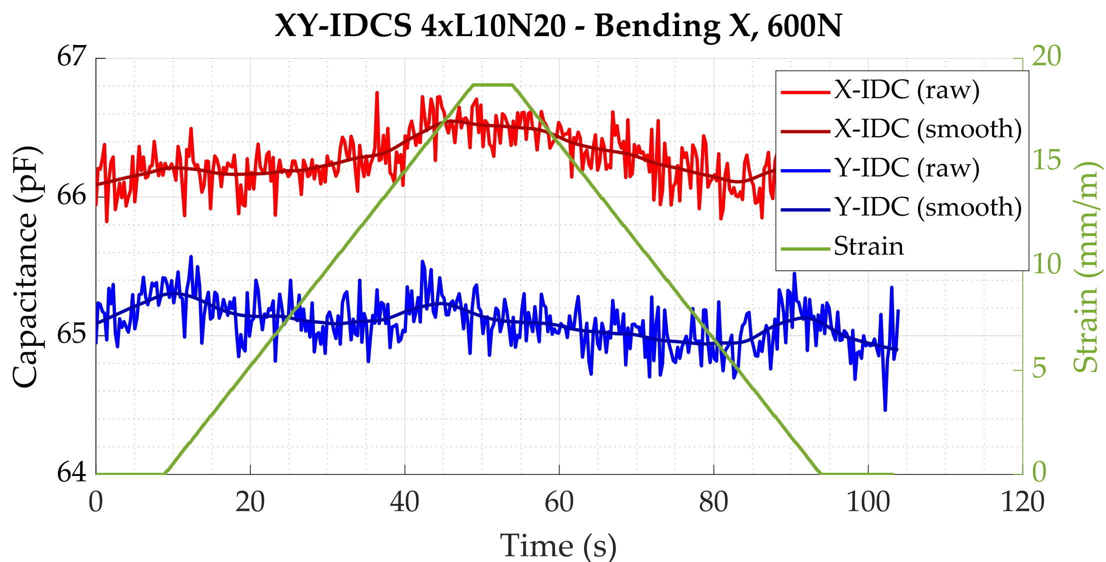

Figure 6.33: Strain sensitivity of XY IDCS 4xL10 N20. Capacitance for measurement in X direction and applied strain (green), shield floating. Y data similar.

Comparing results of the shielded and unshielded versions, no significant difference can be recognized, apart from capacitance baseline, which is about 3 times higher. Both absolute noise level and strain-induced capacitance change are similar in between the two designs. Regarding the experiments for strain in the other direction, results are also found to be similar. As the specimen material is isotropic (e. g. no strengthening fibers present), this is to be expected. For the $L = 5\,\text{mm}$ versions, signal to noise ratio was even lower, as base capacitance is much smaller (see Section 6.2.6). The respective data consequently does not contribute any new information, so it is not displayed here.

Summarizing the findings of the bending tests in air, it can be concluded that capacitance change is not measurable with the prototypical circuit and the IDCs tested, and shield presence does not make any noticeable difference, neither on capacitance change nor on noise. To improve strain sensitivity, both finger number and length should be increased. Also, higher permittivity of the surrounding dielectric will be beneficial for higher capacitance change.

6.2.11 Double-sided IDC Layout

Following the results of the prior experiments and the absolute capacitance changes predicted by the analytical calculations in Section 6.1, another type of IDC was designed, with the intention of increasing IDC sensitivity to strain, to make it easier to measure. To that end, a double-sided IDC structure was devised, implementing the same electrode geometry both on the top and bottom copper layer of the FPCB, to increase the number of electrodes per area. This was done both for the bidirectional XY-design with $L = 10\,\mathrm{mm}$ (see Figure 6.11), and another, unidirectional IDC design with an overall larger outline. The latter was designed to achieve an even higher signal magnitude by simply adding finger length and number. To still fit the general dimensions of the sensor tag, a design of $L = 20\,\mathrm{mm}$ and $N = 50$ was chosen. For measurements, the specimens were suspended in air and capacitance was measured 40 times.

Resulting average capacitances for two specimens of each design are displayed in Figure 6.35. For the $L = 20\,\mathrm{mm}$ version, it can be found that in between the two single sided specimens, capacitance varies ca. 3 pF, while for the double-sided version, capacitance difference is around 9 pF. Contrary to the obvious expectation, capacitance of the double-sided version does not double in comparison with the single-sided design, but only increases about 19 pF for the average between the two specimens of $L = 20\,\mathrm{mm}$. Relatively speaking, this is an increase of ca. 32 %. For the double-sided XY-version, average capacitance increase of the double sided versions is ca. 8 pF for both X and Y IDCs, resulting in an average increase of ca. 38 %. Absolute variance between identical specimens of the XY design is much lower than for the L20 design, measuring less than 1 pF. Visual inspections under the microscope yielded no explanation for this difference in variance, though fabrication related aspects or parasitic elements of the measurement circuit might play a role. Summarizing the findings, doubling the IDC electrode structure on the opposite side of the FPCB increases total IDC capacitance about one third of the initial capacitance.

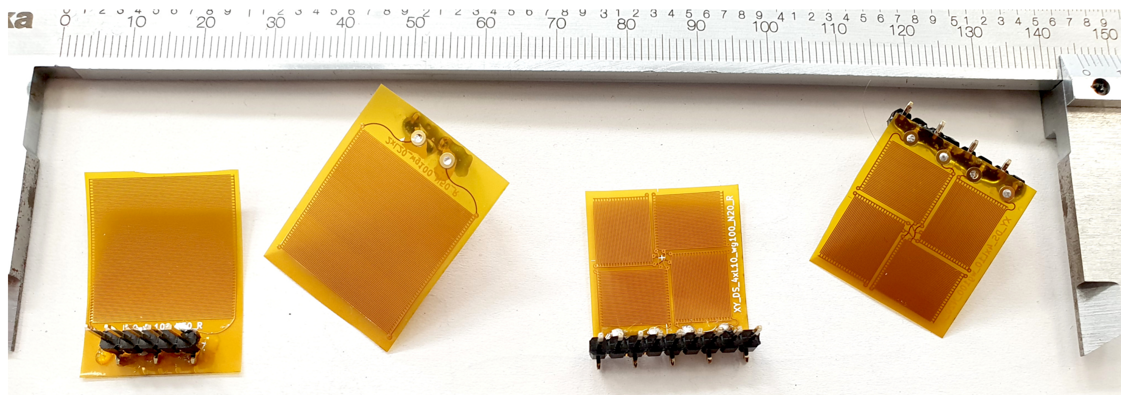

Figure 6.34: Double sided IDC prototypes, electrode structure on both PCB copper layers. Left: L20 N50; Right: XY 8xL10 N20.

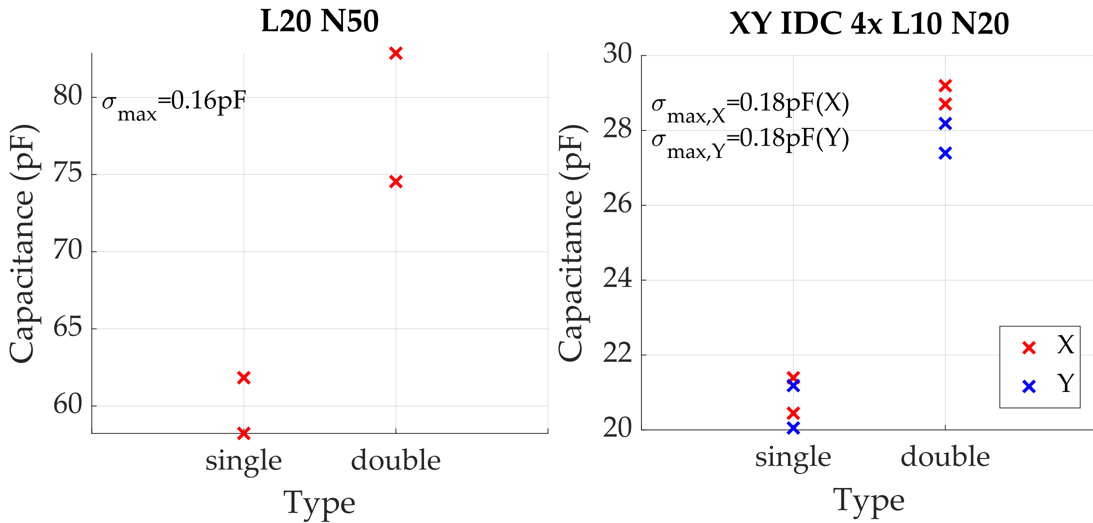

Figure 6.35: Averaged IDC capacitance for single and double sided versions of otherwise same design, n=40 for each data point.

6.2.12 Summary and Conclusions

Summarizing the findings of this section, several important insights could be gained. These will be briefly described here, first stating general findings and subsequently those specific to the intended sensor application, i. e. FRP fabrication and load monitoring.

6.2.12.1 General Findings

Capacitance of the fabricated IDCs does show a decreasing dependency on excitation frequency, though this can be neglected for fixed operation points, i. e. for measurements which do not change excitation frequency in the order of MHz. Surrounding the IDC with cured epoxy increases overall capacitance, as is expected due to higher permittivity. Also, due to its dielectric properties, slope of the correlation increases a little bit, i. e. capacitance is slightly more dependent on excitation frequency for the IDC surrounded by epoxy. In context of application on the sensor tag, this is still not deemed significant, as application-induced changes of resonant frequency are expected to be several magnitudes smaller.

Regarding overall capacitance values, as predicted by literature and the analytical calculations (see sections 2.4.6 and 6.1), linear correlations could be found for both IDC capacitance and finger number N, and capacitance and finger length L, respectively. Normalizing average capacitance to finger size and length, the unshielded, single layer variant exhibits a capacitance of 0.047 pF/mm for 1.44 MHz excitation, measured in air. Introducing a shield, i. e. metallized back plane, increases capacitance. For the shield left floating, average capacitance per finger increases to 0.163 pF/mm. Applying a defined potential to the shield roughly doubles capacitance in comparison to the shield left floating, resulting in 0.317 pF/mm for

both GND and supply voltage potential. Considering the data on reproducibility of absolute IDC capacitance for identical layouts, measured deviations are negligible in context of the intended application. This is supported by the absolute difference in between specimens being a systematic error that can easily be compensated for by on-tag calibration, i. e. measurement and substraction of baseline capacitance in steady state. Considering placement of the sensors in different environments, this is potentially necessary anyway for comparison of application-induced capacitance change in between sensors. In this context, usage of a shield can be advantageous, as experiments on substrate dependency show. While capacitance of the unshielded variants shows a distinct increase when moved from air to FRP substrate, the shielded variants do not, indicating relocation of IDC sensitivity to one side, i. e. away from the shield. Comparing measured capacitances to the calculations done in Section 6.1, it can be found that results correlate well, with measured data for IDCs surrounded by epoxy being in the range predicted by the different calculation approaches (see Figure 6.27).

For the experiments conducted, temperature dependency of IDC capacitance is measurable, though approximately linear for IDCs surrounded by cured epoxy glue. Results show a temperature dependency of $m = 0.143\,\text{pF/K}$ for an unshielded IDC and $m = 0.172\,\text{pF/K}$ for the shielded variant, which are probably due to temperature dependency of epoxy permittivity. Using the temperature sensor present on the sensor tag, this cross sensitivity could therefore be compensated for via calculation. During epoxy cure measurements, this cross-sensitivity might be neglected, as capacitance changes during cure are much larger than those induced by changing temperature.

For the three unconventional IDC layouts, i. e. the single sided XY-configuration and the two double sided variants (see Figure 6.34), accordance of measurement results and expectations diverges – while the resulting parallel circuit of the two IDC structures per axis doubles overall capacitance, as was expected, doubling the IDC electrodes on substrate backside does not double overall capacitance. Instead, capacitance increases only about one third, which might be attributed to substrate thickness, i. e. parallel distance between the electrode layers, being smaller than penetration depth of the electric field, thereby causing effects by the field lines overlapping.

6.2.12.2 Application-related Findings

For the experiments related to fabrication and load monitoring, important knowledge could also be gained. Concerning fabrication monitoring, resin arrival, i. e. presence, is distinctly reflected in measurement data of all IDCs examined, yielding a sharp increase in capacitance. Comparing the different IDC layouts, best sensitivity for resin arrival is found for the unshielded IDC variant, with the shielded versions being approximately thirty percent less sensitive for the shield floating and approximately ten percent less sensitive for the shield connected to ground.

Pot life time, as given by epoxy data sheet, is probably reflected in capacitance data by a nearly constant or very slightly increasing capacitance (increase probably temperature induced). With the start of resin cure, capacitance starts to reduce rapidly, resulting in an exponentially decreasing curve. For the different IDC layouts investigated, normalized capacitance changes ($\Delta C/(LN)$) during cure are very similar, yielding an average of 0.02 pF/mm decrease per finger for the first 20 minutes, independent of shield presence. For the IDC with grounded shield, this decrease is slightly higher (0.028 pF/mm), possibly indicating a slightly higher sensitivity of this configuration for resin cure. In other words, absolute capacitance changes during cure are the same for the IDCs of same finger length and number, indicating that presence of a floating shield only increases baseline capacitance and not sensitivity during cure. As expected, it could also be found that the shielded IDC versions are sensitive only on the unshielded side. While this can be interpreted as a limitation, it could also be used for special applications, where resin impregnation is to be monitored at a specific position, or close to the mold surface. Considering noise level during the curing experiments, no significant difference in absolute noise level could be found for the shielded and unshielded IDC prototypes, for both finger lengths investigated and shield floating, though shield presence seems to slightly increase standard deviation of the measurements. Shield potential does make a difference though, as standard deviation of the measurements for the IDC with grounded shield was found to be more than twice as high.

Regarding strain sensitivity for the bending tests in air, it could be found that strain-induced capacitance change is not measurable with the prototypical circuit and the IDCs tested, which is probably mainly due to the comparatively high noise and small capacitance changes. Shield presence does not make any noticeable difference on strain sensitivity, neither on capacitance change nor on noise. Regarding IDC usage on the sensor tag, relative change of capacitance for a material-integrated IDC is expected to be of higher magnitude, as capacitance and therefore strain-induced capacitance change of IDC structures is dependent on relative permittivity of the medium present in the vicinity of the electrodes. Also, in contrast to the measurements presented in this section, which were conducted with the prototypical breadboard circuit (see Figure 6.8), lengths and parasitic influence of IDC connection with the on-tag measurement circuit are likely less pronounced. For successful measurement of strain, i. e. usage of the IDCs as capacitive strain gauges, increasing finger number and / or finger length therefore seems to be necessary to achieve sufficiently high changes in capacitance, if minimal structure size (w and g) is kept above 100 µm. Especially smaller gap distances would increase strain sensitivity, as it is influenced in a non-linear way (see Figure 6.4b). As this work focuses on simple and cost-effective producibility, this restriction on minimum feature size is though considered important. To that end, strain

sensitivity of the larger geometry and the double-sided variants is investigated in Section 7.3.4.

6.2.12.3 Summary

To summarize the most important findings at a glance, these are itemized below:

- Linear dependency of capacitance and finger length L & finger number N could be experimentally confirmed.
- Excitation frequency does not significantly influence capacitance of the fabricated IDCs in context of intended application.
- Measured capacitances of fabricated prototypes is in good agreement with calculations, with Endres et. al. and Mukhopadhyay et. al. fitting best.
- Presence of a floating shield:
  - increases normalized capacitance about 3.5 times.
  - moves sensitivity distribution towards the unshielded side, making the IDC immune to changing substrates.
  - apparently does not significantly influence noise level.
- A defined shield potential of U_0 or GND:
  - increases capacitance ca. 6 times in comparison to an unshielded IDC.
  - increases capacitance ca. 2 times in comparison to a floating shield IDC.
  - apparently increases noise level with an approximate factor of 2.
- Double sided IDC layout does not double overall capacitance, but increases it with an approximate factor of 1.32.
- Temperature dependency of the examined IDCs is approximately linear for $20\,°\mathrm{C} \leq T \leq 75\,°\mathrm{C}$, giving temperature coefficients of ca. 0.143 pF/K (unshielded) and 0.172 pF/K (shielded) for the L10 N40 variant in epoxy glue.
- Resin arrival and subsequent cure is very well measurable, even with very small IDCs (e. g. L5 N40), reflecting data sheet information on pot life time and cure.
- Presence of a floating shield decreases sensitivity for resin arrival, but not for curing.
- A grounded shield results in only slightly lower sensitivity for resin arrival, but potentially increases sensitivity for curing.
- For strain measurement, capacitance change of the examined geometries is not sufficiently high to be measured with the prototypical circuit.

6.2.12.4 Conclusion

Based on the knowledge gained in this section, three different IDC geometries are selected for usage in consecutive experiments with the sensor tag developed. As unshielded IDC layouts showed best overall performance in the experiments related to fabrication monitoring, they will be used in two of the three designs. In order to examine performance regarding bi-axial strain measurement, an XY-configuration with four $L = 10\,\text{mm}$ and $N = 20$ IDCs is chosen for the first design. For maximized strain sensitivity, bi-axial capability is sacrificed in favor of higher finger length and number in the second design, which are chosen to be $L = 20\,\text{mm}$ and $N = 50$, to use all available space on the tag. To increase overall sensitivity, these two configurations will be implemented as double sided layouts. Finally, to further investigate potentially higher sensitivity for cure monitoring as suggested by the preliminary curing experiments, a shielded version with the shield connected to ground is also designed (XY 4xL10 IDC-S N20).

Chapter 7
Capacitive Sensor Tag

After developing the sensor presented in Chapter 5, another sensor tag was designed, building on the knowledge gained during its design and the investigations on IDC behavior (Chapter 6). The sensor intends to improve upon many aspects of the prior design, targeting higher information depth for process monitoring and less complex sensor assembly. Its electronics and software have been completely redesigned, and a different sensing element, i. e. an IDC, is used. This chapter will give a detailed account of all steps taken during development and provide in-depth information on its design and experimental results. First, motivation for the new design is laid out. Secondly, sensor design and fabrication is illustrated, focusing on the new aspects and improvements as compared to the prior sensor tag. Tag functions are then investigated and characterized in several experiments, and system limitations are examined consecutively. Finally, the chapter concludes with a summary and discussion of the most important findings.

7.1 Motivation

Though the results on process monitoring obtained with the piezoresistive sensor tag allow for estimation of flow front position and cure progress, a precise inference of actual viscosity or current glass transition temperature of the matrix is not possible with temperature measurements only. This is mainly due to the indirect nature of temperature measurements in context of resin cure. Deduction of the current flow front position is only possible if a measurable temperature difference is present between resin and dry textile, which is influenced by initial resin temperature and also thermal conductivity of both resin and mold / textile layup. Regarding cure monitoring with temperature sensors, progression of the curing reaction can also only be inferred indirectly, given that prior knowledge exists on matrix curing kinetics. Though material-integrated measurements in that regard present a considerable advantage as compared to surface based measurement, as could be shown in the preceding chapter, a more direct method for cure quantification seems desirable.

One of the the suitable methods for this task is Dielectric Analysis (DEA), (see Section 4.1.2 for details). It is able to give very detailed insights into curing behavior of FRP, which is why it has been an established technique for some decades. As could previously been shown in e. g. [50, 52, 65] and many others, usage of IDCs yields good measurement results, while the sensors themselves are easy to fabricate. The sensor developed in this chapter aims to transfer the basic principle of DEA onto a wireless sensor tag, to combine the advantages of DEA, the sensor tag approach, and material-integrated measurements. To further simplify sensor tag composition, and to reduce cost for assembly and the sensing element itself, the sensing element is directly incorporated into PCB design of the sensor tag. This way, using inexpensive fabrication of FPCBs via standardized processes and automated placement of the electronic components, overall sensor cost is expected to be very low, facilitating industrial usage and subsequent optimization of FRP fabrication processes.

Finally, additional usage of the IDC sensor element for strain measurement, similar to a capacitive strain gauge (see Section 2.4.7) is investigated, to examine if the same sensor could additionally be used for SHM related applications during FRP material usage. This way, the sensor could be used for the whole FRP component life cycle, similar to the concept targeted with the piezoresistive sensor tag. Though capacitive strain gauges are not a new topic in itself, usage of IDCs made via common PCB fabrication techniques is of special interest, due to the associated simplification and reduced cost.

7.2 Sensor Design and Fabrication

Implementing the knowledge gained with the preliminary experiments, the capacitive sensor tag is developed.[1] In the first part of this section, the overall concept is presented, giving details about the general idea, the ICs used, and design of the antenna and the capacitive sensor element. Subsequently, sensor fabrication is described, elaborating on substrate, assembly and software.

The sensor implements the same basic concept as the piezoresistive sensor, and is consequently also based on the "Sensor Tag Approach" (see Section 3), aiming for a rectangular shape of minimal dimensions and minimal thickness, while operating completely without wires or battery. To make sufficient energy transfer possible, the antenna cannot be too small (see e. g. experiments on the smaller sensor tag version or small antenna diameter in Sections 5.1.6.2 and 7.2.2), so the antenna was similarly designed to encircle the electronics, thereby saving space. Overall tag thickness was reduced, both for maximum height and substrate thickness, aiming to reduce the wound effect created by sensor integration.

Comparing tag electronics, circuitry of the capacitive tag has completely been redesigned, based on lessons learned during prior sensor tag design. The most important improvement is usage of a different RFID transponder, allowing for a much better power supply by providing a dedicated energy harvesting output (see Section 7.2.1 for details). Characterization of power supply is described in Section 7.4.1. The higher output voltage of this transponder allows for usage of a dedicated voltage regulator, improving voltage stability. Similar to the prior design, all components are chosen to have a maximum operation temperature of at least 125 °C to be able to withstand conditions present during FRP fabrication. Also, component selection similarly focuses on usage of "off-the-shelf" components, reducing overall sensor cost and simplifying producibility. In this regard, designing the IDC sensor element "in-place" as copper structure on the PCB is a distinct advantage as compared to gluing and contacting a dedicated strain gauge. This way, tag assembly only includes soldering of the electronics on the PCB, eliminating any further steps. Full circuit schematics are given in Figure A.10.

Based on results of the IDC investigations as described in Section 6.2, several IDC geometry modifications were made to increase signal to noise ratio, in order to possibly allow for strain measurement. For this reason, multiple tag versions were fabricated, implementing different IDC designs, to provide a basis for comparison of fabrication monitoring and strain measurement capabilities. Section 7.2.3 elaborates on the IDC designs used.

Figure 7.1 illustrates sensor tag concept. Communication and power supply is handled by the RFID transponder, which outputs the voltage (U_{EH}) harvested

[1] As considerable similarity exists between the two designs, this section shall only highlight the main differences, to avoid repetition. If the reader finds some details lacking, Chapter 5 will hopefully provide answers.

from the reader-supplied field to the voltage regulator, that in turn stabilizes and adjusts it for circuit supply (U_0). For this function, the TPS7A03 [131] by Texas Instruments was chosen for its efficiency and very small footprint. For stable function of the regulator, capacitors C_{In} and C_{Out} are required. Further voltage stabilization is done via several additional bypass capacitors (C_B), as suggested by data sheets of the ICs and the micro controller. Similar to the piezoresistive tag, temperature measurement is done by the TMP117 temperature sensor, that is connected to the micro controller via I^2C. Pull up resistors R_{Pu} supply the I^2C lines. The same applies to the FDC2212, that measures resonance frequency of the resonant circuit connected to it, allowing for calculation of IDC capacitance. Due to its measurement principle, resonant capacitors C_{res} and inductors L_{res} are required, making up the resonant circuit together with the IDC. To provide a defined clock for resonant frequency quantification, the micro controller supplies its master clock (set to 8 MHz) to the FDC2212. For user feedback, a Light Emitting Diode (LED) is connected to a GPIO pin. Micro controller programming, debugging and serial output (UART) is done via a Zero Insertion Force (ZIF) connector implemented in the FPCB.

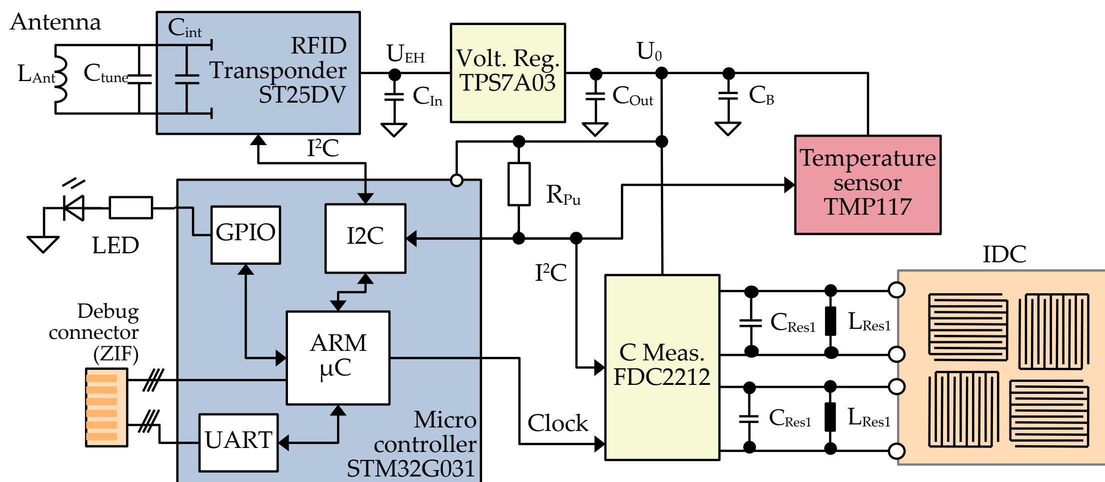

Figure 7.1: Schematic illustration of circuit concept for capacitive sensor tag.

7.2.1 RFID-Transponder and Micro Controller

As harvested power and especially supply voltage provided by the NHS3152 was very low (≤2 mW at 1.6-1.8 V, see Section 5.3.1), a different transponder was chosen for wireless communication and energy transfer. Based on energy harvesting performance, form factor, temperature specifications and successful development results on passive sensors for material integration presented in e. g. [132, 133], the ST25DV04K model from STMicroelectronics was chosen [134]. Via its energy harvesting pin, it can deliver up to 19 mW at 1.7V (see Section 7.4.1). At 2.7 V, which is minimum supply voltage for the FDC2212, total available power was found to be approximately 6 mW. Regarding communications, it implements both the ISO 15693 and NFC standard, which is also different from the transponder used on the piezoresistive sensor tag. Depending on package, it is specified for temperatures from −40 to 125 °C and provides up to 64 kBit of memory. Here, the 2x3 mm UFDFPN8 package is used, to allow for manual soldering, though smaller packages are available.

Opposed to the NHS3152, the ST25DV does not include a micro controller, so that a dedicated one was included in the circuit for measurement data acquisition and tag control. Based on component availability, a generic micro controller from STMicroelectronics was chosen (STM32G031G8U6, [135]), which incorporates all features necessary for communicating with the other ICs and is delivered in sufficiently small form factors, i. e. packages (4x4 mm UFQFPN28 in this case). For future reduction of power consumption, usage of a low power micro controller is possible, though none were deliverable during the design phase of this tag. Regarding operation temperatures, the micro controller is also specified for −40 to 125 °C. To ease re-usability of the created sensor platform, software has been completely rewritten, focusing on modularity of the different modules (see Section 7.2.7).

7.2.2 Antenna

For antenna design, the same basic process was done as already described for the piezoresistive sensor tag (see Section 5.1.3). Consequently, following approximate inductance calculation, several antenna prototypes were designed and fabricated, to find the best possible antenna dimensions and resulting inductance of the prototype resonating at a usable frequency. In order to anticipate influence on resonance frequency, the footprints and tracks of the electronic circuitry were already included in the PCB design of the prototypical antennas. As with the smaller prototypes developed for the piezoresistive sensor tag, another, different overall tag layout was designed, in another attempt to further reduce overall dimensions i. e. outline. In this layout, dimensions are reduced by making the antenna only encircle the electronics and not the sensor element, i. e. IDC, resulting in a reduced footprint of the antenna itself and the overall tag. A visual comparison of the two designs is given in Figure 7.2. In the calculations, it could be found that the number of turns

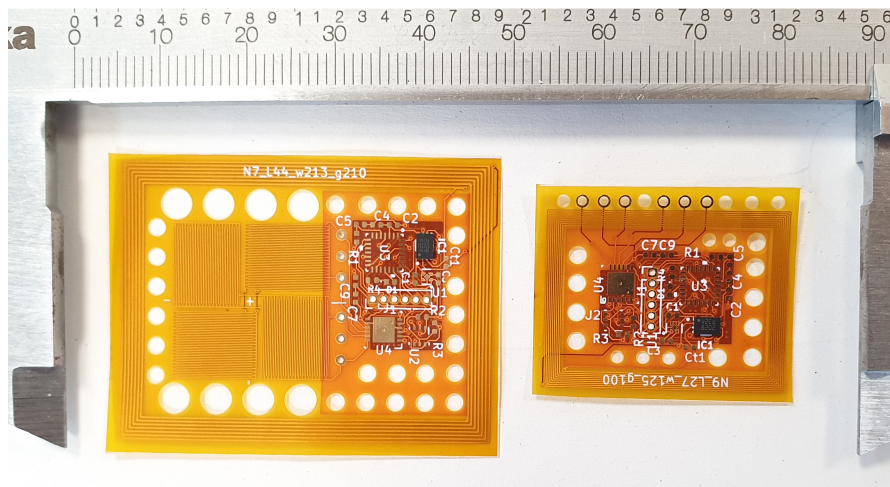

Figure 7.2: Different approaches for antenna design. Left: antenna encircling sensor element and electronics; right: smaller antenna, encircling only electronics.

needs to be increased, to make up for the reduced antenna diameter, in order to achieve the necessary inductance.

The prototypes were fabricated via the same manufacturing process as used for production of the full sensor tag, to minimize fabrication related deviations. Placement of the IDC and electronics was done with a minimum distance of 4 mm to the antenna, as suggested in [111].

To investigate the resulting resonance frequencies for the fabricated FPCB, the prototypes were measured via an impedance analyzer, the same way as already described for the piezoresistive sensor tag (see Section 5.1.3). Results for the different antenna geometry prototypes are displayed in Figure 7.3, showing absolute impedance over frequency. Comparing resonance frequencies, it can be found that those of the larger prototypes (i. e. the designs with $6 \leq N \leq 7$) are generally in the expected range. The smaller prototypes however exhibit resonance in much higher regions, ranging from 14.6 MHz to more than 20 MHz. Also, the magnitude of the impedance maximum marking the resonance frequency reduces drastically with decreasing antenna size, indicating a lesser quality factor of the antenna and reduced efficiency of the energy transfer. Based on these findings, it might be concluded that the calculations are less accurate for smaller overall dimensions, or that model parameters need to be adjusted to improve approximation quality. In context of the tag design in general, the larger antenna geometry (i. e. N7_L44_w213_g210) is consequently chosen for further development.

7.2.3 Sensor Element: Interdigital capacitor

Based on the insights gained during the experiments on IDCs (see Section 6.2.12.4), three different IDC layouts are implemented on the sensor tag (see Figure 7.4).

As unshielded IDCs showed the best performance for epoxy presence and cure

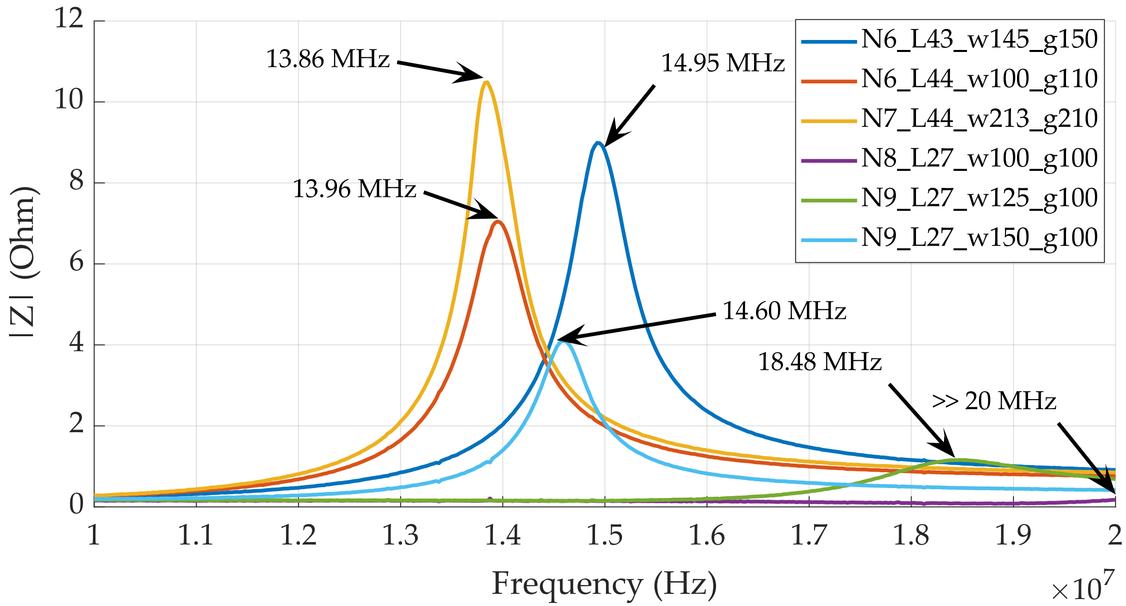

Figure 7.3: Resonance frequencies of different antenna geometry prototypes for the capacitive sensor tag.

monitoring, two of the three layouts do not implement a shield. Instead, to increase IDC sensitivity, these were designed as double-sided designs. The first one bears a XY 4xL10 N20 IDC structure both on the front and back copper layer. This design still incorporates orthogonal IDCs for bidirectional strain measurement and easy temperature compensation by allowing for differential capacitance measurement. The second design sacrifices bidirectional measurement capability in favor of higher signal to noise ratio by incorporating an unidirectional IDC structure spanning the complete free space of the tag's inside (see Figure (7.4)). This results in a L20 N50 geometry for PCB top and bottom copper layer. The third design uses a shield, i. e. metallized back plane, connected to ground, to further investigate potentially higher sensitivity for cure monitoring as suggested by the preliminary curing experiments. To protect the IDC structure from environmental influences, i. e. mechanical abrasion or corrosion, and to prevent potential short circuits, the IDCs are coated with a thin polyimide film. IDC design considerations and layer buildup are described in Section 6.2.1 and Figure 6.12.

The IDC is directly connected to the FDC, with the resonant elements C_{reso} and L_{reso} connected in parallel (see Figure 7.1). In contrast to the strain gauge configuration used for the piezoresistive sensor tag (see Chapter 5), strain in longitudinal and transversal direction are therefore independently measurable. As the IDCs for the two directions are connected to a measurement channel each, lateral contraction is consequently not superimposed on measurement signal.

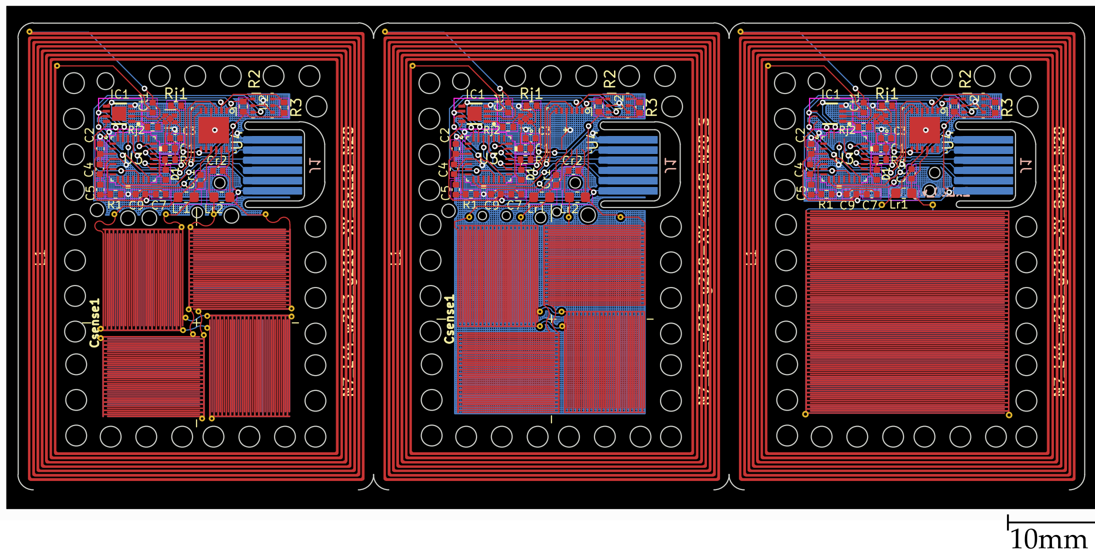

Figure 7.4: CAD view of tag versions with different IDC geometries: double sided XY (XY 8xL10 IDC N20), shielded XY (XY 4xL10 IDC-S N20), double sided unidirectional (L20 IDC N50)

7.2.4 Capacitance Measurement

As suggested by calculations on IDC capacitance presented in Section 6.1, capacitance measurement needs to be sufficiently precise to allow for strain quantification. To this end, for capacitance measurement of the IDC sensor element, an FDC2212 IC by Texas Instruments [58] is chosen, as it is specified to have a high resolution (28 Bit) and a very low system noise floor of 0.3 fF. It is also specified for the extended industrial temperature range of −40 to 125 °C at a minimum supply voltage of 2.7 V. It was chosen for its wide operating temperature range and because it is a small-footprint, low power solution with high resistance to electromagnetic interference, which is to be expected due to the reader RF field. Other ICs for capacitance or (bio)impedance measurement exist (e. g. ADS129x, MCP3901, AD5940, MAX30009, AD5933/5934, ...) and some even allow for full impedance measurement of magnitude and phase. Unfortunately, these are either only specified to lower operating temperatures of usually 85 °C or shipped in very big package sizes (e. g. SSOP-16 for the AD5933/5934). For the scope of this proof-of-concept sensor tag, measurement of capacitance was therefore deemed sufficient. Related publications for cure measurements also used capacitance measurement or similar ICs, e. g. [15, 50, 53]. The same is true for capacitance measurement for strain quantification, e. g. [54, 96, 97]. Technically, the FDC2212 should therefore very easily be able to measure the changes in capacitance previously calculated in Section 6.1. It uses a resonance based principle (see Section 2.4.8), therefore capacitance is calculated from a shift in resonance frequency of a parallel resonant circuit. As the IC itself does not include a fixed resonance circuit, an additional capacitance and inductance are necessary, which, together with the capacitance of

the sensoric capacitance, in turn determine the excitation frequency of the sensor, i. e. the IDC. Resonance frequency of a parallel LC resonant circuit can be calculated as

$$f_r = \frac{1}{2\pi\sqrt{LC}}. \tag{7.1}$$

For application on the sensor tag, footprint size and height of all components is highly relevant to minimize the wound effect generated in the host material. As package sizes of both capacitors and inductors approximately scale with their value, excitation frequency cannot be set as low as the kHz-region with available components, without the geometric size of the components getting too large for material integration. For experiments conducted, the resonant circuit was therefore built with nominal values of L = 33 µH and C = 330 pF, resulting in a (sensor-less) resonance frequency of $f_r \approx 1.525$ MHz. Including the IDC, overall resonance frequency will be correspondingly lower, with component fabrication tolerances and parasitic elements also having a slight influence. As already shown in Section 6.2.3, this is negligible in the context of this work, as IDC capacitance is not significantly influenced by excitation frequency. During application, the different base excitation frequencies of each tag can be taken into account by in-place calibration, i. e. prior resin infusion, or by differential interpretation of the measured values for each tag (e. g. during strain measurements with XY IDCs). Regarding polarization phenomena occurring at low frequencies (Hz to kHz regions) this frequency also seems a good choice to prevent actual migration of ions and possibly reduce measurement dependency on specific material composition. Examples for these effects are interfacial polarization and Maxwell-Wagner-Polarization, which can influence capacitance measurement results due to charge accumulation at the electrodes [46, 50]. Though most literature mentioning these effects report these for non-isolated, i. e. metallic electrodes in direct contact with a fluid dielectric, [46] describes it as also happening at “inner boundary layers separating two dielectric components”. In [50], this effect could be observed for (non-isolated) IDC epoxy cure measurements at frequencies up to 10 kHz, causing a frequency-dependent increase in dielectric constant of more than 20 % as compared to higher frequencies and later-on measurements, where ion mobility was inhibited by higher viscosity. Similarly, initially very high impedance values were reported in [65] for frequencies between ca. 0.1-1 kHz, also using non-isolated IDCs for cure monitoring of matrix resins. Regarding the above considerations and design limitations, the chosen resonance frequency seems suitable for the experiments of this work. For future investigations, choice of a different frequency could be worth examining, as polarization behavior changes with frequency, potentially providing additional insights in matrix curing behavior.

7.2.5 Temperature Measurement

As with the piezoresistive sensor tag, this tag also implements a precise digital temperature sensor for monitoring of matrix temperature. Due to the good results obtained with it, the same IC is utilized as already described in Section 5.1.5. It is similarly located as far away as possible from the circuit elements handling the power management (e. g. the transponder and the voltage regulator, see Figure 7.5), to minimize influence of the generated heat on the temperature measurement. Apart from using the local resin temperature for process optimization, similar to the approach described for the piezoresistive tag, temperature data can also be used to compensate for the temperature dependency of IDC capacitance that was observed during the preliminary experiments (see Section 6.2.8). For further description of the temperature sensor see Section 5.1.5.

7.2.6 Sensor Fabrication

The sensor tag substrate was fabricated via a commercial PCB process, the same way the antenna and IDC prototypes were made. For assembly of the sensor tag, i. e. mounting of the electronic components, the same procedure was used as has already been described for the piezoresistive sensor tag (see Section 5.1.6), using manually dispensed soldering paste and a hotplate for reflow soldering. A fully assembled tag (ca. 44 mm $\times$ 33 mm) is displayed in Figure 7.5. At its thickest point, which is where the resonance inductors are mounted, the tag has a maximum total thickness of 939 µm, while the tag itself has a thickness of ca. 111 µm for both copper layers present. The height of the two biggest IC packages with the FPCB beneath amounts to a total thickness of ca. 895 µm for the FDC and 732 µm for the micro controller. As the main sensory element (the IDC) is designed in-place during PCB layout, further assembly steps are not necessary.

7.2.7 Software

After assembly, the sensor is programmed with the firmware developed via the programming contacts. As a different micro controller is used (as compared to the piezoresistive tag), the firmware has been completely rewritten, building on knowledge gained. In particular, software development was focused on low power consumption, high readout frequency, i. e. short measurement acquisition time, and modularity, to improve re-usability. To that end, functionalities have been implemented in separate sub modules, i. e. for communication with the different ICs (FDC2212, ST25DV, TMP117). As scientific relevance of the software development conducted is limited, only its general function shall briefly be described in the following paragraph.

After initialization of the several peripheral functions of the micro controller, I^2C communication is established with the other ICs, intializing the respective

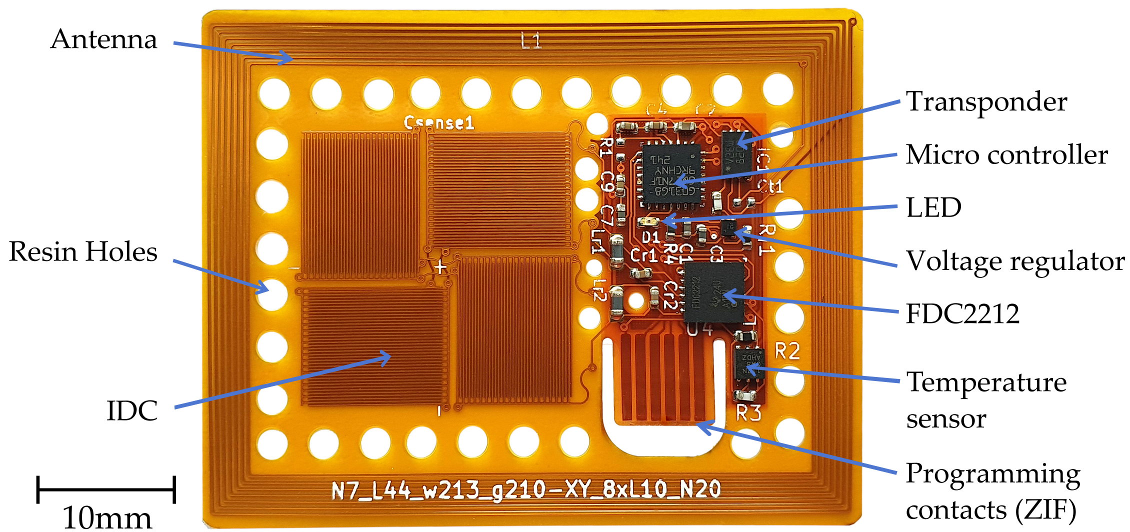

Figure 7.5: Fully assembled capacitive sensor tag with component descriptions, double sided XY IDC sensor configuration.

startup configurations. Regarding the RFID transponder, this encompasses opening the security session between micro controller and transponder, to allow writing into memory and configuration of system registers. This is subsequently done to activate the energy harvesting functionality. The status of the system registers is non-volatile, ensuring that voltage is available during next start-up of the tag. Following this, FDC configuration is done, setting up the capacitance measurement with the necessary parameters. These are mainly selection of an external clock source (in this case the master clock output by the micro controller), and parameters regarding channel selection and filtering. To save energy, the time during which the FDC is powered on is controlled by using the shutdown pin provided by the FDC, which is in turn connected to a GPIO pin of the micro controller. This is especially relevant during the phases in which data transfer between the micro controller and the other ICs is happening, as I^{2}C communications was found to consume a lot of power. For the temperature sensor, no further initialization is necessary, as factory configuration is sufficient for the usage intended. After completing the setup routine, the micro controller waits for the FDC to provide the measured capacitance values. When these are sent, the raw readout data is first converted into the corresponding resonance frequency of the LC-tank, i. e. the parallel resonant circuit connected to each channel, using the reference clock and several configuration parameters. The equations relevant are described in the FDC data sheet [58]. Using the resonance frequency and the known values of the resonant circuit elements (L_{reso} and C_{reso}), capacitance of the IDC can be calculated (see Equation 2.35). Tag software then writes the calculated capacitance values to RFID transponder memory via I^{2}C. To provide user feedback, the LED is then

activated for 100 ms. The software then waits for reset, which is automatically triggered by the reader switching off the electromagnetic field.

As programming of the prior tag version was a time consuming process, especially due to the small through-hole diameter and number of contacts (see Figure 5.7), this tag version implements a ZIF connector for programming and debugging. The connector structure is designed in-place on the PCB. As the substrate material is flexible, the connector can easily be inserted into a corresponding socket for programming. Even though the ZIF connector has a slightly larger footprint on the PCB, interfacing the tag is very much simplified by plugging in the PCB into the connector (see Figure 7.6). For possible later on tag versions produced in an industrial scale, this connector could be easily exchanged for needle probe pads or similar, allowing for further tag miniaturization.

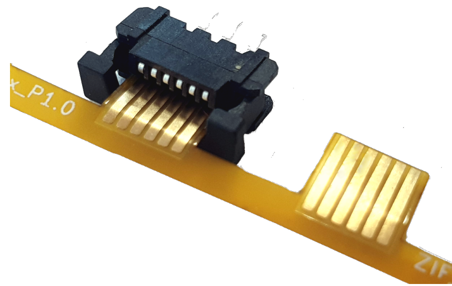

Figure 7.6: ZIF connector for sensor tag interfacing and programming.

7.3 Experiments and Results

This section describes experiments conducted with the capacitive sensor tag and corresponding results. The first subsection investigates temperature influence on the measured capacitance due to temperature dependent detuning of the resonant circuit. The second section then illustrates investigations on fabrication monitoring capabilities, utilizing a VARI process for tag integration into FRP. The resulting, sensor-integrated specimens are then examined regarding strain sensor function and influence of mechanical loading on sensor response. Finally, limitations of the sensor system are investigated, encompassing quality of on-tag power supply, maximum reading distance and operating temperature range.

7.3.1 Temperature Influence on Capacitive Measurement

As the sensor tag is exposed to strongly differing temperatures during its intended application, influence of temperature on the measured values is investigated in an individual experiment. Temperature dependency of the IDC structures themselves was already investigated in Section 6.2.8. Here, the fully assembled sensor tag (double sided XY 4xL10 IDC N20) is investigated, exposing it to a temperature range of 0-100 °C in a climate chamber. To this end, the sensor tag was attached to a glass support, where it was suspended in air via heat resistance adhesive tape, and placed in a climate chamber. The tag was powered and read out wirelessly via an RFID reader during the whole experiment. To reduce influence of thermal conductivity and thermal capacities, temperature was increased with a small slope of 0.4 K/min. The experiment was conducted for both the whole sensor tag and the same tag without its IDC connected, to differentiate the influence of temperature on the IDC and the electronics themselves.

Results Measured capacitance is plotted in Figure 7.7, for both scenarios, i. e. with and without IDC connected. A strong dependency of measured capacitance and temperature is observed in measurement results. In the examined interval, capacitance initially rises with increasing temperature, until a local maximum is found at ca. 37 °C. With temperature further increasing, capacitance decreases significantly. This is true both for the IDC connected and without IDC, with the IDC generally resulting in a capacitance offset (see Figure 7.7). Relating measurement data to the resonance frequency of the measurement circuit (Equation 2.35), this behavior is equivalent to resonance frequency falling, reaching a local minimum at 37 °C, before rising again with further increasing temperature.

In comparison to the temperature effect on the electronics themselves, temperature dependency of the IDC itself is negligible. It can therefore be concluded that the main contribution to temperature dependency is made by the electronics, e. g. the resonant circuit, the micro controller clock, or the FDC itself. As the FDC is specified for a temperature range of −40 to 125 °C and no temperature effect on

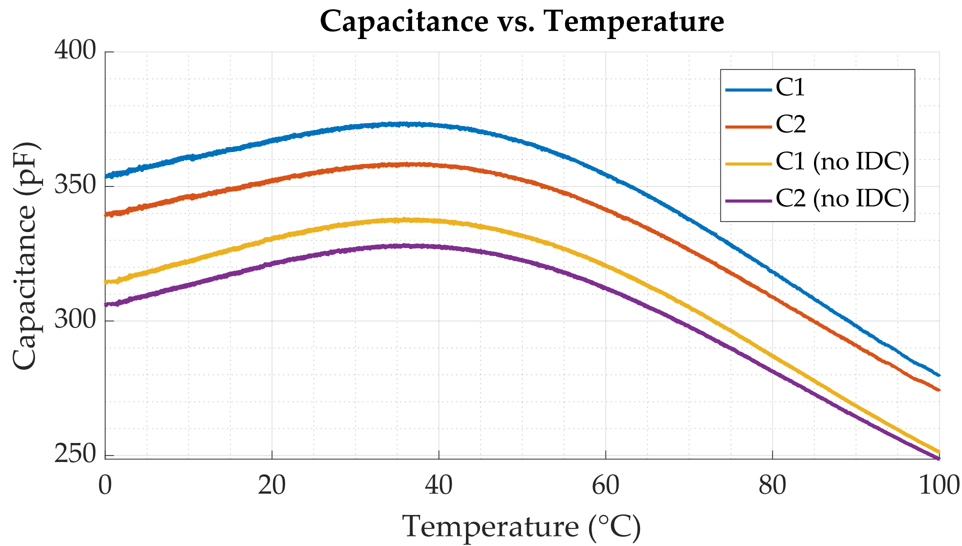

Figure 7.7: Temperature dependency of equivalent capacitance for fully assembled sensor tag, with and without IDC connected.

measurement accuracy is given in the data sheet [58], it seems unlikely that this is the major contribution. As the reference clock used by the FDC is supplied by the micro controller, this could also contribute to the behavior observed, as the data sheet [135] gives a temperature dependency of a maximum of −2 to 1.5 % for the interval −40 to 125 °C. As only resonance frequency is measured by the tag, it cannot be discerned which of the circuit elements contributes in which way to the overall dependency found. Nonetheless, system response to temperature can be obtained from the measurements and be used for compensation via the temperature sensor present on the sensor tag.

Given the above considerations, for further calculations, temperature compensation is conducted with fit data acquired for the circuit only, i. e. without IDC. This is to prevent possibly different influences of the different IDC designs used in the following experiments, and also to prevent masking of other possible effects on measured capacitance. To obtain a function for temperature compensation, polynomials of different degree are successively fitted to measurement data using MATLAB's "polyfit()" function. The resulting curves are displayed in Figure 7.8, alongside the raw data. It can be found that the difference between measured values and the polynomial fits decreases with rising degree of the polynomial. To visualize this, fit difference has additionally been given in Figure 7.9. For polynomials of 6th and and 8th degree, fit difference seems to be appropriately small (≤1 pF), so the fit parameters for a 6th degree polynomial are chosen to reduce later on computation times.

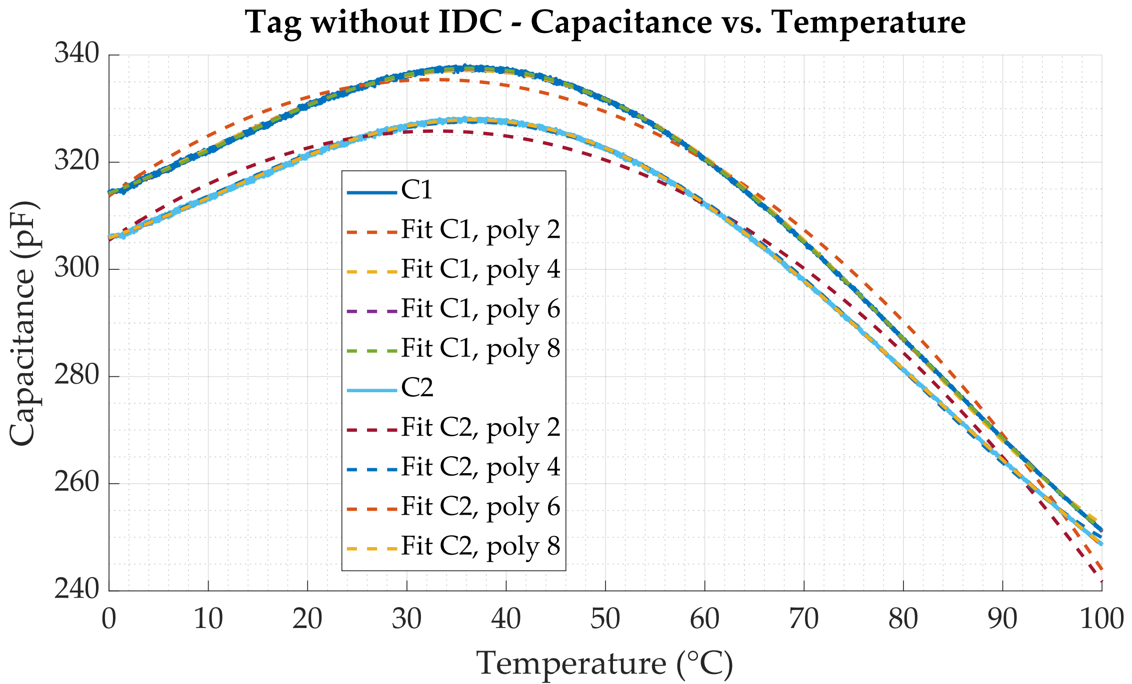

Figure 7.8: Temperature dependency and polynomial fits of equivalent capacitance, for resonant circuit only (no IDC connected).

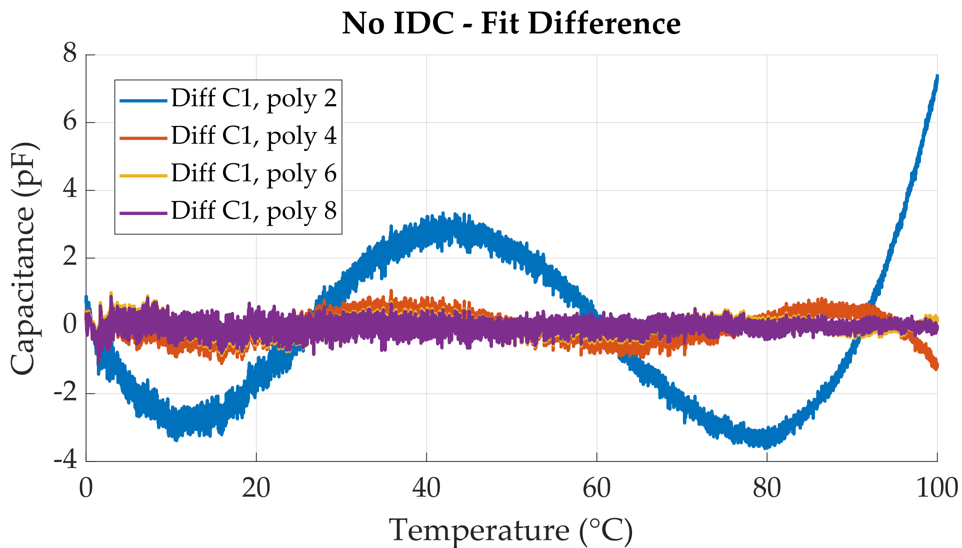

Figure 7.9: Difference of measured capacitance and calculated fits for resonant circuit only (no IDC connected).

7.3.2 Epoxy Cure Test with Sensor Tag

For comparison with the preliminary experiments regarding epoxy cure (see Section 6.2.7), and to confirm overall sensor tag function, a fully assembled tag was integrated into the same epoxy glue [128]. The tag was powered and read out fully wirelessly during the experiment, using an RFID reader positioned above it. Experiment setup is illustrated in Figure 7.10. To begin with, uncovered sensor tag capacitance was measured for reference. Then, the two glue components were mixed in the mold, to make the lower section of the epoxy specimen. The sensor tag was placed onto the fluid resin directly afterwards. For fully submerging the tag, another portion of resin was mixed and poured onto the tag, first covering the IDC and subsequently the electronics, manually distributing the resin via a plastic spoon, to speed up the coverage.

Results Measurement data is visualized in Figure 7.11, giving both capacitance values and tag temperature. To compensate for the slight delay caused by later covering of the temperature sensor itself in relation to the IDCs, temperature data has been time aligned to the peak visible in capacitance data, resulting in a correction of about 23 s. Measured capacitances clearly reflect the temperature dependency previously investigated in Section 7.3.1, giving a strongly decreasing capacitance with rising temperature. As the amount of resin mixed for the experiment is comparably large, the exothermic temperature increase is strong, resulting in a peak temperature of 95.1 °C. This is also partly due to the nature of the resin chosen, which is configured to cure comparably fast (tangibility after approximately 20 min, according to data sheet, [128]), resulting in a very active reaction.

Using the temperature fit obtained in Section 7.3.1, temperature influence can be reduced, the results of which are given in Figure 7.12. IDC coverage yields the expected sharp increase in capacitance, which happens in two steps, following the consecutive coverage of IDC back and front sides. Then, after a short period of "noisy" measurement data, which was caused by the successive, manual addition of colder, mixed resin, measurement data shows a clear trend, analogous to the

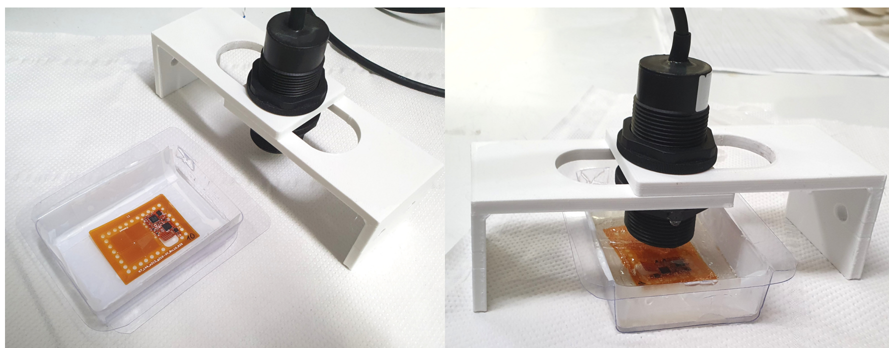

Figure 7.10: Experiment setup for wireless epoxy cure test with sensor tag. Left: Components without resin; Right: sensor tag submerged in resin.

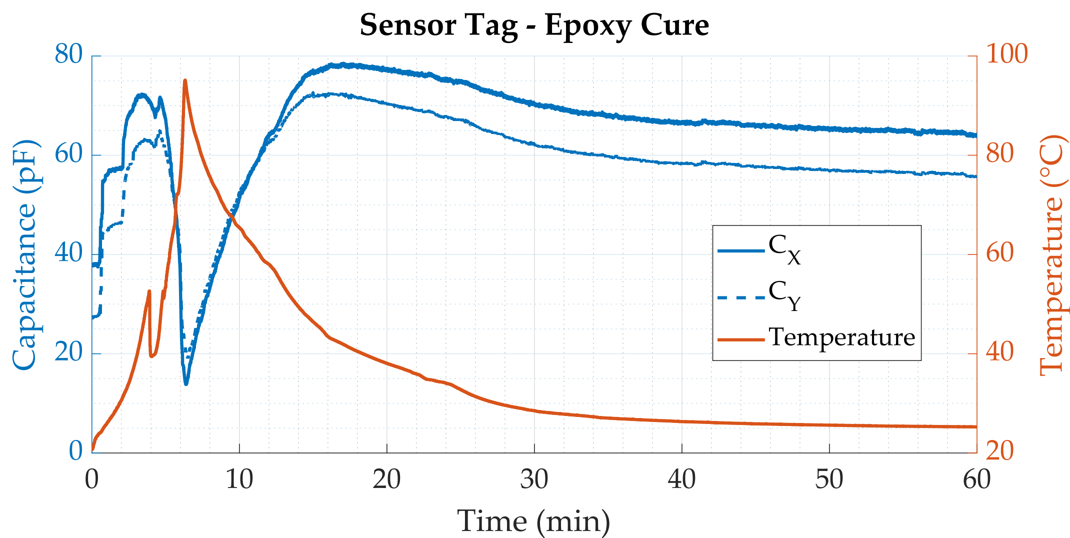

Figure 7.11: Measured capacitances and temperature during epoxy cure test for fully assembled sensor tag, no temperature compensation.

experiments conducted with only the IDCs themselves (see Section 6.2.7). Similar to the curves obtained in Section 6.2.7, a small, almost linear increase in capacitance is recorded for a period of ca. 5 min. Following this, capacitance exponentially decreases with progressing cure, which could be associated with decreasing mobility of charge carriers inside the material. Overall, correct sensor tag function for epoxy cure monitoring can therefore be confirmed with this experiment.

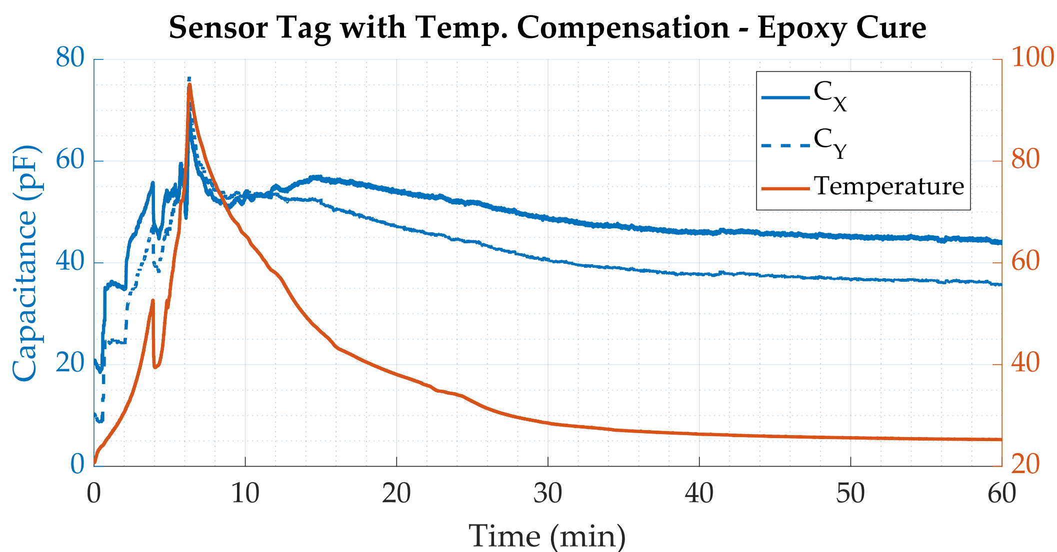

Figure 7.12: Temperature compensated, measured capacitances and temperature during epoxy cure test for fully assembled sensor tag.

7.3.3 Fabrication Monitoring

To test process monitoring capabilities of the sensor in a realistic context, six sensors were integrated into GFRP, using a similar process as described in Section 5.2.1. This section gives a detailed account on the experiment setup and its results, reporting on how the sensor can be used to observe resin infusion and subsequent curing.

7.3.3.1 Setup

Overall setup is very similar to that used in Section 5.2.1, so here only important differences shall be described, to avoid repetition. To investigate the difference in capacitance behavior of the different IDC designs during FRP fabrication and later on strain measurement, two tags each of the the three designs chosen were used in this experiment (see Section 7.2.3 for details). Experiment setup is visualized in Figure 7.13. The stacked textiles were arranged on a heated table surface and embedded within a VARI setup. The sensors were read out every 300 ms for the entire experiment duration via RFID readers mounted above them. As only 5 readers were available due to delivery problems, the sixth sensor had to remain unpowered during infusion and cure. Resin temperature and curing temperature stages were chosen similar to the integration experiment conducted with the piezoresistive sensor tag, successively increasing heating temperature setpoint to avoid overheating due to the exothermic resin reaction. Also, resin and curing agent were chosen to match those of the prior experiment (*EPIKOTE RIMR 135* (resin) + *RIMH137* (curing agent)).

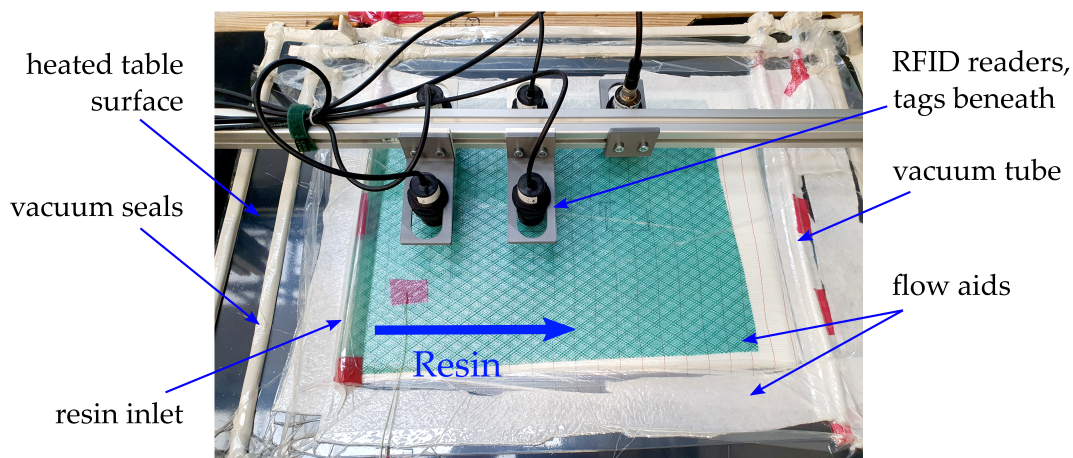

Figure 7.13: FRP integration setup for capacitive sensor tag, readers mounted above the sensors. Resin flow indicated for reference.

The tags were arranged in three rows of two, so that each row was reached by the resin flow front at the approximately same time. Prior to the experiment, the sensor tags were dried in an oven at 60 °C to remove any humidity present in

the polyimide substrate. Tag distribution is additionally illustrated in Figure A.3. Next to the sensor-integrated specimens, six sensor-less specimens were produced for later on comparison. Similar to the previous integration experiment, the tags were positioned between the 6th and 7th textile layer (see also Figure 5.10), so that they will experience a tensile force during subsequent bending tests (distance from neutral plane at specimen center). To simplify calculation of lateral contraction during bending, an unidirectional glass fiber textile was chosen (E glass).

7.3.3.2 Results

Raw measurement data of both temperature and capacitance is given in Figures 7.14 and 7.15. For the subsequent fabrication stages, i. e. relevant events, annotations are also given with dashed lines. For the tags comprising XY IDCs, only one of the two measured capacitances is given, to improve figure clarity. Also, for better comparability, baseline capacitances of the different tags have been normalized, resulting in all capacitances starting at 0 pF for the initial, dry state in the textile layup. Reasons for the different baselines include both the different IDC layouts themselves, and different actual values of the resonant circuit elements (fabrication tolerance).

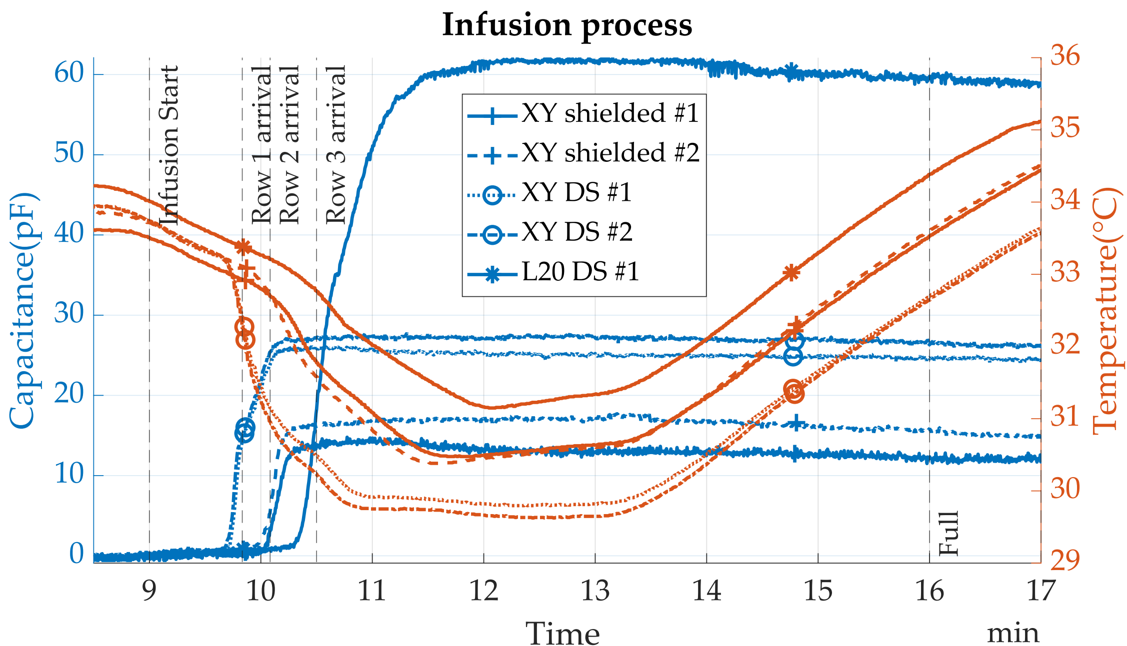

Figure 7.14: Raw capacitance and temperature data during the infusion process.

For the L20 sensor (“L20 DS #1”), acquired data is very noisy and shows eventual and randomized drop outs. This might be due to problems in power supply of the reader, as the power supply used was later found to be unstable. Nonetheless, the data is still usable, and has been smoothed out, using a moving median for filling up outliers. To generally improve readability of the diagrams, all

capacitance data has been filtered with a moving average filter, using a window size of 10 samples (equivalent to ca. 3 s). At about 1:50 h, the experiment setup was disturbed by a dislocation of the readers, causing a brief drop out of sensor data. Repositioning of the readers could easily restore the data acquisition process. Though inconvenient for the experiment itself, this proves durability of the system and its ability to recover from temporary signal loss.

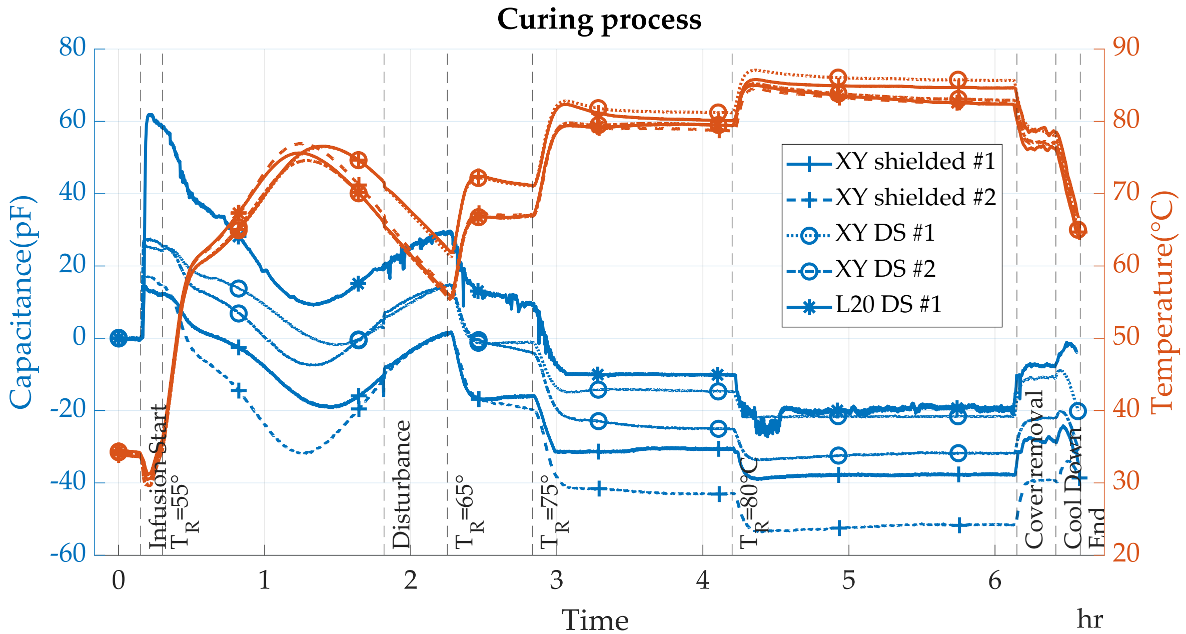

Figure 7.15: Raw capacitance and temperature data for the whole experiment duration.

During infusion (Figure 7.14), resin arrival at the individual sensor tag positions is distinctly reflected in a sharp capacitance increase, the magnitude of which is higher for higher number and length of fingers present in the respective IDC geometry. This is to be expected and confirms results of the investigations on capacitance size and cure monitoring (see Section 6.2). Also, as the resin is slightly cooler than the dry textile, resin arrival is visible as a drop in measured temperature, similar to the results of Section 5.2.1. Temperature then rises, as the heated table warms the fluid resin. For infusion monitoring, results therefore prove superior information depth as compared to the temperature only approach (i. e. the first sensor tag).

Looking at the complete experiment duration (Figure 7.15), it can be easily deduced that strong dependency exists between local temperature and measured capacitance. Though the different events are reflected in the measured data, temperature cross-sensitivity makes identification of cure-induced capacitance change difficult. To reduce the influence of the observed temperature influence, two strategies have been devised, which are described in detail in the following section.

7.3.3.3 Temperature Influence

As visible in the results of Section 7.3.1, the effect of temperature on the resonant circuit itself is of higher magnitude than the temperature dependency of the IDC capacitance (see Section 6.2.8). Following that logic, the polynomial fit data acquired for the sensor tag without IDC connected, in other words, the fit for the measurement system on its own, should be able to remove the observed cross-sensitivity. Figure 7.16 displays the resulting data. It can be found that temperature influence can indeed be reduced, and to no small amount. Still, a direct influence is visible, which is most clearly discernible towards the end of cure.

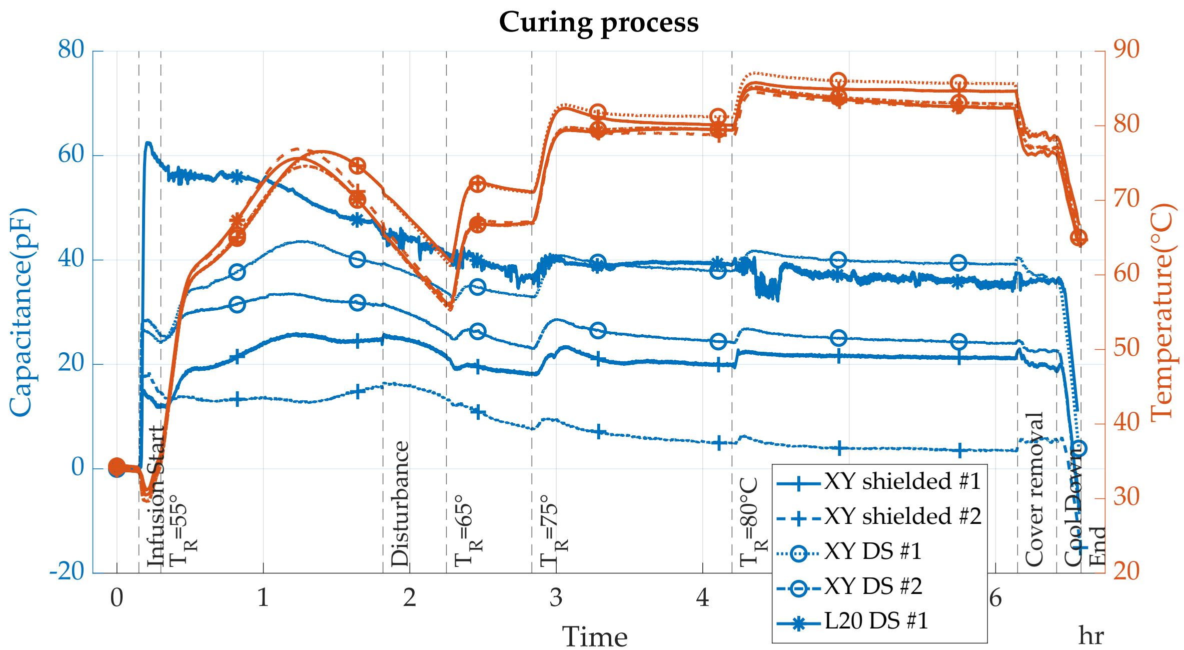

Figure 7.16: Temperature compensated capacitance and temperature data, using the previously acquired polynomial fit.

Using a simulation model developed by the Faserinstitut Bremen e.V. (FIBRE), where the experiment was conducted, the approximate degree of cure can be calculated for a given temperature profile. This data has kindly been provided and included in Figure 7.17. This way, measured capacitance and cure degree can directly be compared. Looking at the data, especially following the 4 h mark, where resin cure is largely complete and therefore cure-induced capacitance change is expected to be small, it can be found that variation of temperature still leads to a direct increase in measured capacitance. This leads to the conclusion that the fit data obtained is to some degree insufficient. Possible reasons include slightly different temperature behavior of resonant circuit elements for each tag, temperature dependent permittivity of the surrounding material, or inhomogeneous temperature distribution across the table surface (this could already be observed in Section 5.2.1).

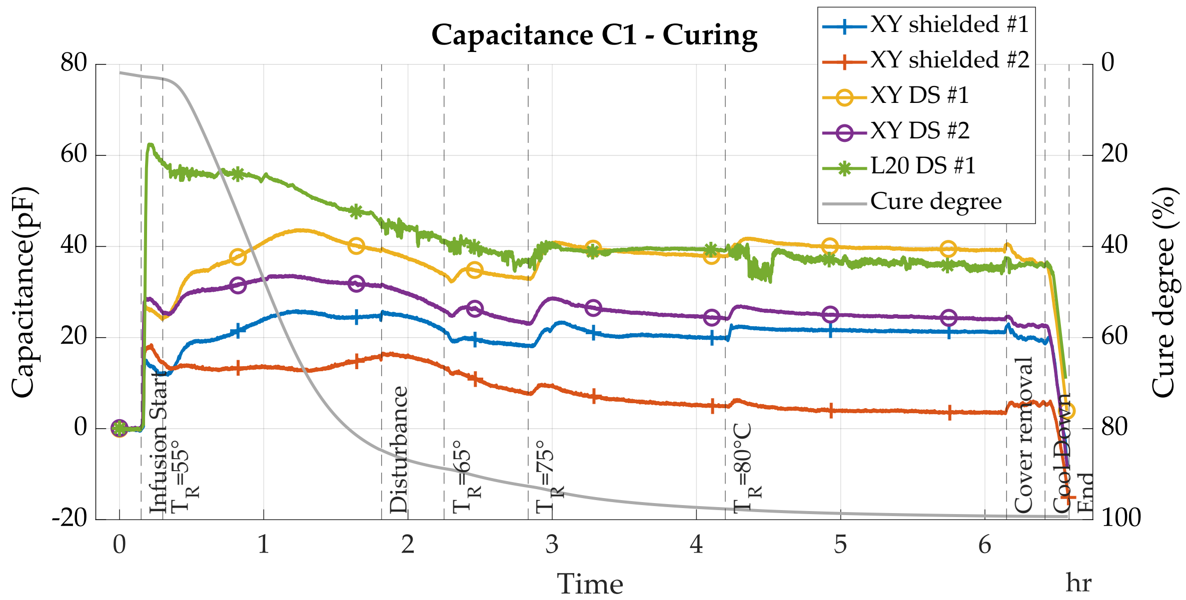

Figure 7.17: Temperature compensated capacitance data, using the previously acquired polynomial fit, versus calculated degree of cure.

Once again looking at the raw measurement data (Figure 7.15), another approach for temperature compensation was investigated. Especially looking at the later stages of curing, comparison of the capacitance curve with that of temperature shows that the slope near the times where the table temperature was changed resembles a nearly linear dependency. Assuming this, a slope of approximately $-1.3\,\mathrm{pF/K}$ for the unshielded variant, and $-1.5\,\mathrm{pF/K}$ for the shielded variant was calculated. For the larger, unshielded variant (L20 N50 DS, i. e. "L20 DS"), a slope of ca. $-1.6\,\mathrm{pF/K}$ was found. Using this simple linear dependency, influence of temperature on capacitance can also very much be reduced, as visualized in Figure 7.18. Comparing this with the polynomial fit, the changes of temperature in the second half of the experiment seem to be better compensated for.

Contrasting the behavior of the three IDC geometries, comparison is impeded by the strong temperature dependency, but trends towards different sensitivities can be observed nonetheless. Most obvious is the highest sensitivity of the large IDC (L20 DS), which is found both for infusion, i. e. resin presence, and capacitance change during cure. Though noise level is high, it shows the strongest capacitance increase during infusion, with the other two double sided IDCs ("XY DS #1/2") following in line, and the shielded IDCs showing the comparably smallest sensitivity for resin presence. During cure, the curve of the L20 DS IDC most closely resembles the expected behavior, with capacitance distinctly decreasing during epoxy cure. For the other IDC geometries, this trend is also generally visible in the experimental data, but results are still strongly influenced by temperature and the compensation method utilized. Higher sensitivity of the shielded IDC, as suggested

by the preliminary experiments, can therefore not be confirmed with the data acquired.

Concluding the experiment after cool down, the FRP was cut to quadratic specimens of 100 mm length for later on bending tests (see Section 7.3.4), the filled textile lay-up amounting to a total thickness of about 6.7 mm for the specimens.

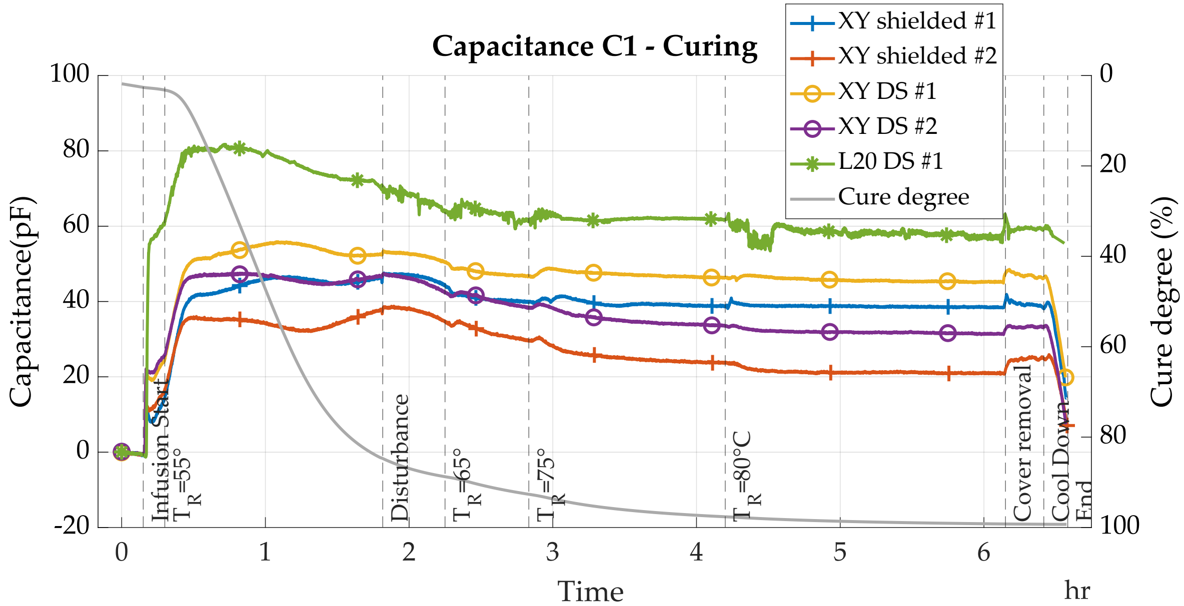

Figure 7.18: Temperature compensated capacitance data, using a variant-dependent linear fit, versus calculated degree of cure.

7.3.3.4 Discussion

Comparing the two approaches for temperature compensation, especially during the first 2 h, both show slightly diverging trends for measured capacitance of the individual tags. Also, especially during infusion and subsequent, initial heating, compensation results diverge greatly. For the polynomial fit, it could be assumed that fabrication tolerances lead to differences in the actual values of the resonant elements, thereby influencing resonant frequency with a slightly different magnitude for the same change in temperature. For the linear approach, this deviation can be explained by the compensation being derived from observations made in the later stages of cure, where the resin is already solid. As mobility and therefore polarization behavior of the resin molecules are very different in fluid form, it is to be expected that transferability of the compensation is poor. Explaining this linear relationship with a thermal dependency of epoxy seems plausible, due to the nearly solid state at the later parts of cure. Indeed, in literature, and also during the preliminary experiments (see Section 6.2.8), a nearly linear dependency of temperature and relative epoxy permittivity is reported [130]. Contrary to the findings of the experiment at hand though, the reported temperature coefficient is

positive (ca. 0.02 K^{-1}), so the effect observed is likely caused by a different relation. Another possible explanation for the observed negative temperature coefficient could be thermal expansion and shrinkage of the matrix material. As the resonant circuit elements later have been found to be sensitive to mechanical loads, the surrounding material deforming around them will likely also influence resonance frequency. This could be shown in Section 7.3.5 – mechanical compression of the resonant circuit leads to an overall increase of resonance frequency, resulting in a decrease of the calculated, i. e. measured capacitance value. This effect likely overshadows the positive influence of rising permittivity on measured capacitance. Overall, the linear temperature compensation seems to give results better fitting to the capacitance behavior expected from experimental results described in Section 6.2.7. The actual causes for this need further investigation though, to better understand the influence temperature has on the individual parts of the overall system.

7.3.4 Strain Sensor Characterization

Using the specimens created during the fabrication monitoring experiments (see Section 7.3.3), this section evaluates strain sensing capabilities of the different IDC designs. Similar to the experiments done with the piezoresistive sensor tag, a three point bending test is used for applying strain to the specimens. One of the specimens used is displayed in Figure 7.19. Specimen geometry was again chosen so that symmetrical loading in both X (longitudinal) and Y (transversal) direction could be achieved. The IDC was therefore positioned in the very center of the quadratic specimen. Tag coordinate system is chosen according to Figure 7.20, with X direction being equal to fiber direction.

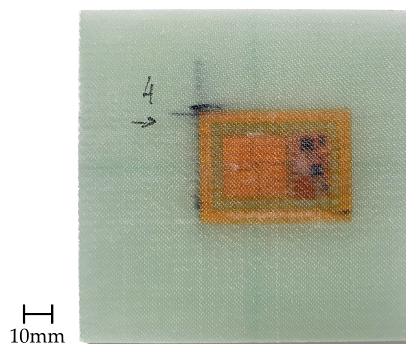

Figure 7.19: FRP bending specimen with integrated capacitive sensor tag.

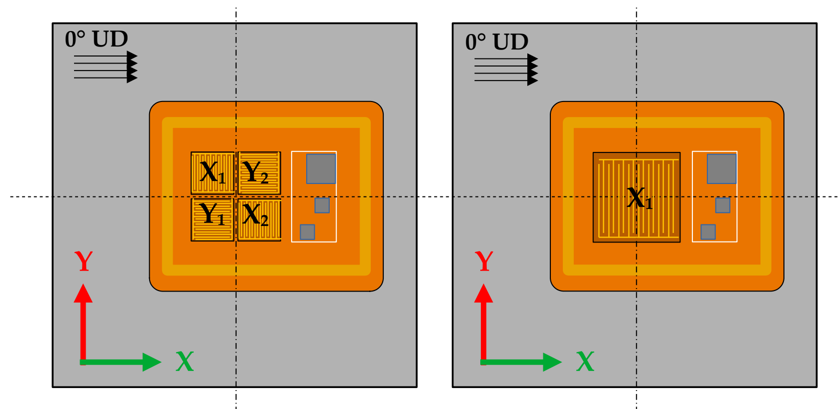

Figure 7.20: Coordinate system definition for bending specimens, corresponding direction of the electrode fingers and main fiber direction. Tag drawing not to scale.

7.3.4.1 Setup

Experiment setup is similar to that used for the experiments with the piezoresistive tag (Section 5.2.2), though using a maximum deflection force of 2 kN due to higher FRP strength, and slightly higher deflection speed of 0.03 mm/s.

To examine the influence of strain direction, especially for the XY IDCs, specimens were first bent in X direction, i. e. perpendicular to main fiber direction, before they were rotated 90 degrees for bending in Y direction. As an unidirectional textile was used and the FRP is correspondingly much weaker for bending in Y direction, specimens were deflected with reduced force of 1 kN in Y orientation. Deflection was done three times for each axis. Then, to investigate the effect of bending in Y direction, each specimen was again rotated back 90 degrees to be loaded a final time, to see if the measurements for the prior X deflections are repeatable.

7.3.4.2 Results

Resulting data for the consecutive loading scenarios is illustrated in Figure 7.21, using specimen 2 as a representative example. Both capacitance values and the corresponding loading force are given, the force diagram being intentionally made smaller to not disturb the capacitance curves. For better comparison in between the different designs, capacitance baseline has been normalized for all measurements. This way, the initial capacitance starts at zero for all experiments. To improve readability of this section, all other data obtained is given in Section A.2.

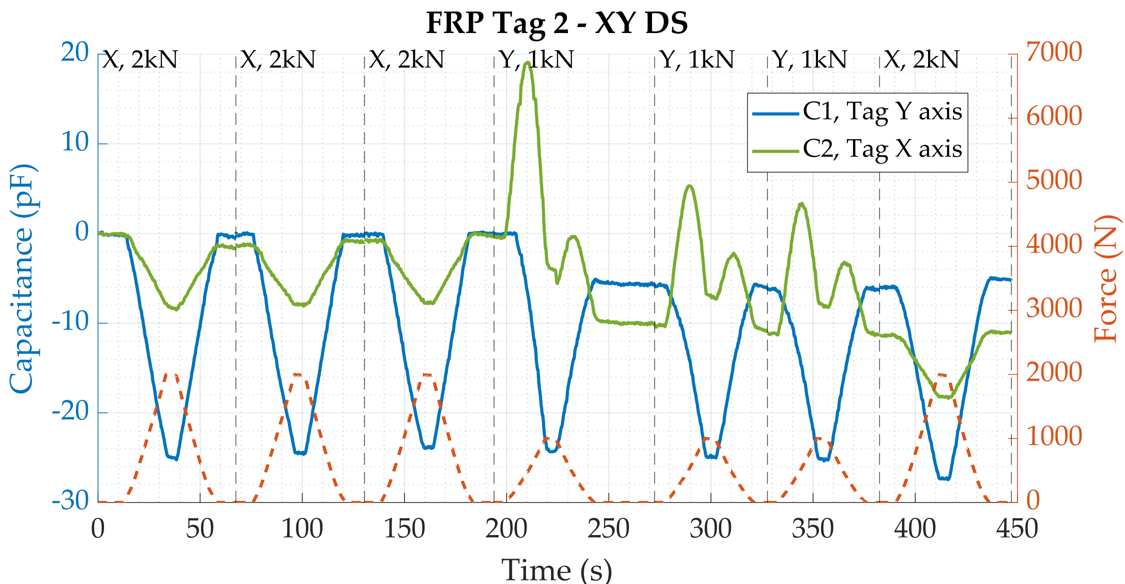

Figure 7.21: Measured capacitances and respective forces for bending tests conducted with specimen 2 (XY DS).

Measured capacitance shows effects proportional to the applied force, though contrary to expectations, both regarding magnitude and effect on the two measurement directions. For tag 2, loading in X direction results in a strong decrease of measured capacitance for the Y channel, and a proportionally smaller capacitance decrease for the X channel, with both being proportional to the applied force. In theory, capacitance of the IDC oriented in X direction should decrease, while measured values for the Y channel should increase. This is expected because

distance of the X IDC fingers will increase due to strain, while the distance of the Y IDC fingers will decrease due to lateral contraction. For the unidirectional FRP material utilized, this is strong for bending perpendicular to fiber direction ($\nu_{\perp\|} \approx 0.3$ [1],[136]), causing compression of the IDC oriented in Y direction.

Bending in Y (parallel to fiber direction) results in different behavior than bending in X. With increasing force, measured capacitance for the X axis first rises strongly instead of falling (as is observed for X), then, at the point where approximately half of the force is applied, X capacitance starts to decrease again. The reverse behavior is found for decreasing force, though to a lesser extent. In this case, the expected behavior is a decrease in Y capacitance, simultaneous to a (small) increase in X capacitance (lateral contraction here is much smaller due to the strengthening fibers). Following the first deflection in Y direction, capacitance baseline has shifted for both channels, indicating a permanent effect on resonance frequency of the circuit. The subsequent additional bending in X then results in similar behavior as the first deflections in X, apart from the shifted baselines.

Comparing the results in between specimens, behavior is also controversial. While the effect on Y capacitance during X bending is stronger for tag 2, the opposite is observed for tag 1 (Figure A.4), which is of same design. Behavior during Y deflection is similar, though of different magnitude. For the specimens bearing sensor tags with shielded IDCs, the expected capacitance change is smaller, due to the smaller number of electrode figures. The behavior observed is albeit nearly identical to that of specimens 1 and 2, and also similarly opposite for the effect on the two measurement directions. The tags with the large, single-direction IDC, i. e. specimens 5 and 6, exhibit generally equal behavior (L20 DS, Figures A.7-A.8). For these, (X) capacitance decreases in a similar magnitude for loading in X direction, and similarly smaller magnitude for bending in Y direction. Though decreasing X capacitance is expected for loading in X, the decrease measured is noticeably related to that of the other specimens, while, due to the higher amount and increased length of the electrode fingers, the capacitance decrease is expected to be stronger than for the other IDC variants. Also, a similar shift in capacitance baseline after bending in Y is observable.

Finally, though not as pronounced for specimen 2, another phenomenon can be found in the data acquired. During capacitance change, a "step-like" behavior is visible, where measured capacitance stays nearly constant (except for the observed noise) for a short interval, even though actual resonance frequency of the resonant circuit, and thereby equivalent capacitance, is changing. Corresponding measurement data is given in Figures A.4-A.8). This behavior is repeatable and distinct for each individual tag. For this reason, it has been investigated in a dedicated experiment (see Section 7.3.6), indicating a systematic error of the FDC for the given operating conditions.

7.3.4.3 Discussion

Results show that the bending effects on measured, equivalent capacitance are much higher than initially calculated (see Section 6.1). Also, the observed influences on the individual measurement directions are contrary to the initial expectations. In order to explain this behavior, further investigation of the origin of the measured capacitance value needs to be done. The capacitance reported by the sensor tag is calculated from the resonant frequency of the parallel resonant circuit connected to the FDC input terminals, which is in turn measured by the FDC. A detailed explanation of the measurement principle is given in Section 2.4.8. Using equation 2.35, IDC capacitance is then calculated by assuming fixed values for L_{reso}=33 µH and C_{reso}=330 pF. Though fabrication tolerances exist between the individual instances of L_{reso} and C_{reso}, the relative change in resonance frequency is expected to be similar for a changing C_{sensor}, i. e. C_{IDC}. This is albeit only applicable, if indeed L_{reso} and C_{reso} are constant. As could later be shown in several experiments (see Section 7.3.5), the resonant circuit elements themselves unfortunately exhibit a strong sensitivity on mechanical loading, resulting in changing values of L_{reso} and C_{reso}. In the given circuit configuration, this can however not be distinguished from a change in IDC capacitance, resulting in a strong influence on reported capacitance. In effect, even though the measurement system is assumed to be sufficiently precise for the expected small changes in strain-induced IDC capacitance, mechanical sensitivity of the supposedly constant resonant circuit elements overshadows strain-induced capacitance changes. This can be used to explain the different behavior of the measurement channels during bending in Y: As shown in Figure 7.22, the orientations of the two resonant capacitors on the PCB differ for the channels measuring X and Y direction. Taking into account the difference in lateral contraction for the two loading orientations, this results in different amounts of compression applied to the resonant capacitors. As loading the capacitors results in an equivalent increase of measured capacitance, the effect is more pronounced for bending in Y direction, where compression is stronger.

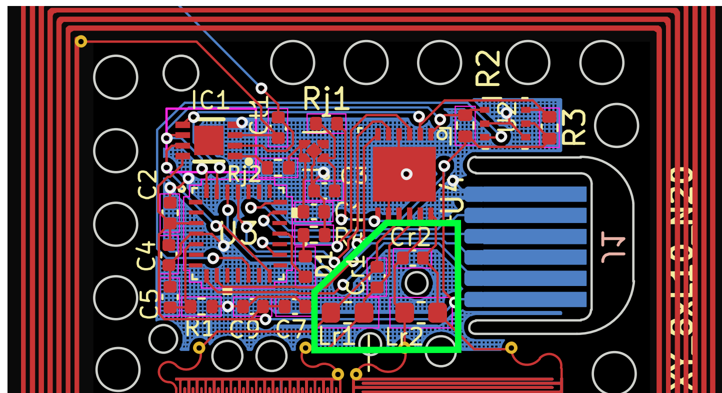

Figure 7.22: Location and orientation of LC components $L_{r1/2}$ and $C_{R1/2}$, i. e. soldering pads, on PCB of capacitive sensor tag

In summary, to allow usage of the IDC for strain measurement, either steps need to be taken to remove mechanical sensitivity of L_{reso} and C_{reso}, or the effect needs to be intentionally used by respectively aligning these and assuring repeatability. Further discussion of this is given in Section 7.3.5.

7.3.5 Effects of Mechanical Loading on Resonant Circuit

To investigate causes for unexpected sensor behavior during the characterization experiments, influence of mechanical load, i. e. compression, on the fixed elements of the sensing resonant circuit was studied in a separate experiment. Effects on the measurement value, i. e. the equivalent capacitance for an otherwise unchanged resonant circuit, were studied for both the inductor and capacitor, to isolate the respective effect. To that end, a test fixture was made, allowing for contacting and loading the SMD packages (see Figure 7.23). Also, to confirm transferability of the results, compression was applied to a sensor-integrated FRP specimen. It is

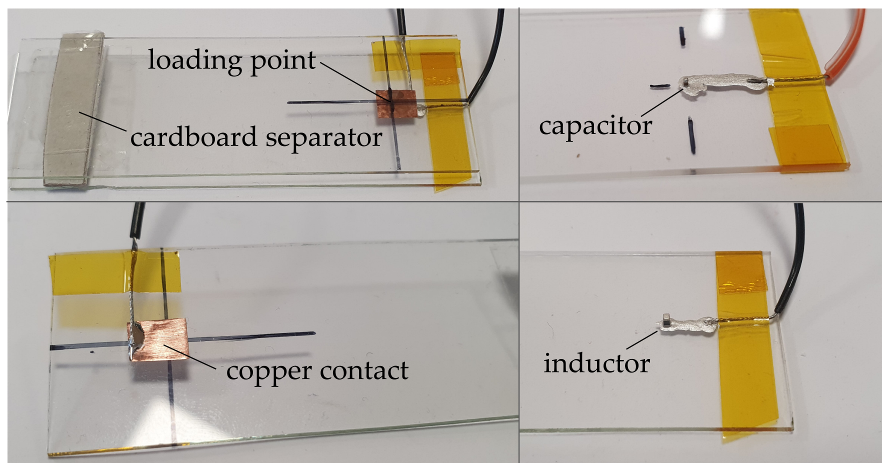

Figure 7.23: Glass fixture for loading resonant circuit elements via fixed weight application.

comprised of two glass plates that are used to contact the package on each end, respectively. The inductor and capacitor are placed on a bottom glass plate via conductive glue. This fixes the package in position, so that it is aligned vertically between the two glass plates, resulting in transversal compression of the specimen (see right side of Figure 7.23). The glue is in turn also used to connect the bottom package side to the measurement circuit with a wired connection. For the top plate, contacting is done via a small copper plate glued to top glass plate, to which a wire was soldered (see bottom left picture in Figure 7.23). A similar setup was used for lateral compression of the two elements, where these were glued horizontally on a glass plate, also via conductive glue. To balance the top plate on the small package surface, a cardboard separator is placed between the two glass plates, allowing for a balanced application of weights on top of the packages. This of course takes some of the applied weight, so not all gravitational force is exerted directly on

the specimens. To minimize this, the weights were placed as well centered on the specimens as possible (as indicated by marks on top of the glass surface). After initial calibration of the resulting circuit (compensation of parasitic capacitances via the function described in Section 6.2), two different weights were placed on the top plate, resulting in different compression forces exerted on the specimens.

Results Measurement results are displayed in Figures 7.24-7.25. Results of the two compression scenarios are plotted consecutively, with a dashed line dividing the two. It can be found that for both load cases, compression has opposite effects on measurement values for the inductor and the capacitor. Increasing compression leads to a decreasing equivalent capacitance, indicating a higher resonant frequency and therefore a decreased inductance, while the opposite is true for compression of the capacitor. For transversal compression of the inductor, application of the relatively small weight of 200 g causes a decrease of 1 pF measured equivalent capacitance, while for the 1.1 kg, capacitance decrease is about 8 pF. For the capacitor, this results in approximately 2.5 pF and 7 pF for the same load cases.

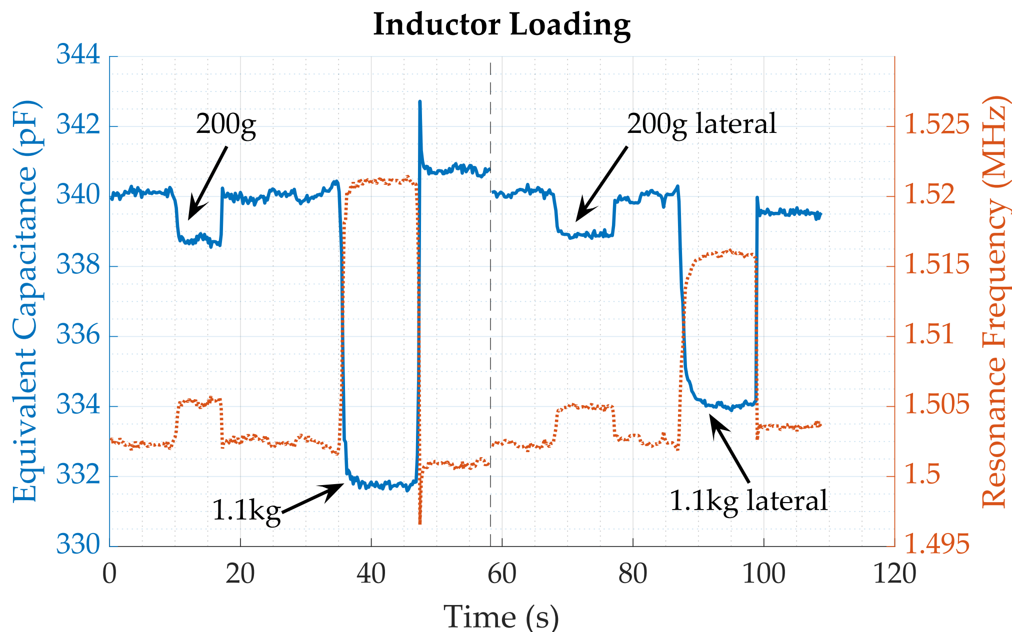

Figure 7.24: Measurement results of equivalent capacitance and resonance frequency for different loading scenarios on the resonant circuit SMD inductor.

Regarding lateral compression, results are similar, though for the capacitor, these are of generally smaller magnitude. This can possibly also be attributed to the comparatively larger area, the same force is applied to, resulting in an overall lesser compression as compared to the transversal, i. e. longitudinal load case, or a difference in internal structure of the specimens. Generally speaking, the results show a high sensitivity of the measurement circuit towards mechanical stress. Regarding the application of the circuit for strain measurement in FRP,

this consequently needs to be taken into account. Possible measures to reduce the magnitude of this effect include encapsulation of the resonant circuit elements, to prevent or reduce compression and selection of other, less mechanically sensitive components. Also, as the effects on measured capacitance are opposite, this could be used by accordingly aligning the two components on the sensor, so that the influences cancel each other out, especially if they are closed close to each other, where loads are similar.

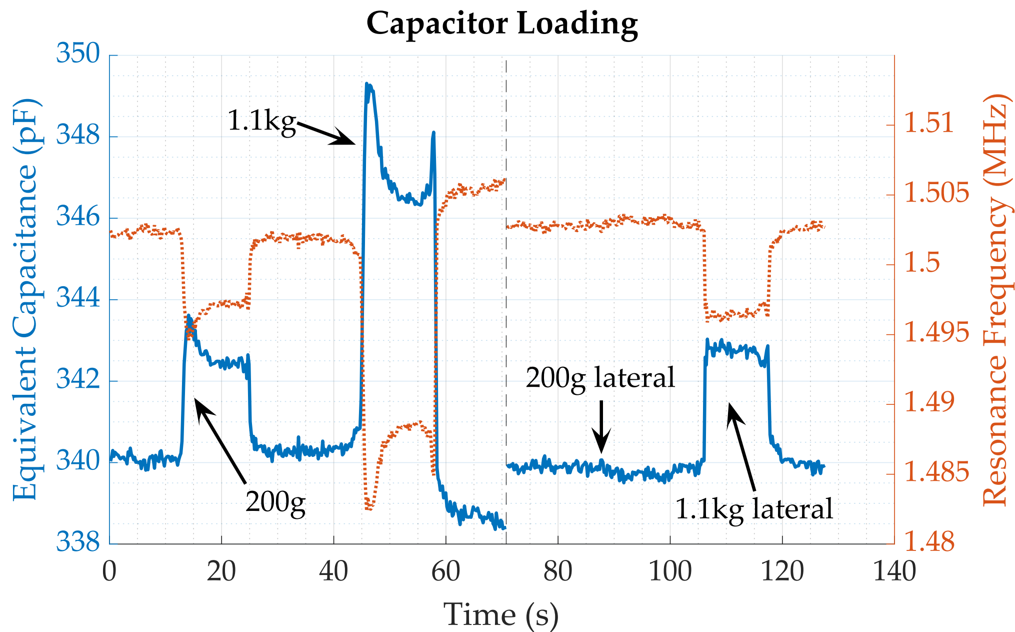

Figure 7.25: Measurement results of equivalent capacitance and resonance frequency for different loading scenarios on the resonant circuit SMD capacitor.

FRP Loading To transfer the prior findings to the data acquired with bending tests of the sensor integrated FRP specimens, another loading experiment was conducted, this time distinctly loading the area of the FRP specimen where the resonant circuit elements are located. This was done by gluing a small, rectangular piece of FRP on both sides of the specimen, right above and beneath the resonant circuit elements (see Figure 7.26). This way, applying a force will result in loading of the resonant inductor and capacitor only, without affecting the IDC. No bending of the specimen occurs in this configuration, and therefore, the IDC is not strained. Force is applied manually with a screw clamp, and the sensor is read out wirelessly via an RFID reader. The clamp is tightened by hand, using only a very moderate amount of strength.

Resulting measurement data is visualized in Figure 7.27. It can be found that exerting force onto the resonant circuit elements leads to a distinct change in resonant frequency, resulting in a change of the equivalent, i. e. measured, capacitance. For comparison with the results of Section 7.3.4.2, the value of the

resonant capacitor (330 pF) has not been compensated for, resembling the theoretical capacitance of the IDC, for the assumption of a stable resonant circuit, i. e. no mechanical sensitivity of the resonant elements. The fact that the capacitance values are negative is very likely due to the compression already exerted on the circuit by the surrounding material shrinking in comparison to cure end, where temperature was much higher (thermal expansion of matrix material). Otherwise, measured capacitance should be positive, as both the base capacitance of the IDC and the higher permittivity of epoxy (as compared to air) contribute positively to the overall measured capacitance. Though the exact amount of force exerted cannot be quantified in this experiment, it does nonetheless serve to prove sensitivity of the resonant circuit to mechanical compression. This supports the interpretations made in Section 7.3.4.2.

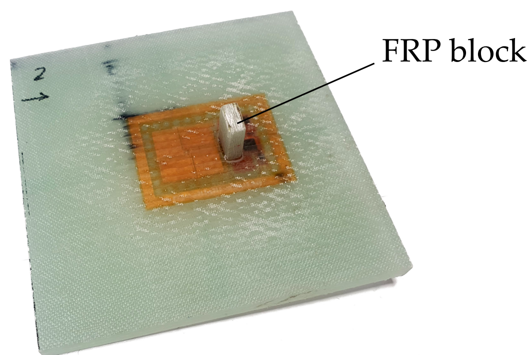

Figure 7.26: FRP specimen with rectangular blocks (top and bottom) for force focus

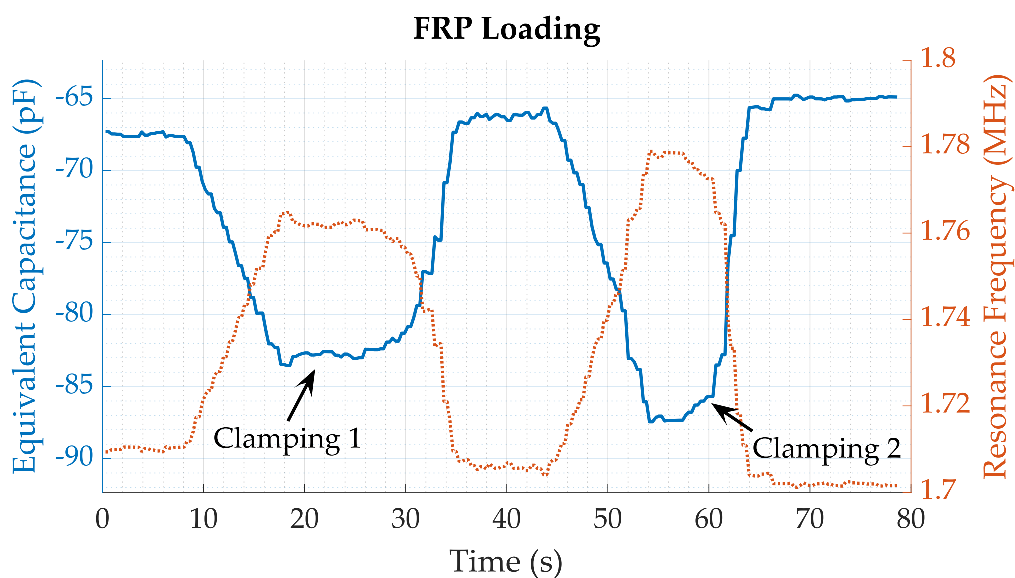

Figure 7.27: Measurement results of equivalent capacitance and resonance frequency for different loading scenarios on the resonant circuit SMD capacitor.

7.3.6 Continuous Variation of Capacitance

Following experiments on strain sensor function and the "step-like" behavior of the measured capacitance for increasing loading (see Section 7.3.4), an additional experiment was conducted to investigate the cause. The phenomenon observed was a nearly constant measurement value given by the FDC2212 for a supposedly continuously increasing capacitance of the resonant circuit, which seemed to appear over a certain range of increasing capacitance, after which measured capacitance started to increase again in the expected fashion. To investigate this, the measurement circuit was connected to a variable capacitor, which was in turn used to continuously increase the capacitance measured. The circuit was powered and read out wirelessly, using the same antenna as present on the sensor tag. The capacitor chosen [137] is an IC which implements a capacitor between two of its terminals, the capacitance of which can be adjusted by applying a voltage between two other terminals. To complete the resonant circuit, the same fixed inductor of 33 µH was added, as during the other experiments. Using a slow voltage ramp provided by a function generator, and manual addition of three fixed capacitances to move through the relevant capacitance range, the input capacitance was varied and the values measured by the sensor circuits were recorded. To allow for comparison with previous measurement data, an offset of 330 pF was substracted, as this is the fixed capacitance used in the sensor circuit.

Results Measurement results are displayed in Figure 7.28. The system can be found to exhibit the same behavior as observed during the bending experiments, showing certain intervals where the reported capacitance does not change, even though actual capacitance increases continuously. Comparing different runs of the same experiment, the values at which the steps appear are reproducible, indicating a systematic problem.

To ascertain if the occurrence of these steps is associated with wireless operation of the circuit, the same experiment was repeated with the circuit being powered by connection to a USB port. Comparison of results showed that the steps only appear for wireless power supply. This might be explained by the FDC2212 being used at the lower limit of its specified supply voltage, while supplied wirelessly. Though previous experiments indicated normal function during wireless operation, available power might be just slightly too low for precise operation at every input capacitance. For further research, this limitation could easily be overcome by reduction of circuit power requirements, i. e. by using a low-power micro controller. Other possible measures regarding circuit optimization are discussed in Section 7.5.

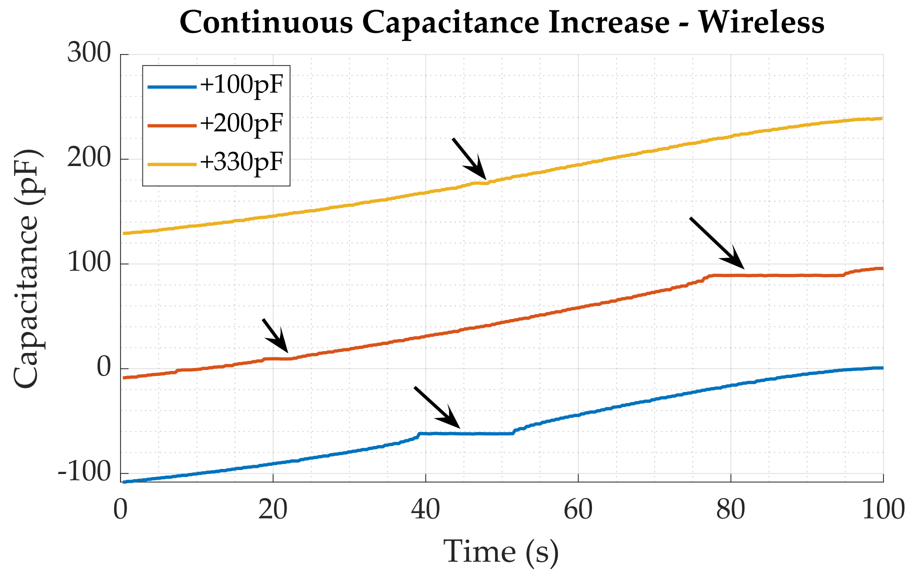

Figure 7.28: Measurement results of the wireless circuit for continuous variation of to be measured capacitance. Visible "steps" indicated by arrows.

7.4 Investigation of System Limitations

This section examines general sensor tag limits in several experiments, starting with quality of the voltage supplied by the energy harvesting output of the RFID transponder and subsequently the regulated output of the voltage regulator. Following this, maximum distance between sensor and reader was determined at which tag-reader communication is still functional. Finally, operating temperature range of the whole system is inspected using a climate chamber.

7.4.1 Power supply

To investigate the power available on the tag during passive operation, average voltage output of the transponder energy harvesting pin was measured at different load resistances. For this, the tag antenna was connected to the transponder (ST25DV) and placed 10 mm from the antenna of a reader development board supplied by STMicroelectronics. The reader field was activated and resistors of different size were consecutively connected to the energy harvesting pin of the transponder, while measuring the resulting voltage drop with an oscilloscope, averaging the measurement results ($n = 20$). The measured voltages and the corresponding power, which was calculated from the resistance and voltage values, are displayed in Figure 7.29. It can be found that total available power shows a local maximum at a load resistance of ca. 150 Ω, yielding a power of 19.27 mW at a voltage level of ca. 1.7 V. Below 150 Ω, both output voltage and power reduce sharply, resulting in 0.95 V for a load of 68 Ω. With increasing resistance, energy

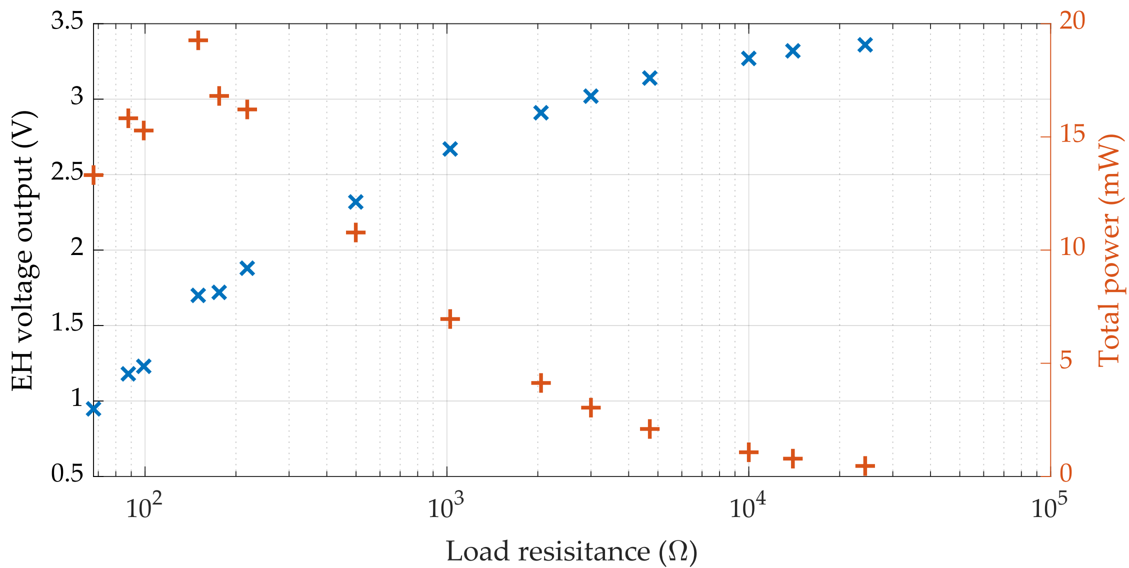

Figure 7.29: Total available power and voltage supplied by the energy harvesting output of the ST25DV, measured at 10mm distance.

harvesting voltage saturates at ca. 3.48 V for infinite resistance, i. e. open contacts / no resistor connected.

Regarding the actual electronics on the sensor tag, the component with the highest minimum supply voltage is the CDC. According to data sheet, it (the FDC2212) needs a supply voltage of $U_0 \geq 2.7\,\mathrm{V}$. For the completely assembled sensor tag, an average supply voltage of 2.7 V could be measured at the terminals of the regulator, at a distance of 10 mm and with the sensor tag electronics operating normally. The systems consequently operates at the lower limit of available power without further optimization of energy consumption. Correlating the resulting voltage with the data from Figure 7.29, it can be concluded that ca. 6 mW are necessary to power the fully assembled sensor tag.

To examine voltage quality of the energy harvesting output and the output of the voltage regulator, a Fast Fourier Transform of the output voltages was recorded. The spectra were averaged with a number of $n = 10$ samples and are displayed in Figure 7.30. It can be found that, apart from small peak at the operating frequency of the reader field (13.56 MHz), which is present in all spectra, supply voltage and energy harvesting voltage are largely clean, i. e. DC. Only for the 499 Ω load case, another narrow peak can be observed at ca. 4.2 MHz.

A similar peak could be observed during measurements with the piezoresistive sensor tag (see Section 5.3.1), which could lead to the assumption of a systematic error in the measurement setup or (sub)harmonic content in the reader field. In contrast to the measurements conducted there, where an overall lower noise level could be observed for the loaded case, the regulated output with the sensor tag operating normally does not show a different noise spectrum than the unregulated output of the energy harvesting pin. This is also the case for the 499 Ω load case.

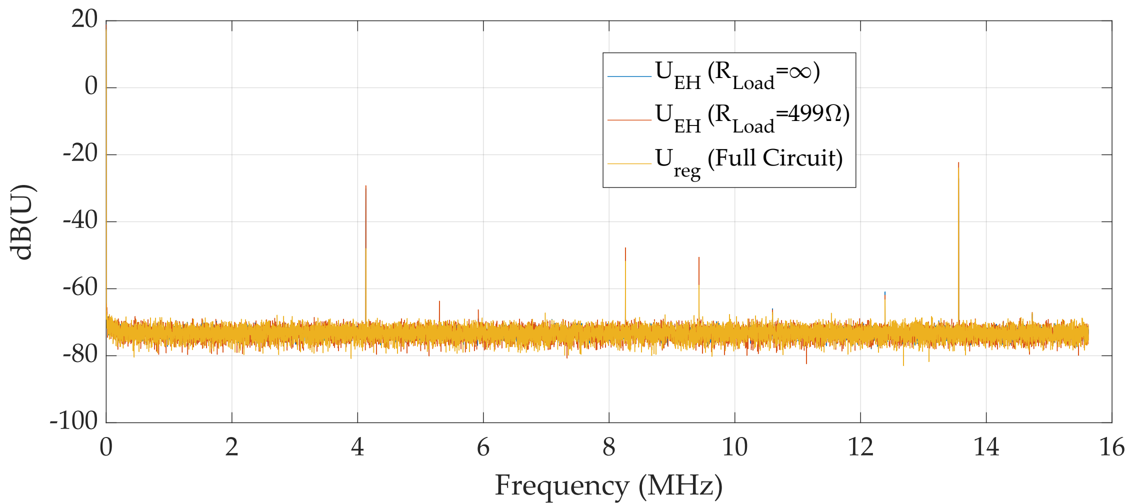

Figure 7.30: Average spectra (FFT) of the voltage supplied by the energy harvesting output of the ST25DV and the voltage regulator (TPS7A0328) at different load cases, measured at 10mm distance, n=10, with PicoScope© 2206B MSO.

As the output voltage of the voltage regulator does not reach the set point of 2.8 V, it can be concluded that power demand of the full circuit is too high for the input voltage (i. e. the harvested voltage) to stay above 2.7 V. This consequently eliminates any possibility for the regulator to smooth the supply voltage output and reduce noise. Looking at the overall system, the measured noise level does not seem to have any negative effect on correct sensor tag function. For future version of the circuitry, reduction of power consumption is albeit easily achievable, as previously mentioned, e. g. by selection of a low power micro controller.

7.4.2 Noise level

To examine noise level of the capacitance measurement on the circuit prototype and compare it with that of the final sensor tag, an experiment was conducted measuring the system output in steady state, without changing the input capacitance. This was done for an unshielded and a shielded type, using an IDC of the same layout each, to make results more comparable and investigate shield influence on noise level. For a time span of five minutes, measurement data was recorded with the IDC suspended in air at a constant temperature of 21 °C, resulting in a total of ca. 1670 samples per measurement. The circuit prototype was powered via USB, as was done during all the other preliminary experiments, while the sensor tag was powered wirelessly. For the experiments with the prototype, measurement data was read out via the virtual COM port of the prototyping board, while for the sensor tag measurement this was done via the wired UART connection included in the on-tag ZIF connector.

Measurement results are displayed in Figures 7.31a and 7.31b. Apart from a different capacitance baseline and a slight absolute difference in IDC capacitance

between prototype and sensor tag, it can be found that measurement data does not differ significantly. Comparing standard deviation of the capacitance measurements, this is also true – no trend towards a lower noise level for either shielded or on-tag IDCs can be observed. Visually, this observation can be confirmed by looking at diagram scaling. Both graphs are scaled to the same resolution, but no significant difference in apparent noise is discernible. Regarding usable, i. e. application-specific signal to noise ratio, this observation is of limited relevance though, as no relevant change in condition, i. e. the to-be-measured physical phenomenon has happened. Nonetheless, this experiment gives a reasonable basis for system noise estimation in steady state condition.

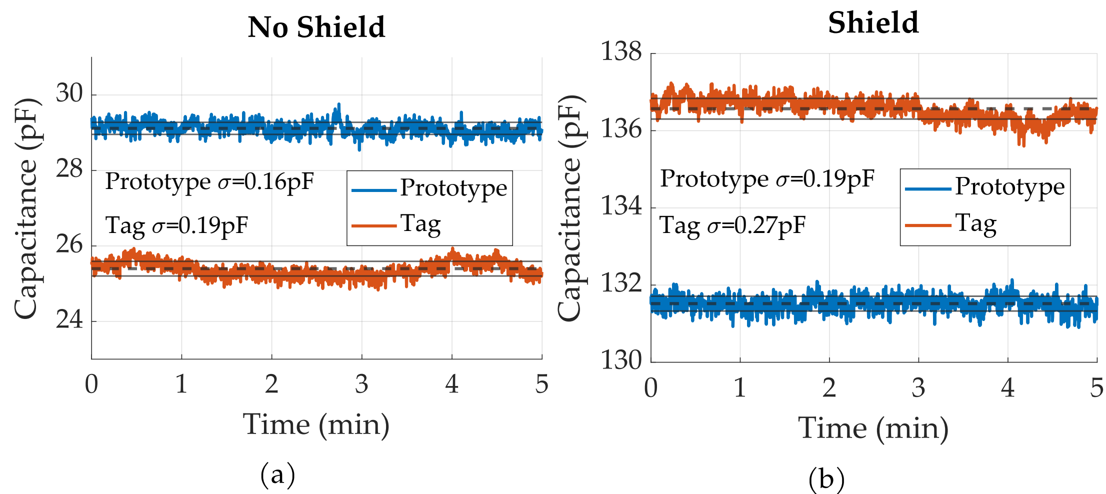

Figure 7.31: Measurement output of sensor tag and breadboard in steady state. IDC used: a) XY 8xL10 N20 (double sided); b) XY 4xL10 N20 (shielded, GND).

To compare absolute noise between the different signals, similar to the comparison done in Section 6.2.7, local noise was also calculated as a difference of the absolute capacitance and the same signal previously filtered via a moving average filter (windows size = 50 samples). This way, results are independent of capacitance baseline. The resulting data is visualized in Figure 7.32. Again, no significant difference can be found for the different designs or circuit states. It can therefore be concluded, that shield presence has no effect on system noise, and that noise level of the prototpye and the final tag do not differ significantly.

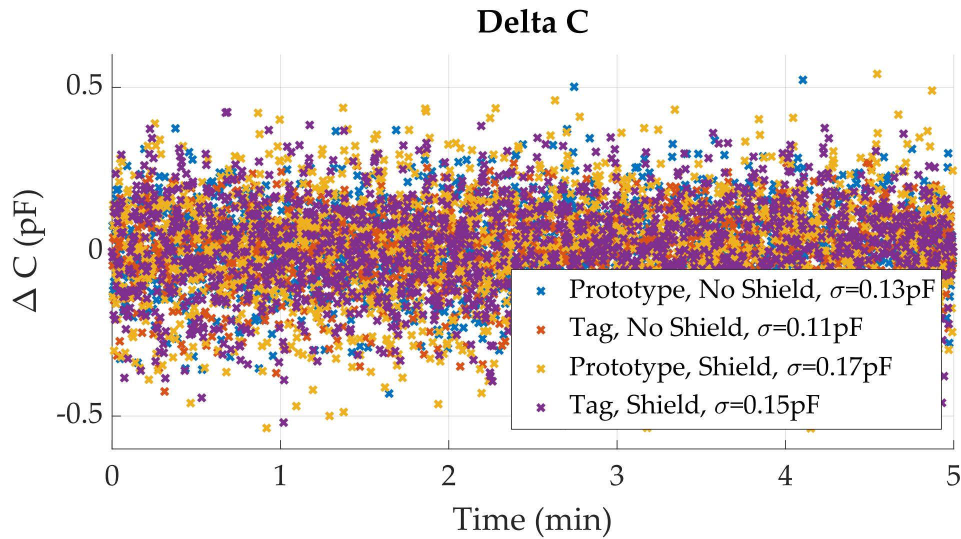

Figure 7.32: Comparison of IDC capacitances for sensor tag and prototype, using difference of raw capacitance values to locally averaged capacitance.

7.4.3 Reading Distance

Experiments with varying tag-reader distance were carried out for both lose and material-integrated sensor tags to investigate maximum reading distance of the sensor system and possible deviations of this between integrated and unintegrated state. Distance between tag and reader was subsequently increased until the first dropouts could be observed in sensor tag data. Experiment setup was done as described in Section 5.3.2, with a slight difference regarding tag placement. To prevent the glass substrate from influencing IDC capacitance, the tag is held in the air above the glass surface by adhesive tape attached to two plastic blocks left and right of the tag (see Figure 7.33). Also, as no significant difference could be observed for increasing FRP strength in between sensor tag and reader, no additional FRP layers were added, simplifying the diagrams. Two tags for each IDC geometry were tested: Tags 1&2 implement a double sided XY configuration, while tags 3&4 use a shielded XY configuration and tags 5&6 contain a double sided L20 N50 geometry.

Measurement results are given in Figure 7.34, both for the separate i. e. lose tags and the same tags integrated into GFRP. Opposed to the "constant values"-phenomenon observed with the piezoresistive sensor tags (see Section 5.3.2), maximum reading distance for the capacitive sensor tags is indicated by at least one of the FDC channels starting to frequently report a capacitance of "$-$inf". This corresponds to the FDC being unable to make a valid measurement. For the experiment conducted, no significant difference of maximum reading distance can be found in between the three different tag types, though the shielded variant seems to exhibit a slight trend towards shorter distances. Similar to the experiments

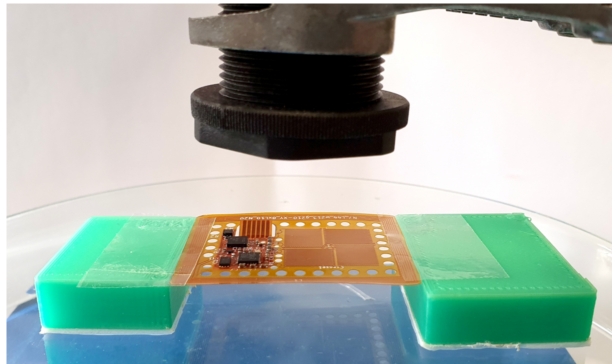

Figure 7.33: Setup for reading distance measurement. Tag held in air via supporting blocks and adhesive tape to prevent substrate influence on IDC capacitance.

with the piezoresistive sensor tag (see Section 5.3.2), integration seems to reduce reading distance. For the capacitive tag, this is reduction amounts to ca. 3 mm.

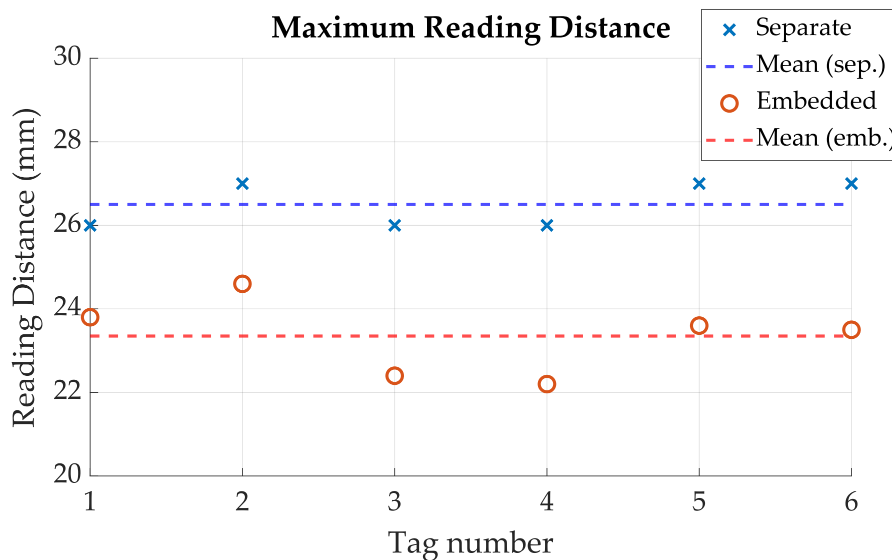

Figure 7.34: Results for reading distance measurement seperate and integrated sensor tags, mean values given for comparison (dashed).

7.4.4 Operating Temperature

To investigate thermal system limitations, experiments regarding the range of operational temperature were also carried out with the capacitive sensor tag. To that end, a sensor tag was placed inside a climate chamber, with a reference temperature sensor attached to it (Pt-100 in 4-wire configuration). Reference and sensor tag data were read out simultaneously, while chamber temperature was varied. The sensor tag was powered wirelessly via the same reader as used in the other experiments (MicroSensys M30, [116]), while the Pt-100 was measured via a digital mutlimeter (Keithley 2100 Series). Before variation of temperature, chamber temperature was

set to 20 °C for one hour, to achieve a stable condition. For the lower temperature range, temperature was then slowly decreased from 20 °C to −40 °C, the latter marking the lower limit of the temperature chamber's specifications. To achieve a continuous temperature change and take into account the speed of the thermal transfers, a duration of two hours was chosen for the experiment, resulting in a temperature slope of approximately 0.5 °C/min. The upper range was investigated using the same setup, increasing temperature from a stable 20 °C up to 150 °C with the same temperature slope, resulting in a duration of 4:20 hours.

Sensor tag and reference data is given in Figure 7.35. It can be found that minimum operating temperature of the tag is not discernible with the equipment available, as the minimum achievable temperature was −43 °C, where the tag was still working as intended. The upper limit of the temperature range was found to be about 128.9 °C, as the tag stopped providing consistent data at that temperature. Regarding the capacitive measurement, first dropouts appeared at temperatures above 112.1 °C, until no valid capacitance data could be read at temperatures above 116.2 °C. This is roughly ten degrees lower than the −40 to 125 °C specified range of the FDC, and might be caused by the FDC being used at the lower limit of its specified supply voltage. The temperature range of −40 to 125 °C targeted with the sensor tag design can therefore only be partially fulfilled, with only the temperature sensor and overall tag operating as intended over the full range. In an application context however, this slightly reduced temperature range should still be sufficient for common curing conditions of VARI processes.

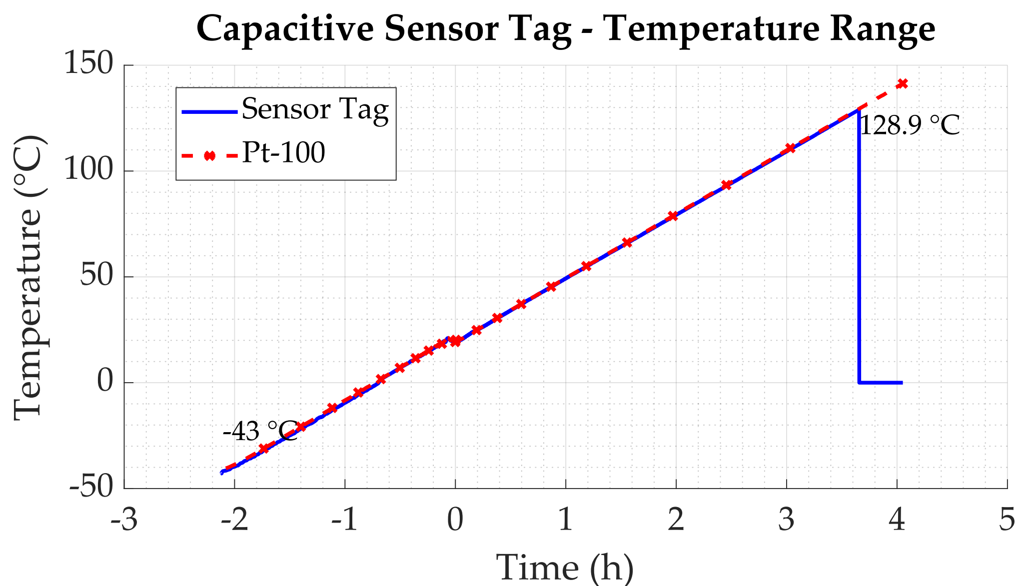

Figure 7.35: Results for determining the operational temperature range of the capacitive sensor tag.

7.5 Conclusions – IDC-based Sensor Tag

This chapter presented the second sensor tag design for FRP integration, elaborating on sensor concept, design and fabrication, before reporting experiments and results conducted to characterize its function and usability. Three different geometries of the sensing element (i. e. the IDC) were implemented on the sensor tag, to compare performance for the intended applications. In the first experiment, influence of temperature on the capacitive measurement was investigated, both with and without the IDC connected, to allow for compensation of temperature-induced changes of the resonant circuit, via the on-tag temperature sensor. Temperature influence was found to be strong, and a polynomial fit was calculated for compensation of temperature-induced resonance frequency drift. To confirm overall sensor tag function, a fully assembled tag was then integrated into the epoxy material already used during the investigations on IDC behavior (Chapter 6), where the system was found to work as expected, producing measurements similar to the prior experiments on epoxy cure. Influence of temperature on measured capacitance was found to be high, as suggested by the corresponding experiment, with the acquired fit allowing for adequate compensation.

Following this, six sensor tags were integrated into an FRP board using a VARI process, to examine sensor function in a realistic context. Experiment results show that detection of the resin flow front is precisely discernible, even without temperature difference of resin and textile, which is a considerable improvement compared to thee prior sensor tag. Regarding monitoring of epoxy cure, results confirm the trends and general behavior observed during the investigations on IDC usage for epoxy cure (Section 6.2.7), though temperature cross sensitivity of the resonant circuit elements strongly influences measured capacitance. The polynomial fit previously calculated for compensation is able to reduce, but not sufficiently eliminate this effect. Additionally, a simple linear compensation was examined and found to provide results conforming slightly better to expectations originating from the previous cure experiments, especially towards the end of cure. Comparing the different IDC geometries, a higher number of electrode fingers increases sensitivity for both resin presence and cure, as was expected, but temperature influence is too strong to allow for precise conclusions in this regard. Higher sensitivity of the shielded versions, as suggested by the preliminary investigations, could therefore not be confirmed.

In order to reduce influence of temperature, it would be possible to select different types of the two resonant circuit elements, that exhibit smaller temperature coefficients. Also, further further investigations of the temperature effect on the circuit could provide a better understanding and successively allow for more precise compensation models. Generally, choice of different values for the resonant elements and a correspondingly different IDC excitation frequency might

also be worth investigating regarding cure monitoring sensitivity, as the dielectric response of the resin is different in other frequency regimes.

Regarding additional, subsequent usage of the IDC for strain measurement of the surrounding FRP, experiment results reveal a strong cross-sensitivity of the resonant circuit elements to mechanical compression. This results in a compression-induced change in resonance frequency of the measurement circuit. Due to measurement principle, this effect is indistinguishable from the strain-induced change of IDC capacitance and corresponding change of resonance frequency, even though the system's resolution is theoretically sufficient to measure these. In other words, the mechanical sensitivity of the resonant circuit itself overshadows the changes in resonance frequency that were supposed to be used for strain measurement, preventing further evaluation of IDC strain sensitivity. Correspondingly, the initially predicted sensitivity difference between IDC geometries could not be confirmed with the experiments conducted.

Potential measures to reduce the negative effect of compression include selection of mechanically less sensitive capacitors and inductors, encapsulation of these in a mechanically stable material, and intentional incorporation of the effect into the measurement principle, e. g. by corresponding orientation of the packages on sensor substrate and characterization of the effect.

Additionally, another phenomenon was observed during the bending experiments, concerning capacitance measurement via the FDC2212. In particular, a "step-like" behavior of measured capacitance, i. e. constant measurement results, is observed for a short interval of actually changing resonance frequency. This of course influences strain measurement results. The effect could be confirmed by an additional experiment and is probably due to the comparably low supply voltage during wireless operation. For later circuit versions, this could easily be prevented by reducing circuit power consumption, e. g. by selecting a low-power micro controller.

Investigating general sensor tag system limitations, maximum obtainable power via energy harvesting was found to be about 19.3 mW at a voltage level of 1.7 V, which is a significant improvement compared to the power obtainable on the prior tag design. For higher voltage levels, i. e. higher loads, available power reduces, resulting in ca. 6 mW for the targeted supply voltage. Noise level of the capacitive measurement was also examined in a dedicated experiment. Results show that noise level does neither change for the embedded version, as compared to circuit prototype, nor is a significant difference discernible for presence of a grounded IDC shield, which was initially assumed. In the application context, noise level is sufficiently low to allow for measurement of expected capacitance changes during fabrication monitoring.

Regarding reading distance, an average maximum of about 26.5 mm was found for the sensor tag in air, and about 23.5 mm for the embedded state. Similar to the results obtained for the piezoresistive tag, integration reduces reading distance

about 3 mm. Concerning temperature, experimental results show that the operational temperature range is sufficiently broad for common applications (e. g. VARI processes). The maximum temperature for the capacitive measurement is slightly lower than expected, as it was found to only work reliably below 112 °C.

In summary, the system was found to partially fulfill the intended purpose, allowing for precise measurement of resin presence (i. e. infusion) and temperature, but failing to precisely measure resin cure in the VARI experiment. Still, the experiments conducted show a great potential of the proposed approach, if cross-sensitivities towards temperature and mechanical compression of the resonant circuit can be reduced, which should be possible. As the system is built with only "off-the-shelf" components and by using standardized fabrication processes, it is easily producible and very cost-efficient, especially compared to established cure monitoring systems. In comparison with the prior tag design, assembly complexity and cost have been simplified even further, by incorporating the sensing element into the tag substrate. Moreover, for applications without the need for subsequent strain measurement, a significant reduction of sensor tag size could be achieved for future designs, assuming a reduction of the cross sensitivities. As epoxy arrival during infusion and subsequent cure is distinctly measurable even with the smallest IDCs investigated in Chapter 6, IDC space requirements and therefore overall substrate outline could be scaled down, reducing cost and the wound effect created in the host material.

Chapter 8
Thesis Conclusion

In this work, two sensor systems have been developed that aim to improve aspects of FRP production and usage, being usable for the whole material life cycle. Focusing on simple and cost-effective producibility, the sensors are designed for application in increasingly automated FRP production environments. Since the sensors are developed for integration into FRP, they are made to operate completely wirelessly and without need for a battery, tremendously reducing the drawbacks associated with wired sensor integration. As general requirements for industrial application, and to ensure low sensor cost and wide compatibility with existing reader hardware, sensor electronics are entirely built from commercially available components, and standardized RFID communication is used.

The first sensor system, as presented in Chapter 5, was found to fully function as intended, using a digital temperature sensor and a piezoresistive strain gauge for monitoring of infusion and cure, and subsequent mechanical loading of the host FRP material. Given a temperature difference between dry textile and fluid resin, the sensors can be used to monitor flow front position, and progressing matrix cure could also be deduced from temperature measurements. Concurrently, material-integrated temperature measurement with the sensor tag was found to be superior to surface-based measurement. Using the strain gauge, bidirectional quantification of host material strain is also possible with the sensors. An average error of less than 60 µm/m could be found for this, though sensor error is nonlinear without further calibration, resulting in higher maximum error values. Maximum measurable strain of the system was found to be ca. 9000 µm/m, while specified strain gauge full scale is 1800 µm/m according to data sheet [112]. A negative effect of sensor presence on mechanical integrity of the surrounding material could not be found, though further experiments are necessary to investigate integration effects in detail. All things considered, overall sensor function could successfully be demonstrated in a proof-of-concept context.

Subsequently, for usage on the second sensor system, properties and behavior of flexible, PCB-integrated IDCs have been investigated in detail. Most importantly, it could be proven that, despite the comparably large electrode sizes, IDCs fabricated via common PCB production techniques can be used for sensing epoxy presence and cure, even if overall finger number is low. Theoretical calculations show that usage of the same IDCs for material-integrated strain measurement should be possible for the larger IDC geometries investigated, given a sufficiently precise measurement system. Experimentally, this could not be confirmed due to high

noise of the prototypical measurement circuit. More details and other aspects on IDC characterization results are given in Section 6.2.12.

Building on the knowledge gained, the second sensor tag was developed, aiming to improve on FRP fabrication monitoring capabilities. The sensor uses shifts in resonant frequency of a parallel resonant circuit for calculation of application-induced IDC capacitance change. To compensate for temperature-induced changes of base resonance frequency, a polynomial fit was calculated from characterization data. During an integration experiment with epoxy glue, the fit could be used to adequately reduce the effect of temperature on measurement data, generally confirming sensor tag function for measurement of epoxy glue cure. Following this, six tags were integrated into FRP using a VARI fabrication setup, to evaluate sensor tag function in a more realistic context. Results show that precise detection of the resin flow front is possible with the second tag, the significance of which is superior to the approach solely using temperature for detection of resin arrival. Measurement data acquired during subsequent cure reflects the general trends expected, using both the calculated polynomial and a linear fit for temperature compensation. However, for a usable quantification of epoxy cure degree, temperature compensation was found to be insufficient. In order to investigate additional usage of the IDC for subsequent strain measurement in the FRP, similar to a capacitive strain gauge, bending tests were conducted with the sensor-integrated samples. The results show a further cross sensitivity of the resonant circuit towards mechanical compression, overshadowing strain-induced influence of IDC capacitance on the resonant circuit. Relating this behavior to the prior cure measurements, temperature-induced FRP deformation could correspondingly potentially explain the difficulties reported with optimally compensating for temperature influence. To reduce these two cross-sensitivities, selection of resonant circuit elements less sensitive to temperature and mechanical compression is the evident approach, possible aided by encapsulation of the resonant circuit in a mechanically stable material. As the effects are of opposing sign for the capacitor and inductor, geometric alignment of these could potentially also be used to make the effects cancel out. Still, the presented approach was found to provide great potential for further research.

For both tags, experiments show that the effective reading distance of the sensors is sufficient for monitoring of most laminate structures. Optimization of power consumption and antenna tuning will nonetheless be able to further increase reading distance, for applications requiring an increased reading range. Resilience to the elevated temperatures occurring during common epoxy curing scenarios could also be proven for both sensor tags, with maximum temperatures of full sensor function being 126.9 °C and 112 °C for tags one and two, respectively. Minimum operation temperatures could not be tested below −40 °C, at which all sensors were still operating.

Although the systems were only evaluated in GFRP, sensor usage in other FRP is possible (e. g. materials using aramide or plastic fibers, or other matrix systems),

with the exception of conductive environments. Regarding mechanical influence on the host material, it could be shown that an inlay in the form of the presented sensor tags did not have a negative effect on breaking strength of the GFRP material investigated. As number of the specimens was low and only bending strength was examined, further research is albeit necessary to make any definite assertions in this regard.

In conclusion, the work presented provides a broad knowledge basis for harnessing the potential offered by optimization of FRP production processes with material-integrated, wireless sensors. This way, time, energy, and resources can be saved, and quality control is simplified. During FRP application, the piezoresistive tag can be used for strain measurement in SHM. Additionally, the sensor concept provides advantages for component handling and maintenance tasks, by allowing for storage of user-specific data, enabling multi-purpose sensor usage for the whole FRP life cycle.

To summarize the most important findings of this work at a glance, these are listed subsequently:

- Completely wireless and battery-less operation of sophisticated sensory electronics is possible, even inside thick FRP laminates and at high temperatures, and with sensors made from common electronic components.
- The sensors survive both the integration process and later on conditions inside mechanically loaded FRP material.
- Reading distance of the sensors presented is sufficiently high to allow tag placement even in thick laminates.
- Bidirectional strain measurement could be successfully be performed inside FRP with the wireless sensors, using resistive strain gauges.
- Experiments show that material-integrated temperature measurements can be used to track the resin flow front and give insights in curing progress, providing a superior information depth compared to surface-based measurements.
- IDCs made on flexible polyimide foils could be used to monitor epoxy presence and cure in the experiments conducted, even if the IDCs are made via common PCB fabrication processes, comprising comparably large geometric features. Resin presence, i. e. flow front progression, is precisely detectable, even without temperature difference between textile and resin.
- Capacitive measurement could be shown to be sufficient for measurement of epoxy presence and cure, opposed to full impedance spectroscopy, as commonly used.
- For the small number of experiments conducted, presence of a sensor tag inlay has no negative effect on breaking strength of the host FRP material.

Acronyms

ADC Analog to Digital Converter.

CDC Capacitance to Digital Converter.

CFRP Carbon Fiber Reinforced Polymer.

DEA Dielectric Analysis.

FBG Fiber Bragg Grating.

FPCB Flexible Printed Circuit Board.

FRP Fiber Reinforced Polymer.

GFRP Glass Fiber Reinforced Polymer.

GPIO General Purpose Input Output.

I^2C Inter-Integrated Circuit.

IA Impedance Analyzer.

IC Integrated Circuit.

IDC InterDigital Capacitor.

INA Instrumentation Amplifier.

IoT Internet-of-Things.

LED Light Emitting Diode.

MUT Material Under Test.

NFC Near Field Communication.

PCB Printed Circuit Board.

PLC Programmable Logic Controller.

RAM Random Access Memory.

RFID Radio Frequency Identification.

RTM Resin Transfer Molding.

SHM Structural Health Monitoring.

VARI Vacuum Assisted Resin Infusion.

ZIF Zero Insertion Force.

List of Figures

1.1 Schematic representation of RTM and VARI processes with optional preforming step, according to [9]. . . . 3
1.2 Sensor Tag in FRP, schema . . . 7

2.1 Schematic representation of fibers and matrix . . . 10
2.2 Schematic representation of inductive transponder coupling . . . 17
2.3 Transponder equivalent circuit . . . 18
2.4 Spiral, planar antenna coil (square) . . . 18
2.5 Spiral, planar antenna coil (rectangular) . . . 19
2.6 Example measurement for transponder resonance frequency . . . 22
2.7 Schematic illustration of three point bending test . . . 23
2.8 Schematic representation of strain gauge principle and application . 24
2.9 Wheatstone bridge circuit . . . 25
2.10 Full bridge Wheatstone bridge circuit, in plane . . . 27
2.11 Parallel Plate Capacitor . . . 28
2.12 Polarization mechanisms across the frequency spectrum . . . 29
2.13 Transition from parallel plate to planar capacitor . . . 31
2.14 Interdigital Capacitor, schematic representation . . . 32
2.15 Schematic representation of capacitive strain gauge concept . . . 33
2.16 Parallel resonant circuit for C measurement . . . 35
2.17 Schematic circuit layout of FDC2212 measurement principle . . . 36

3.1 Automated handling of textiles and sensor tags, schema . . . 37
3.2 CAD rendering of sensor tag applicator for robot operation . . . 39

4.1 DEA principle, schematically . . . 42
4.2 Schematic comparison of DEA sensors for FPR production monitoring 43

5.1 Schematic representation of the sensor tag circuit . . . 56
5.2 Resonance frequencies of different antenna geometries for piezoresistive sensor tag . . . 58
5.3 Antenna Resonance Frequencies Piezoresistive Tag . . . 59
5.4 Loop antenna for resonance measurements . . . 59
5.5 Strain gauge configuration and glued gauge . . . 60
5.6 Conceptual drawing of piezoresistive sensor tag . . . 63
5.7 Fully assembled sensor tag with component descriptions. . . . 65
5.8 Sensor-integrated FRP specimen and bending test . . . 65
5.9 Fiber orientations used for fabrication monitoring experiments. . . . 67

5.10 Laminate layup and experiment concept in fabrication monitoring experiment. 68
5.11 FRP fabrication setup for sensor tag integration. 69
5.12 Sensor tag and reference temperature measurements during infusion. Visible arrival times of resin flow front marked by dashed lines. 70
5.13 Sensor tag and reference temperature measurements for the whole production process. Changes in heating set points indicated by dashed lines. 71
5.14 Sensor-integrated FRP specimen and bending test 72
5.15 All deflections for specimen I4 73
5.16 Mean deflections during non-destructive testing (X and Y) 74
5.17 Strain measurement specimen I4, X direction 75
5.18 Strain measurement specimen I4, Y direction 76
5.19 Strain values during non-destructive testing (X) 77
5.20 Strain values during non-destructive testing (Y) 78
5.21 Mean standard deviations during non-destructive testing (X and Y) 80
5.22 Deflection values during non-destructive testing 82
5.23 Strain values during destructive testing: Sensor tag 83
5.24 Strain values during destructive testing: Sensor tag and reference . . 83
5.25 Failure comparison for FRP specimen with and without sensor tag. Both specimen show delamination close to the top layer. 84
5.26 Exerted force during destructive tests for specimens with (dashed lines) and without (solid lines) sensor tags. 85
5.27 Total available power for piezoresistive sensor tag 86
5.28 Spectrum of NHS3152 high drive GPIO output 87
5.29 Schematic illustration of distance measurement setup 88
5.30 Distance measurement setup 88
5.31 Distance at which sensor values did not change anymore vs. FRP thickness for integrated and unintegrated sensor tags. 89
5.32 Maximum reading distance vs. FRP thickness for integrated and unintegrated sensor tags. 90
5.33 Operating Temperature Measurements 92

6.1 Equivalent circuit model for C calculation using approach by Igreja et.al. 96
6.2 Unit cell definition for IDC C calculation 97
6.3 Analytical C calculation comparison N_{abs} and g 99
6.4 Analytical C calculation comparison w and strain 100
6.5 Max IDC finger number for combinations of w and g in fixed width . 101
6.6 IDC capacitance for combinations of w and g in fixed width 102
6.7 Analytical C calculation comparison w and strain 103
6.8 Circuit Prototype for Capacitive Sensor Tag 104
6.9 Capacitor interface of prototype sensor tag circuit 105
6.10 Rounded-off IDC corners 106
6.11 XY IDC footprint 106
6.12 FPCB layer stack up 107

6.13 IDC prototypes with pin headers mounted for preliminary experiments . . . 107
6.14 IDC frequency dependency without shield . . . 109
6.15 IDC Frequency dependency with Shield . . . 109
6.16 Spectral Analysis of resonance circuit with FDC2212 . . . 110
6.17 Qualification measurements for tag circuitry using FDC2212 . . . 112
6.18 IDC prototypes mounted on GFRP . . . 113
6.19 IDC substrate dependency comparison with/without shield . . . 114
6.20 Different IDC geometries fabricated for preliminary experiments on C size . . . 115
6.21 Capacitances for different IDC geometries with/without shield . . . 116
6.22 Comparison of measured C and calculated C for prototypical IDCs . 119
6.23 Preliminary Cure Measurement Experiments - IDC Setup . . . 120
6.24 L5 N40 IDC cure test . . . 120
6.25 L10 N40 IDC cure test . . . 120
6.26 L10 N60 IDCS cure test . . . 121
6.27 Comparison of calculated and measured IDC capacitance . . . 123
6.28 IDC Noise comparison . . . 125
6.29 IDC temperature dependency in epoxy glue . . . 127
6.30 IDC capacitance temperature dependency with/without shield in cured epoxy glue . . . 127
6.31 XY IDC finger length dependency comparison with/without shield . 128
6.32 Strain sensitivity of XY IDC 4xL10 N20, X-direction . . . 129
6.33 Strain sensitivity of shielded XY IDC 4xL10 N20, X-direction . . . 130
6.34 Double sided IDC prototypes . . . 131
6.35 IDC capacitance for single and double sided versions . . . 132

7.1 Block diagram of capacitive sensor tag . . . 140
7.2 Different approaches for antenna size (capacitive sensor tag) . . . 142
7.3 Resonance frequencies of different antenna geometry prototypes for capacitive sensor tag . . . 143
7.4 CAD view of tag versions with different IDCs . . . 144
7.5 Fully assembled capacitive sensor tag . . . 147
7.6 ZIF connector for sensor tag interfacing and programming . . . 148
7.7 Influence of temperature on capacitive sensor tag measurements . . 150
7.8 Influence of temperature on measured capacitance and polynomial fits . . . 151
7.9 Fitting difference for temperature compensation of resonant circuit . 151
7.10 Setup for epoxy cure test . . . 152
7.11 Tag measurements during epoxy cure test . . . 153
7.12 Temperature compensated tag measurements during epoxy cure test 153
7.13 FRP integration setup for capacitive sensor tag . . . 154
7.14 Raw Capacitance and Temperature during Infusion . . . 155
7.15 Raw Capacitance and Temperature for Integration Experiment . . . 156
7.16 Capacitance and Temperature for Integration Experiment, polynomial fit . . . 157

7.17 Capacitance and calculated degree of cure for Integration Experiment, polynomial fit 158
7.18 Capacitance and calculated degree of cure for Integration Experiment, linear fit 159
7.19 FRP bending specimen with integrated capacitive sensor tag 161
7.20 Coordinate system of bending specimen with capacitive sensor tag . 161
7.21 Bending test results for capacitive sensor tag, Tag Nr.2 162
7.22 Location of LC components on PCB of capacitive sensor tag 164
7.23 Fixture for loading resonant circuit elements 165
7.24 Influence of applied load on measured equivalent capacitance for resonant inductor 166
7.25 Influence of applied load on measured equivalent capacitance for resonant capacitor 167
7.26 FRP specimen for clamping experiment 168
7.27 Influence of applied load on measured equivalent capacitance for resonant capacitor 168
7.28 System response to continuous variation of input capacitance 170
7.29 Total available power for capacitive sensor tag 171
7.30 Voltage spectrum energy harvesting output and regulator 172
7.31 Noise measurements for capacitive sensor tag with grounded shield 173
7.32 Comparison of local noise for sensor tag and prototype 174
7.33 Reading distance measurement setup for capacitive sensor tag 175
7.34 Reading distance measurement results for capacitive sensor tag . . . 175
7.35 Operation temperature range for capacitive sensor tag 176

A.1 Connection diagram PC-Reader-Tag 203
A.2 RFID reader script flow chart 207
A.3 Arrangement of capacitive sensor tags during integration 208
A.4 Bending test results for capacitive sensor tag, Tag Nr.1 209
A.5 Bending test results for capacitive sensor tag, Tag Nr.3 209
A.6 Bending test results for capacitive sensor tag, Tag Nr.4 210
A.7 Bending test results for capacitive sensor tag, Tag Nr.5 210
A.8 Bending test results for capacitive sensor tag, Tag Nr.6 211
A.9 Schematic for Piezoresistive Tag 212
A.10 Schematic for Piezoresistive Tag 213
A.11 PCB Layout for piezoresistive sensor tag 214
A.12 PCB Layout for capacitive sensor tag 215

List of Tables

2.1 Tensile strength and density of FRPs compared to metals 10
2.2 Comparison of different fiber materials 12
2.3 Comparison of different RFID standards 16
2.4 Turn exponents and C_p for planar, rectangular, spiral inductors . . . 20

3.1 Young's modulus for some exemplary duroplastic matrix materials . 40

5.1 Antenna geometry parameters for piezoresistive sensor tag 57
5.2 Maximum sensor errors for the bending tests 79
5.3 Maximum forces before breakage of FRP specimens. 84

6.1 Measured results of IDC capacitance sizes for different designs . . . 117
6.2 Comparison of measured C and calculated C for prototypical IDCs . 118
6.3 Capacitances and capacitance changes relative to prior event for different IDCs and relevant events during curing tests 124

A.1 Reader message description 204
A.2 Tag command list 206

References

[1] H. Schürmann, *Konstruieren mit Faser-Kunststoff-Verbunden: mit 39 Tabellen* (VDI-[Buch]), 2., bearb. und erw. Aufl. Berlin Heidelberg: Springer, 2007, 672 pp., ISBN: 978-3-540-72189-5.

[2] Federation of Reinfoced Plastics, *Der europäische markt für faserverstärkte kunststoffe / composites 2021*, 2022. Accessed: 2023-03-24. [Online]. Available: https://www.avk-tv.de/files/20220503_pm_04_2022_marktbericht_2021_2.pdf.

[3] AVK – Industrievereinigung Verstärkte Kunststoffe e. V., Ed., *Handbuch Faserverbundkunststoffe/Composites*, Wiesbaden: Springer Fachmedien Wiesbaden, 2013, ISBN: 978-3-658-02754-4 978-3-658-02755-1. DOI: 10.1007/978-3-658-02755-1. Accessed: 2023-03-27. [Online]. Available: http://link.springer.com/10.1007/978-3-658-02755-1.

[4] K. Lechler and M. Menner, *FASERVERBUNDWERKSTOFFE Lehrerhandbuch*. Augsburg: Carbon Composites e.V./Universität Augsburg, 2016. [Online]. Available: https://www.lehrplanplus.bayern.de/sixcms/media.php/71/CCeV_Lehrerhandbuch_Faserverbundwerkstoffe.pdf.

[5] L. Bertram, M. Brink, K.-D. Thoben, and W. Lang, "A passive, wireless sensor node for material-integrated strain and temperature measurements in glass fiber reinforced composites," in 2022-09-04, pp. 182–193, ISBN: 978-3-031-16280-0. DOI: 10.1007/978-3-031-16281-7_18.

[6] L. Bertram, M. Brink, and W. Lang, "Material-integrated temperature sensors for wireless monitoring of infusion and curing in composite production," presented at the Sensor and Measurement Science International, Nuremberg, 2023-05-08, pp. 261 –263, ISBN: 978-3-9819376-8-8. DOI: 10.5162/SMSI2023/E5.4.

[7] L. Bertram, M. Brink, and W. Lang, "Wireless, material-integrated sensors for strain and temperature measurement in glass fibre reinforced composites," *Sensors*, vol. 23, no. 14, p. 6375, 2023-07-13, ISSN: 1424-8220. DOI: 10.3390/s23146375. Accessed: 2023-07-27. [Online]. Available: https://www.mdpi.com/1424-8220/23/14/6375.

[8] L. Bertram, M. Brink, and W. Lang, "A wireless strain sensor for measurement in composites," in *Eurosensors XXXIV - Proceedings*, Lecce, Italy, 2023-09-10. DOI: 10.3390/proceedings2024097049.

[9] M. Neitzel, P. Mitschang, and U. Breuer, Eds., *Handbuch Verbundwerkstoffe: Werkstoffe, Verarbeitung, Anwendung*, 2., aktualisierte und erw. Aufl, München: Hanser, 2014, 554 pp., ISBN: 978-3-446-43697-8 978-3-446-43696-1.

[10] M. J. Lodeiro and D. R. Mulligan, *Cure Monitoring Techniques for Polymer Composites, Adhesives and Coatings*. Middlesex, United Kingdom, TW11 0LW: National Physical Laboratory Teddington, 2005. [Online]. Available: https://www.npl.co.uk/special-pages/guides/mgpg75.aspx?ext=.pdf.

[11] S. Konstantopoulos, E. Fauster, and R. Schledjewski, “Monitoring the production of FRP composites: A review of in-line sensing methods,” *Express Polymer Letters*, vol. 8, no. 11, pp. 823–840, 2014, ISSN: 1788618X. DOI: 10.3144/expresspolymlett.2014.84. Accessed: 2022-03-18. [Online]. Available: http://www.expresspolymlett.com/letolt.php?file=EPL-0005435&mi=c.

[12] M. Kahali Moghaddam *et al.*, “Design, fabrication and embedding of microscale interdigital sensors for real-time cure monitoring during composite manufacturing,” *Sensors and Actuators A: Physical*, vol. 243, pp. 123–133, 2016-06, ISSN: 09244247. DOI: 10.1016/j.sna.2016.03.017. Accessed: 2023-04-12. [Online]. Available: https://linkinghub.elsevier.com/retrieve/pii/S0924424716301169.

[13] T. E. Twardowski, S. E. Lin, and P. H. Geil, “Curing in thick composite laminates: Experiment and simulation,” *Journal of COMPOSITE MATERIALS*, no. 27, pp. 216–250, 1993.

[14] Q. Ai, “Variotherme Verarbeitung von Epoxidharz zur Zyklusverkürzung im RTM Prozess,” Publication Title: Technische Universität Berlin, Doctoral Thesis, Universitätsverlag der TU Berlin, Berlin, 2018. DOI: 10.14279/depositonce-6664. [Online]. Available: http://dx.doi.org/10.14279/depositonce-6664.

[15] L. Sorrentino, C. Bellini, D. Capriglione, and L. Ferrigno, “Local monitoring of polymerization trend by an interdigital dielectric sensor,” *The International Journal of Advanced Manufacturing Technology*, vol. 79, no. 5, pp. 1007–1016, 2015-07, ISSN: 0268-3768, 1433-3015. DOI: 10.1007/s00170-015-6892-x. Accessed: 2023-01-30. [Online]. Available: http://link.springer.com/10.1007/s00170-015-6892-x.

[16] D Kranbuehl, P Haverty, M Hoff, R. D. Hoffman, and J. J. Godfrey, “Dynamic dielectric analysis for nondestructive cure monitoring and process control,” *Journal of REINFORCED PLASTICS AND COMPOSITES*, no. 8, p. 10, 1989. [Online]. Available: https://journals.sagepub.com/doi/pdf/10.1177/073168448900800501.

[17] H. Rocha, C. Semprimoschnig, and J. Nunes, “Sensors for process and structural health monitoring of aerospace composites: A review,” *Engineering Structures*, vol. 237, p. 112 231, 2021-06-01. DOI: 10.1016/j.engstruct.2021.112231.

[18] M. A. Dimassi, M. John, and A. S. Herrmann, “Investigation of the temperature dependent impact behaviour of pin reinforced foam core sandwich structures,” *Composite Structures*, vol. 202, pp. 774–782, 2018, Publisher: Elsevier BV, ISSN: 0263-8223. [Online]. Available: http://dx.doi.org/https://doi.org/10.1016/j.compstruct.2018.04.012.

[19] D. Kinet, P. Mégret, K. Goossen, L. Qiu, D. Heider, and C. Caucheteur, “Fiber bragg grating sensors toward structural health monitoring in composite materials: Challenges and solutions,” *Sensors*, vol. 14, no. 4, pp. 7394–7419, 2014-04-23, ISSN: 1424-8220. DOI: 10.3390/s140407394. Accessed: 2022-12-04. [Online]. Available: http://www.mdpi.com/1424-8220/14/4/7394.

[20] H. Montazerian, A. Rashidi, A. S. Milani, and M. Hoorfar, “Integrated sensors in advanced composites: A critical review,” *Critical Reviews in Solid State and Materials Sciences*, vol. 45, no. 3, pp. 187–238, 2020-05-03, ISSN: 1040-8436, 1547-6561. DOI: 10.1080/10408436.2019.1588705. Accessed: 2022-05-10. [Online]. Available: https://www.tandfonline.com/doi/full/10.1080/10408436.2019.1588705.

[21] W. Hellerich, G. Harsch, and E. Baur, *Werkstoff-Führer Kunststoffe: Eigenschaften, Prüfungen, Kennwerte*, 10., [vollst. überarb.] Aufl. München: Hanser, 2010, 588 pp., ISBN: 978-3-446-42436-4.

[22] H. Lengsfeld, *Faserverbundwerkstoffe : Prepregs und ihre Verarbeitung* (Hanser eLibrary). München: Hanser, 2015, ISBN: 978-3-446-44080-7. [Online]. Available: http://dx.doi.org/10.3139/9783446440807.

[23] J. Qureshi, "A review of recycling methods for fibre reinforced polymer composites," *Sustainability*, vol. 14, no. 24, p. 16 855, 2022-12-15, ISSN: 2071-1050. DOI: 10.3390/su142416855. Accessed: 2023-07-09. [Online]. Available: https://www.mdpi.com/2071-1050/14/24/16855.

[24] M. Ribeiro *et al.*, "Recycling approach towards sustainability advance of composite materials' industry," *Recycling*, vol. 1, no. 1, pp. 178–193, 2016-06-09, ISSN: 2313-4321. DOI: 10.3390/recycling1010178. Accessed: 2023-07-09. [Online]. Available: http://www.mdpi.com/2313-4321/1/1/178.

[25] K. Finkenzeller, *RFID-Handbuch : Grundlagen und praktische Anwendungen von Transpondern, kontaktlosen Chipkarten und NFC* (Hanser eLibrary), 7., aktualisierte und erweiterte Auflage. München: Hanser, 2015, ISBN: 978-3-446-44439-3. [Online]. Available: http://dx.doi.org/10.3139/9783446444393.

[26] A. Lazaro, R. Villarino, and D. Girbau, "A survey of NFC sensors based on energy harvesting for IoT applications," *Sensors*, vol. 18, no. 11, p. 3746, 2018-11-02, ISSN: 1424-8220. DOI: 10.3390/s18113746. Accessed: 2020-10-02. [Online]. Available: http://www.mdpi.com/1424-8220/18/11/3746.

[27] F. Costa, S. Genovesi, M. Borgese, A. Michel, F. A. Dicandia, and G. Manara, "A review of RFID sensors, the new frontier of internet of things," *Sensors*, vol. 21, no. 9, p. 3138, 2021-04-30, ISSN: 1424-8220. DOI: 10.3390/s21093138. Accessed: 2023-05-22. [Online]. Available: https://www.mdpi.com/1424-8220/21/9/3138.

[28] K. Sattlegger and U. Denk, *Navigating your way through the RFID jungle*, 2014. [Online]. Available: https://www.ti.com/lit/wp/slyy056/slyy056.pdf.

[29] S. Lermthong, S. Airphaiboon, and S. Wisavataksin, "Tire pressure monitoring system using low-frequency RFID energy harvesting," in *2023 International Electrical Engineering Congress (iEECON)*, Krabi, Thailand: IEEE, 2023-03-08, pp. 142–145, ISBN: 9798350332360. DOI: 10.1109/iEECON56657.2023.10126689. Accessed: 2023-08-03. [Online]. Available: https://ieeexplore.ieee.org/document/10126689/.

[30] STMicroelectronics NV, *AN2866 application note - how to design a 13.56 MHz customized antenna for ST25 NFC / RFID tags*, 2020. Accessed: 2023-08-25. [Online]. Available: https://www.st.com/resource/en/application_note/an2866-how-to-design-a-1356-mhz-customized-antenna-for-st25-nfc--rfid-tags-stmicroelectronics.pdf.

[31] NXP Semiconductors B.V., *NTAG antenna design guide*, 2018. [Online]. Available: https://community.nxp.com/pwmxy87654/attachments/pwmxy87654/nfc/6155/1/AN11276.pdf.

[32] H. Wheeler, "Simple inductance formulas for radio coils," *Proceedings of the Institute of Radio Engineers*, vol. 16, no. 10, pp. 1398–1400, 1928-10, Conference Name:

Proceedings of the Institute of Radio Engineers, ISSN: 2162-6626. DOI: 10.1109/JRPROC.1928.221309.

[33] S. Mohan, M. del Mar Hershenson, S. Boyd, and T. Lee, "Simple accurate expressions for planar spiral inductances," *IEEE Journal of Solid-State Circuits*, vol. 34, no. 10, pp. 1419–1424, 1999-10, Conference Name: IEEE Journal of Solid-State Circuits, ISSN: 1558-173X. DOI: 10.1109/4.792620.

[34] Keysight Technologies Inc., *Using a network and impedance analyzer to evaluate 13.56 MHz RFID tags and readers/writers*, 2017. Accessed: 2023-08-25. [Online]. Available: https://www.keysight.com/us/en/assets/7018-02030/application-notes/5990-3442.pdf.

[35] Keysight Technologies Inc., *Non-contact measurement method for 13.56 MHz RFID tags*, 2022-09-19. Accessed: 2022-09-19. [Online]. Available: https://www.keysight.com/us/en/assets/7018-02031/application-notes/5990-3443.pdf?success=true.

[36] M. Gebhart, R. Neubauer, M. Stark, and D. Warnez, "Design of 13.56 MHz smartcard stickers with ferrite for payment and authentication," in *2011 Third International Workshop on Near Field Communication*, 2011-02, pp. 59–64. DOI: 10.1109/NFC.2011.14.

[37] S. Paul and R. Paul, *Grundlagen der Elektrotechnik und Elektronik 3*. Berlin, Heidelberg: Springer Berlin Heidelberg, 2017, ISBN: 978-3-662-44977-6 978-3-662-44978-3. DOI: 10.1007/978-3-662-44978-3. Accessed: 2023-08-04. [Online]. Available: http://link.springer.com/10.1007/978-3-662-44978-3.

[38] W. Grellmann, S. Seidler, and V. Altstädt, Eds., *Kunststoffprüfung*, 3., [aktualisierte] Aufl, München: Hanser, 2015, 715 pp., ISBN: 978-3-446-44390-7 978-3-446-44350-1.

[39] B. Heine, "Mechanische Eigenschaften rissfreier Proben bei steigender Beanspruchung," in *Werkstoffprüfung*, 3rd ed. München: Carl Hanser Verlag GmbH & Co. KG, 2015-06-08, pp. 150–254, ISBN: 978-3-446-44455-3 978-3-446-44505-5. DOI: 10.3139/9783446445055.006. Accessed: 2021-08-04. [Online]. Available: http://www.hanser-elibrary.com/doi/10.3139/9783446445055.006.

[40] W. Lang, *Sensors and Measurement Systems* (River Publishers Series in Electronic Materials and Devices). Aalborg: River Publishers, 2019, ISBN: 978-87-7022-028-6. [Online]. Available: https://search.ebscohost.com/login.aspx?direct=true&db=nlebk&AN=2018166&site=ehost-live.

[41] K. Hoffmann, *Eine Einführung in die Technik des Messens mit Dehnungsmeßstreifen*. Darmstadt: Hottinger Baldwin Messtechnik, 1987. [Online]. Available: http://katalog.suub.uni-bremen.de/DB=1/LNG=DU/CMD?ACT=SRCHA&IKT=8000&TRM=14112874*.

[42] W. Lang, *Messen in der Elektrotechnik*, 1. Auflage. Norderstedt: BoD – Books on Demand, 2020, 180 pp., ISBN: 978-3-7519-5419-8.

[43] S. Paul and R. Paul, *Grundlagen der Elektrotechnik und Elektronik 2 : Elektromagnetische Felder und ihre Anwendungen*. Berlin, Heidelberg: Springer Berlin Heidelberg, 2012.

[44] E. Ivers-Tiffée and W. v. Münch, *Werkstoffe der Elektrotechnik: mit 40 Tabellen* (Lehrbuch Elektrotechnik), 10., überarb. und erw. Aufl. Wiesbaden: Teubner, 2007, 266 pp., OCLC: 180067532, ISBN: 978-3-8351-0052-7. [Online]. Available: http://

doku01ae.item.uni-bremen.de/agae/AG_Studi/5600_SeeRoad/Ivers-TifféeundMünch-2007-WerkstoffederElektrotechnikmit40Tabellen.pdf.

[45] Keysight Technologies Inc., *Basics of measuring the dielectric properties of materials - application note*, 2020. Accessed: 2023-07-29. [Online]. Available: https://www.keysight.com/us/en/assets/7018-01284/application-notes/5989-2589.pdf.

[46] V. F. Lvovich, *Impedance spectroscopy: applications to electrochemical and dielectric phenomena*. Hoboken, N.J: Wiley, 2012, 353 pp., OCLC: ocn668195856, ISBN: 978-0-470-62778-5.

[47] A. Mamishev, K. Sundara-Rajan, F. Yang, Y. Du, and M. Zahn, "Interdigital sensors and transducers," *Proceedings of the IEEE*, vol. 92, no. 5, pp. 808–845, 2004-05, Conference Name: Proceedings of the IEEE, ISSN: 1558-2256. DOI: 10.1109/JPROC.2004.826603.

[48] X. Hu and W. Yang, "Planar capacitive sensors – designs and applications," *Sensor Review*, vol. 30, no. 1, pp. 24–39, 2010-01-26, ISSN: 0260-2288. DOI: 10.1108/02602281011010772. Accessed: 2023-06-21. [Online]. Available: https://www.emerald.com/insight/content/doi/10.1108/02602281011010772/full/html.

[49] X. Li, S. Larson, A. Zyuzin, and A. Mamishev, "Design principles for multichannel fringing electric field sensors," *IEEE Sensors Journal*, vol. 6, no. 2, pp. 434–440, 2006-04, Number: 2, ISSN: 1530-437X. DOI: 10.1109/JSEN.2006.870161. Accessed: 2020-02-28. [Online]. Available: http://doku01ae.item.uni-bremen.de/agae/AG_Studi/5600_SeeRoad/Lietal.-2006-Designprinciplesformultichannelfringingelectr.pdf.

[50] Y. Yang *et al.*, "Design and fabrication of a flexible dielectric sensor system for in situ and real-time production monitoring of glass fibre reinforced composites," *Sensors and Actuators A: Physical*, vol. 243, pp. 103–110, 2016-06, ISSN: 09244247. DOI: 10.1016/j.sna.2016.03.015. Accessed: 2022-09-19. [Online]. Available: https://linkinghub.elsevier.com/retrieve/pii/S0924424716301157.

[51] R. Igreja and C. Dias, "Analytical evaluation of the interdigital electrodes capacitance for a multi-layered structure," *Sensors and Actuators A: Physical*, vol. 112, no. 2, pp. 291–301, 2004-05, ISSN: 09244247. DOI: 10.1016/j.sna.2004.01.040. Accessed: 2023-06-21. [Online]. Available: https://linkinghub.elsevier.com/retrieve/pii/S0924424704000779.

[52] Y. Yang, G. Chiesura, T. Vervust, J. Degrieck, and J. Vanfleteren, "Design and fabrication of a shielded interdigital sensor for noninvasive *In situ* real-time production monitoring of polymers: FULL PAPER," *Journal of Polymer Science Part B: Polymer Physics*, vol. 54, no. 20, pp. 2028–2037, 2016-10-15, ISSN: 08876266. DOI: 10.1002/polb.24101. Accessed: 2023-01-17. [Online]. Available: https://onlinelibrary.wiley.com/doi/10.1002/polb.24101.

[53] M. Hübner, D. Gräbner, A. Özdemir, and W. Lang, "Influence of strain on miniaturized flexible sensor for on-line monitoring of CFRP production," *Procedia Manufacturing*, vol. 24, pp. 173–178, 2018, ISSN: 23519789. DOI: 10.1016/j.promfg.2018.06.043. Accessed: 2023-07-24. [Online]. Available: https://linkinghub.elsevier.com/retrieve/pii/S2351978918305602.

[54] R. Zeiser, T. Fellner, and J. Wilde, "Capacitive strain gauges on flexible polymer substrates for wireless, intelligent systems," *Journal of Sensors and Sensor Systems*, vol. 3, no. 1, pp. 77–86, 2014-04-10, ISSN: 2194-878X. DOI: 10.5194/jsss-3-77-2014. Accessed: 2022-04-14. [Online]. Available: https://jsss.copernicus.org/articles/3/77/2014/.

[55] K. L. Ranganatha *et al.*, "A wireless, multi-channel printed capacitive strain gauge system for structural health monitoring," in *2021 IEEE Sensors*, ISSN: 2168-9229, 2021-10, pp. 1–4. DOI: 10.1109/SENSORS47087.2021.9639749.

[56] O. Atalay, "Textile-based, interdigital, capacitive, soft-strain sensor for wearable applications," *Materials*, vol. 11, no. 5, p. 768, 2018-05-10, ISSN: 1996-1944. DOI: 10.3390/ma11050768. Accessed: 2023-08-22. [Online]. Available: http://www.mdpi.com/1996-1944/11/5/768.

[57] T. Mühl, *Elektrische Messtechnik*. Wiesbaden: Springer Fachmedien Wiesbaden, 2017, ISBN: 978-3-658-15719-7 978-3-658-15720-3. DOI: 10.1007/978-3-658-15720-3. Accessed: 2023-08-16. [Online]. Available: http://link.springer.com/10.1007/978-3-658-15720-3.

[58] Texas Instruments Inc., *FDC2x1x EMI-resistant 28-bit,12-bit capacitance-to-digital converter for proximity and level sensing applications - data sheet*, 2015. Accessed: 2022-05-03. [Online]. Available: https://www.ti.com/lit/ds/symlink/fdc2214.pdf.

[59] F. Berkemeyer *et al.*, "Rotor blade temperature monitoring with material integrated wireless sensor tags," in *DEWEK 2017, 13th German Wind Energy Conference. Proceedings*, Bremen, 2017.

[60] J.-H. Ohlendorf, M. Richrath, J. Franke, M. Brink, and K.-D. Thoben, "Towards automation of wind energy rotor blade production: A review of challenges and application examples," *Advanced Manufacturing: Polymer & Composites Science*, vol. 6, no. 4, pp. 173–190, 2020-10-01, ISSN: 2055-0340, 2055-0359. DOI: 10.1080/20550340.2020.1838224. Accessed: 2023-06-23. [Online]. Available: https://www.tandfonline.com/doi/full/10.1080/20550340.2020.1838224.

[61] "Reproduzierbare Applikation von drahtloser Sensorik in technischen Textilien für Faser-Kunststoff-Verbundbauteile auf Basis passiver RFID-Sensortags : Schlussbericht vom 01.05.23 zu IGF-Vorhaben Nr. 20941 N : Berichtszeitraum: 01.12.2019 bis 30.11.2022," [Bremer Institut für Produktion und Logistik GmbH (BIBA)]; Universität Bremen; Bremen, 2023. [Online]. Available: https://www.tib.eu/de/suchen/id/TIBKAT%3A1852596937.

[62] W. Lang *et al.*, "From embedded sensors to sensorial materials—the road to function scale integration," *Sensors and Actuators A: Physical*, vol. 171, no. 1, pp. 3–11, 2011-11, ISSN: 09244247. DOI: 10.1016/j.sna.2011.03.061. Accessed: 2022-04-12. [Online]. Available: https://linkinghub.elsevier.com/retrieve/pii/S0924424711002317.

[63] G. Dumstorff, "Modellierung und experimentelle untersuchung von materialintegrierten sensoren," Ph.D. dissertation, University of Bremen, Bremen, 2015. [Online]. Available: http://nbn-resolving.de/urn:nbn:de:gbv:46-00105038-17.

[64] H. Domininghaus, P. Elsner, T. Hirth, and O. Altmann, *Die Kunststoffe und ihre Eigenschaften* (VDI-Buch), 6., neu bearb. und erw. Aufl., P. Eyerer, Ed. Berlin Heidelberg: Springer, 2005, 1633 pp., ISBN: 978-3-540-21410-6.

[65] M. Hübner, "Überwachung von faserverbundwerkstoffen mit miniaturisiertenflexiblen interdigital sensoren," Ph.D. dissertation, Universität Bremen, Bremen, 2019. Accessed: 2022-04-25. [Online]. Available: https://core.ac.uk/download/pdf/268924148.pdf.

[66] M. Hübner and W. Lang, "Online monitoring of composites with a miniaturized flexible combined dielectric and temperature sensor," in *Proceedings of Eurosensors 2017, Paris, France, 3–6 September 2017*, MDPI, 2017-08-11, p. 627. DOI: 10.3390/proceedings1040627. Accessed: 2022-03-18. [Online]. Available: https://www.mdpi.com/2504-3900/1/4/627.

[67] M. K. Moghaddam, D. Boll, and W. Lang, "Embedding rigid and flexible inlays in carbon fiber reinforced plastics," in *2014 IEEE/ASME International Conference on Advanced Intelligent Mechatronics*, Besacon: IEEE, 2014-07, pp. 1387–1392, ISBN: 978-1-4799-5736-1 978-1-4799-5735-4. DOI: 10.1109/AIM.2014.6878276. Accessed: 2023-07-21. [Online]. Available: https://ieeexplore.ieee.org/document/6878276.

[68] *Datasheet - EPIKOTE™ resin MGS BPR 135g-series and EPIKURE™ curing agent MGS BPH 134g-137gf*, in collab. with Hexion Inc., 2020. Accessed: 2023-08-25. [Online]. Available: https://www.hexion.com/CustomServices/PDFDownloader.aspx?type=tds&pid=45668d44-5814-6fe3-ae8a-ff0300fcd525.

[69] H. L. Lee, *The Handbook of Dielectric Analysis and Cure Monitoring*, 2nd Edition. Cambridge, USA: Lambient Technologies, LLC, 2019. [Online]. Available: https://static1.squarespace.com/static/59627b143e00be4fb1e3aed9/t/5d44fbaed9552b0001c4b026/1564801988994/Handbook+of+Dielectric+Analysis+and+Cure+Monitoring+Ed2+v1.00+2019Aug02.pdf.

[70] J. Steinhaus, B. Hausnerova, T. Haenel, M. Großgarten, and B. Möginger, "Curing kinetics of visible light curing dental resin composites investigated by dielectric analysis (DEA)," *Dental Materials*, vol. 30, no. 3, pp. 372–380, 2014-03, ISSN: 01095641. DOI: 10.1016/j.dental.2013.12.013. Accessed: 2022-06-10. [Online]. Available: https://linkinghub.elsevier.com/retrieve/pii/S0109564113005253.

[71] NETZSCH-Gerätebau GmbH, *DEA 288 ionic – dielektrische analyse des aushärteverhaltens methode, technik, applikationen*, 2022. Accessed: 2023-08-25. [Online]. Available: https://analyzing-testing.netzsch.com/_Resources/Persistent/5/5/b/0/55b048a7ba40c0a196b1ddc94a753609956d4b6c/DEA_288_Ionic_de_web.pdf.

[72] N. Pantelelis and E. Bistekos, "Process monitoring and control for the production of CFRP components," *International SAMPE Symposium and Exhibition (Proceedings)*, 2010-01-01. Accessed: 2023-04-05. [Online]. Available: https://www.researchgate.net/publication/287467295_Process_monitoring_and_control_for_the_production_of_CFRP_components.

[73] C. Garschke, C. Weimer, P. Parlevliet, and B. Fox, "Out-of-autoclave cure cycle study of a resin film infusion process using in situ process monitoring," *Composites Part A: Applied Science and Manufacturing*, vol. 43, no. 6, pp. 935–944, 2012-06, ISSN: 1359835X. DOI: 10.1016/j.compositesa.2012.01.003. Accessed: 2023-04-05. [Online]. Available: https://linkinghub.elsevier.com/retrieve/pii/S1359835X12000097.

[74] P. Zapp, A. Kühn, and N. Pantelelis, "ONLINE INTELLIGENT CURE MONITORING FOR AEROSPACE APPLICATIONS," presented at the SAMPE Europe Conference 2017, Stuttgart, 2017, p. 8. Accessed: 2023-08-25. [Online]. Available: https://www.synthesites.com/resources/files/Online%20intelligent%20cure%20monitoring%20for%20aerospace%20applications%20-%20Philipp%20Zapp%20German%20Aerospace%20Center%20DE.pdf.

[75] R. Matsuzaki, S. Kobayashi, A. Todoroki, and Y. Mizutani, "Full-field monitoring of resin flow using an area-sensor array in a VaRTM process," *Composites Part A: Applied Science and Manufacturing*, vol. 42, no. 5, pp. 550–559, 2011-05, ISSN: 1359835X. DOI: 10.1016/j.compositesa.2011.01.014. Accessed: 2023-08-21. [Online]. Available: https://linkinghub.elsevier.com/retrieve/pii/S1359835X11000376.

[76] Y. Yang *et al.*, "Design and integration of flexible sensor matrix for in situ monitoring of polymer composites," *ACS Sensors*, vol. 3, no. 9, pp. 1698–1705, 2018-09-28, ISSN: 2379-3694, 2379-3694. DOI: 10.1021/acssensors.8b00425. Accessed: 2023-08-04. [Online]. Available: https://pubs.acs.org/doi/10.1021/acssensors.8b00425.

[77] G. Tuncol, M. Danisman, A. Kaynar, and E. M. Sozer, "Constraints on monitoring resin flow in the resin transfer molding (RTM) process by using thermocouple sensors," *Composites Part A: Applied Science and Manufacturing*, vol. 38, no. 5, pp. 1363–1386, 2007-05, ISSN: 1359835X. DOI: 10.1016/j.compositesa.2006.10.009. Accessed: 2023-04-05. [Online]. Available: https://linkinghub.elsevier.com/retrieve/pii/S1359835X06002818.

[78] P. Wang, J. Molimard, S. Drapier, A. Vautrin, and J. Minni, "Monitoring the resin infusion manufacturing process under industrial environment using distributed sensors," *Journal of Composite Materials*, vol. 46, no. 6, pp. 691–706, 2012-03, ISSN: 0021-9983, 1530-793X. DOI: 10.1177/0021998311410479. Accessed: 2023-04-05. [Online]. Available: http://journals.sagepub.com/doi/10.1177/0021998311410479.

[79] A. Dimassi, M. G. Vargas Gleason, M. Hübner, A. S. Herrmann, and W. Lang, "Using piezoresistive pressure sensors for resin flow monitoring in wind turbine blades," *Materials Today: Proceedings*, S2214785320305988, 2020-02, ISSN: 22147853. DOI: 10.1016/j.matpr.2020.01.493. Accessed: 2020-09-29. [Online]. Available: https://linkinghub.elsevier.com/retrieve/pii/S2214785320305988.

[80] K. Kuang, L. Zhang, W. Cantwell, and I. Bennion, "Process monitoring of aluminum-foam sandwich structures based on thermoplastic fibre–metal laminates using fibre bragg gratings," *Composites Science and Technology*, vol. 65, no. 3, pp. 669–676, 2005-03, ISSN: 02663538. DOI: 10.1016/j.compscitech.2004.09.005. Accessed: 2023-04-05. [Online]. Available: https://linkinghub.elsevier.com/retrieve/pii/S0266353804002076.

[81] K. Jung and T. Jin Kang, "Cure monitoring and internal strain measurement of 3-d hybrid braided composites using fiber bragg grating sensor," *Journal of Composite Materials*, vol. 41, no. 12, pp. 1499–1519, 2007-06, ISSN: 0021-9983, 1530-793X. DOI: 10.1177/0021998306068088. Accessed: 2023-04-05. [Online]. Available: http://journals.sagepub.com/doi/10.1177/0021998306068088.

[82] Liren Tsai, Tsung-Chieh Cheng, Chih-Lang Lin, and Chia-Chin Chiang, "Application of the embedded optical fiber bragg grating sensors in curing monitoring of gr/epoxy laminated composites," presented at the Proc.SPIE, vol. 7293, 2009-04-09, p. 729 307. DOI: 10.1117/12.817520. [Online]. Available: https://doi.org/10.1117/12.817520.

[83] T. Stöven, F. Weyrauch, P. Mitschang, and M. Neitzel, "Continuous monitoring of three-dimensional resin flow through a fibre preform," *Composites Part A: Applied Science and Manufacturing*, vol. 34, no. 6, pp. 475–480, 2003-06, ISSN: 1359835X. DOI: 10.1016/S1359-835X(03)00059-9. Accessed: 2023-08-22. [Online]. Available: https://linkinghub.elsevier.com/retrieve/pii/S1359835X03000599.

[84] E. Schmachtenberg, J. Schulte Zur Heide, and J. Töpker, "Application of ultrasonics for the process control of resin transfer moulding (RTM)," *Polymer Testing*, vol. 24, no. 3, pp. 330–338, 2005-05, ISSN: 01429418. DOI: 10.1016/j.polymertesting.2004.11.002. Accessed: 2023-08-22. [Online]. Available: https://linkinghub.elsevier.com/retrieve/pii/S0142941804001631.

[85] M Rath, J Döring, W Stark, and G Hinrichsen, "Process monitoring of moulding compounds by ultrasonic measurements in a compression mould," *NDT & E International*, vol. 33, no. 2, pp. 123–130, 2000-03, ISSN: 09638695. DOI: 10.1016/S0963-8695(99)00029-8. Accessed: 2023-08-22. [Online]. Available: https://linkinghub.elsevier.com/retrieve/pii/S0963869599000298.

[86] N. Liebers, F. Raddatz, and F. Schadow, "Effective and flexible ultrasound sensors for cure monitoring for industrial composite production," presented at the Deutscher Luft- und Raumfahrtkongress, Braunschweig and Stade, Germany: German Aerospace Centre (DLR), Institute of Composite Structures and Adaptive Systems, 2012. Accessed: 2023-08-25. [Online]. Available: https://www.dglr.de/publikationen/2013/281405.pdf.

[87] C. Tuloup, W. Harizi, Z. Aboura, Y. Meyer, K. Khellil, and R. Lachat, "On the use of in-situ piezoelectric sensors for the manufacturing and structural health monitoring of polymer-matrix composites: A literature review," *Composite Structures*, vol. 215, pp. 127–149, 2019-05, ISSN: 02638223. DOI: 10.1016/j.compstruct.2019.02.046. Accessed: 2023-03-10. [Online]. Available: https://linkinghub.elsevier.com/retrieve/pii/S0263822318347342.

[88] A. Horoschenkoff, Ed., *Structural integration of strain gages*, Hottinger Baldwin Messtechnik GmbH, 2006. [Online]. Available: http://2007.parcfd.org/seminar/strain-gage/integ.pdf.

[89] H. Cui, H. Du, F. Zhao, and M. Hong, "Damage identification in a plate structure based on a cross-direction strain measurement method," *Measurement*, vol. 158, p. 107 714, 2020-07-01, ISSN: 0263-2241. DOI: 10.1016/j.measurement.2020.107714. [Online]. Available: https://www.sciencedirect.com/science/article/pii/S0263224120302529.

[90] H. Jo, J.-W. Park, and H.-J. Jeong, "Develoment of high-sensitivity wireless strain sensor for structural health monitoring," *Smart Structures and Systems*, vol. 11, no. 5, pp. 477–496, 2013-05-25. DOI: 10.12989/SSS.2013.11.5.477. Accessed: 2022-03-18. [Online]. Available: https://doi.org/10.12989/SSS.2013.11.5.477.

[91] H. Choi, S. Choi, and H. Cha, "Structural health monitoring system based on strain gauge enabled wireless sensor nodes," in *2008 5th International Conference on Networked Sensing Systems*, 2008-06, pp. 211–214. DOI: 10.1109/INSS.2008.4610888.

[92] M. Miskiewicz, L. Pyrzowski, and B. Sobczyk, "Short and long term measurements in assessment of FRP composite footbridge behavior," *Materials*, vol. 13, no. 3, p. 525, 2020-01-22, ISSN: 1996-1944. DOI: 10.3390/ma13030525. Accessed: 2023-04-06. [Online]. Available: https://www.mdpi.com/1996-1944/13/3/525.

[93] F. L. Marques dos Santos, B. Peeters, J. Lau, W. Desmet, and L. C. S. Goes, "The use of strain gauges in vibration-based damage detection," *Journal of Physics: Conference Series*, vol. 628, p. 012 119, 2015-07-09, ISSN: 1742-6588, 1742-6596. DOI: 10.1088/1742-6596/628/1/012119. Accessed: 2023-04-06. [Online]. Available: https://iopscience.iop.org/article/10.1088/1742-6596/628/1/012119.

[94] Dongning Zhao *et al.*, "Development of an embedded thin-film strain-gauge-based SHM network into 3d-woven composite structure for wind turbine blades," presented at the Proc.SPIE, vol. 10171, 2017-04-19, p. 101710C. DOI: 10.1117/12.2259808. [Online]. Available: https://doi.org/10.1117/12.2259808.

[95] D. G. Bekas, Z. Sharif-Khodaei, D. Baltzis, M. F. Aliabadi, and A. S. Paipetis, "Quality assessment and damage detection in nanomodified adhesively-bonded composite joints using inkjet-printed interdigital sensors," *Composite Structures*, vol. 211, pp. 557–563, 2019-03, ISSN: 02638223. DOI: 10.1016/j.compstruct.2019.01.008. Accessed: 2023-08-23. [Online]. Available: https://linkinghub.elsevier.com/retrieve/pii/S0263822318342338.

[96] K. T. Fujimoto *et al.*, "Aerosol jet printed capacitive strain gauge for soft structural materials," *npj Flexible Electronics*, vol. 4, no. 1, p. 32, 2020-12, ISSN: 2397-4621. DOI: 10.1038/s41528-020-00095-4. Accessed: 2022-07-27. [Online]. Available: http://www.nature.com/articles/s41528-020-00095-4.

[97] H. Cao *et al.*, "Development and characterization of a novel interdigitated capacitive strain sensor for structural health monitoring," *IEEE Sensors Journal*, vol. 15, no. 11, pp. 6542–6548, 2015-11, Conference Name: IEEE Sensors Journal, ISSN: 1558-1748. DOI: 10.1109/JSEN.2015.2461591.

[98] G Zhou and L. M. Sim, "Damage detection and assessment in fibre-reinforced composite structures with embedded fibre optic sensors-review," *Smart Materials and Structures*, vol. 11, no. 6, pp. 925–939, 2002-12-01, ISSN: 0964-1726. DOI: 10.1088/0964-1726/11/6/314. Accessed: 2022-07-01. [Online]. Available: https://iopscience.iop.org/article/10.1088/0964-1726/11/6/314.

[99] S. Tian, Z. Yang, X. Chen, and Y. Xie, "Damage detection based on static strain responses using FBG in a wind turbine blade," *Sensors*, vol. 15, no. 8, pp. 19 992–20 005, 2015-08-14, ISSN: 1424-8220. DOI: 10.3390/s150819992. Accessed: 2023-04-06. [Online]. Available: http://www.mdpi.com/1424-8220/15/8/19992.

[100] G. Pereira, C. Frias, H. Faria, O. Frazão, and A. Marques, "On the improvement of strain measurements with FBG sensors embedded in unidirectional composites," *Polymer Testing*, vol. 32, no. 1, pp. 99–105, 2013-02, ISSN: 01429418. DOI: 10.1016/j.polymertesting.2012.09.010. Accessed: 2022-12-04. [Online]. Available: https://linkinghub.elsevier.com/retrieve/pii/S0142941812001894.

[101] H.-Y. Tang, C. Winkelmann, W. Lestari, and V. La Saponara, "Composite structural health monitoring through use of embedded PZT sensors," *Journal of Intelligent Material Systems and Structures*, vol. 22, no. 8, pp. 739–755, 2011-05, ISSN: 1045-389X, 1530-8138. DOI: 10.1177/1045389X11406303. Accessed: 2023-04-12. [Online]. Available: http://journals.sagepub.com/doi/10.1177/1045389X11406303.

[102] J. Zhang, G. Tian, A. Marindra, A. Sunny, and A. Zhao, "A review of passive RFID tag antenna-based sensors and systems for structural health monitoring applications," *Sensors*, vol. 17, no. 2, p. 265, 2017-01-29, ISSN: 1424-8220. DOI: 10.3390/s17020265. Accessed: 2022-03-18. [Online]. Available: http://www.mdpi.com/1424-8220/17/2/265.

[103] M. Salas, O. Focke, A. S. Herrmann, and W. Lang, "Wireless power transmission for structural health monitoring of fiber-reinforced-composite materials," *IEEE Sensors Journal*, vol. 14, no. 7, pp. 2171–2176, 2014-07, ISSN: 1530-437X, 1558-1748, 2379-9153. DOI: 10.1109/JSEN.2014.2305578. Accessed: 2022-04-12. [Online]. Available: http://ieeexplore.ieee.org/document/6736058/.

[104] J. Groh, W. B. Lee, J. Schür, F. Distler, and M. Vossiek, "Compact substrate integrated wireless cure monitoring sensor for epoxy resin," in *2018 48th European Microwave Conference (EuMC)*, 2018-09, pp. 243–246. DOI: 10.23919/EuMC.2018.8541434.

[105] S. Rajawat, M. Hübner, L. Kempen, and W. Lang, "Flexible passive LC resonator for wireless measurement during curing of thermosets," *Journal of Physics: Conference Series*, vol. 1837, no. 1, p. 012 001, 2021-03-01, ISSN: 1742-6588, 1742-6596. DOI: 10.1088/1742-6596/1837/1/012001. Accessed: 2022-04-25. [Online]. Available: https://iopscience.iop.org/article/10.1088/1742-6596/1837/1/012001.

[106] M. G. V. Gleason, R. Jedermann, A. Dimassi, and W. Lang, "Wireless piezoresistive pressure sensors used for quality control in glass fiber composite laminates," in *2018 IEEE SENSORS*, ISSN: 2168-9229, 2018-10, pp. 1–4. DOI: 10.1109/ICSENS.2018.8589933.

[107] M. G. Vargas Gleason, R. Jedermann, A. Dimassi, and W. Lang, "Embedded wireless sensor systems for resin flow monitoring in glass and carbon fiber composites," *IEEE Sensors Journal*, vol. 19, no. 22, pp. 10 654–10 661, 2019-11-15, ISSN: 1530-437X, 1558-1748, 2379-9153. DOI: 10.1109/JSEN.2019.2928635. Accessed: 2020-09-29. [Online]. Available: https://ieeexplore.ieee.org/document/8762212/.

[108] M. Veigt, E. Hardi, M. Koerdt, A. S. Herrmann, and M. Freitag, "Curing transponder – integrating RFID transponder into glass fiber-reinforced composites to monitor the curing of the component," *Procedia Manufacturing*, vol. 24, pp. 94–99, 2018, ISSN: 23519789. DOI: 10.1016/j.promfg.2018.06.014. Accessed: 2022-04-21. [Online]. Available: https://linkinghub.elsevier.com/retrieve/pii/S2351978918305316.

[109] E. Hardi, M. Veigt, M. Koerdt, A. S. Herrmann, and M. Freitag, "Monitoring of the vacuum infusion process by integrated RFID transponder," *Procedia Manufacturing*, vol. 52, pp. 20–25, 2020, ISSN: 23519789. DOI: 10.1016/j.promfg.2020.11.005. Accessed: 2022-04-21. [Online]. Available: https://linkinghub.elsevier.com/retrieve/pii/S2351978920321466.

[110] NXP Semiconductors B.V., *NXP - therapy adherence resistive monitor. NFC sensor tag*, 2018. [Online]. Available: https://www.nxp.com/docs/en/data-sheet/NHS3152.pdf.

[111] Texas Instruments Inc., *TI - passive NFC temperature patch reference design*, 2016. [Online]. Available: https://www.ti.com/lit/ug/tidubt8/tidubt8.pdf?ts=1649853303540.

[112] MicroMeasurements, Vishay Precision Group, *Datasheet s5020 - transducer-class® strain gages with advanced sensors technology*, 2019. [Online]. Available: https://docs.micro-measurements.com/?id=2622.

[113] Texas Instruments Inc., *TI - INA333 micro-power (50ua), zero-drift, rail-to-rail out instrumentation amplifier*, 2015. Accessed: 2023-08-25. [Online]. Available: https://www.ti.com/lit/ds/symlink/ina333.pdf.

[114] Texas Instruments Inc., *TI - ADS7052 - 14-bit,1-MSPS,single-EndedInput, small-size,low-PowerSAR ADC*, 2015. Accessed: 2023-08-25. [Online]. Available: https://www.ti.com/lit/ds/symlink/ads7052.pdf.

[115] Texas Instruments Inc., *TMP117 high-accuracy, low-power, digital temperature sensor with SMBus™- and i2c-compatible interface*, 2021-04. [Online]. Available: https://www.ti.com/lit/ds/symlink/tmp117.pdf.

[116] MicroSensys GmbH, *M30 RFID HEAD*, 2020. [Online]. Available: https://www.microsensys.de/fileadmin/user_upload/pdf-dateien/ds_reader_industry/M30head-05.pdf.

[117] SAERTEX GmbH, *SAERfix®EP // SAERfix®UP KLEBEMATERIALIEN - produkt-flyer*, 2022. [Online]. Available: https://www.saertex.com/de/service/downloads/saerfix/file/3a01f3af1d97f092dedccf5256905b94/0143-14-066_SAERTEX_Produktflyer_SAERfix_DEU.pdf.

[118] G. Alley, "Interdigital capacitors and their application to lumped-element microwave integrated circuits," *IEEE Transactions on Microwave Theory and Techniques*, vol. 18, no. 12, pp. 1028–1033, 1970-12, ISSN: 0018-9480. DOI: 10.1109/TMTT.1970.1127407. Accessed: 2023-08-27. [Online]. Available: http://ieeexplore.ieee.org/document/1127407/.

[119] J. Hobdell, "Optimization of interdigital capacitors," *IEEE Transactions on Microwave Theory and Techniques*, vol. 27, no. 9, pp. 788–791, 1979-09, ISSN: 0018-9480. DOI: 10.1109/TMTT.1979.1129730. Accessed: 2023-08-27. [Online]. Available: http://ieeexplore.ieee.org/document/1129730/.

[120] R. Esfandiari, D. Maki, and M. Siracusa, "Design of interdigitated capacitors and their application to gallium arsenide monolithic filters," *IEEE Transactions on Microwave Theory and Techniques*, vol. 31, no. 1, pp. 57–64, 1983-01, ISSN: 0018-9480. DOI: 10.1109/TMTT.1983.1131429. Accessed: 2023-08-27. [Online]. Available: http://ieeexplore.ieee.org/document/1131429/.

[121] J. Wei, "Distributed capacitance of planar electrodes in optic and acoustic surface wave devices," *IEEE Journal of Quantum Electronics*, vol. 13, no. 4, pp. 152–158, 1977-04, ISSN: 0018-9197, 1558-1713. DOI: 10.1109/JQE.1977.1069319. Accessed: 2023-08-27. [Online]. Available: http://ieeexplore.ieee.org/document/1069319/.

[122] R. Hoffmann and H. Howe, *Handbook of Microwave Integrated Circuits* (Artech House microwave library). Artech House, 1987, ISBN: 978-0-89006-163-3.

[123] M. M. Adnan *et al.*, "The structure, morphology, and complex permittivity of epoxy nanodielectrics with in situ synthesized surface-functionalized SiO2," *Polymers*,

vol. 13, no. 9, p. 1469, 2021-05-01, ISSN: 2073-4360. DOI: 10.3390/polym13091469. Accessed: 2023-08-29. [Online]. Available: https://www.mdpi.com/2073-4360/13/9/1469.

[124] DuPont de Nemours, Inc., *DuPont™ kapton® polyimide film . general specifications*, 2021. Accessed: 2023-08-29. [Online]. Available: https://www.dupont.com/content/dam/dupont/amer/us/en/ei-transformation/public/documents/en/EI-10167-Kapton-General-Specifications.pdf.

[125] H.-E. Endres and S. Drost, "Optimization of the geometry of gas-sensitive interdigital capacitors," *Sensors and Actuators B: Chemical*, vol. 4, no. 1, pp. 95–98, 1991-05, ISSN: 09254005. DOI: 10.1016/0925-4005(91)80182-J. Accessed: 2023-07-04. [Online]. Available: https://linkinghub.elsevier.com/retrieve/pii/092540059180182J.

[126] S. C. Mukhopadhyay, B. George, J. K. Roy, and T. Islam, Eds., *Interdigital Sensors: Progress over the Last Two Decades*, vol. 36, Smart Sensors, Measurement and Instrumentation, Cham: Springer International Publishing, 2021, ISBN: 978-3-030-62683-9 978-3-030-62684-6. DOI: 10.1007/978-3-030-62684-6. Accessed: 2023-06-21. [Online]. Available: https://link.springer.com/10.1007/978-3-030-62684-6.

[127] "KiCad EDA," Accessed: 2023-09-05. [Online]. Available: https://www.kicad.org/.

[128] UHU GmbH & Co. KG, *UHU PLUS SCHNELLFEST BINDER + HÄRTER BLISTER 35 g*, 2022. Accessed: 2023-06-07. [Online]. Available: https://www.uhu.de/content/dam/boltonadhesives/products/import/55/de/62976/50.pdf.

[129] S. Chişcă, V Musteata, I Sava, and M Bruma, "Study of dielectric behavior of aromatic polyimide films," in *CAS 2010 Proceedings (International Semiconductor Conference)*, Sinaia: IEEE, 2010-10, pp. 325–328, ISBN: 978-1-4244-5782-3 978-1-4244-5783-0. DOI: 10.1109/SMICND.2010.5650686. Accessed: 2023-07-26. [Online]. Available: http://ieeexplore.ieee.org/document/5650686/.

[130] W. A. Hussain, A. A. Hussein, J. M. Khalaf, A. H. Al-Mowali, and A. A. Sultan, "Dielectric properties and a.c. conductivity of epoxy/alumina silicate NGK composites," *Advances in Chemical Engineering and Science*, vol. 05, no. 3, pp. 282–289, 2015, ISSN: 2160-0392, 2160-0406. DOI: 10.4236/aces.2015.53028. Accessed: 2023-06-30. [Online]. Available: http://www.scirp.org/journal/doi.aspx?DOI=10.4236/aces.2015.53028.

[131] Texas Instruments Inc., *TPS7a03 nanopower IQ, 200-nA, 200-mA, low-dropout voltage regulator with fast transient response*, 2022. Accessed: 2023-10-03. [Online]. Available: https://www.ti.com/lit/ds/symlink/tps7a03.pdf.

[132] S. Bornemann, J. N. Haus, M. Sinapius, B. Lüssem, A. Dietzel, and W. Lang, "Stainless-steel antenna on conductive substrate for an SHM sensor system with high power demand," *Sensors*, vol. 21, no. 23, p. 7841, 2021-11-25, ISSN: 1424-8220. DOI: 10.3390/s21237841. Accessed: 2023-10-12. [Online]. Available: https://www.mdpi.com/1424-8220/21/23/7841.

[133] S. Bornemann and W. Lang, "Considerations and limits of embedding sensor nodes for structural health monitoring into fiber metal laminates," *Sensors*, vol. 22, no. 12, p. 4511, 2022-06-14, ISSN: 1424-8220. DOI: 10.3390/s22124511. Accessed: 2023-10-12. [Online]. Available: https://www.mdpi.com/1424-8220/22/12/4511.

[134] STMicroelectronics NV, *ST25dv04k - dynamic NFC/RFID tag IC*, 2023. Accessed: 2023-10-13. [Online]. Available: https://www.st.com/resource/en/datasheet/st25dv04k.pdf.

[135] STMicroelectronics NV, *STM32g031x4/x6/x8 - micro controller data sheet*, 2021. Accessed: 2023-10-13. [Online]. Available: https://www.st.com/resource/en/datasheet/stm32g031g8.pdf.

[136] M. Götz, "Grundelastizitätsgrößen am Mehrschichtverbund," Ph.D. dissertation, TU Graz, Graz, 2012. Accessed: 2021-05-05. [Online]. Available: https://diglib.tugraz.at/download.php?id=576a8678255ef&location=browse.

[137] L. Murata Manufacturing Co., *Variable capacitor LXRW19v201-058*, 2018. Accessed: 2023-12-01. [Online]. Available: https://www.murata.com/products/productdata/8807789363230/M19X-LXRW-058.pdf.

Chapter A
Appendix

A.1 Tag-Reader Interface Specification and command list

This section specifies the textual interface for communicating with the sensor tag via a serial connection (RS232) and the RFID reader (MicroSensys M30 RFID Head). For read out, the reader is connected to a host, e. g. a computer or a PLC via a serial connection, e. g. USB or RS232, as illustrated in Figure A.1. This way, commands and data can be communicated via the serial connection to the reader, which in turn communicates with the sensor tag. Reader programming

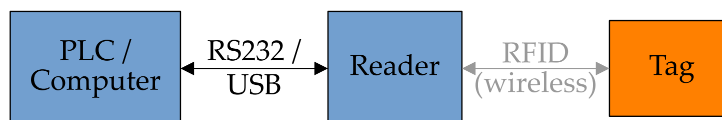

Figure A.1: Schematic illustration of connections between tag, reader and host (PC/PLC).

is schematically displayed in Figure A.2. The reader script periodically sends a “heartbeat” containing the reader serial number, if the reader is connected to the computer and no tag readout is ongoing. This is to allow the connected device to know if the reader is online and working, which is especially relevant for reader usage with a PLC. All the time, the reader listens for a command on the serial bus. If a “∼START” command is received by the reader and a tag is within reading distance, the reader starts reading part of the tag memory (containing the measurement data) and sends the data via serial bus. Reception of a “∼STOP” command returns the reader to sending its “heartbeat”.

Example of a ‘heartbeat’ string:

`:26S8DEC01AE11982680@<CR><LF>`

The data read from the tag sent by the reader as a string, that contains one data set per readout / message.: General structure of tag data:

`:TagID;Para1;Para2;Para3;` [:,; = separating character(s), placeholder]

Real transponder data (example, piezoresistive tag):

```
:21B048438002F1B09<29>1Q;19852;5900;<LF>@<CR><LF>
```

More details on message structure are given in Table A.1. Transponder data is separated from the tag ID and other characters by semicolons. Following the tag ID the first value / parameter is the current temperature value, multiplied by 1000. The second value is either the current strain value (for the piezoresistive sensor tag, multiplied by 100), or the two capacitance values (for the capacsitive sensor tag).

Table A.1: Detailed description of reader message data structure as implemented by MicroSensys GmbH.

Reader → application (Tag found and read sucessfully)		
Field	**Content**	**Info**
SOH	:	
Data Identifier	21B	TID data follows
Data	018DD6BD00000000	ASCII TID of the transponder (HEX-String)
Data divider	<GS>	ASCII with value in HEX: 0x1D
Data Identifier	1Q	Transponder Data follows
Data	00112233...FF	ASCII NTAG memory (16B) data
EOF	@<CR><LF>	
Reader → application (Tag found, read error)		
Field	**Content**	**Info**
SOH	:	
Data Identifier	21B	TID data follows
Data	018DD6BD00000000	ASCII TID of the transponder (HEX-String)
Data divider	<GS>	ASCII with value in HEX: 0x1D
SOH	:	
Data Identifier	1Q	TID data follows
Data	24	Error code (0x24 – TAG not found)
EOF	@<CR><LF>	
Reader → application (TAG not found)		
Field	**Content**	**Info**
SOH	:	
Data Identifier	21B	TID data follows
Data	24	Error code (0x24 – TAG not found)
EOF	@<CR><LF>	

Tag command list On the piezoresistive tag[1], the tag software accepts a number of custom commands that can be send via the serial connection in order to influence certain measurement parameters and settings. The table below summarizes all commands, their function and current implementation status. Every command consists of four byte. The first two byte define the command function, i.e. "key", while the last two bytes give a corresponding value:

```
byte nr:  12 34
function: KK VV
```

Depending on command function, the value bytes have different meanings and ranges of allowed values, which also are given in the table below. In order to send a command to the tag, it must be sent in a certain format for the reader to identify the message as tag command. Just like the "∼START" and "∼STOP" commands, the *cmdToTag* command is preceded with a "∼", while the actual command is appended to the string "CMD_":

```
~CMD_KKVV
```

After receiving a command via the serial bus, the reader writes "KKVV" to the tags command in register, where the command is checked and interpreted in the following measurement cycle. If a valid command has been issued, the tag answers by sending an answer string instead of measurement data. Answer strings are marked via a preceding "#" character, i.e.

```
#AV_changed
#CONF_READ_ERR
#CONF_RESET_DONE.
```

[1]Though not actually implemented during the scope of this thesis, the functionality described can easily be transferred to the capacitive sensor tag as well.

Table A.2: List of possible Key value pairs to be sent to the tag

Key (Ascii)	Key (Hex)	Value (Hex)	Function	Description	Implem. status
'AV'	'4156'	'0000'-'FFFF'	Average	Sets number of samples to be taken for strain measurement averaging. AV = 0000 (n==1) AV = FFFF (n==65 535)	done
'CA'	'4341'	'0000'-'0001'	Calibration on/off	Calibration of strain measurement for current situation. Stores the currently measured strain value in a non-volatile register and sets the internal "calibrationOn" flag. The calibration value is then substracted from all following strain measurement values. CA = 0000 (offset == bitrange / 2) CA = 0001 (offset == last measured bit value)	Done
'GC'	'4743'	'0000'-'FFFF'	Get Config	Reads current configuration settings from internal registers and sends them over the next cycles.	tbd
'I1'	'4931'	'0000'-'FFFF'	Set ID part 1	Sets the first two bytes of the custom user id.	Done
'I2'	'4932'	'0000'-'FFFF'	Set ID part 2	Sets the last two bytes of the custom user id.	Done
'ID'	'4944'	'0000'	Identification	Requests the currently set user user id stored in the tag configuration to be displayed in the next cycle. Id can be set via I1/I2.	Done
'LE'	'4C45'	'0000'-'0001'	LED on/off	Switches usage of tag LED for status indication: LE = 0000 (LED aktiviert) LE = 0001 (LED deaktiviert)	tbd
'MM'	'4D4D'	'0000'-'0001'	Message mode	Sets communication mode to be used by the tag (experimental): MM = 0000 (MIFARE mode activated) MM = 0001 (NDEF mode activated)	tbd
'RS'	'5253'	'0000'	Reset	Resets internal tag configuration: AV = 0010 CA = 0000 LE = 0001 MM = 0000 TP = 0003 I1=I2=0000	Done
'ST'	'5354'	'0000'-'0001'	Strain on/off	Switches strain measurement on or off: ST = 0000 (strain measurement inactive) ST = 0001 (strain measurement active)	tbd
'TE'	'5445'	'0000'-'0001'	Temp on/off	Switches temperature measurement on or off: TE = 0000 (temperature meas. inactive) TE = 0001 (temperature meas. active)	tbd

'TO'	'544F'	'0000'-'00FF'	Time power on	Sets waiting time (ms) the tag should wait before acquiring measurement values.
				
				TO <= 0003 (t==3ms) //3ms is minimum
				TO >= 00FF (t==255ms) //255 is maximum
					tbd

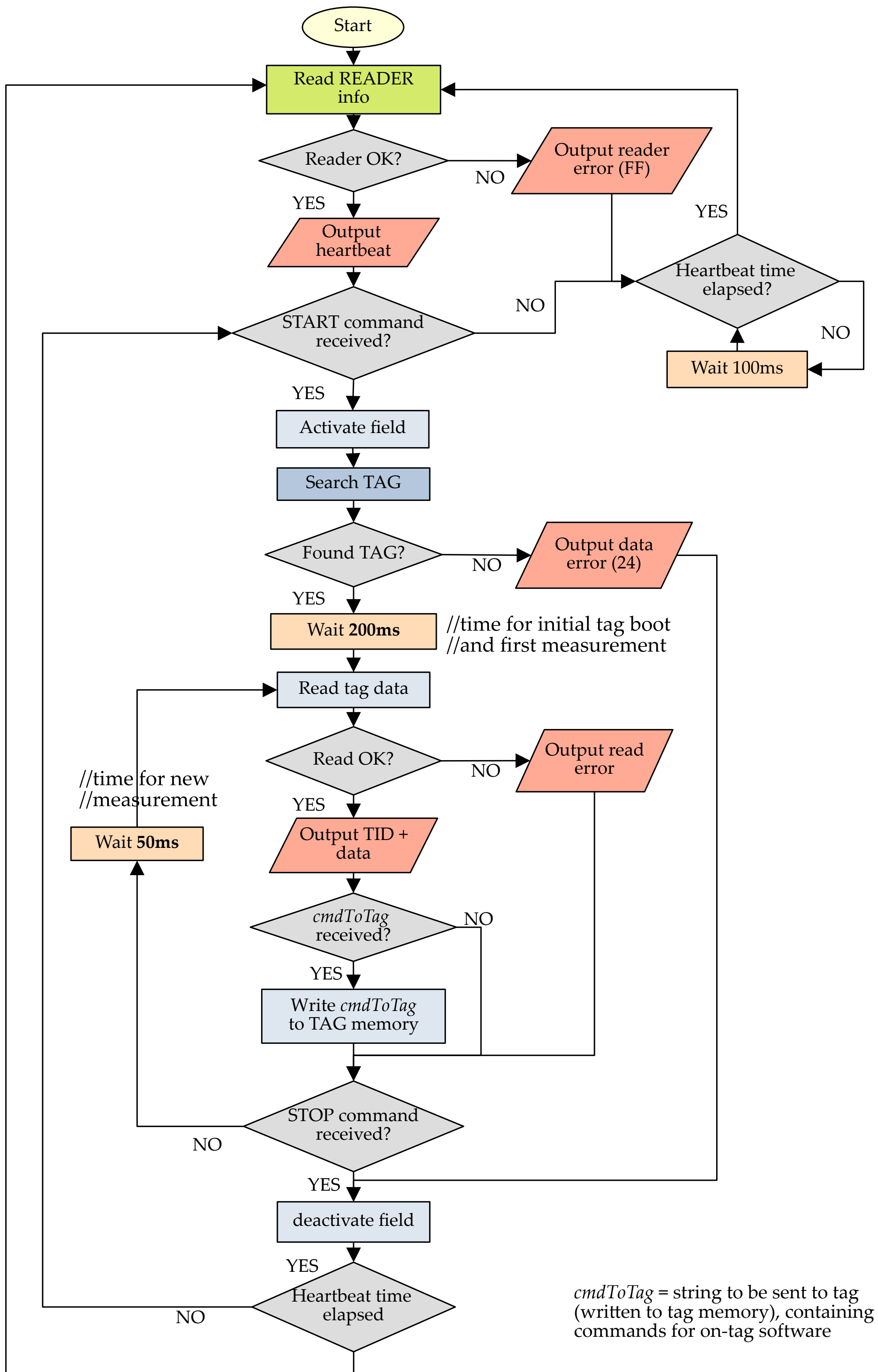

Figure A.2: Flow chart of RFID reader programming for sensor tag readout

A.2 Additional Figures

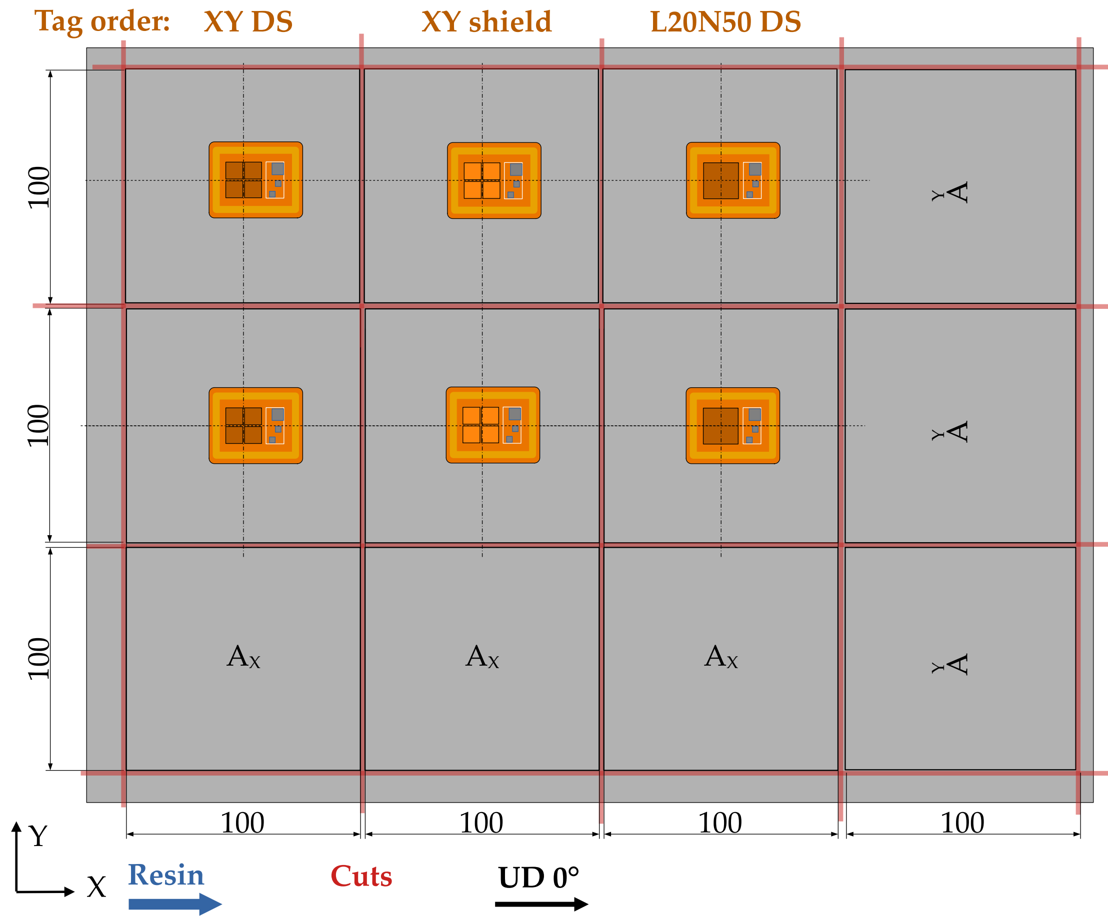

Figure A.3: Tag arrangement and order for FRP integration of capacitive sensior tags, coordinate system, directions of fibers and resin flow indicated.

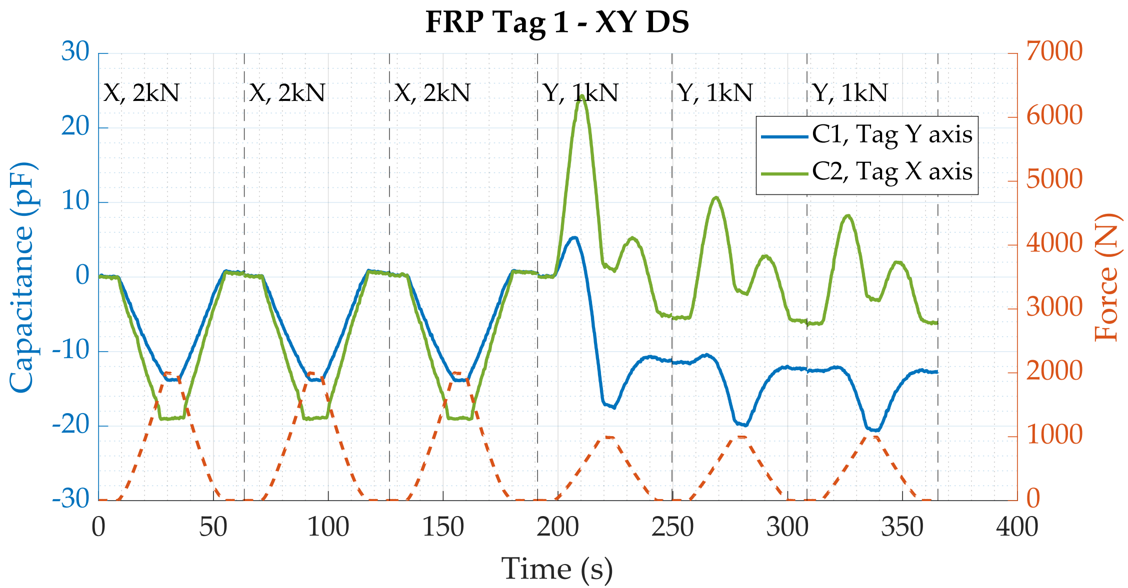

Figure A.4: Measured capacitances and respective forces for bending tests conducted with specimen 1 (XY DS).

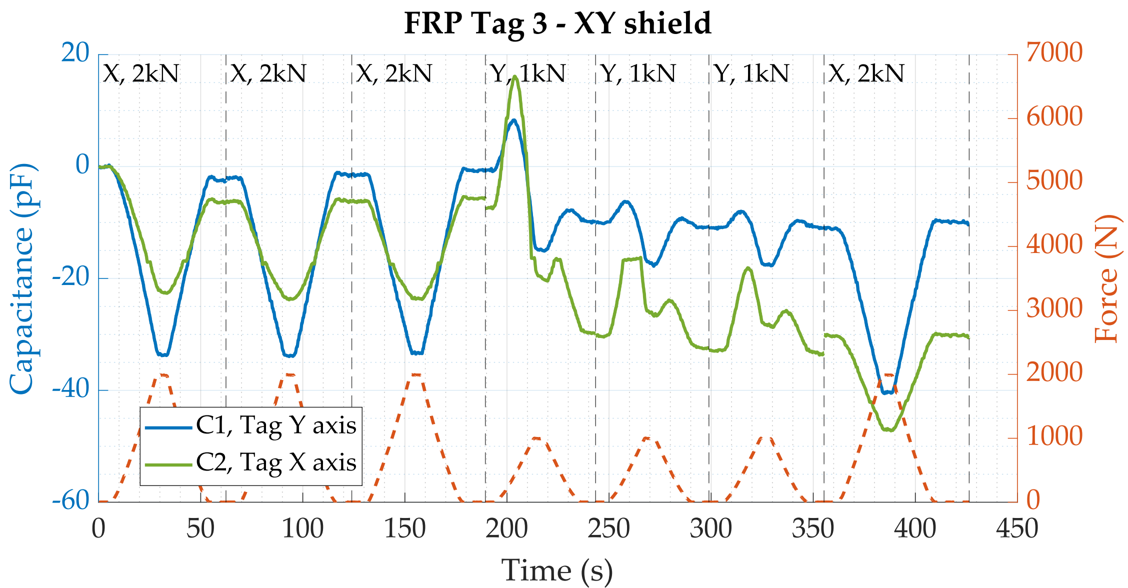

Figure A.5: Measured capacitances and respective forces for bending tests conducted with specimen 3 (XY shield).

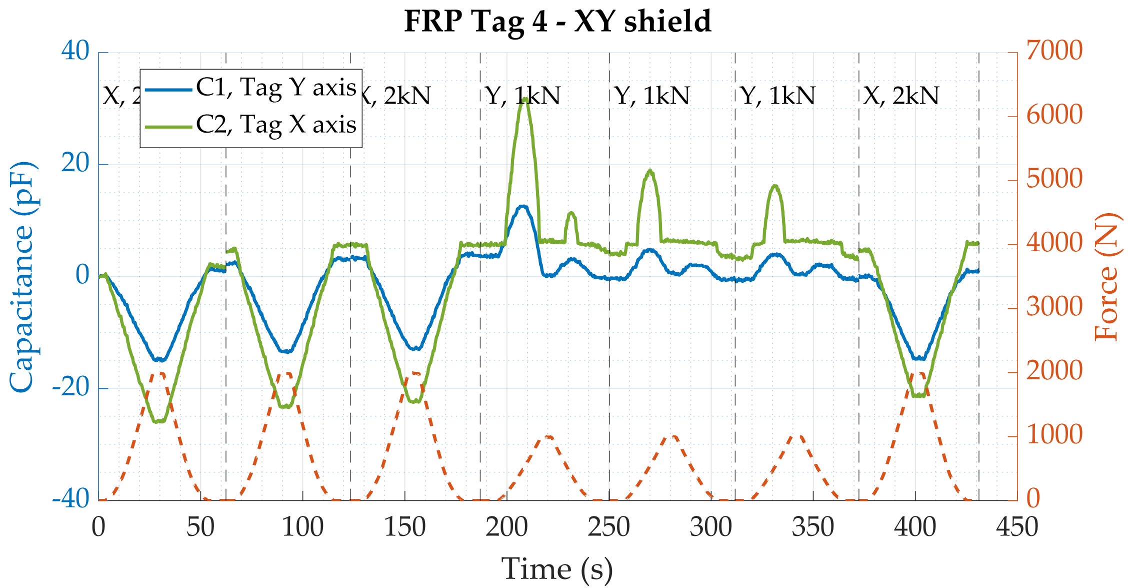

Figure A.6: Measured capacitances and respective forces for bending tests conducted with specimen 4 (XY shield).

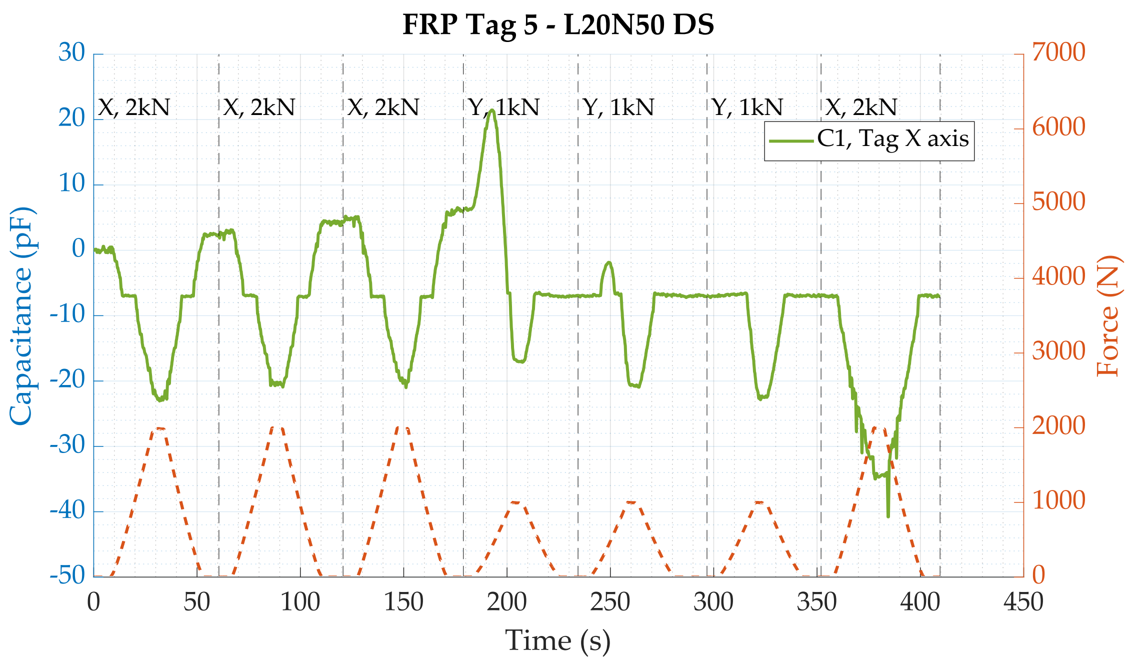

Figure A.7: Measured capacitance and respective forces for bending tests conducted with specimen 5 (L20 DS).

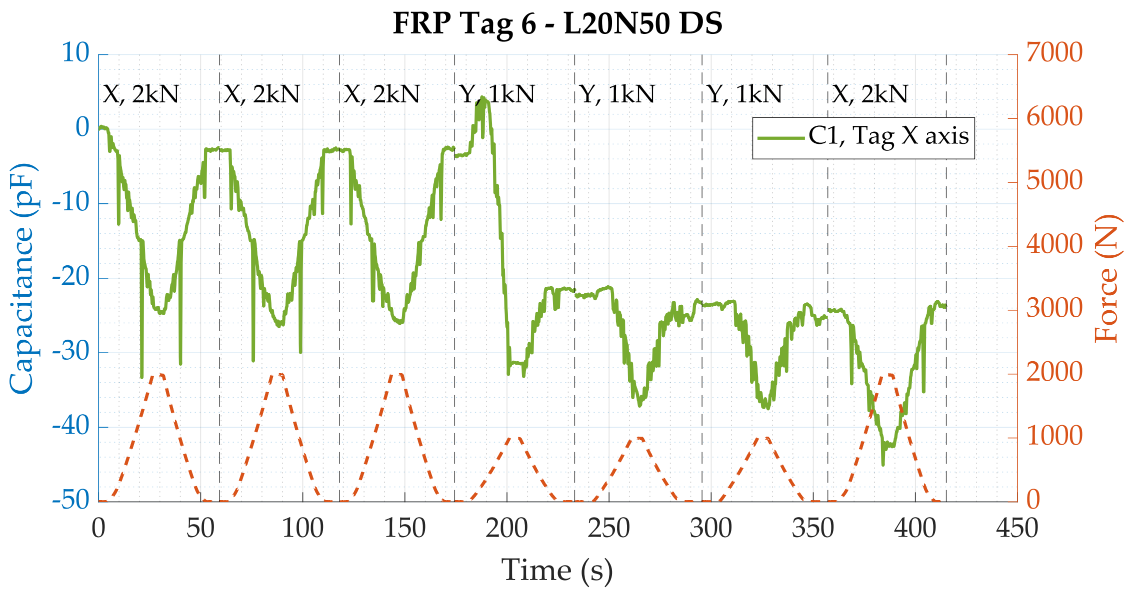

Figure A.8: Measured capacitances and respective forces for bending tests conducted with specimen 6 (L20 DS).

A.3 Schematics

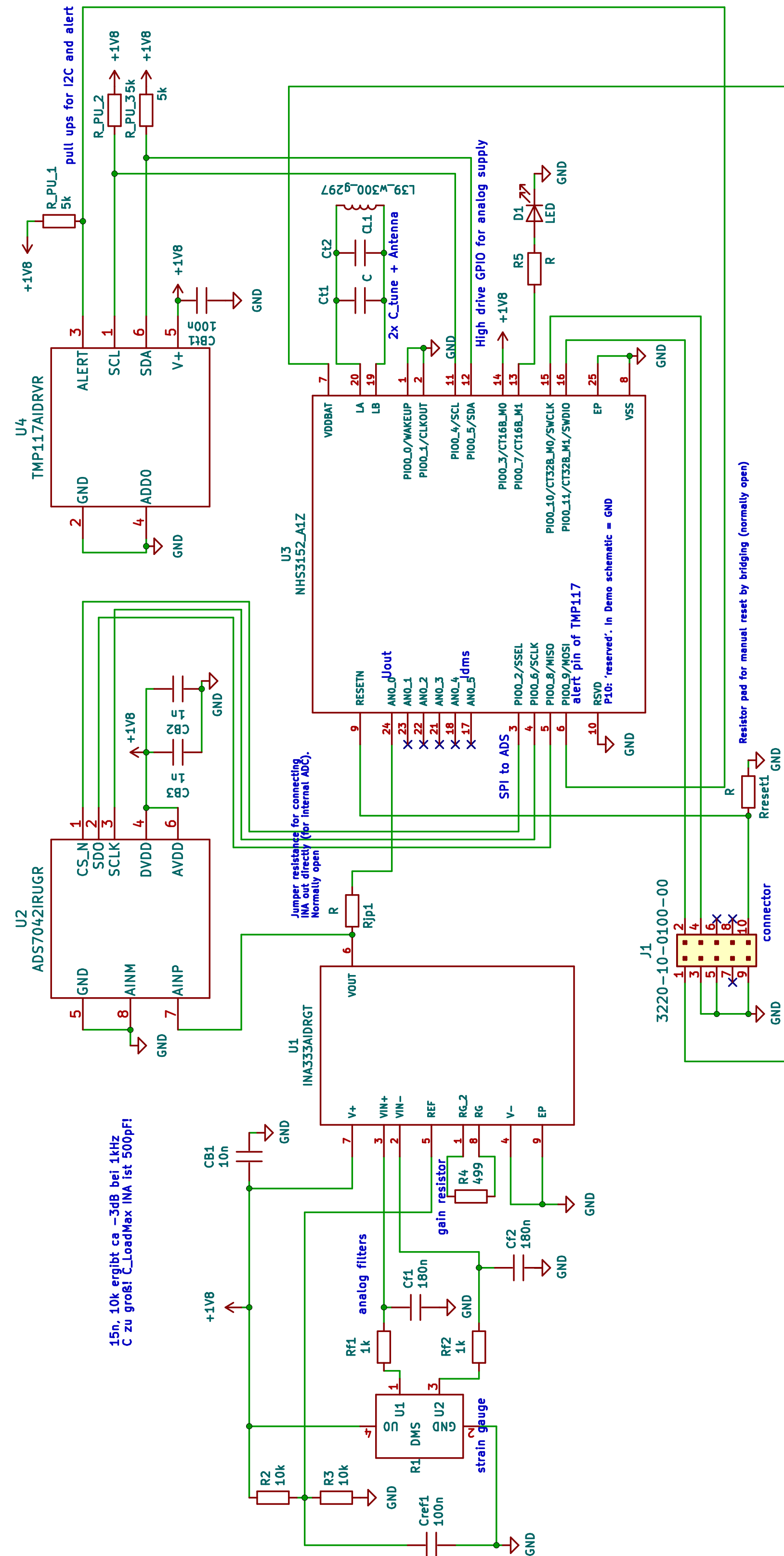

Figure A.9: Schematic for Piezoresistive Sensor Tag, designed in kiCad, [127].

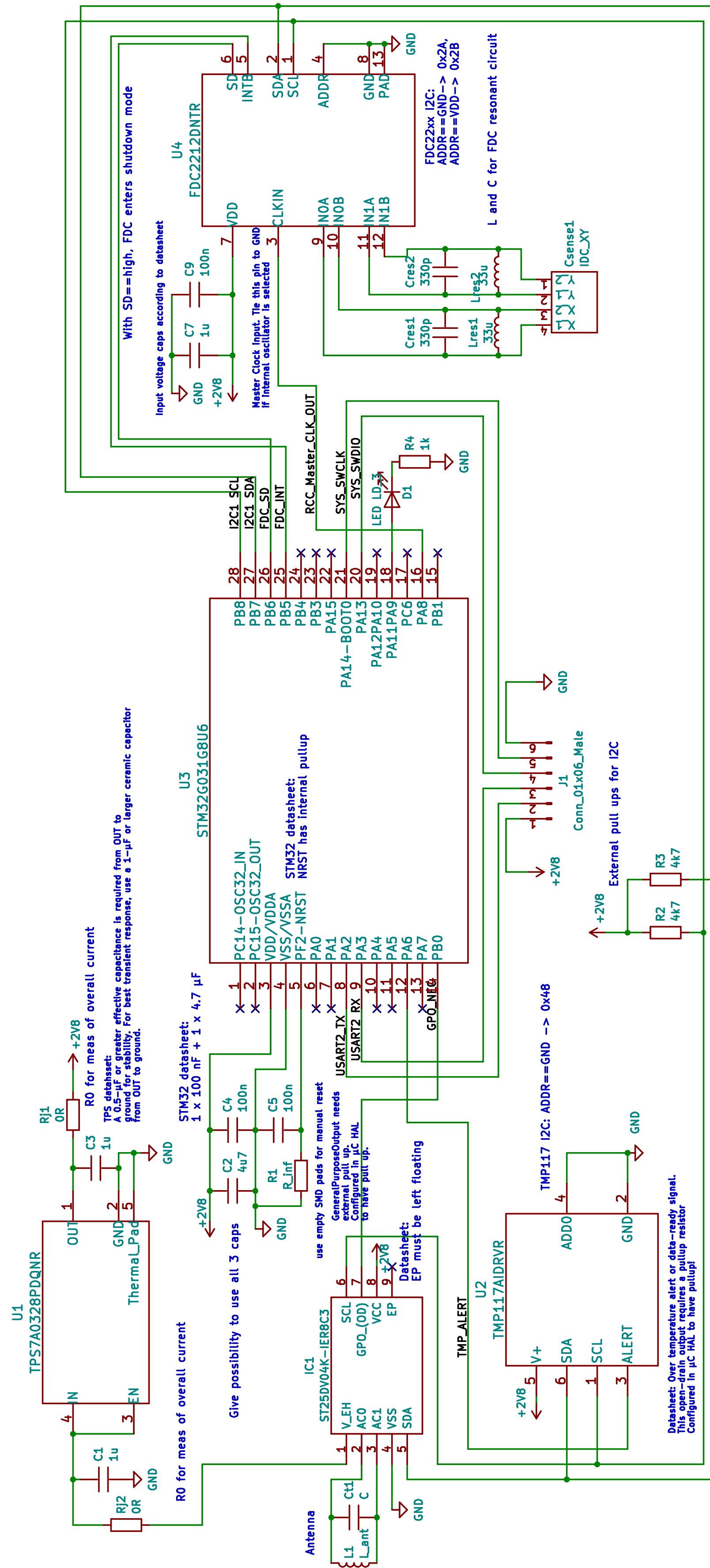

Figure A.10: Schematic for Capacitive Sensor Tag, designed in kiCad, [127].

A.4 PCB Layouts

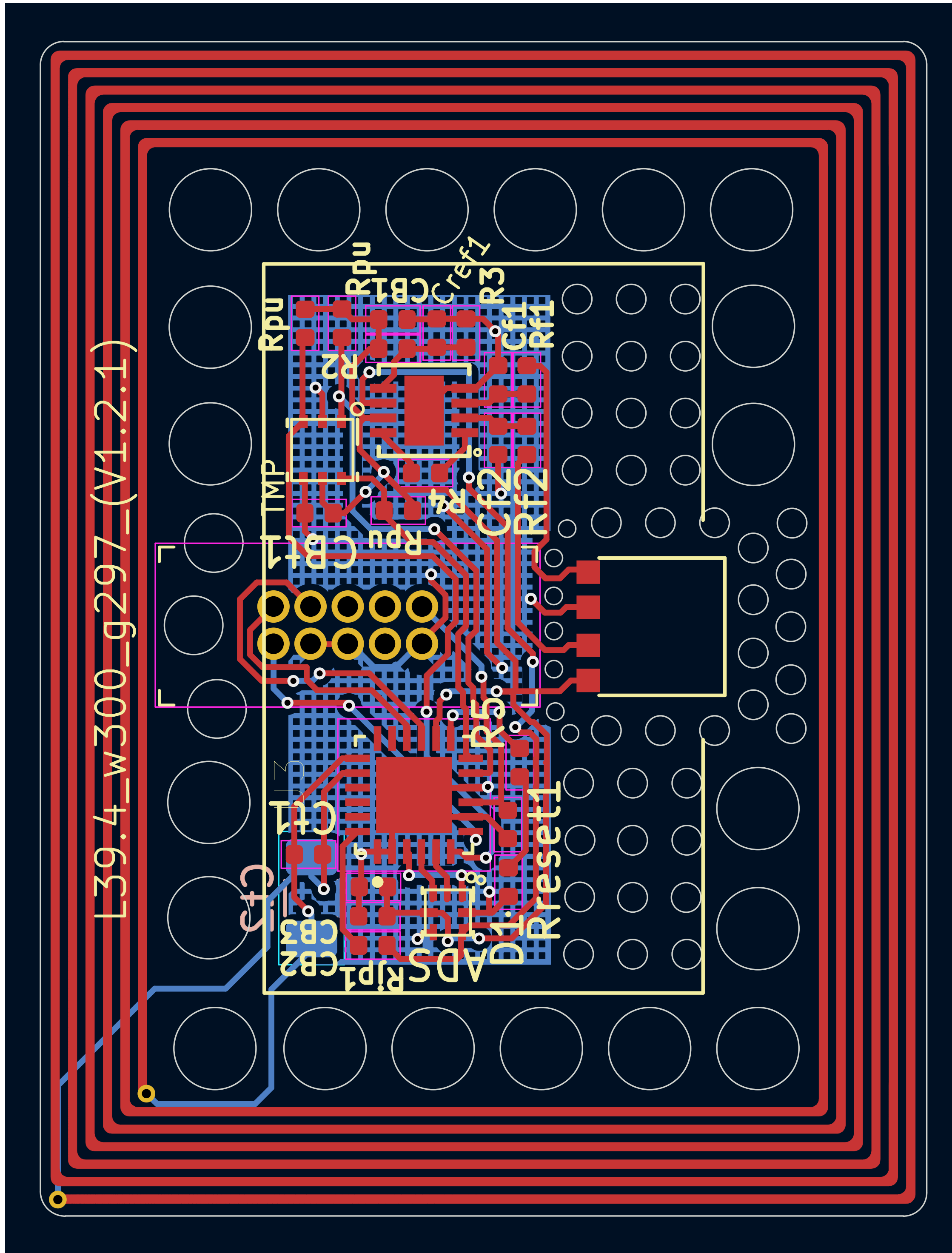

Figure A.11: PCB Layout for piezoresistive sensor tag, designed in kiCad, [127].

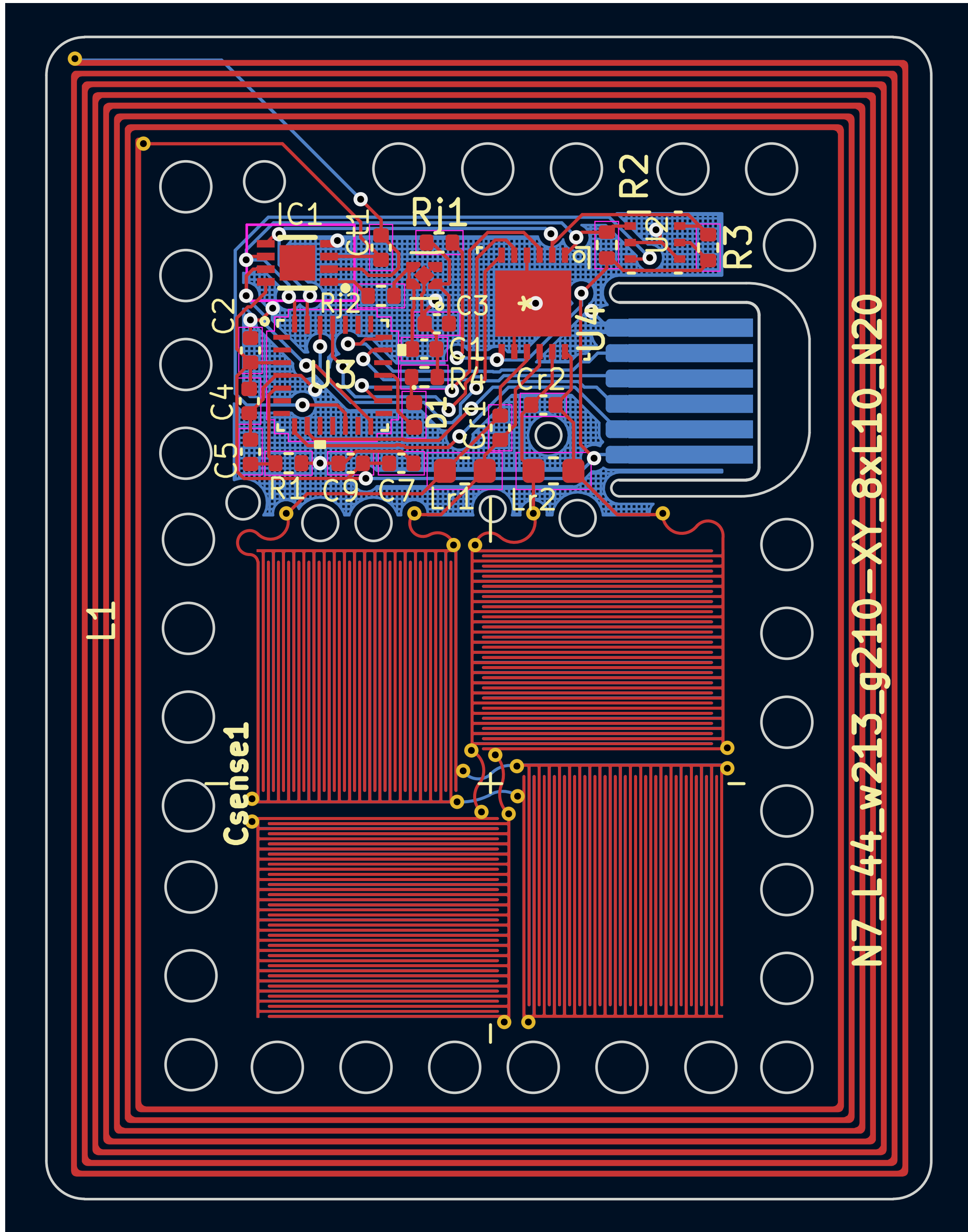

Figure A.12: PCB Layout for capacitive sensor tag, designed in kiCad, [127].

A.5 Publications

This section lists all peer-reviewed works that have been published in context of this thesis.

- **Lukas Bertram**, Michael Brink, Walter Lang, und Klaus-Dieter Thoben. *„A passive, wireless sensor node for material-integrated strain and temperature measurement in glass fiber reinforced composites“*.
  SysInt2022, Genova, Italy, 2022-09-04, pp. 182–193, ISBN: 978-3-031-16280-0.
  https://doi.org/10.1007/978-3-031-16281-7_18.
- **Lukas Bertram**, Michael Brink and Walter Lang, *„Material-integrated Temperature Sensors for Wireless Monitoring of Infusion and Curing in Composite Production“*, pp. 261–263. SMSI 2023, Nuremberg.
  https://doi.org/10.5162/SMSI2023/E5.4.
- **Lukas Bertram**, Michael Brink and Walter Lang, *„Wireless, Material-Integrated Sensors for Strain and Temperature Measurement in Glass Fibre Reinforced Composites“*. Sensors vol. 23, Nr. 14 p. 6375, 2023-07-13, ISSN: 1424-8220.
  https://doi.org/10.3390/s23146375.
- **Lukas Bertram**, Michael Brink, and Walter Lang. *„A wireless strain sensor for measurement in composites“*.
  In Eurosensors XXXIV - Proceedings. Lecce, Italy, 2023-09-10.
  https://doi.org/10.3390/proceedings2024097049.

A.6 Supervised Works

The following student works have been conducted in context of this thesis:

- Master project: *Modelling and Simulation of Glass Fibre Reinforced Polymer with Sensor inlay*, Euphemia Agwa
- Master thesis: *Development, Assembly and Characterization of an Electronic Circuit for Measurement Data Acquisition on a Passive RFID Sensor Tag*, Hiril Patel
- Master thesis: *Characterization of a Wireless Temperature Sensor on a Passive RFID Tag*, Euphemia Agwa
- Master project: *Entwicklung eines RFID-Transponders mit integriertem OECT-Sensor (Development of an RFID interface for an OECT sensor)*, Nico Busch